

Dissertation
submitted to the
Combined Faculties for the Natural Sciences and for Mathematics
of the Ruperto-Carola University of Heidelberg, Germany
for the degree of
Doctor of Natural Sciences

Put forward by

Diplom-Physiker:
Born in:

Akın Yıldırım
Stuttgart, Germany

Oral examination:
20 July 2015

Compact Elliptical Galaxies

Akın Yıldırım

Max Planck Institute for Astronomy

Referees:

Dr. Glenn van de Ven
Prof. Dr. Volker Springel

Zusammenfassung / Abstract

In dieser Doktorarbeit wird ein Sample nahegelegener, kompakter, elliptischer Galaxien mit hohen zentralen stellaren Geschwindigkeitsdispersionen untersucht. Mittels qualitativ hochwertiger photometrischer und spektroskopischer Daten analysieren wir ihre strukturellen Eigenschaften und erstellen orbit-basierte dynamische Modelle um den Beitrag der stellaren und dunklen Materie sowie den Beitrag des supermassiven schwarzen Lochs zum Gesamtmassenbudget zu ermitteln. Wir zeigen, dass unser Sample kompakter elliptischer Galaxien Ausreißer in der Population lokaler elliptischer Galaxien darstellt, ihre Eigenschaften jedoch konsistent sind mit denen massiver und nicht-sternentstehender Galaxien bei Rotverschiebungen von $z \simeq 2$. Wir nehmen an, dass sich unser Sample seit $z = 2$ passiv weiterentwickelt hat, was uns ermöglicht diese Relikte nun in präzedenzloser Ausführlichkeit zu untersuchen. Alle unsere Objekte sind scheibenförmig und rotieren schnell, bar einer druckunterstützten Bulge Komponente, mit einem dominanten stellaren Massenanteil innerhalb des effektiven Radius. Wir finden ein übermassives schwarzes Loch in einer unserer Galaxien vor und vermuten, dass noch weitere Entdeckungen in unserem Sample folgen werden. Dies deutet stark darauf hin, dass das Wachstum eines supermassiven schwarzen Lochs nicht unmittelbar an das Wachstum eines Bulges gebunden ist. Abschliessend zeigen wir, dass drei von sieben Galaxien in unserem Sample in ein dunkles Halo eingebettet sind, mit eindeutigen Hinweisen für ein sehr massives Halo in insbesondere einem Objekt. Das dunkle Halo in diesem Object, NGC 1281, stellt innerhalb von 5 effektiven Radien 90 Prozent der Gesamtmasse dar. Die Verteilung der dunklen Materie ist jedoch nicht in Einklang zu bringen mit jenen, die im Rahmen kalter, dunkler Materie Simulationen prognostiziert werden.

—

In this thesis, a sample of nearby, compact, elliptical galaxies with high central stellar velocity dispersions are studied. By means of high quality photometric and spectroscopic observations, we analyse their structural properties and construct state-of-the-art orbit-based dynamical models to constrain their total mass budgets, including the contribution of stars, dark matter and a supermassive black hole. We demonstrate that our sample of compact ellipticals are outliers of the local population of elliptical galaxies, but their properties are consistent with massive and non-starforming galaxies at much earlier times ($z \simeq 2$). We postulate that our sample has passively evolved since $z = 2$, which allows us to investigate these relic galaxies in unprecedented detail. All our objects are disky fast-rotators, devoid of a prominent pressure supported bulge, with a dominant stellar mass component inside one effective radius. We were able to detect an over-massive supermassive black hole in one galaxy and suspect that more will be detected in our sample. This strongly indicates that the growth of a supermassive black hole is not necessarily linked to the growth of a bulge. Finally, we show that at least three out of seven galaxies in our sample are embedded in a dark halo, with unambiguous evidence for a very massive dark halo in one particular object. The dark halo in this object, NCG1281, constitutes 90 per cent of the total mass content within 5 effective radii, and the dark matter distribution cannot be reconciled with that predicted by cold dark matter simulations.

Acknowledgements

This thesis is a product of expensive data, hard labour, sleepless nights, endless days, passion and despair. It is centred on improving our knowledge of distant galaxies, which, however, would not have been possible without the support and encouragement of many people within reach. Some of them, I would like to mention here:

I owe much gratitude to my supervisors Remco van den Bosch and Glenn van de Ven for giving me the opportunity to join them on this incredible journey. They have been to me the best possible supervisors in every aspect. Thank you for sharing your enthusiasm, knowledge and wisdom. Your contributions to this thesis have been invaluable, and you have been a role model of a scientist for me. Simply put, you have been great.

I would like to thank my thesis committee members Thorsten Lisker and Ralf Klessen for their unwavering support and guidance. Volker Springel and André Schönig for their interest in my scientific work and their willingness to join my examination committee.

I would like to acknowledge my collaborators, colleagues and friends, who have, one way or the other, contributed to this work and to my professional and personal development throughout these years. In particular, Ronald Läsker, Mariya Lyubenova, Bernd Husemann, Jonelle Walsh, Karl Gebhardt, Kayhan Gültekin, Jenny Greene, Ignacio Martín-Navarro, Arjen van der Wel, Aaron Dutton, Robert Singh, Alex Büdenbender, Anahi Caldu Primu, Richard Hanson, Deniss Stepanovs and Maria Elena Manjavacas.

Many thanks also to Hans-Walter Rix for accepting me at MPIA, to Christian Fendt for being an exceptional coordinator of IMPRS, and to all employees of the Max Planck Institute for Astronomy for the wonderful atmosphere.

Last but not least, this thesis is dedicated to my family - my father, mother, brother and fiancée -, the most important people in my life and my backbone all along. There is no way to acknowledge their love, support and the sacrifices they have made during all these years. They had nothing but gave everything, providing me with all opportunities to pursue my dream. This work is as much yours as it is mine.

For my family

Contents

Zusammenfassung / Abstract	i
Acknowledgements	iii
Dedication	v
Contents	vii
1 Introduction	1
1.1 Galaxies	1
1.2 Early-Type Galaxy Evolution	3
1.2.1 Scaling Relations And Fundamental Plane	3
1.2.2 The Growth Of Early-Type Galaxies	4
1.2.3 The Merging Hypothesis	6
1.3 Supermassive Black Holes	9
1.3.1 The Black Hole Scaling Relations	9
1.3.2 Black Hole Demographics At High Redshift	11
1.4 Dark Matter Halos	14
1.4.1 Evidence And Nature	14
1.4.2 Dark Halo Structure And Properties	16
1.4.3 Controversies, Difficulties And Challenges	17
1.5 Compact, Elliptical, High Central Velocity Dispersion Galaxies	20
2 MRK 1216 & NGC 1277 - An orbit-based dynamical analysis of compact, elliptical, high central velocity dispersion galaxies	25
2.1 Introduction	26
2.2 Photometry	27
2.2.1 HST Imaging	27
2.2.2 MRK 1216	30
2.2.3 NGC 1277	32
2.3 Stellar Kinematics	33
2.3.1 PPAK	33
2.3.2 HET	35
2.3.3 MRK 1216	35
2.3.4 NGC 1277	36
2.4 Dynamical Analysis	36

2.4.1	Schwarzschild's Method	38
2.4.2	Mass Profiles	39
2.4.2.1	MRK 1216	39
2.4.2.2	NGC 1277	43
2.5	Discussion	45
2.5.1	Orbital Structure	45
2.5.1.1	MRK 1216	46
2.5.1.2	NGC 1277	47
2.5.1.3	Classification And Comparison	49
2.5.2	Black Hole	50
2.5.2.1	Masses	50
2.5.2.2	Scaling Relations	52
2.5.3	Dark Matter Halo	54
2.5.3.1	Dark Halo Detection	54
2.5.3.2	Dark Halos In Elliptical Galaxies	56
2.5.3.3	NFW Profiles	57
2.5.4	The Origin Of Compact, Elliptical, High Central Velocity Dispersion Galaxies	57
2.6	Uncertainties	59
2.7	Summary	64
3	The massive dark halo of the compact, early-type galaxy NGC 1281	67
3.1	Introduction	68
3.2	Data	69
3.2.1	HST Imaging	69
3.2.2	PPAK Kinematics	71
3.3	Dynamical Analysis	72
3.3.1	Schwarzschild Models	72
3.3.2	Modelling Results	73
3.4	Discussion	77
3.4.1	Alternative Halo Parameterisations	77
3.4.2	Implications And Caveats	77
3.4.2.1	The Dark Halo Profile	77
3.4.2.2	The Constant Stellar M/L	79
3.4.2.3	The Stellar IMF	79
3.4.2.4	The Black Hole	82
3.5	Summary	82
4	The structural and dynamical properties of compact, elliptical, high central velocity dispersion galaxies	85
4.1	Introduction	86
4.2	Data	88
4.2.1	HST Imaging	88
4.2.2	PPAK Kinematics	91
4.3	Classification	94
4.3.1	Fundamental Plane	94
4.3.2	Specific Stellar Angular Momentum	95
4.4	Dynamical Analysis	97
4.4.1	Schwarzschild Models	97
4.4.2	Modelling Results	98
4.5	Discussion	100
4.5.1	The Mass-Size Relation	100
4.5.2	The Stellar Mass Surface Density	102

4.5.3	Stellar And Dynamical Masses	104
4.5.4	The Total Mass Density Slope	105
4.6	Summary	107
5	Summary & Outlook	109
5.1	Summary	109
5.2	Outlook	112
A	Multi-Gaussian Expansion	115
	Bibliography	120

"If I have seen further it is by standing on ye sholders of Giants"

Isaac Newton

Introduction

1.1 Galaxies

Galaxies are among the largest scale structures in the universe, held together by the gravitational forces of its constituents, namely stars, interstellar gas and dark matter. They come in a variety of shapes and sizes, spanning multiple orders of magnitude in mass. While some of them are rather isolated, most of them are gravitationally bound to even larger structures, commonly referred to as galaxy groups, which in turn are associated with galaxy clusters and superclusters. Despite their association with the aforementioned larger scale structures, galaxies are usually treated as single building blocks of the universe, which have evolved in space and time through internal processes and external interactions. But, their formation and evolution into the structures that we commonly observe today is no coincidence.

Investigations by Edwin Hubble already indicated that the bulk of galaxies are made up of three individual classes, where each object can be placed into one of these according to their shape and appearance [Hubble, 1926]. Following Hubble, galaxies can be divided into: (i) Elliptical, featureless galaxies, (ii) flattened, spiral galaxies and (iii) lenticular galaxies which are also flattened, consisting of a bulge and an outer disk but devoid of any prominent spiral features. This morphological classification, also known as the *Hubble Sequence of Galaxies* or commonly referred to as *Hubble's Tuning Fork*, represents one of the earliest attempts to characterise and link galaxies and to draw conclusions about their evolutionary history. Despite improvements in observational facilities, leading to the detection of finer substructures such as bars, rings, tighter and looser spiral arms as well as irregular and dwarf galaxies, the *Hubble Sequence Of Galaxies* has proven to be an efficient, easy and robust tool for the characterisation and understanding of these objects.

On the left hand side of the Hubble tuning fork (Fig. 1.1) are the ellipticals, starting with the most spherical objects which have an ellipticity of $\epsilon = 1 - b/a = 0$, where b and a are the apparent minor and major axis lengths. The fork itself is comprised of barred (bottom) and non-barred spiral galaxies (top), while lenticular galaxies are usually placed where the two prongs of the fork meet each other.

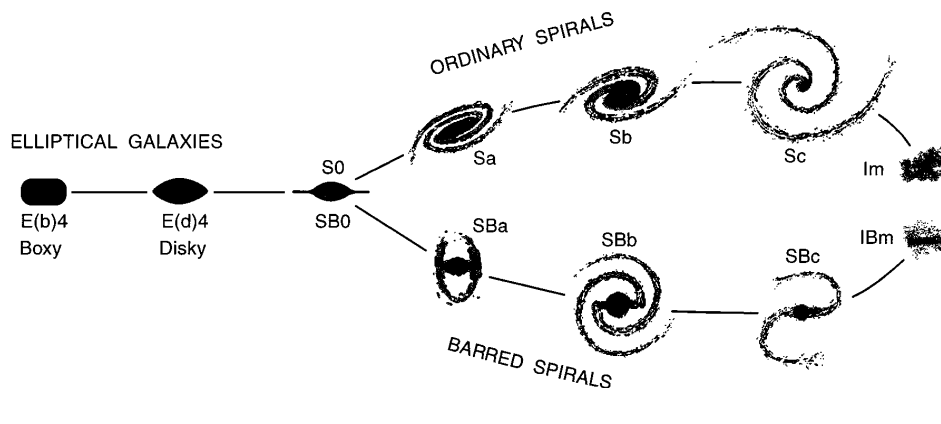


Figure 1.1: The revised *Hubble Sequence of Galaxies*, also commonly known as the *Hubble Tuning Fork*. Credit: Kormendy & Bender [1996].

Hubble realised that the different classes in his *tuning fork* illustrate a continuous sequence of galaxies with increasing structural complexity from the left to the right, and therefore concluded that these objects do not represent the end stage of different galaxy formation channels but rather depict different epochs in the evolution of galaxies of one and the same formation channel. According to Hubble, ellipticals (also labeled as "early-type galaxies") evolve into spiral galaxies (also referred to as "late-type galaxies"). This simple yet powerful description of galaxy evolution, however, turned out to be false. We now know that the *Hubble Sequence Of Galaxies* is more than just a morphological sequence but also tightly coupled to the different physical properties of galaxies, such as their luminosity, mass, colour, star formation rate etc. For instance, stars in ETGs are generally older than their counterparts in LTGs. LTGs do also show a higher rate of specific star formation in contrast to ETGs, which have depleted much of their gas reservoir. Moreover, LTGs are rotationally supported whereas the most massive elliptical galaxies do not show any significant amount of net rotation at all. These arguments are difficult to reconcile with an evolution from the left to the right in the *Hubble Tuning Fork*. On the contrary, we have now gathered a body of evidence, from an observational as well as theoretical point of view, that LTGs are more likely to evolve into ETGs than the other way round.

The details of this evolution, however, remain elusive and provide the overall motivation for this work. In the following subsections, the state of affairs in galaxy formation and evolution will be presented: Sec. 1.2 will revisit the progress in our understanding of the physical properties of the apparently very uniform population of local (≤ 100 Mpc) ETGs, and in particular of its stellar content. We will trace their evolution back in time, to redshifts of $z \simeq 2$, and uncover their drastic growth in mass and size. This, in turn, yields information regarding the feasibility of different formation and evolution mechanisms. We will highlight the success and shortcomings of these mechanisms.

Supermassive black holes will be discussed in Sec. 1.3, where we illustrate the tight relationship between their masses and several host galaxy properties and hence their importance in shaping the evolution of galaxies. However, these relations, also commonly known as the "black hole scaling relations", break down at higher redshift indicating that we yet lack a complete theory in which black hole and galaxy grow in lockstep.

Sec. 1.4 then covers dark matter, the principal mass component of galaxies, which is responsible for the large-scale evolution of galaxies in a universe where structures grow hierarchically. We will focus on

efforts and difficulties to constrain the dark matter content in galaxies, which is necessary to provide the missing link between baryonic and non-baryonic matter. And finally introduce the sample of compact, elliptical galaxies with high central velocity dispersions in Sec. 1.5, which are powerful laboratories to gain insight into the role of stars, black holes and dark matter, and key for a more thorough understanding of galaxy formation and evolution in general.

1.2 Early-Type Galaxy Evolution

1.2.1 Scaling Relations And Fundamental Plane

Early-type galaxies constitute only a small fraction of the total galaxy population ($\sim 20\%$), but comprise a majority of the total stellar mass ($\sim 60\%$) [Fukugita et al., 1998; Hogg et al., 2002; Bell et al., 2003; Baldry et al., 2004]. In addition, most ETGs are more abundant in dense environments, while LTGs seem to prefer less dense populated regions in space [Dressler, 1980]. Understanding how the bulk of stellar mass ended up in a rather small and apparently very uniform sample of galaxies, and why these preferentially are found in cluster-like environments poses one of the most difficult but important challenges in the field of galaxy formation and evolution.

To seek insight into the processes which drive this evolution, and further propelled by the advent of large scale sky surveys such as the Sloan Digital Sky Survey (*SDSS*) [York et al., 2000; Stoughton et al., 2002; Abazajian et al., 2003], statistically meaningful samples of ETGs have been investigated. As indicated earlier, the *Hubble Sequence of Galaxies* does not only depict a continuous sequence in morphology, but also in physical parameter space. Galaxy properties vary smoothly as a function of morphology. More interestingly, though, many of these parameters are narrowly correlated. Strong correlations between velocity dispersion and luminosity [Minkowski, 1962; Faber & Jackson, 1976], half-light radius and luminosity [Kormendy, 1977], the strength of the Mg_2 line and the velocity dispersion [Terlevich et al., 1981; Dressler, 1984; Burstein et al., 1987; Bender et al., 1993] and between colour and magnitude [Faber, 1973; Sandage & Visvanathan, 1978a,b; Bower et al., 1992] have been found. These investigations culminated in the discovery of the "Fundamental Plane" (FP) [Djorgovski & Davis, 1987; Dressler et al., 1987], a relation between effective size, effective velocity dispersion and effective surface brightness. The FP can be used as a tool for the determination of distances, but more importantly holds clues concerning galaxy evolution. Since two of the three parameters are approximately distance independent, the relation is generally expressed in terms of:

$$R_e \propto \sigma_e^a I_e^{-b} \quad (1.1)$$

The measurement of the coefficients of this relation, by e.g. minimising the scatter in R_e , yields best-fitting values of $1.2 \leq a \leq 1.5$ and $b \simeq 0.8$ [e.g. Jorgensen et al., 1996; Pahre et al., 1998; Bernardi et al., 2003; Hyde & Bernardi, 2009] (Fig. 1.2). Assuming that ETGs are systems in virial equilibrium (i.e. in a state where the time averaged potential and kinetic energies are in balance), however, one would expect:

$$G M_{dyn} R^{-1} \propto M_{dyn} L^1 R^{-2} R L^{-1} \propto M_{dyn} I R L^{-1} \propto \sigma^2 \quad (1.2)$$

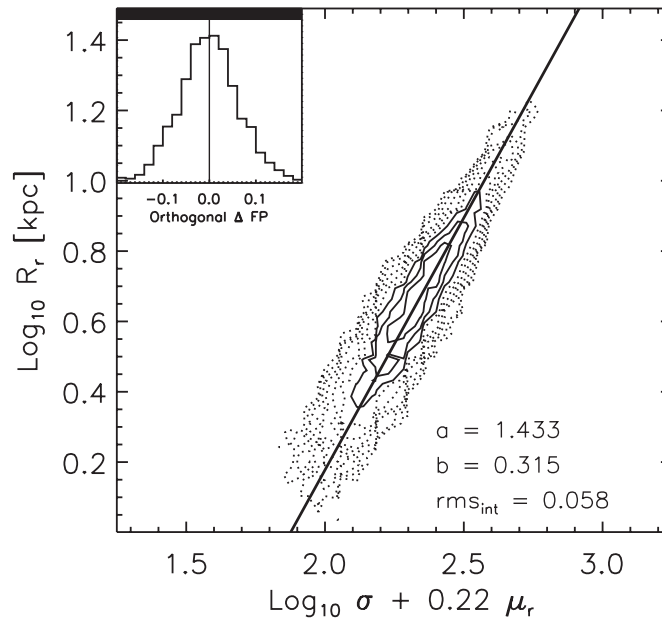


Figure 1.2: The Fundamental Plane in r -band of $\sim 50\,000$ early-type galaxies from the *SDSS* (DR4). Credit: Hyde & Bernardi [2009].

and ergo $a = 2$ and $b = 1$. Non-homology (i.e. variations in their structural and orbital properties) cannot account for a significant deviation from the virial predictions. And the difference, also commonly known as the "tilt" of the FP, is therefore interpreted as a gradual change of the dynamical mass-to-light ratio ($M_{dyn}/L = \Upsilon_{dyn}$) as a function of e.g. stellar mass. The change in Υ_{dyn} , again, is explained by either a change in the stellar populations (e.g. brighter and more massive galaxies tend to be more metal rich, even if metallicity alone cannot account for the tilt) and hence in the stellar mass-to-light ratio (Υ_*) or in the dark matter fraction of ETGs along the FP [e.g. Renzini & Ciotti, 1993]. While it is difficult to dissect the contributions of dark matter and Υ_* to the tilt of the FP, the tightness is remarkable and hints at processes which are very effective in producing a uniform galaxy population where the stellar structure and content are closely related to the underlying total mass. Most recent investigations point at strong variations in the stellar M/L, also partially attributable to changes in the stellar initial mass function (IMF), as the main driver of the observed tilt [e.g. Cappellari et al., 2006; Treu et al., 2010; Auger et al., 2010a; Cappellari et al., 2013a] [but see e.g. Padmanabhan et al., 2004, arguing the contrary]. Therefore, understanding the stellar populations becomes key to our understanding of ETGs in general.

1.2.2 The Growth Of Early-Type Galaxies

The stellar populations of a galaxy present a fossil record of its evolutionary history. Stellar age estimates of present-day ETGs indicate a very old stellar population (≥ 10 Gyr) [Bower et al., 1992; Gallazzi et al., 2006; Jimenez et al., 2007; Graves et al., 2009a,b]. In the "monolithic collapse" model [Eggen et al., 1962], galaxies are assumed to form very early and on short time scales from the collapse of large, Jeans-unstable gas clouds [Jeans, 1902] in a single star burst event [Larson, 1969]. Depending on the relative timescales of star formation and the dissipative nature of the collapse, ETGs or LTGs are

formed. If the collapse is dissipationless, the motion of stars - which emerge through the gravitational collapse of small gas instabilities in the cloud - is random, resembling systems which look like ETGs. On the other hand, if the release of gravitational energy during the collapse can be dissipated through, e.g. radiative cooling, then angular momentum conservation during the shrinking phase will result in a rotationally supported system of stars, similar to LTGs. According to this picture, though, ETGs should have formed very early and are expected to undergo a long phase of passive evolution with little to no structural evolution. While the old stellar populations of present-day ETGs match the predictions of the monolithic collapse scenario, observations at higher redshift draw a vastly different picture and point at inconsistencies between both, model and observations. First, the number density of ETGs steadily increases since $z = 1$, in contrast to modelling expectations where it is assumed to remain constant [Kauffmann & Charlot, 1998]. The growth in number density is accompanied by a "downsizing" effect [Cowie et al., 1996], which shows that less massive systems quenched star formation later and entered the red, passive ETG branch only recently. Second, studies at redshift $z \simeq 2$ reveal a population of massive, red galaxies [Franx et al., 2003; van Dokkum et al., 2003]. These are presumably descendants of the submillimeter galaxy population at $z = 3$ [see Toft et al., 2014, and references therein] where the intense star formation rates have been triggered by gas-rich major mergers at even higher redshifts [Khochfar & Silk, 2006; Naab et al., 2007; Wuyts et al., 2010], or products of Toomre unstable disks [Toomre, 1964] which are fuelled by cold gas from the intergalactic medium (IGM) along filaments through the halo [Birnboim & Dekel, 2003; Kereš et al., 2005; Dekel et al., 2009; Dekel & Burkert, 2014]. While these massive ETGs are found to be very compact at $z \simeq 2$ [Daddi et al., 2005; Trujillo et al., 2006; Zirm et al., 2007; van der Wel et al., 2008; van Dokkum et al., 2008; Szomoru et al., 2010; Newman et al., 2012; van der Wel et al., 2014], following their evolution through cosmic time by tracing a population of galaxies at constant number density shows that their sizes increase by a factor of 4-5 while their masses nearly double [e.g. Bezanson et al., 2009]. Since star formation is already quenched at $z \simeq 2$ for roughly 50 per cent of this massive galaxy population [Williams et al., 2009], it is insufficient to explain the mass and size growth [Kriek et al., 2006; Toft et al., 2007; Cimatti et al., 2008; Kriek et al., 2008]. Moreover, most of the mass is added in the outer parts which promotes and inside-out growth [Hopkins et al., 2009a; van Dokkum et al., 2010; Auger et al., 2011; Pérez et al., 2013; Patel et al., 2013] (Fig. 1.3). Also, the compact, quiescent galaxies at higher redshift are found to be much more flattened and disky than their potential counterparts today [Toft et al., 2005; Trujillo et al., 2006; van Dokkum et al., 2008; van der Wel et al., 2011; Szomoru et al., 2012], with Sérsic indices $n \leq 4$ in most cases (i.e. with shallower surface brightness distributions than the classical de Vaucouleurs profile [de Vaucouleurs, 1948]).

The stellar populations in the remote regions of present-day ETGs should therefore provide information concerning the violent growth in size and mass since $z = 2$, which cannot be explained by a simple passive evolution of the stellar populations, as suggested by the monolith collapse scenario. Spatial colour information, a tracer of stellar population gradients, have been a useful tool to understand the stellar build-up of ETGs and suggest that ETGs are bluer towards the outer parts [Franx et al., 1989; Peletier et al., 1990a,b]. However, the lack of suitable spectral data inhibits to break the degeneracy between age and metallicity which can equally well account for the colour change [Worthey et al., 1994]. Spectral information of $z = 0$ ETGs are now ample, but usually confined to the stellar populations in their central regions due to the rapid decline in their surface brightness distributions [Rawle et al., 2008; Graves et al., 2009a,b; Tortora et al., 2010; Kuntschner et al., 2010]. Recently, however, data well beyond the effective radius have become available which show a decrease in metallicity and an

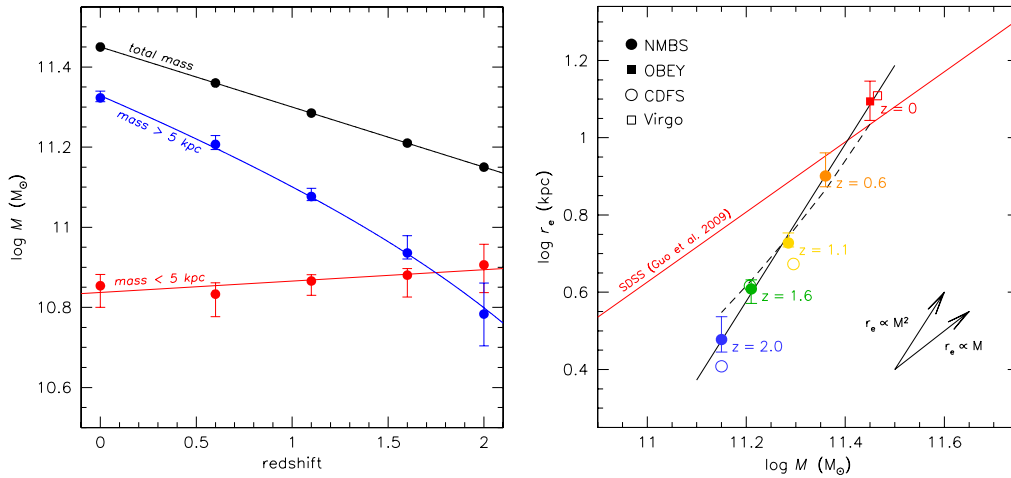


Figure 1.3: *Left:* The mass evolution of early-type galaxies since $z = 2$, within different distances from the centre. The mass increase is due to mass addition beyond 5 kpc. *Right:* The mass-size evolution of early-type galaxies since $z = 2$, following a relation similar to $R_e \propto M_*^2$. Credit: van Dokkum et al. [2010].

increase in α -abundance towards the most outer parts [Greene et al., 2012, 2013; La Barbera et al., 2012] [but see: Sánchez-Blázquez et al., 2007, for contradicting results]. Lower metallicities indicate lower gravitational potential wells in which the stars have formed [Larson, 1974], while the high α -abundance traces the relative abundance of Type II to Type I Supernovae (SNe) and therefore hints at rapid formation timescales [Matteucci & Greggio, 1986; Thomas et al., 2005a]. These results indicate a two-phase growth, where the recent mass-size evolution of ETGs since $z \simeq 2$ is likely to be of extragalactic nature, with a central, flat and massive component which has formed early ($z \geq 2$) followed by a subsequent assembly of stars from smaller galaxies through cannibalism, which have then been deposited in the outer parts leading to a puffed up massive host.

1.2.3 The Merging Hypothesis

Faced by an increasing amount of observables which could not be reconciled with predictions of the monolithic collapse theory, alternative formation and evolution scenarios have been put forward. Based on observations of tidal tails and irregularities during mergers of galaxies, the idea of hierarchical merging has emerged [Toomre & Toomre, 1972; Toomre, 1977]. Adopted and put into a cosmological framework - where hierarchical merging becomes a natural outcome of the purely gravitational interactions between luminous galaxies which are embedded in massive dark halos [White & Rees, 1978] - numerical N -body simulations of equal mass (spiral-)mergers have been carried out, which can reproduce spheroids that share many of the physical properties of today's ETG population [Barnes, 1988, 1989; Kauffmann et al., 1993; Kauffmann, 1996; Barnes & Hernquist, 1996]. Shortcomings to this picture however remain, concerning e.g. the higher phase space density in ellipticals in contrast to the lower phase space density in spiral galaxies [Ostriker, 1980; Carlberg, 1986]. If today's ETG population is a remnant of spiral galaxy interactions, then the phase space density should be conserved or decline during the merging process, according to the collisionless Boltzmann equation. Shortcomings have been alleviated, e.g. i) by assuming more concentrated progenitors to solve the phase space discrepancy [Hernquist, 1993], ii)

by considering dissipational and dissipationless mergers to recover the tilt in the FP [Robertson et al., 2006; Hopkins et al., 2009b] and iii) by allowing equal and non-equal mass mergers [Naab et al., 1999; Bendo & Barnes, 2000; Naab & Burkert, 2003] to account for the observed variety in the kinematic and photometric properties of brighter, boxy, slow-rotating and fainter, disk, fast-rotating ETGs [Davies et al., 1983; Bender, 1988; Kormendy & Bender, 1996] [but see also: Cox et al., 2006]. However, these simulations imply strong assumptions regarding the dynamical structure and physical properties of the progenitors, namely i) their bulge-to-disk fractions, the bulge- and disk parameterisation as well as non-rotating dark matter halos which have to serve as a storehouse for the removal of angular momentum from the baryonic matter through resonant interactions ii) non-negligible gas fractions, and prescriptions for star formation, black hole accretion and SNe feedback and iii) the spin-alignment and orientation of the progenitors. More importantly, though, these simulations cannot explain the strong mass-size evolution and the stellar population characteristics of present-day ETGs and their likely progenitors at $z = 2$, which raise a purely wet (i.e. gas-rich) or dry (i.e. gas-poor) major merger scenario into question. Major mergers are not only rare [Bundy et al., 2007, 2009; Hopkins et al., 2010b; Man et al., 2012] but to reconcile both the mass-size relation of ETGs at high and low redshift, the required level of mergers would result in an overabundance of massive galaxies in the local universe, in conflict with the galaxy stellar mass function [McLure et al., 2013]. Moreover, binary mergers of disk galaxies fail to reproduce the detailed dynamical properties of a large sample of local ETGs [Cappellari et al., 2007] - such as the relationship between their intrinsic ellipticity (ϵ_{intr}) and anisotropy parameter (δ) [Burkert et al., 2008] - as well as the masses and metallicities of typical ellipticals [Naab & Ostriker, 2009].

Based on the assumption of a two-phase growth, as promoted by the observations, numerical merger remnants of highly unequal mass mergers have been studied [Bournaud et al., 2008; Naab et al., 2009; Oser et al., 2010, 2012; Lackner et al., 2012; Hilz et al., 2012, 2013; Bédorf & Portegies Zwart, 2013]. There is now a general agreement that dry minor mergers with mass ratios of $\sim 1:5$ can indeed recover the mass-size evolution, in contrast to equal-mass mergers which will result in a comparable evolution in mass and size (Fig. 1.4). But, doubling the mass since $z = 2$ would thus require ~ 5 minor mergers for each progenitor. For a $\simeq 10^{10} - 10^{11} M_{\odot}$ progenitor the minor companion would still have a significant mass at which gas-rich systems are more common than gas-poor at those redshifts. This should result in more recent nuclear star formation activity, increasing the central stellar densities, which however is in contrast to the lower central densities that are commonly observed in regular, massive present-day ETGs. In addition, the minor merging process is governed by dynamical friction [Chandrasekhar, 1943] which ultimately leads to an orbital decay of the smaller merging partner until it is dispersed by the tidal forces of the larger host. The orbital decay and merging process for highly unequal mass mergers, however, will not only take several Gyrs [e.g. Colpi et al., 1999], but i) the rate of minor mergers since $z = 2$ is too low [Lotz et al., 2011], ii) their contribution to the mass-size evolution most likely overestimated [Newman et al., 2012; Cimatti et al., 2012; Oogi & Habe, 2013] and iii) successive minor merging events would yield an increased scatter in ETG scaling relations, stronger than currently observed [Nipoti et al., 2012].

Hopkins et al. [2010a] examined the contribution of various processes which might contribute equally well to this evolution, including major and minor mergers, adiabatic expansion through significant mass loss e.g. due to quasar feedback [Fan et al., 2008, 2010], the presence of stellar M/L gradients (which can induce differences between the measurement of the optical effective radius and the stellar mass

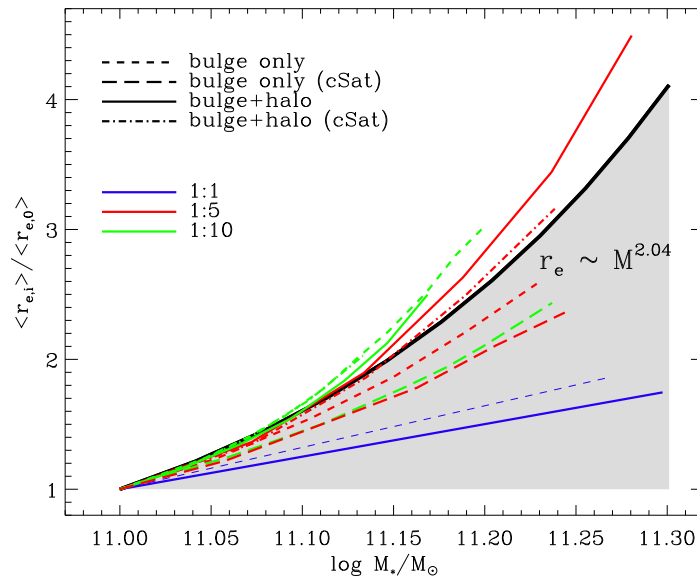


Figure 1.4: The simulated mass-size evolution of massive galaxies for equal and non-equal mass mergers, including and excluding a dark matter halo. Credit: Hilz et al. [2013].

effective radius) as well as redshift dependencies in e.g. the stellar mass estimates. Each of these processes will yield a different path in the mass-size plane and hence a galaxy population with different characteristics. By limiting the impact of each mechanism, through comparison with different observational properties of ETGs through redshift, one can reconstruct a track where the contribution of each channel is then optimally weighted to recover the observational constraints. As indicated earlier, minor merging alone cannot account for the evolution - even though it is the dominant driver - and each of the remaining mechanisms apparently has a non-negligible role in explaining the evolution. Certainly, minor and major merging is not only mandatory in a universe where structures grow hierarchically (see Sec. 1.4) but also required given the strong growth in size and mass and the morphological transition from flat, disk and rotationally dominated structures to more spherical and pressure supported systems [e.g Chang et al., 2013]. However, given the many additional mechanisms that had to be taken into account in the simulations of Hopkins et al. [2010a] to recover their evolution, it remains puzzling how galaxies can fine-tune these in order to evolve into a uniform population that obeys such remarkably tight scaling relations.

An alternative interpretation of the observations indicates that other factors, such as the appearance of a significant population of quenched ETGs at later epochs, might be important too, to account for the extreme increase in the number density of ETGs with time [Valentinuzzi et al., 2010; Cassata et al., 2011; Poggianti et al., 2013; Newman et al., 2012; Carollo et al., 2013; Cassata et al., 2013]. With decreasing redshift, the average size of ETGs increases; the decrease in the number density of compact ETGs, however, cannot sustain the increase in the total number density of ETGs at $0 \leq z \leq 1$. This might hint at two distinct physical processes that drive the evolution of ETGs. An early phase, which - as outlined above - is generally attributed to the successive minor merging growth of quiescent, compact ETGs since $z \leq 2$, and an independent late phase at $z \leq 1.5$ where massive and already larger galaxies

join the ETG population by bypassing the compact phase.

Summary:

ETGs are comprised of a uniformly old stellar population, which has evolved passively for the last 10 Gyr. The analysis of stellar population gradients indicates that stars in the remote regions have formed in different environments than the bulk of stars in the centre. This is supported by observations of ETGs through cosmic time, where the violent growth in their sizes since $z \simeq 2$ outpaces their mass growth and hints at processes which have changed their structural properties more efficiently than their total stellar mass content. This is at odds with the monolithic collapse scenario, where galaxies are assumed to undergo little structural evolution since their formation. Mergers, as expected in a hierarchically growing universe, can recover many properties of today's ETGs. Dissipationless major mergers can reproduce boxy, slow-rotating galaxies while dissipative mergers tend to result in fast-rotating, disk galaxies. But major mergers are rare and cannot recover the mass-size evolution of ETGs. Simulations of dissipationless minor mergers have been able to grow galaxy sizes while increasing their masses only moderately. However, the minor merging rate is inefficient in both time and number and the (observational) mass and size contribution due to minor merging most likely insufficient to explain the pace in the overall mass-size evolution. Additional processes are therefore necessary, but simulations show that these have to be fine-tuned in order to recover the tight scaling relations, such as the FP. Finally, observations at high redshift are prone to many systematic uncertainties. In particular tracing the number density through cosmic time as a function of size is difficult, but most recent observations can be interpreted as a two-channel evolution where compact ETGs at $z \simeq 2$ evolve mainly through (minor-)merging events and get company by a population of already larger ETGs at $0 \leq z \leq 1$, which have evolved differently.

1.3 Supermassive Black Holes

1.3.1 The Black Hole Scaling Relations

Pioneering work via ground based detections have provided unambiguous evidence for the presence of supermassive black holes (SMBH) in the centre of most, if not all, galaxies [Sargent et al., 1978; Tonry, 1984; Kormendy, 1988]. While initial detections based only on a handful of galaxies [Kormendy & Richstone, 1995], where measurements were barely feasible, the advent of the Hubble Space Telescope (*HST*) quickly propelled the exploration and identification of more objects. After two decades of black hole mass estimates via dynamical modelling [e.g. Magorrian et al., 1998], reverberation mapping [e.g. Wandel et al., 1999] and maser kinematics [e.g. Kuo et al., 2011], their masses have been constrained in more than 90 galaxies and we have gained deeper insight into their role and significance in the formation and evolution of stellar systems.

As intuitively anticipated, the most massive black holes tend to reside at the most luminous/massive galaxies. More interesting, though, is the discovery of correlations between the dynamically inferred black hole masses and several host galaxy properties. These correlations link the central black hole mass (M_{\bullet}) to the stellar velocity dispersion ($\propto \sigma^{4.2}$) [Gebhardt et al., 2000; Ferrarese & Merritt, 2000;

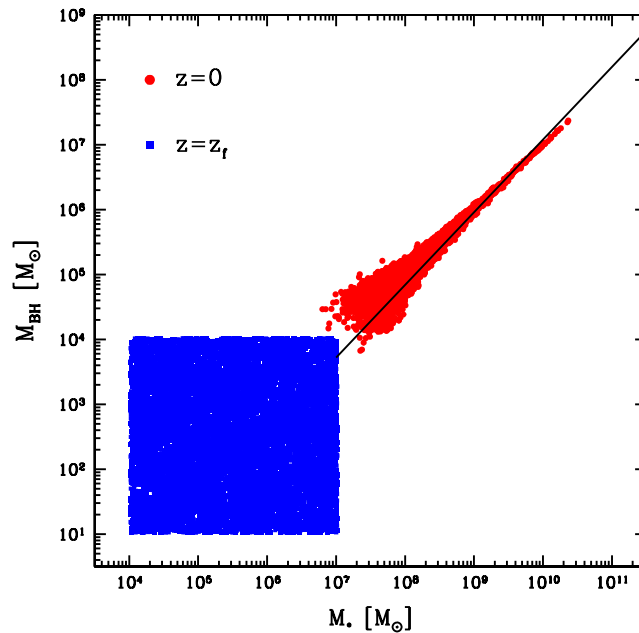


Figure 1.6: The emergence of the black hole scaling relations from an initially uncorrelated distribution of galaxies with central SMBHs, following a hierarchical merger tree. Credit: Jahnke & Macciò [2011].

Alternatively, Peng [2007] as well as Jahnke & Macciò [2011] reduce the relations to hierarchical galaxy-galaxy mergers. Following a Λ CDM merger tree, the black hole scaling relations emerge as a result of a purely statistical convergence process without the need of any physical coupling (Fig. 1.6). More intuitive theories, on the other hand, try to trace the relations back to a co-evolving black hole and bulge, which are simultaneously fed by material during subsequent galaxy-galaxy mergers [Kormendy et al., 2011].

Since the prediction of very tight scaling relations is common to all aforementioned theories, the true origin that links and regulates black hole and galaxy growth still remains unknown. However, internal processes, such as secular evolution [see: Kormendy & Kennicutt, 2004, for a review], will move galaxies differently in the mass-size plane than external processes [see: Cappellari et al., 2013b], such as merging (as is expected if the BHSR arise solely through an averaging of galaxy properties due to merging). But, the sample of available black hole masses is strongly clustered in their host galaxy properties and most importantly in the mass-size plane [van den Bosch et al., 2015]. Such being the case, the current crop of local black hole masses is insufficient to distinguish between the different co-evolutionary paths.

1.3.2 Black Hole Demographics At High Redshift

As an alternative, investigating the black hole demographics at higher redshifts could be helpful in ruling out individual scenarios, as for instance Jahnke & Macciò [2011] predict an increased scatter with increasing lookback time. However, the aforementioned theories appear to be at odds with the evolution of black hole mass vs. host galaxy velocity dispersion over cosmic time. Based on broad emission line widths to constrain the black hole masses of AGN at high redshift, the correlation between black hole mass and host galaxy properties are significantly offset by $\Delta \log M_{\bullet} = 0.62 \pm 0.1$, already at $z \simeq 0.5$

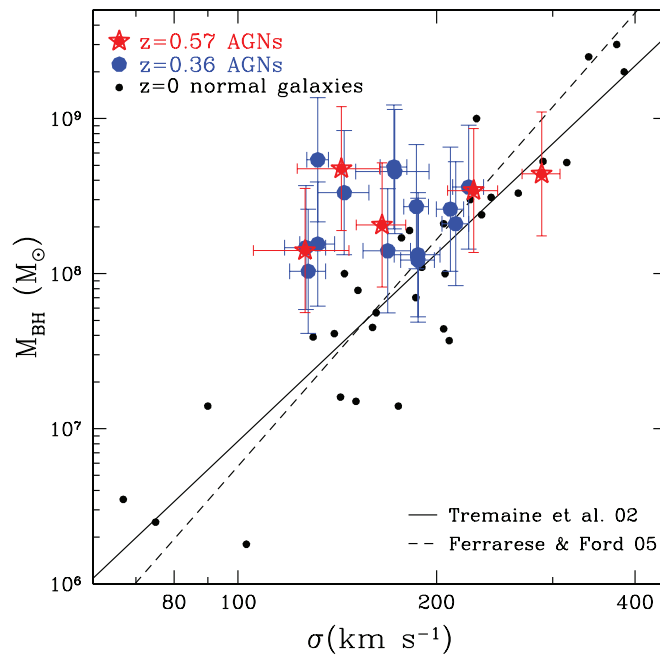


Figure 1.7: The distribution of black hole mass vs. bulge velocity dispersion for AGNs at different redshift. Credit: Woo et al. [2008].

[Woo et al., 2006, 2008](Fig. 1.7). Similarly, Jahnke et al. [2009] find no evolution in the relation between black hole mass and galaxy total stellar mass. But as galaxies at high redshift are disk dominated, this strongly implies an evolution in the black hole mass-bulge mass relation, with processes being at work which have redistributed mass from the disk to the bulge since $z = 2$ efficiently.

More recent studies even go one step further and claim an evolution in both the $M_{\bullet} - M_{\star}$ and $M_{\bullet} - M_{bul}$ relation [Merloni et al., 2010; Bennert et al., 2011], and evidence for very massive black holes at even higher redshifts ($3 \leq z \leq 6$) have mounted in the meantime [e.g. Fan et al., 2001, 2003; Barth et al., 2003; Walter et al., 2004; Willott et al., 2005; Greene et al., 2010a].

The detection of black holes in the range of $M_{\bullet} \geq 10^9 M_{\odot}$ at $z = 6$, i.e. at times where the universe was less than 10 per cent of its current age [e.g. Mortlock et al., 2011; Wu et al., 2015], is not only a challenge for theories which predict a mutual growth of black hole and host galaxy, but also to models of black hole formation and evolution itself. To grow so rapidly they warrant a constant, ceaseless accretion at the Eddington rate (assuming a common radiative efficiency of ~ 0.1), which appears to be very unlikely. Thus, alternative scenarios have been explored, including massive black hole seeds - e.g either through the formation and subsequent collapse of massive, metal-free Population III stars [e.g. Omukai & Nishi, 1998; Bromm et al., 1999; Abel et al., 2000, 2002; Madau & Rees, 2001; Tan & McKee, 2004] or the direct collapse of protogalactic, molecule-free gas in dark halos [Haehnelt & Rees, 1993; Loeb & Rasio, 1994; Bromm & Loeb, 2003] - which then grow through mergers [Petri et al., 2012] and/or by temporarily super Eddington accretion rates [Volonteri & Rees, 2005; Wyithe & Loeb, 2012]. Note though that photoionisation by massive population III stars can evacuate their vicinity and expel gas totally if the surrounding dark halo is not massive enough [Whalen et al., 2004; Kitayama et al., 2004], thus leaving no fuel for the later growth of the black hole, whereas it remains to be seen if the paucity

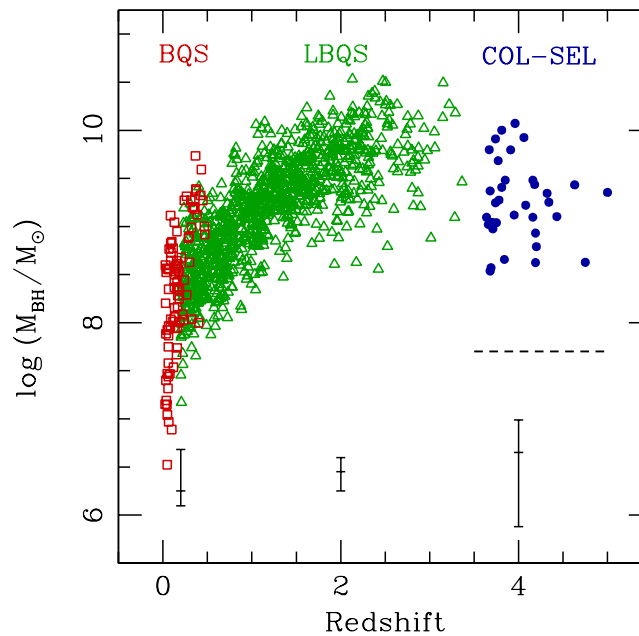


Figure 1.8: The distribution of black hole mass estimates for different quasar samples at different redshifts. The bars on the bottom depict the typical measurement errors at the corresponding redshifts. Credit: Vestergaard & Osmer [2009].

of cloud fragmentation and molecular hydrogen can be maintained in the direct collapse scenario [e.g. Dijkstra et al., 2008][but see: Volonteri, 2010, for a detailed review of early black hole formation].

The detection of SMBHs at high redshifts indicates that massive black holes do not follow the mass assembly history of their hosts, thus questioning both a causal and non-causal relation between both [Shields et al., 2006; Vestergaard, 2009; Vestergaard & Osmer, 2009]. At the same time, however, numerous studies [e.g. Richstone et al., 1998] show that the peak of AGN activity ($2 \leq z \leq 3$) [Richards et al., 2006] roughly coincides with the peak in the star formation rate (SFR) density [Boyle & Terlevich, 1998; Hopkins & Beacom, 2006; Madau & Dickinson, 2014]. While both black hole accretion and star formation rate depend on a cold gas supply, which is more abundant at higher redshift than at lower, the spatial scales at which star formation and black hole accretion work are substantially different and it remains difficult to bridge both. Moreover, a correlation between the peak of AGN activity and the culmination in the cosmic star formation history is at variance with our intuitive understanding of AGN feedback, which is assumed to remove gas and hence quench star formation efficiently.

In any case, the quasar distribution function shows that massive black holes have formed very early (Fig. 1.8), and were overwhelmingly more numerous at high redshift than at low redshift. Thus it is obvious that many (potentially over-)massive black holes should be lurking in present-day galaxies and that this may alter the currently adopted black hole scaling relations. In fact, recent detections of over-massive black holes in galaxies with small bulges [Greene et al., 2008; Rusli et al., 2011; McConnell et al., 2011; Husemann et al., 2011; Bogdán et al., 2012; van den Bosch et al., 2012; Walsh et al., 2015] and under-massive black holes in galaxies with large bulges [Nowak et al., 2008; Schulze & Gebhardt, 2011] question the current picture of a tight, universal relation and point out that the physical mechanisms of a putative co-evolution are far from being well understood.

The discovery of massive outliers, however, puts more at stake than just our understanding of the underlying black hole physics, but also our understanding of galaxy formation and evolution in general. Semi-analytical models have successfully implemented AGN feedback loops, which can in principle not only explain the coupling between SFR and black hole growth and the black hole-host galaxy co-evolution but are also essential to recover e.g. the exponential decline in the galaxy stellar mass function at the upper end [Di Matteo et al., 2005; Bower et al., 2006; Croton et al., 2006; Somerville et al., 2008]. Therefore, investigating the (statistical and physical) shortcomings and uncertainties in the quantification of the black hole scaling relations, i.e. its universality and functional form and/or validity at the high- and low mass end, is important. Currently, the shortcomings of the black hole scaling relations are most evident in the restricted sample of dynamically inferred black hole masses, with less than a hundred measurements to date; the non-negligible scatter; the unaddressed role and significance of the outliers, the only sparsely sampled massive side of this relation, which is due to the steep decline in the number of galaxies with very high velocity dispersion [Sheth et al., 2003; Bezanson et al., 2011], and the sparse sampling in host galaxy properties in general. Furthermore, there is a discrepancy in the prediction of the $M_{\bullet} - \sigma$ and $M_{\bullet} - L$ relation, which becomes apparent at the high mass end [Lauer et al., 2007].

As a consequence, more measurements are necessary to overcome the limitations and to get a better insight into the nature and extent of the black hole-galaxy connection, if there is any.

Summary:

Relations between the masses of supermassive black holes in the centres of galaxies and their host galaxies' properties indicate a tight coupling between both. Theoretical arguments based on AGN feedback or averaging of galaxy properties - by means of random hierarchical mergers in the context of a cold dark matter dominated universe - have been successful in explaining this link. Observations at higher redshift, however, show strong deviations from the currently adopted scaling relations and indicate that massive black hole formation has preceded galaxy formation. Moreover, the quasar distribution function shows that many (over-)massive black holes must still be lurking in the centres of nearby galaxies. Indeed, recent detections over- and under-massive black holes question a tight universal relation. Increasing the sample of black hole masses (at high and low redshift) will be helpful to further explore the link and relation between black hole and host galaxy, and could be able to discriminate between the different formation and coupling mechanisms.

1.4 Dark Matter Halos

1.4.1 Evidence And Nature

Dark matter is a natural, ubiquitous element in the universe. Due to its non-interacting nature with electromagnetic radiation, though, it has defied an easy and early detection and we had and still have to rely on indirect measurements to establish its presence. First indications were based on the motion of stars in the Milky Way (MW) disk [Oort, 1932] and the motion of galaxies within the Coma cluster [Zwicky, 1937]. In particular Zwicky's investigations have provided unambiguous evidence for the existence of

dark matter. Based only on simple virial arguments, he found an average galaxy mass of $\bar{M} = 5 \times 10^{10} M_{\odot}$ in the Coma cluster. Given the cluster's total luminosity, this implied an astonishing mass-to-light ratio of $\simeq 500$, clearly suggesting the presence of an unknown dark component. Corroborating evidence for dark matter in individual galaxies have followed [Ostriker et al., 1974; Einasto et al., 1974], with the most compelling evidence based on extended, flat HI rotation curves in spiral galaxies [Rubin et al., 1980; van Albada et al., 1985].

Dynamically independent measurements of anisotropies in the cosmic microwave background (CMB) [Spergel et al., 2003], combined with distance measurements of Type Ia SNe [Riess et al., 1998; Perlmutter et al., 1999], have lent further support for the presence of dark matter. With the establishment of a standard cosmological model, in which dark energy and dark matter dominate the universe, accounting for $\sim 95\%$ of the total mass-energy content and hence vastly outnumbering the mass-energy content of baryonic matter ($\sim 5\%$) [Komatsu et al., 2009], the search for the nature of dark matter has started. Stellar remnants, i.e. brown dwarfs, white dwarfs, neutron stars and ordinary black holes (in contrast to their supermassive kin) have been put forward as a plausible explanation for dark matter. However, mass and chemical abundance arguments strongly disfavour such a scenario. First, to account for the total dynamical mass, as measured by the motion of MW disk stars and its associated globular clusters (GCs) and satellite galaxies [Kochanek, 1996; Wilkinson & Evans, 1999] a significant amount of stellar remnants would be necessary. But this, in turn, would lead to an over-abundance of heavy elements generated and ejected during the nucleosynthesis of many massive stars, such as carbon and nitrogen, which would be far in excess than current observations indicate [Gibson & Mould, 1997]. Second, the Massive Compact Halo Object (MACHO) survey [Alcock et al., 1996], has monitored over 20 million stars in the Magellanic Cloud and Galactic bulge in order to detect gravitational micro-lensing effects, triggered by faint stellar remnants in the foreground. While the detections favour a non-negligible amount of dark stellar remnants that could account for up to 30 per cent of the total halo mass, a non-baryonic component is nonetheless necessary [Gates et al., 1996]. Third, the lower mass end of the stellar remnants has been ruled out, too. Given conservative estimates of a mass function below the hydrogen burning limit, the mass density in brown dwarfs is assumed to be only in the order of a few per cent of the halo mass density. [Graff & Freese, 1996].

Non-baryonic dark matter - and particularly cold dark matter [Blumenthal et al., 1984], which is generally associated with weakly interacting massive particles (WIMPs) as predicted by supersymmetric extensions of the standard model of particle physics [e.g. Wess & Zumino, 1974] - is therefore not only vital but also the most promising candidate. In this picture, the collisionsless, massive dark matter particles cool down due to the expansion of the universe. Their cross-sections drop rapidly and they fall out of thermal equilibrium before the epoch of recombination. Primordial dark matter density inhomogeneities first grow linearly and collapse as soon as a critical over-density is reached. Amplified by gravitational interactions, they grow independently from the radiation dominated hot plasma and structures build up hierarchically in a bottom-up fashion, giving rise to a dark halo mass function which is well approximated by the Press-Schechter formalism [Press & Schechter, 1974] (Fig. 1.9). By the time baryonic matter decouples from the radiation field, it is attracted by the gravitational potential wells of the underlying dark matter halos and can start to collapse. The outcome of this primordial gas collapse depends on the rate of radiative cooling. The collapsing gas is initially shock-heated and will try to reach hydrostatic

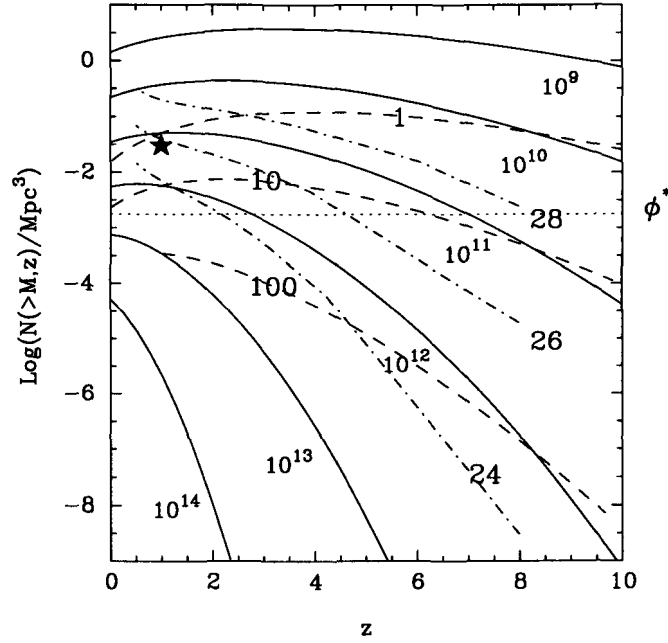


Figure 1.9: The co-moving number densities of halos (solid lines) with different masses (numbers next to solid lines), derived from the Press-Schechter theory for the evolution of the dark halo mass function. The results are in agreement with cosmological N -body simulations and show the hierarchical build-up of dark halos, with more massive halos forming later. Credit: Efstathiou [1995].

equilibrium, but baryonic structure formation on galaxy scales can start if radiative cooling of the gas is efficient [Binney, 1977; Rees & Ostriker, 1977; Silk, 1977].

1.4.2 Dark Halo Structure And Properties

While the search for WIMPs is under way [e.g. CDMS II Collaboration et al., 2010], cosmological N -body simulations within this standard cold dark matter paradigm (Λ CDM) have been developed [White & Rees, 1978; White & Frenk, 1991]. These simulations do not only allow for a detailed study of the hierarchical build-up of virialised dark matter halos, showing a remarkable agreement with the analytical Press-Schechter theory, but also for an analysis of their structural properties. According to high resolution simulations which span multiple orders of magnitude in mass, the profiles of dark halos are well approximated by a self-similar density distribution following a nearly spherical Navarro-Frenk-White (NFW) profile [Navarro et al., 1996, 1997]:

$$\rho(r) = \frac{\delta_c \rho_{crit}}{(r/r_s)(1+r/r_s)^2} \quad (1.3)$$

with r_s being the scale radius of the halo where the profile changes its slope from $\rho \propto -1$ to $\rho \propto -3$, $\rho_{crit} = 3H^2(z)/8\pi G$ being the critical density in an Einstein-de Sitter universe and δ_c reflecting a characteristic contrast density. The total mass of the halo is then given by:

$$M_{200} = \frac{800 \rho_{crit} r_{200}^3}{3} \quad (1.4)$$

where r_{200} is the radius within which the mean halo density reaches 200 times the critical density² and related to the scale radius r_s via the concentration parameter c ($r_{200} = r_s c$). The NFW profile is formally a two parameter family and fully described by its total mass M_{200} and halo concentration c (respectively $\rho_s = \delta_c \rho_{crit}$ and r_s), but reduces to a one parameter function as mass and concentration have been shown to be tightly correlated [e.g. Bullock et al., 2001; Duffy et al., 2008; Macciò et al., 2008].

Certainly, a complete model of galaxy formation must be able to recover both, the evolution and distribution of galaxies and of dark matter. The abundance of dark halos of a given mass, i.e. the dark halo mass function, is given by cosmological N -body simulations and well approximated by the Press-Schechter theory and its extensions, as mentioned above. Here, the total dark mass in the universe is distributed among halos which span many orders of magnitude in mass. On the other hand, the stellar mass function, well defined by large photometric and spectroscopic surveys, indicates that most of the stellar mass is locked-up in galaxies which span only a small range (of about three orders of magnitude) in mass [e.g. Li & White, 2009]. This can be interpreted as evidence that the efficiency of galaxy and star formation is tightly coupled to its host dark halo environment, with less massive halos being less capable to form stars, due to e.g. the inability to contain gas which is expelled during SNe driven winds [Larson, 1974; Dekel & Silk, 1986]. The most forward approach to statistically link stars and dark matter, without worrying about the detailed underlying physics, is through the method of abundance matching (AM) [Vale & Ostriker, 2004]. In this case, (sub-)halos in a numerical N -body simulation are populated by (satellite-)galaxies, assuming e.g. a one-to-one relation between the stellar and halo mass function. Given the steeper fall-off of the stellar mass function at the high mass end and the shallower slope at the low mass end, the stellar-to-halo mass relation (SHM) (or respectively the offset between both mass functions) cannot be constant, but will be a complex function with a peak in the star formation efficiency at a host halo mass of about $10^{12} M_\odot$ [Moster et al., 2010; Guo et al., 2010; Behroozi et al., 2010].

1.4.3 Controversies, Difficulties And Challenges

Despite this non-triviality to link the dark and luminous matter content of galaxies, the Λ CDM cosmological model has been successful in explaining the large scale structures of the universe [Springel et al., 2006; Spergel et al., 2007] (Fig. 1.10) while the NFW profile appears to be a fair assumption of dark matter structures at the largest galactic scales [e.g. Buote et al., 2007; Schmidt & Allen, 2007]. Yet, discrepancies emerge as we move to scales where individual galaxy halos are resolved by means of high resolution simulations. The NFW profile predicts a linear increase in the density distribution towards the centre and therefore the presence of a cusp [see also: Navarro et al., 2004]. The quantification of the slope of the central density distribution in numerical N -body simulations is a much debated issue and highly depends on the resolution limit of the simulations as well as on the analytical fitting functions, but even though various authors report different values for the inner slope [e.g. Moore et al.,

²Actually, in the Einstein-de Sitter cosmology ($\Omega_m = 1, \Omega_\lambda = 0$), the collapsed halo is defined by a radius r_{178} within which the mean halo density is only ~ 178 times the critical density at that redshift [Peebles, 1980].

1999b; Klypin et al., 2001] (ranging from -0.8 to -1.5) the lack of a density plateau is well established. This, however, is in contrast to observations of the dark matter density profiles in dwarf and low surface brightness (LSB) galaxies. Dominated by dark matter, these objects serve as powerful laboratories for the investigation of dark matter structures on galaxy scales and reveal the presence of a core-like central dark matter density distribution ($\rho \propto 0$) [e.g. Moore, 1994; McGaugh & de Blok, 1998]. In addition to the "core-cusp" issue, the discrepancies reach further into the regime of MW sized galaxies, where the lack of an appreciable amount of smaller dark matter sub-halos - also known as the "Missing Satellites Problem" - poses a challenge for structure formation within the Λ CDM framework [Kauffmann et al., 1993; Klypin et al., 1999; Moore et al., 1999a]. As indicated earlier, Λ CDM posits that dark halos grow hierarchically with the smallest structures forming first. Given their high concentrations, reflecting the background density at the halo formation epoch, and the non-negligible time for the accretion of smaller substructures due to dynamical friction, a significant amount of smaller dark matter halos are expected to have survived as satellite galaxies [e.g. Diemand et al., 2008; Springel et al., 2008]. This, again, is at odds with the small number of satellites currently observed in the Local Group [Mateo, 1998]. Solutions to this problem include i) a bias due to technical limitations to detect faint companions which populate the lower end of the galaxy luminosity function, ii) the inefficiency of low mass dark halos to form stars [e.g. Bullock et al., 2000] and iii) the underestimation of satellite circular velocities [e.g. Peñarrubia et al., 2008]. Recent detections of new satellites [e.g. Willman et al., 2005; Zucker et al., 2006] and volume completeness corrections [e.g. Koposov et al., 2008] seem to be able to mitigate the discrepancy. Conversely, modern simulations report an increase in the abundance of subhalos [e.g. Madau et al., 2008] and an accordance between observations and theory therefore recedes into the distance. Furthermore, even if a sizeable fraction of the satellite galaxy population has not been able to sustain its baryonic matter in order to form stars due to e.g. photoheating [Crain et al., 2007], the sheer number of predicted massive dark sub-halos should heat up and tidally disturb the host galaxy's stellar disk [Moore et al., 1999a]. Additional arguments based on the anisotropic orbital alignment of the brightest MW satellite galaxies [Lynden-Bell, 1976; Kroupa et al., 2005] further increase the friction between both models and simulations. These ought to be distributed isotropically to first order in cosmological simulations, unless they have been accreted, for instance, along cosmic web filaments [Libeskind et al., 2005].

Unfortunately, the situation of massive host galaxies is not very comforting either, in particular in the case of ETGs. Since we lack extended dynamical tracers, such as HI in LTGs, we rely on other dynamical measurements, such as the motion of stars to infer the host's gravitational potential. In a way, this is even preferable; in contrast to cold gas which settles in a plane and is easily disturbed by density perturbations, stars are effectively collisionless, probe the potential in all three dimensions and are present at all radii. However, due to the rapid decline of their SB distribution we are usually confined to probe the stellar kinematics only out to 1-2 effective radii, a region which is still dominated by the stellar mass [Kronawitter et al., 2000; Gerhard et al., 2001]. Kinematic information at larger radii, where the dark halo is expected to dominate the mass profile and hence the orbit distribution, are preferable but expensive; one needs high signal-to-noise (S/N) spectra to be able to reliably exploit the information in the higher order Gauss-Hermite moments of the line-of-sight velocity distribution (LOSVD) [van der Marel & Franx, 1993; Bender et al., 1994], which are crucial to break the mass-anisotropy degeneracy in the dynamical models [Gerhard, 1993]. It is therefore notoriously difficult within this small spatial extent to dissect the dark and luminous matter contribution to the total mass budget and, as a consequence,

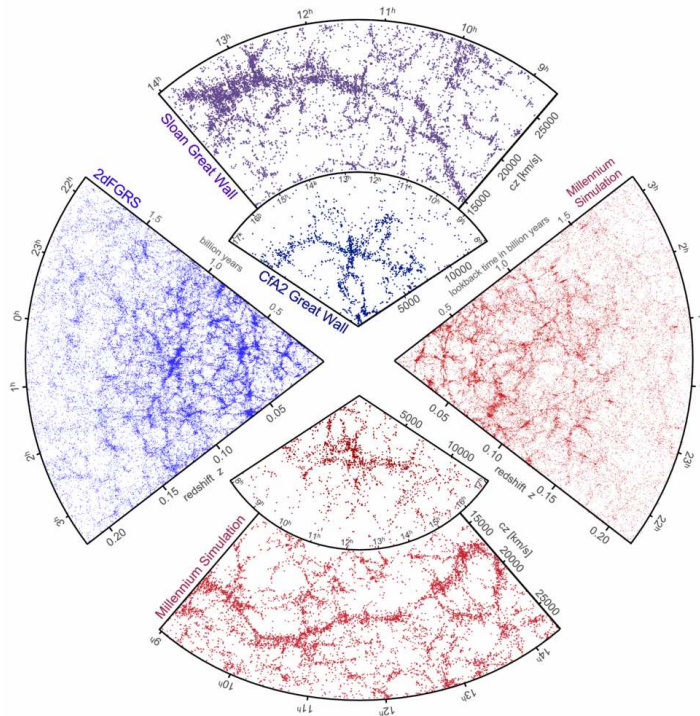


Figure 1.10: Comparison of the large scale galaxy distribution as observed from several galaxy surveys and predicted by cosmological simulations within the Λ CDM framework. Credit: Springel et al. [2006].

dynamical studies of ETGs cannot discriminate between a cored or cuspy dark halo, which seem to be able to recover the dynamics equally well [e.g Mamon & Łokas, 2005a,b; Thomas et al., 2007]. Different approaches to split up the stellar and dark content have been employed, e.g. by carrying out stellar population synthesis (SPS) fits or line index measurements to independently constrain the stellar M/L [e.g. Cappellari et al., 2006; Thomas et al., 2011]. These indicate a dark matter fraction of $\sim 10 - 30$ per cent in ETGs within one effective radius. However, the recovery of the stellar M/L still depends on the choice of an IMF, which is basically untested beyond the local neighbourhood. And the contribution of dark matter could erode if one assumes that the IMF is not universal but rather varies across the spectrum of ETGs.

Indeed, recent studies faced difficulties to explain the systematic increase of the total M/L (including luminous and dark matter) as a function of velocity dispersion with an increase in the dark matter fraction only. Independent results from stellar dynamics, spectral synthesis fits to IMF sensitive features and gravitational lensing now promote a variation towards a more bottom-heavy IMF with increasing stellar velocity dispersion [e.g. Auger et al., 2010b; van Dokkum & Conroy, 2010, 2012; Conroy & van Dokkum, 2012; Treu et al., 2010; Cappellari et al., 2012; Spiniello et al., 2012; Dutton et al., 2012, 2013; Tortora et al., 2013], and leave even less room for dark matter [but see: Clauwens et al., 2014; Smith, 2014, for a critical discussion regarding the ATLAS^{3D} results].

In principle, other tracers which map the dark halo potential can be employed as well, and observations of i) the hot interstellar medium (ISM) in X-ray [e.g. Forman et al., 1985; Mushotzky et al., 1994; Humphrey et al., 2006], ii) globular clusters (GCs) [e.g. Huchra & Brodie, 1987; Côté et al., 2003; Woodley et al., 2010] and iii) planetary nebulae (PNe) [e.g. Ciardullo et al., 1993; Hui et al., 1995; Arnaboldi et al., 1996;

Méndez et al., 2001; Douglas et al., 2007; Napolitano et al., 2011] have been carried out to obtain large scale kinematic information. However, i) X-ray gas is usually scarce in ETGs and even if present it is questionable if hydrostatic equilibrium holds [Diehl & Statler, 2007], ii) the usually modest number of GCs is insufficient to tightly constrain the freedom in the orbital distribution [but see: Schuberth et al., 2010]. Moreover, GCs might have formed during violent mergers of gas rich galaxies and do not necessarily need to be dynamically relaxed in the host potential [Bournaud et al., 2008], and iii) it is possible that PNe do not trace the bulk of the underlying stellar population and are therefore not suitable representatives of the overall gravitational potential of the host [Dekel et al., 2005; Sambhus et al., 2006][but see e.g. Coccato et al., 2009]. Thus, studies of individual galaxies based on both GCs and PNe are at discord [Romanowsky et al., 2003; Pierce et al., 2006] and investigations even if based on the same single tracer can be ambiguous [Romanowsky et al., 2003; Dekel et al., 2005].

Accordingly, stellar kinematics remain the most reliable tracer for a dynamical investigation of dark matter in ETGs and current efforts focus on increasing the range in spatial information [e.g. Weijmans et al., 2009], in contrast to studies in the amalgamated literature which are confined to the innermost regions.

Summary:

We have indirect observational evidence for the presence of cold, non-baryonic dark matter, independently from galaxy and cluster dynamics and investigations of the CMB. Theoretical models predict that primordial gas has settled in the peaks of the underlying gravitational potential wells of small dark matter substructures. The gravitational collapse of the gas gave rise to stars and galaxies, which have grown since then hierarchically by the gravitational clustering of bigger and bigger structures. Collisionless N -body simulations have provided insight into this hierarchical build-up and enabled a detailed analysis of the structural properties of dark matter halos. These are well described by a NFW profile. However, the simulations are at odds with observations on the level where individual galaxies are resolved. The dark matter density distributions do not agree and an underabundance of satellite galaxies is observed. Moreover, in ETGs, the detection of dark matter becomes highly difficult due to the lack of extended dynamical tracers. Stellar dynamics have been the most reliable kinematic tracer and investigations of large samples of ETGs indicate that dark matter is present. However, the degeneracy between stars and dark matter is strongly affecting the results and indications of variations in the stellar IMF will further add to this inaccuracy. Hence, we currently fall short in determining the structural properties of dark matter halos in ETGs on an individual basis. Investigating the link between galaxies and their host dark halos in particular and the role of the dark halo in the formation and evolution of ETGs in general therefore proves to be difficult.

1.5 Compact, Elliptical, High Central Velocity Dispersion Galaxies

To understand the formation and evolution of ETGs and the content and link between their luminous and dark matter, we need reliable measurements of their masses and sizes through cosmic time. In fact, the feasibility of the different evolutionary paths for ETGs since $z \simeq 2$ (e.g. only minor merging vs. minor merging and internal processes vs. the appearance of additional quenched ETGs at later times)

will also stem from our ability to reliably quantify their physical properties. At low redshift, we have gathered an astonishing amount of observations which have resulted in the findings presented above, although with the corresponding caveats. At high redshift, however, measurements are sparse. To understand their stellar populations and stellar mass content we rely on measurements of their spectral energy distribution (SED). But besides being hampered by many systematic uncertainties [Conroy et al., 2009], for measurements at redshift $z = 2$ the spectra moves into the near-infrared (NIR), where suitable spectrographs have only recently become available [e.g. Vernet et al., 2011, VLT X-shooter]. On the other hand, the measurement of sizes (and hence a thorough quantification of the mass-size evolution) becomes difficult too. Investigations with the *HST* have addressed initial concerns regarding the reliability of their compactness, due to shallow imaging and hence missing of low SB wings [e.g. Buitrago et al., 2008; Szomoru et al., 2012], but the pace in the mass-size evolution will nevertheless strongly be affected by differences in measurement and fitting techniques as well as sample selection effects. Naturally, the same issues strongly affect any attempt to investigate the black hole mass and dark matter content and profile of galaxies at high redshift. Dynamical models to constrain both rely on deep imaging and a wealth of high spatial and spectral resolution measurements of the LOSVD, but neither for the centre nor for the remote regions is this feasible with current observational facilities.

Ideally, one would like to investigate the likely progenitors of today's ETG population in the local universe and thus in more detail (at both the smallest and largest spatial scales to study its stellar and dark content as well as its black hole), which is currently not possible for their analogues at higher redshifts. Early efforts to find old, compact, high velocity dispersion galaxies at low redshift ($z \sim 0$) turned out to be largely unsuccessful [e.g. Trujillo et al., 2009; Taylor et al., 2010], with only a handful detections. Given the stochastic nature of mergers, though, a non-negligible fraction (≤ 5 per cent) of these galaxies is assumed to survive [Hopkins et al., 2009b]. A complete lack of these relic galaxies would point at inconsistencies with the minor merger scenario for the growth and evolution of ETGs, and whether this dearth is real or rather driven by incompleteness and sample selection effects of large surveys, such as *SDSS*, is a matter of debate [e.g. Poggianti et al., 2013]. However, more recent investigations now hint at a good agreement between the observed and predicted number density of these objects of $\sim 10^{-6} \text{ Mpc}^{-3}$ in the present-day universe [Damjanov et al., 2014; Quilis & Trujillo, 2013].

The Hobby-Eberly Telescope Massive Galaxy Survey [van den Bosch et al., 2015, HETMGS] was a long-slit spectroscopic survey to measure the stellar velocity dispersions of ~ 1000 galaxies. The goal was to find galaxies with the highest stellar velocity dispersions and hence largest spheres of influence that could be resolved by follow-up high spatial resolution observations to robustly measure their black hole masses. Interestingly, the HETMGS discovered a sample of compact, elliptical, high central velocity dispersion galaxies in the nearby volume ($\leq 100 \text{ Mpc}$), which bear resemblance to the compact galaxies at high redshift.

An analysis of these compact, elliptical, high central velocity dispersion galaxies is the theme of this thesis and important for various reasons, which will help to gain further insight into the aforementioned challenges regarding galaxy and black hole (co-)evolution as well as the connection between baryonic and non-baryonic matter:

- i) While this sample is still too small to be statistically meaningful, it could allow for a first, unprecedented and detailed investigation of the putative progenitors of today's massive ETG population.

- ii) With respect to the evolution of the stellar content of ETGs (as outlined in Sec. 1.2), we can investigate their stellar population properties and thus infer their ages, formation timescales and formation environments. This will not only provide a link between the massive, quenched ETG population at $z = 2$ and their likely progenitors at even higher redshifts, but also enable us to further constrain the characteristics of stellar populations which are assumed to join the host at later times (as expected if the mass-size evolution is driven by minor mergers).
- iii) Their dynamical and photometric structures and build-up hold clues of their recent evolutionary history. Investigating these fossil records will yield information concerning their violent or non-violent growth through cosmic time.
- iv) Literature black hole masses are heavily biased towards the densest systems, tracing a tight locus in their host galaxies' properties [van den Bosch et al., 2015, Fig. 8]. A secondary goal of the HETMGS was to increase the diversity in the properties of their hosts, which is crucial to investigate the nature and tightness of the BHSR at $z = 0$ and to probe the different black hole formation channels. Increasing the diversity in their host galaxies' properties is key to measurements of black hole masses at higher redshift, too, as the BHSR are used as calibrators of secondary and tertiary black hole mass measurement methods (e.g. reverberation mapping). The compact, elliptical, high central velocity dispersion galaxies are not only ideal to increase the leverage in the BHSR, but they will also enable us to dynamically measure the black hole masses of the progenitors of today's ETG population and in this way to simultaneously investigate the black hole co-evolution at higher redshift.
- v) These galaxies are very compact, with effective sizes of $1 \leq R_e \leq 3$ kpc. Combining deep imaging and wide-field integral field unit (IFU) measurements of their LOSVD out to several effective radii, we can probe the regions where the dark halo dominates, necessary to break the degeneracy between the stellar and dark mass. Constraining their dark matter content and profile will provide the missing link between baryonic and non-baryonic matter in galaxies, crucial to our understanding of structure formation and evolution in general.

This thesis is organised as follows:

In **Chapter 2**, we set the stage for a thorough and comprehensive analysis of our compact galaxy sample by studying the two galaxies MRK 1216 and NGC 1277. We introduce the data and our methods. The data quality for these particular objects is worse than for the remaining sample and therefore outlines the limits of our analysis. We derive their total mass profiles and the contributions of black hole, stars and dark matter to the total mass budget. We discuss the implications of the inferred black hole masses for models of black hole-galaxy co-evolution. We present a dark halo detection and, in addition, investigate their photometric and dynamical structures in order to unveil the processes that have dictated their recent evolution.

In **Chapter 3**, we focus on the compact, early-type galaxy NGC 1281. Based on wide-field integral field unit kinematics, we tightly constrain its dark and luminous matter content. Moreover, we investigate its stellar content by means of spectral synthesis fits. In particular IMF sensitive features are used to trace the dwarf-to-giant star ratio. The spectral analysis implies a strong spatial variation in the IMF, while the

dynamical analysis hints at a massive dark halo which, however, is at odds with the dark halo profile that is predicted by cold dark matter simulations.

We present an analysis of the structural and dynamical properties of a larger sample of compact, elliptical, high central velocity dispersion galaxies in **Chapter 4**. We show that these galaxies substantially deviate from the local ETG population, and provide ample evidence for a tight connection to the massive and passive ETG population at $z = 2$, which are thought to be the progenitors of today's most massive ellipticals. In addition, we investigate their total mass density profiles and the growth of the largest galaxies in our sample, which yield additional information concerning their formation and evolution mechanisms.

Finally, a summary is given in **Chapter 5**, followed by prospects for future work and concluding remarks.

MRK 1216 & NGC 1277 - An orbit-based dynamical analysis of compact, elliptical, high central velocity dispersion galaxies

Abstract

We present a dynamical analysis to infer the structural parameters and properties of the two nearby, compact, elliptical, high central velocity dispersion galaxies MRK 1216 and NGC 1277. Combining deep *Hubble Space Telescope* imaging, wide-field integral field unit stellar kinematics, and complementary long-slit spectroscopic data out to three effective radii, we construct orbit-based models to constrain their black hole masses, dark matter content and stellar mass-to-light ratios. We obtain a black hole mass of $\log(M_{\bullet}/M_{\odot}) = 10.1^{+0.1}_{-0.2}$ for NGC 1277 and an upper limit of $\log(M_{\bullet}/M_{\odot}) = 10.0$ for MRK 1216, within 99.7 per cent (3σ) confidence. The stellar M/L span a range of $\Upsilon_V = 6.5^{+1.5}_{-1.5}$ in NGC 1277 and $\Upsilon_H = 1.8^{+0.5}_{-0.8}$ in MRK 1216 and are in good agreement with single stellar population models of a single power-law Salpeter initial mass function. Even though our models do not place strong constraints on the dark halo parameters, they suggest that dark matter is a necessary ingredient in MRK 1216, with a dark matter contribution of 22^{+30}_{-20} per cent to the total mass budget within one effective radius. NGC 1277, on the other hand, can be reproduced without the need for a dark halo, and a maximal dark matter fraction of 13 per cent within the same radial extent. In addition, we investigate the orbital structures of both galaxies, which are rotationally supported and consistent with photometric multi-Sérsic decompositions, indicating that these compact objects do not host classical, non-rotating bulges formed during dissipative events or through violent relaxation. Finally, both MRK 1216 and NGC 1277 are anisotropic, with a global anisotropy parameter δ of 0.33 and 0.58, respectively. While MRK 1216 follows the trend of fast-rotating, oblate galaxies with a flattened velocity dispersion tensor in the meridional plane of the order $\beta_z \sim \delta$, NGC 1277 is highly tangential anisotropic and seems to belong kinematically to a distinct class of objects.

2.1 Introduction

The highest velocity dispersion galaxies ($\sigma \geq 300 \text{ km s}^{-1}$) are typically large and massive galaxies. Examples are the central brightest cluster galaxies (BCGs) such as M 87 and NGC 4884. These objects are very round, have half-light radii larger than $R_e > 8 \text{ kpc}$ and absolute magnitudes brighter than $M_{K_s} \geq -25.5$. Surprisingly, the Hobby-Eberly Telescope Massive Galaxy Survey [van den Bosch et al., 2015, HETMGS] found several small galaxies with very high central velocity dispersions. In van den Bosch et al. [2012, hereafter vdB12], six such objects were highlighted with sizes smaller than $R_e \leq 3 \text{ kpc}$ and central stellar velocity dispersions higher than $\sigma_c \geq 300 \text{ km s}^{-1}$.

These features indicate extremely high dynamical mass densities for which there are two possible explanations, assuming reasonable stellar densities: over-massive black holes that weigh a significant fraction of the total baryonic galaxy mass, or high stellar mass-to-light ratios which would increase the stellar dynamical mass considerably but imply a stellar initial mass function (IMF) much more bottom-heavy than a Salpeter IMF.

According to the orbit-based dynamical models of vdB12, NGC 1277 hosts an over-massive SMBH and possesses a stellar IMF that is consistent with a Chabrier IMF, ruling out a Salpeter IMF at 3σ . Interestingly, Emsellem [2013, hereafter E13] showed a hand-picked alternative model with a smaller black hole and a Salpeter-like IMF and no dark matter, which produces a reasonable fit. Furthermore, spatially resolved spectroscopic data along NGC 1277's major axis have been obtained and investigated in Trujillo et al. [2014, hereafter T14] and Martín-Navarro et al. [2015b], which indicate a uniformly old stellar population, high constant α -abundance and bottom heavy IMF. Their reconstructed stellar mass-to-light ratio of $\Upsilon_* \simeq 7$ is consistent with the values reported in vdB12, but much lower than the $\Upsilon_* = 10$ adopted by E13. Clearly, all these differences call for a re-examination of NGC 1277's stellar and central dark component.

Dark matter is not expected to be an important contributor at kpc to sub-kpc scales, but is nonetheless a key ingredient in many early-type galaxies [Rix et al., 1997; Cappellari et al., 2006; Thomas et al., 2007; Cappellari et al., 2013a] that needs to be taken into account in any dynamical analysis due to its degeneracy with the stellar mass-to-light ratio and hence with the black hole mass (M_\bullet) [Gebhardt & Thomas, 2009]. Most studies that aimed to constrain the halo contribution to the overall mass profile either used long-slit spectroscopic observations or spatially limited integral field unit (IFU) data that rarely go beyond ~ 1 -2 effective radii (R_e). The effective radius is only a relative scale that neither guarantees nor excludes the coverage of a substantial amount of dark matter. However, the SAURON and ATLAS^{3D} survey found a mean dark matter contribution of about 30% inside $1 R_e$, which corresponds to a mean absolute scale of only $\leq 5 \text{ kpc}$. The aforementioned HETMGS's compact galaxy sub-sample, though, should provide more interesting constraints in this regard. Their apparent sizes are relatively small and thus allow us to obtain detailed two dimensional stellar kinematics out to several effective radii (which at the same time also corresponds to a larger absolute coverage of up to 10 kpc, given their mean distance) to study their mass profiles and hence to probe the existence of dark matter, which is assumed to dominate the mass budget in these remote regions.

The aim of this chapter is to set the stage for an investigation of compact, high-dispersion galaxies from the HETMGS by combining long-slit spectroscopy with the HET, high-spatial resolution imaging with the

HST and large-field, medium- and low-resolution spectroscopic observations with the *PPAK* IFU at Calar Alto. In doing so, we want to tackle several issues.

1. dynamically infer the black hole mass, mass-to-light ratio and dark matter content of each galaxy,
2. identify the dynamically hot and cold components to see whether violent relaxation or dissipative events played an important role in the recent evolution of these objects,
3. analyse the stellar populations to obtain and further constrain reliable stellar mass-to-light ratios and IMF slopes as well as to gain insight into their formation histories,
4. compare our results with the current picture of how galaxies and their constituents scale and evolve.

In this chapter, we focus on orbit-based dynamical models of only two objects, namely MRK 1216 and NGC 1277, with effective radii smaller than 2.5 kpc and exceptional central dispersion peaks of $\sigma_c \geq 300 \text{ km s}^{-1}$ (Table 2.1). The *PPAK* observations of both were taken with the V1200 medium-resolution grating, covering a wavelength range of 3400-4840 Å. This restricted range makes a stellar population analysis not very suitable for answering IMF related questions. In addition, the kinematics for these two galaxies are currently available to a radius of $\sim 15''$ only, due to a much shorter exposure strategy compared to the rest of the sample. Nevertheless, the wide-field IFU data presented here still covers these objects out to $\sim 3 R_e$ (i.e. $\geq 5 \text{ kpc}$) which should be sufficient for a dynamical examination.

The chapter is organised as follows: In Section 2.2 we present the photometry. Section 2.3 covers the stellar kinematics. In Section 2.4 we carry out a dynamical analysis to constrain the black hole mass, stellar mass-to-light ratio and dark matter content of both galaxies. Section 2.5 rounds up and discusses the results. Section 2.6 highlights uncertainties and potential error sources, followed by a brief summary in Section 2.7.

Throughout this chapter, we adopt 5th year results of the Wilkinson Microwave Anisotropy Probe (*WMAP*) [Hinshaw et al., 2009], with a Hubble constant of $H_0 = 70.5 \text{ km s}^{-1} \text{ Mpc}^{-1}$, a matter density of $\Omega_M = 0.27$ and a cosmological constant of $\Omega_\Lambda = 0.73$.

2.2 Photometry

In this section, we present the photometric data, consisting of high-spatial resolution imaging with the *HST*. The first part of this paragraph covers the reduction and combination of dithered *HST* exposures to a final, super-sampled image. The second part then describes the photometric analysis of MRK 1216 and NGC 1277.

2.2.1 HST Imaging

We obtained single orbit imaging of MRK 1216 with the *HST* WFC3 in *I*- (F814W) and *H*-band (F160W), as part of program GO: 13050 (PI: van den Bosch). The data set comprises three dithered images in *I*-band

Table 2.1: Photometric properties of MRK 1216 and NGC 1277. (1) Morphological classification according to the NED, (2) Hubble flow distance, (3) scale at this distance, (4) effective radius in arcsec or (5) kpc, measured by a circular aperture that contains half of the light, (6) extinction corrected total luminosity of the *HST* F160W (MRK 1216) and F814W (NGC 1277) exposures, (7) peak and effective velocity dispersion in the *PPAK* data, and (8) adopted inclination.

	MRK 1216	NGC 1277
Type	E	S0
Distance [Mpc]	94 ± 2	71 ± 1
Distance Scale [kpc/arcsec]	0.45 ± 0.01	0.34 ± 0.01
R_e [arcsec]	5.1	3.5
R_e [kpc]	2.3	1.2
Luminosity [$\log(L_\odot)$]	11.1	10.3
σ_c / σ_e [km s^{-1}]	$338 \pm 8 / 308 \pm 7$	$355 \pm 7 / 317 \pm 5$
Inclination [deg]	70	75

with a total integration time of 500 seconds and seven images in *H*-band with a total integration time of 1354 seconds. The *H*-band images consist of three dithered full- and four sub-array exposures. The $16'' \times 16''$ sub-array images are short 1.7 second exposures, to mitigate a possible saturation in the 450 seconds full-frames of the high surface brightness nucleus.

For the photometric as well as the dynamical analysis, we give preference to the deep *HST H*-band exposures, mainly due to less dust susceptibility in the near-infrared (NIR) and the fact that the inferred stellar mass-to-light ratios become a weaker function of the underlying stellar populations [Bell & de Jong, 2001; Cole et al., 2001].

The reduction and combination of the individual F160W exposures is performed via Astrodrizzle [Gonzaga et al., 2012] in two major steps. First, a bad pixel mask for each flat-field calibrated image is generated, which then again is used during combination of dithered exposures, while correcting for geometric and photometric distortions. Both the deep full- and sub-array exposures in F160W are dominated by galaxy light of the huge stellar halo and hence the standard sky subtraction routine in Astrodrizzle (consisting of iterative sigma-clipping of uniformly distributed pixels) overestimates the background flux. We therefore measure the background flux separately in all the frames, manually, before combining the images. For the full-frames, the background level is measured in the less contaminated corners of each image, while the background flux in the sub-frames is estimated by measuring the flux difference between the (already) sky subtracted full-frames and the different sub-frames. We don't reach the sky/noise dominated regions in the full-frames, but the surface brightness (SB) in the corners of each image (where the sky estimates have been performed) is more than 10 magnitudes below the central SB, and will thus have little impact on the accurate recovery of the central stellar light/mass.

Fig. 2.1 (top panel) shows the match of the surface brightness profiles of MRK 1216 after subtraction of sky background in the full- and sub-array exposures. Once the sky values have been determined, we combine the frames via Astrodrizzle and obtain a super-sampled image with a resolution of $0.06''/\text{pixel}$ and a FOV of 1.5 arcmin^2 (Fig. 2.2).

For the photometric analysis, we adopt a CANDELS point-spread function (PSF) [van der Wel et al., 2012]. In brief, the PSF has a size of $0.17''$ FWHM and has been generated with TinyTim [Krist, 1995] for the

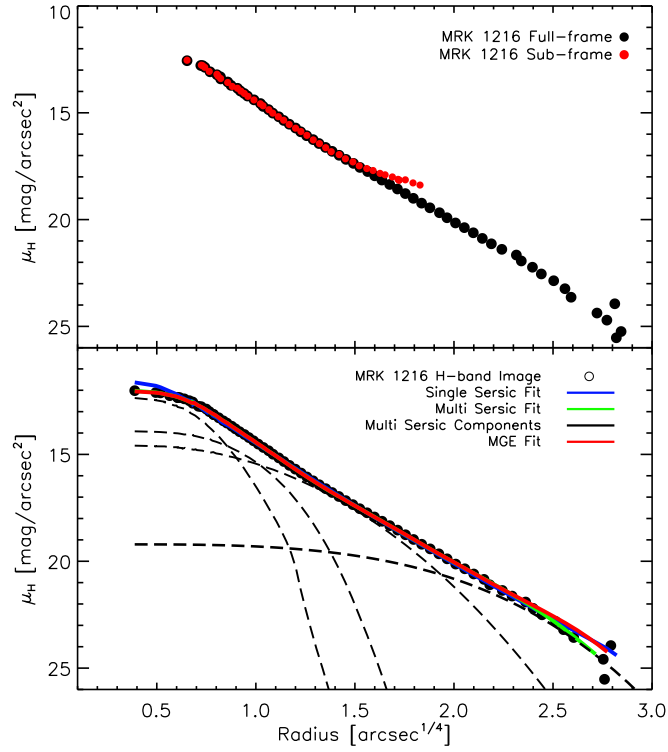


Figure 2.1: *Top*: Surface brightness comparison of the sky subtracted *HST* (F160W) *H*-band full- and sub-frames of MRK1216. The sky of the full-frames was calculated by iterative sigma-clipping of non-contaminated regions. The sky of the sub-frames was inferred by matching their non-sky subtracted SB profile with the sky subtracted SB profile of the full-exposures. At radii beyond $5''$, the SB of the sub-exposures are noise dominated. *Bottom*: Fits to the final, *HST* *H*-band image, showing the match with a single Sérsic, multi-Sérsic and multi-Gaussian expansion. The single Sérsic overestimates both the SB measurement at the inner- and outermost radii. The MGE accurately reproduces the SB in the inner parts but is more extended, whereas the multi-Sérsic fit represents a fair match at all radii.

F160W filter. The PSF is created in the centre of the WFC3 detector, to minimise distortion, and is $10 \times$ sub-sampled. Resampling it back to the original *HST* *IR* scale of $0.13''/\text{pixel}$, and applying a kernel to replicate the effects of inter-pixel capacitance, creates a synthetic star in the centre of each frame. The final PSF is then obtained by drizzling the images and thus the PSFs. In this way, we produce a point-spread function at the same scale as our final science image.

High-resolution imaging of NGC1277 is available in the Hubble Legacy Archive. Observations of this galaxy have been carried out in program GO: 10546 (PI: Fabian), resulting in three dithered exposures in *R*- (F625W) and *V*-band (F550M) with a total integration time of 1654s and 2439s respectively. In contrast to the *I*- and *H*-band images of MRK 1216, the redder *R*-band does not have a significant advantage over the *V*-band. The leverage between the two filters is small and consequently both are equally subject to the effects of extinction (see Section 2.2.3). Here, we employ the *V*-band photometry because of its longer exposure time and for the sake of consistency with the modelling results of vdB12.

The F550M flat-field calibrated images have been sky subtracted, cosmic ray rejected, corrected for photometric and geometric distortions via Astrodrizzle before being combined into a final image with a resolution of $0.05''/\text{pixel}$. The PSF of these observations was recovered with TinyTim, created in each

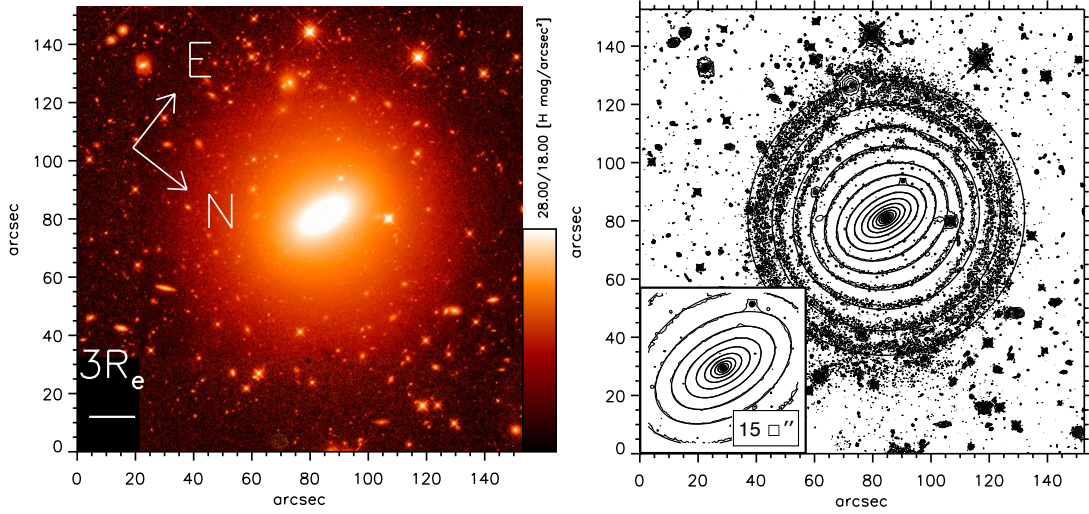


Figure 2.2: *Left:* *HST* *H*-band image of MRK 1216, which covers a field of $\sim 150 \text{ arcsec}^2$ (i.e. $\sim 70 \text{ kpc}^2$), with a final scale of $0.06''/\text{pixel}$. *Right:* Contour map of the same image. The MGE contours are over-plotted in black. The bottom left plot shows the accurate reproduction of the surface brightness profile within the central 15 arcsec^2 ($\sim 3 R_e$).

of the three individual, dithered exposures and drizzled to match the resolution of the corresponding science frame.

2.2.2 MRK 1216

MRK 1216 is a sparsely investigated early-type galaxy (ETG) (R.A.: $08^h 28^m 4^s$, Decl.: $-06^\circ 56'22''$) with strong excess of UV radiation in its centre [Markarian, 1963]. A few redshift measurements have been carried out for this object [Petrosian et al., 2007; Jones et al., 2009], which translate to a Hubble flow distance of $94 \pm 2 \text{ Mpc}$. Given its distance, $1''$ is equivalent to $450 \pm 10 \text{ pc/arcsec}$. The final, combined *HST* image thus covers a field of view (FOV) of 65 kpc^2 .

To examine its photometric properties, structure and morphology we decompose the galaxy into multiple Sérsic components using Galfit [Peng et al., 2002]. The analysis is done for 3 different scenarios: First, a single Sérsic fit is carried out to obtain the single Sérsic index and thus the overall steepness of the light profile. Second, we perform a bulge-disk decomposition, if possible. Although such a decomposition is a matter of debate, we do this for comparison with literature studies, where similar procedures have been carried out to relate central black hole masses to bulge luminosities. Third, we execute a fit with multiple Sérsic components that best matches the light profile ¹.

A single Sérsic fit to MRK 1216's *H*-band image has an apparent magnitude of $m_{H,Vega} = 10.47$, an effective radius of $R_e = 6.34''$, a projected axis ratio (b/a) = 0.58 and a single Sérsic index of $n = 4.93$. Residuals of this fit are strong. In comparison to the SB measurement, the single Sérsic fit shows an excess of light in the very centre and also tends to overpredict the light of the large outer halo (Fig. 2.1, bottom panel).

¹All magnitudes presented throughout this section are corrected for Galactic extinction [Schlafly & Finkbeiner, 2011]; 0.017 mag in *H*-band and 0.431 mag in *V*-band. The sizes are semi-major axis radii, unless mentioned otherwise.

Table 2.2: Sérsic decomposition of MRK 1216's *HST* (F160W) *H*-band image. The columns represent the number of Sérsics for a given fitting scenario (1), their apparent total magnitude (extinction corrected) (2), their effective semi major axis radius (3), the corresponding Sérsic index (4) and their apparent flattening (5).

# of components	mag [H, Vega]	R_e [arcsec]	n	q
1	10.49	6.34	4.93	0.58
1	10.89	3.42	3.61	0.56
2	11.77	17.22	0.96	0.88
1	13.19	0.40	1.27	0.81
2	12.77	1.34	0.99	0.57
3	11.32	5.59	1.61	0.52
4	11.60	19.31	1.05	0.99

We further investigate the stellar structure by gradually increasing the number of Sérsic components. A two-component model yields a very centrally concentrated ($R_e = 3.42''$) bulge with a Sérsic index of $n = 3.61$ - although remarkably flat ($q = 0.56$) - which is embedded in a (close to) exponential, round and very extended ($R_e = 17.22''$) stellar disk/envelope with a Sérsic index of $n = 0.96$. Pronounced residuals remain, hinting at a more complex stellar composition. Even so, the bulge of the two-component fit will serve as an upper limit to the bulge luminosity. According to this fitting scenario, we obtain a bulge-to-total luminosity ratio of $B/T = 0.69$.

A decent fit is obtained with at least four Sérsic components, resulting in notably lower and less prominent residuals. In this case, the outer stellar disk/envelope persists, whereas indications of a bulge-like component totally disappear (Table 2.2). All components show rather low Sérsic indices, which complicates any attempt of a morphological interpretation. We therefore do not present a unique classification but rather stick to the conclusion that MRK 1216 is indeed a compact ETG, harbouring a complex, flat substructure, that is embedded in a round, extended stellar halo. As the innermost component is too small to be considered a bulge, we adopt the luminosity of the second innermost Sérsic as a conservative lower limit of a bulge luminosity, which accounts for 12 per cent of the total light and extends to $1.34''$ (or roughly $0.3 R_e$).

Our orbit-based dynamical models need a stellar mass model, from which we can infer the stellar gravitational potential. This is accomplished by deprojecting the surface brightness distribution of a galaxy which however is a non-unique task, as has been convincingly illustrated by Rybicki [1987]. Even the surface brightness distribution of an axisymmetric stellar system only provides information about its density outside a so-called "cone of ignorance". This means that in principle, and unless the galaxy is observed edge-on, there could be a family of "konus densities" [Gerhard & Binney, 1996] which alter the intrinsic mass distribution but are invisible to the observer as they project to zero surface brightness. Making use of physically and observationally motivated criteria for the luminosity profile of axisymmetric galaxies, van den Bosch [1997] found that the addition of mass due to konus densities cannot be arbitrary and is most likely confined to be less than 10 per cent for (cusped) ellipticals, implying a marginal role in the dynamics of early-type galaxies. We employ a similar, empirically motivated approach by parameterising the surface brightness distribution of galaxies with a set of multiple, two-dimensional Gaussian functions (MGE: Monnet et al. 1992; Emsellem et al. 1994). Although a set of Gaussians does not form a complete set, the MGE method has been very successful in the recovery of the surface

Table 2.3: Multi-Gaussian-Expansion of MRK 1216's *HST* (F160W) *H*-band image. The columns display the number of each Gaussian, beginning with the innermost one (1), the central surface density (2), the dispersion (3) and the corresponding Sérsic index (4) as well as the apparent flattening (5).

# of components	$I [L_{\odot} pc^{-2}]$	σ [arcsec]	n	q
1	89721.780	0.094	0.5	0.72
2	65370.124	0.230	0.5	0.77
3	27564.339	0.458	0.5	0.73
4	14178.182	0.919	0.5	0.59
5	5276.4998	1.711	0.5	0.55
6	2018.3083	3.208	0.5	0.52
7	770.32639	5.905	0.5	0.54
8	201.40331	9.848	0.5	0.67
9	64.074064	14.72	0.5	0.96
10	17.126964	29.80	0.5	0.99

brightness profiles and features of realistic multi-component galaxies [Cappellari, 2002]. We obtain the intrinsic luminosity density by deprojecting the parameterised surface brightness distribution for a given/assumed set of viewing angles, adopting an absolute magnitude of 3.32 for the Sun in *H*-band [Binney & Merrifield, 1998]. In the case of an MGE, the deprojection can be performed analytically while the gravitational potential is then obtained by means of a simple, one-dimensional integral.

Our final MGE contains 10 components with a fixed position angle (PA) of 70.2° (measured counter-clockwise from the *y*-axis to the galaxy major axis, with the image aligned N.-E., i.e. north is up and east is left) and a common centre, as listed in Tab. 2.3. The flattest Gaussian has an axis ratio of $q = 0.52$, which forces the lower boundary of possible inclinations to be greater than 59° (with 90° being edge-on), assuming oblate axial symmetry (see Section 2.6). A dust disc would be helpful in further constraining the inclination of the galaxy, although it would also pose a major concern for the modelling of the stellar mass, but is not evident in either of the *H*- and *I*-band images of MRK 1216.

Fig. 2.2 shows the combined, final *H*-band image of MRK 1216 (left) and its contour map (right). Overplotted are contours of the MGE (black) as well as an excerpt of the central 15 arcsec^2 ($\sim 3 R_e$). The MGE reproduces the SB profile within the central 40 arcsec^2 , but tends to overpredict it at the largest radii. Note that the SB profile lacks any PA twists. The PA is almost constant within $30''$ from the centre ($\Delta\text{PA} \leq 2^{\circ}$) and changes only at larger radii where it is virtually unconstrained as the round outer halo has close to zero ellipticity.

2.2.3 NGC 1277

Given several redshift measurements, NGC 1277 is located at a Hubble flow distance of $71 \pm 1 \text{ Mpc}$ and deeply embedded in the Perseus cluster. It is classified as a lenticular S0 galaxy [Marcum et al., 2001] without any noticeable substructures or prominent features besides the clearly visible central dust disk with a semi-major axis radius of 0.13 kpc and a flattening of $q = 0.3$. The presence of dust complicates the recovery of the central stellar mass and hence the black hole mass in NGC 1277 (see Section 2.6), but assuming that this nearly edge-on disk traces the PA of its host, we can pin down the inclination of

the galaxy to 75° . As in the case of MRK 1216, photometry shows that a superposition of galaxies can be ruled out as an explanation for the observed high velocity dispersions.

The SB profile of NGC 1277 shows a flattened, regular structure with no significant changes in the PA with increasing distance from the centre ($\Delta\text{PA} \leq 2^\circ$). A single Sérsic fit to its V -band image reveals a moderate Sérsic index of $n = 2.24$, a small effective radius of $R_e = 3.9''$ and a projected axis ratio (b/a) of 0.53. The total V -band magnitude is $m_{V,Vega} = 13.39$. This rather simple fitting scenario is, of course, an under-representation of NGC 1277's stellar complexity, leading to strong residuals in the centre - where the luminosity profile shows an excess of light when compared to the Sérsic - and at larger radii.

A further decomposition with two components improves the fit significantly. Here, a flat ($b/a = 0.52$), inner ($R_e = 2.85''$) bulge-like component ($n = 2.25$) is embedded in a rather flat ($b/a = 0.50$), outer ($R_e = 10.35''$) disk like component ($n = 0.37$). The fit has a bulge-to-total ratio of $B/T = 0.75$.

An acceptable fit can be obtained with (at least) 4 Sérsics, as listed in vdB12. An interpretation of the various components, however, is difficult, except for the outermost component which resembles a round stellar halo. None of the components has a high Sérsic index, making it difficult to find any photometric evidence for the presence of a bulge. Devoid of a distinct spheroid component in this multi-Sérsic fit of NGC 1277, we again adopt the bulge of the two-component decomposition as an upper limit to the bulge luminosity ($B/T = 0.75$) whereas the luminosity of the second innermost Sérsic in the four component decomposition will serve as a lower limit ($B/T = 0.24$).

For the stellar mass model we make use of the V -band Multi-Gaussian-Expansion of vdB12 with a fixed PA of 92.7° . E13 provided an alternative MGE, based on the R -band image of NGC 1277. The difference between the two parameterisations, though, is of little account. Both MGEs reproduce the surface brightness profile equally well, and we refer the reader to E13 for an illustration of the 2D isophotes. There is basically not enough leverage between the wide R -band and medium V -band filter to obtain any colour information that would also minimise the effect of obscuration by the central dust disc. The MGE of E13 in R -band yields a lower total luminosity while increasing the central surface brightness only slightly. These values however do not change the inferred stellar dynamical masses substantially (Sec. 2.4.2.2).

2.3 Stellar Kinematics

This section covers the *HET* long-slit and *PPAK* IFU observations. After sketching the reduction of the individual data sets, we extract and present the kinematics which in turn are used as input for our orbit-based dynamical models.

2.3.1 PPAK

Large-field, medium-resolution (V1200) observations of both galaxies have been carried out at the 3.5 m telescope at Calar Alto, with the *Potsdam Multi Aperture Spectrograph* (*PMAS*) [Roth et al., 2005] in the

PPAK mode [Verheijen et al., 2004; Kelz et al., 2006]. The observing details of this run are outlined in Sec. 2.3.3. The *PPAK* IFU consists of 382 fibers, which are bundled to a hexagonal shape. Each fiber has a diameter of $2.7''$, resulting in a FOV of roughly 1.3 arcmin^2 . Using a 3 dither-pointing strategy, the 331 science fibers have a 100% covering factor across the entire FOV. An additional 36 fibers are used to sample the sky, while the remaining 15 fibers are used for calibration purposes. The V1200 grating has a resolving power of $R = 1650$, at 4000 \AA . The spectral resolution across the nominal $3400 - 4840 \text{ \AA}$ spectral range and FOV is homogenised to 2.3 \AA FWHM based on measured line widths in the arc lamp exposure. This spectral resolution corresponds to an instrumental velocity dispersion of 85 km s^{-1} . The low sensitivity at the blue end and vignetting at the red end reduce the useful spectral range to $3650 - 4620 \text{ \AA}$.

The reduction of the *PPAK* data follows the reduction procedure of the Calar Alto Legacy Integral Field Spectroscopy Area (CALIFA) survey. An extensive overview of the reduction pipeline is given in Sánchez et al. [2012] and Husemann et al. [2013]. The data reduction steps by the pipeline include bias subtraction, straylight subtraction, cosmic ray rejection with PyCosmic [Husemann et al., 2012], optimal fiber extraction, fiber flat-fielding, flexure correction, wavelength calibration and flux calibration. The sky subtraction is done by averaging the spectra of 36 dedicated sky fibers which are located $72''$ away from the *PPAK* FOV centre. Given our compact objects' sizes, the sky fibers should be free from any contamination of the galaxy itself. To exclude any potential contamination by field stars or low-surface brightness objects, the sky spectrum is constructed by taking the mean of only the 30 faintest sky fibers. The resulting sky spectrum is then subtracted from its associated science exposure. Finally, the 3 dither-pointings are resampled to the final data cube with a $1''$ sampling using a distance-weighted interpolation algorithm as described in Sánchez et al. [2012].

To measure reliable stellar kinematics, we first spatially bin the data with the adaptive Voronoi tessellation technique, as implemented by Cappellari & Copin [2003]. At the cost of spatial resolution, we co-add spectra into (Voronoi-) zones to reach a minimum S/N of 25 in each bin, after applying a minimum S/N cut of 4 for each spaxel. The binning process, however, is not straightforward. Spectra of grouped pixels are assumed to be uncorrelated, which is not true for our data. Due to the three-point dither-pattern of the *PPAK* observations, correlated errors during binning appear. In the most general case, each spaxel contains information from a number of different fibers (as each fiber contributes to more than just one pixel). Hence, the noise in adjacent spaxels is correlated and spatial covariances have to be taken into account during the S/N estimates of co-added spectra. A correction for the correlation of the S/N in the data has been applied by quantifying the ratio of the real error - directly estimated from residuals of full spectrum continuum fitting - to the analytically propagated error of binned spectra. The ratio can be characterised by a logarithmic function [Husemann et al., 2013]:

$$\epsilon_{real} / \epsilon_{bin} = 1 + \alpha \log n \quad (2.1)$$

with $\alpha = 1.38$ and n as the number of spaxels in each bin. The ratio increases rapidly for small bins, indicating a high correlation between adjacent spaxels, and flattens out for spatially bigger bins, where the correlation between spaxels becomes less.

Once the effect of noise correlation has been taken into account, we adopt the Indo-US stellar library with 328 spectral templates [Valdes et al., 2004]. A non-negative linear combination of these templates

is then convolved with a Gaussian line-of-sight velocity distribution (LOSVD) and fitted to each spectrum in the range of 3750 - 4550 Å (covering prominent stellar absorption line features such as the Balmer and Calcium H- and K lines), while using additive Legendre polynomials of 15th order. In this way, we derive the mean line-of-sight velocity v , velocity dispersion σ and higher order Gauss-Hermite velocity moments h_3 and h_4 (which represent asymmetric and symmetric departures from a Gaussian LOSVD) per bin on the plane of the sky. Sky lines are masked beforehand and corresponding uncertainties of the kinematic moments are determined by means of 100 Monte Carlo simulations (see also Falcón-Barroso et al., in prep. for a full description of the CALIFA stellar kinematics pipeline).

2.3.2 HET

In addition to the medium-resolution wide-field *PPAK* data, *HET* long-slit kinematics along the major axis are in hand. Observations were carried out, using the Marcario Low Resolution Spectrograph (*LRS*) [Hill et al., 1998]. The *LRS* is a classical long-slit spectrograph with a slit length of 4'. We made use of the G2 grating and a slit width of 1'', covering a wavelength range of 4200-7400 Å. This configuration has a resolution of $R = 1300$ which corresponds to a spectral resolution of 4.8 Å FWHM (i.e. an instrumental velocity dispersion of 108 km s^{-1}), at a pixel scale of $0.475''$. Single exposures of 900 s have been taken for each galaxy, in good weather and seeing conditions of 1 arcsec, resulting in a total of 3 individual (apparent) major axis profiles each for MRK 1216 and NGC 1277.

The reduction of the *HET* data is accomplished by a dedicated and fully automated pipeline [van den Bosch et al., 2015], following a standard reduction practice of bad pixel and cosmic ray masking, overscan and bias subtraction, flat fielding correction and wavelength correction. From the reduced data, we then extract kinematic information by applying an updated version of the pPXF code [Cappellari & Emsellem, 2004] with a set of 120 spectral templates from the MILES stellar library [Sánchez-Blázquez et al., 2006; Falcón-Barroso et al., 2011].

The PSF and positioning of our observations are crucial for an accurate determination of the modelling parameters, such as black hole mass and stellar mass-to-light ratio. We recover a reliable PSF in each data set of both galaxies by iteratively fitting a PSF convolved, reconstructed (slit) image to the MGE of the high-resolution *HST* data. The PSF in turn is expanded by multiple, round Gaussians and the (slit) images are well reproduced in all cases by a PSF with one or two components (Tab. 2.4)

2.3.3 MRK 1216

On December 5, 2011, we obtained *PPAK* data using the medium-resolution V1200 grating. The seeing was ~ 1 arcsec. Two science exposures, 900 seconds each, were taken per pointing, resulting in a total exposure time of 1.5 hours on-source.

Fig. 2.3 displays the two-dimensional line-of-sight kinematics. Reliable data are available out to a major-axis radius of $15''$. The kinematic maps show fast and regular rotation with a maximum velocity of 182 km s^{-1} . The velocity dispersion has a very pronounced peak of about 338 km s^{-1} in the centre, indicating a very high mass concentration and hinting at the presence of a SMBH. Superimposed are contours of constant surface brightness from the same data cube.

Table 2.4: Reconstructed point-spread functions of MRK 1216's and NGC 1277's *PPAK* and *HET* data. The rows display the individual data sets with the slit numbers appended (1), the point-spread function of MRK 1216 for this particular data set, expanded by a set of multiple Gaussians with weight and dispersion (2), and the same for NGC 1277 (3).

Data	MRK 1216 [weight] [arcsec]	NGC 1277 [weight] [arcsec]
PPAK	0.77 1.34	0.75 1.21
	0.23 3.72	0.25 2.44
HET 1	0.55 1.19	1.00 0.83
	0.45 3.39	
HET 2	0.78 0.69	1.00 0.83
	0.22 1.89	
HET 3	0.64 1.10	1.00 0.83
	0.36 3.77	

One out of our three *HET* long-slit kinematics along the apparent major axis will be illustrated in Fig. 2.6. The velocity and velocity dispersion profiles are in agreement with the *PPAK* data, revealing a rotation with a maximum velocity of 219 km s^{-1} and a peak in velocity dispersion of 345 km s^{-1} . Furthermore, we measure strong h_3 moments that appear to be anti-correlated with v , commonly observed in axisymmetric galaxies.

2.3.4 NGC 1277

PPAK data of NGC 1277 have been obtained in the same run as data of MRK 1216. The observing strategy, setup as well as data processing and reduction are also identical, resulting in the kinematic maps in Fig. 2.4. Similar to MRK 1216, the kinematic data of NGC 1277 are limited to a radius of $\sim 15''$. The maps reveal very fast rotation around the short axis, peaking at 276 km s^{-1} , and an extraordinarily flat rotation curve out to several effective radii. The peak in velocity dispersion is about 355 km s^{-1} and hence considerably lower than the dispersion in the (three major axis) *HET* slits (415 km s^{-1}) (Fig. 2.7). Moreover, the central h_4 measurements are also lower in the *PPAK* data cube. The difference, though, is largely attributable to the difference in spatial resolution between both data sets (see Section 2.6 for the reliability of the individual measurements and the recovery of the black hole mass).

We observe the same anti-correlation between h_3 and v , which is expected in the case of axial symmetry and reasonable given NGC 1277's apparent flatness and strong rotation around its short axis. We superimpose its contours of constant surface brightness from the same data cube, with slight irregularities due to extensive masking of nearby objects and the presence of faint fore- and background stars.

2.4 Dynamical Analysis

We introduce our orbit-based dynamical modelling technique which fits the observed line-of-sight kinematics and the photometry, simultaneously. We hereby constrain the intrinsic contributions of black

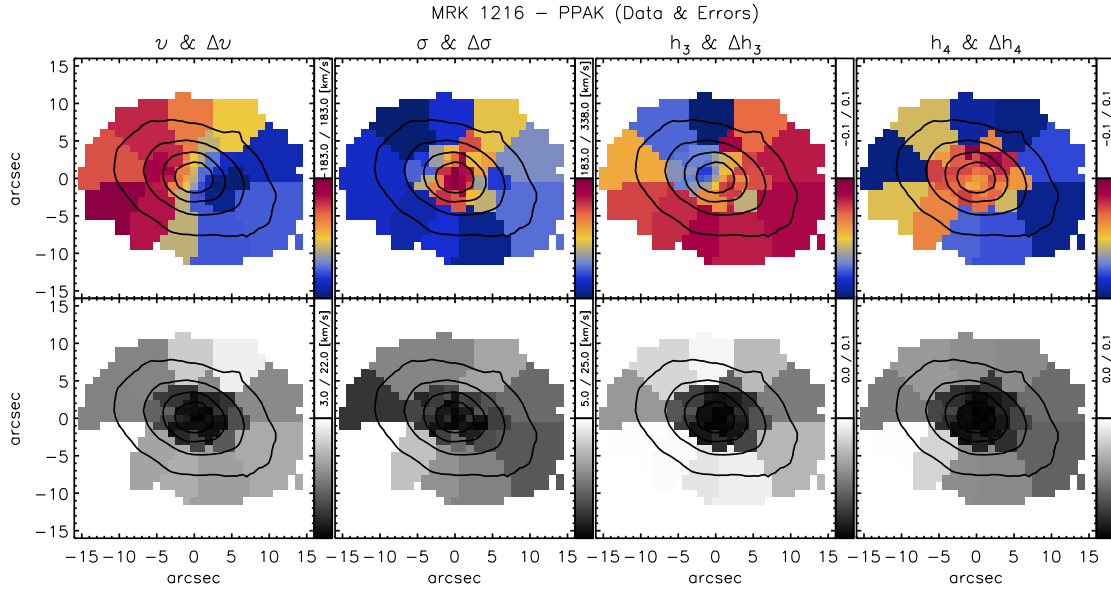


Figure 2.3: *Top*: PPAK IFU stellar kinematic maps of MRK1216, showing the mean velocity (v), velocity dispersion (σ), h_3 and h_4 . The maps show fast rotation around the short axis of 182 km s^{-1} and a central velocity dispersion of 338 km s^{-1} . Given its effective radius of $\sim 5''$, the PPAK data covers the kinematics out to $\sim 3 R_e$. Overplotted are contours of constant surface brightness from the same observing run. *Bottom*: Corresponding uncertainty maps. Maps are oriented N.-E., i.e. north is up and east is left.

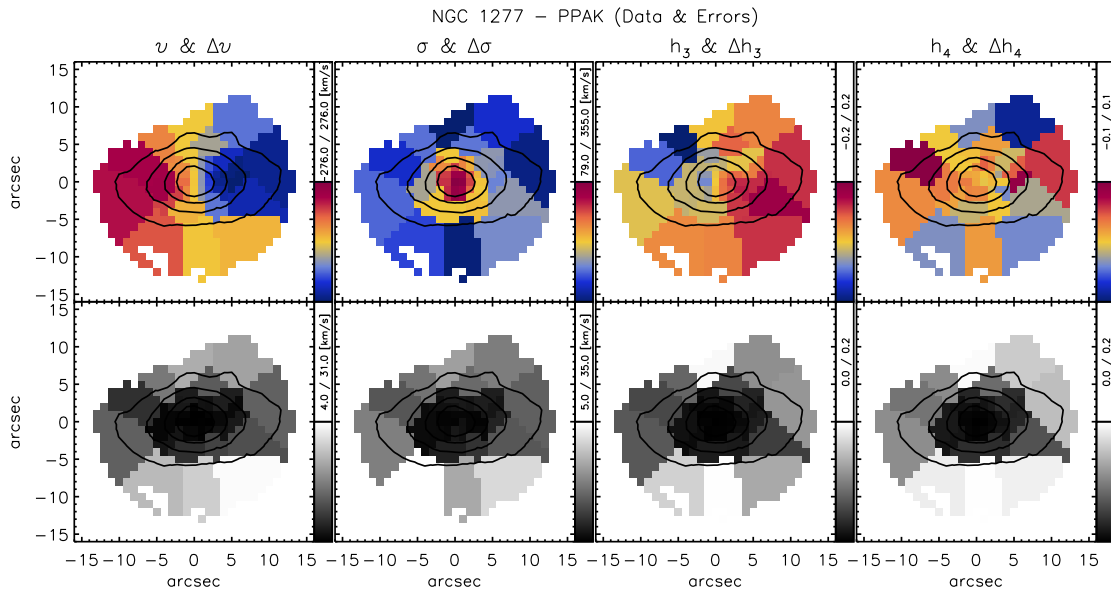


Figure 2.4: *Top*: PPAK IFU stellar kinematic maps of NGC1277 with contours of constant surface brightness, revealing a very fast rotation of 276 km s^{-1} and a peak in velocity dispersion of 355 km s^{-1} . NGC1277 has an effective radius of $\sim 3.5''$, and the data thus covers the kinematics out to $\sim 4 R_e$. *Bottom*: Corresponding uncertainty maps. All maps are oriented N.-E..

hole, stars and dark matter to the overall mass budget and infer the orbital structure of both galaxies.

2.4.1 Schwarzschild's Method

Schwarzschild's orbit superposition method [Schwarzschild, 1979] has proven to be a reliable technique to recover in great detail the dynamical and structural properties of galaxies. The basic idea behind this modelling approach is as simple as it is striking: The motion of astronomical objects, e.g. stars, is governed by the underlying gravitational potential, which in turn can be a sum of not only visible matter but also any non-visible components. This means that once a gravitational potential is assumed, a representative library of orbits can be calculated in that potential that thoroughly samples all integrals of motion (4 in the case of spherical systems and 3 in axisymmetric or triaxial configurations). By assigning weights to the orbits we can then compute their combined properties and compare them to present-day observables, which represent a snapshot of a certain gravitational and dynamical configuration. The implementation of Schwarzschild's method then probes a set of gravitational potentials and tests whether there is a steady-state superposition of orbits in that potential that matches the full LOSVD and the (intrinsic and projected) light/mass distribution.

A wealth of Schwarzschild codes exist. Starting with the modelling of spherical galaxies (e.g. Romanowsky et al. 2003), to axisymmetric galaxies (e.g. Cretton et al. 1999; Gebhardt et al. 2003; Valluri et al. 2004; Thomas et al. 2004; Chanamé et al. 2008) right up to the modelling of triaxial systems (van den Bosch et al. 2008, vdB08 hereafter). In what follows, we make use of the triaxial implementation of Schwarzschild's method. This code represents a very flexible way to reproduce not only all available data but at the same time to recover the internal dynamical structure of galaxies [van de Ven et al., 2008], to constrain their intrinsic shapes [van den Bosch & van de Ven, 2009], their SMBH masses [van den Bosch & de Zeeuw, 2010], their (constant) mass-to-light ratios [Läsker et al., 2013], as well as their dark matter fractions and profiles [Weijmans et al., 2009]. For a detailed overview of the working principles, we refer the reader to vdB08. Here, we confine ourselves to a brief description of the main steps:

1. The implementation begins with a surface brightness distribution that has been parameterised with a set of Gaussians (see Section 2.2.2 and 2.2.3). Once a set of viewing angles are chosen, a de-projection of the surface brightness, corresponding to the surface mass density, can be carried out which yields the intrinsic stellar mass distribution and hence the stellar gravitational potential of the galaxy. For a triaxial deprojection three viewing angles are needed to pin down the shape and orientation of the triaxial ellipsoid. On the other hand, in the axisymmetric case, the intermediate to long axis ratio - i.e. the flattening (q), which is then directly related to the inclination (i) - remains the only free parameter.
2. Within this potential, a representative library of orbits is calculated. In this work, the library consists of more than 7500 orbits (dithering excluded), given by the 9 starting points (in each of the radial and angular directions) at each of the 31 logarithmically sampled equipotential shells between $0.003''$ and $150''$.
3. During orbit integration, intrinsic and projected quantities are stored and then PSF convolved for comparison with the data.

4. For a given potential, χ^2 statistics is used to find a non-negative, linear superposition of orbits that matches the set of kinematic and photometric observables simultaneously. To ensure self-consistency, the models must be able to reproduce the intrinsic mass grid and aperture masses. The masses are constrained to an accuracy of 2 per cent, which reflects the usual uncertainties in the surface brightness parameterisation by the MGE. More precisely, the mass is allowed to vary within the boundaries while we recover the spatially binned 2D LOSVD in a least-squares sense by finding the optimal set of orbital contributions to the Gauss-Hermite moments [Gerhard, 1993; van der Marel & Franx, 1993; Rix et al., 1997].
5. A reiteration of the steps (i - iv) is carried out for differing gravitational potentials, including the presence of an SMBH and dark matter.

For multiple reasons we do not employ regularisation during the construction of the Schwarzschild models. First, we hereby make sure that our models are unbiased with respect to regularisation. Second and more importantly, it is not possible to accurately determine a proper level of regularisation that is needed a priori. Third, it has been shown that regularisation changes neither the values of the best-fitting parameters nor the orbital weights significantly, as long as reasonable values are chosen and an over-smoothing of the distribution function (DF) is prevented [Verolme et al., 2002; van den Bosch et al., 2008; van den Bosch & de Zeeuw, 2010]. And finally, while regularisation can be helpful in individual cases to find the set of orbital weights that best fits the velocity moments and to prevent the weights from varying rapidly, it decreases the degrees of freedom at the same time and leads to an artificial narrowing of the χ^2 contours and thus to smaller confidence intervals for the recovered parameters (but see Valluri et al. 2004, Thomas et al. 2005b and Morganti et al. 2013 for a more detailed discussion of the effects of regularisation in their individual models).

In the case of MRK 1216 and NGC 1277, the photometry and kinematics are consistent with oblate axial symmetry (see: Section 2.6). In constructing dynamical models we will therefore restrict ourselves to an axisymmetric stellar system ².

2.4.2 Mass Profiles

2.4.2.1 MRK 1216

We consider three gravitational sources; the central black hole mass M_\bullet , the stellar mass M_\star (which is the deprojected, intrinsic luminosity density times the constant stellar mass-to-light ratio Υ_\star), and a spherically symmetric dark matter component with an NFW profile [Navarro et al., 1996] with concentration c_{DM} and total virial mass $M_{DM}=M_{200}$. In the case of MRK 1216, the final models will thus probe a four parameter space in $\log(M_\bullet/M_\odot) \in [7, 11]$, $\Upsilon_H \in [0.5, 3]$, $c_{DM} \in [5, 15]$ and $\log(f_{DM}) = \log(M_{DM}/M_\star) \in [-9, 5]$. The search in parameter space is mainly motivated by observational and theoretical constraints on: the stellar mass-to-light ratio for SSP models with a Kroupa and Salpeter IMF [Vazdekis et al., 1996]; the black hole mass from predictions of the black hole scaling relations [Gültekin

²The modelling machinery itself is triaxial, but oblate axisymmetric models can be run in the triaxial limit (i.e. intermediate-to long-axis ratio (b/a) = 0.99). Although the orbits in axisymmetric galaxies are dominated by tube orbits, our slightly triaxial models still benefit from a non-negligible amount of additional triaxial orbit families (e.g. box orbits).

et al., 2009] and the dark halo parameters from investigations of Bullock et al. [2001], Moster et al. [2010] and Macciò et al. [2008] (see also Section 2.5.3).

By design, we do not explore the inclination space. As has been shown in Krajnovi et al. [2005] and van den Bosch & van de Ven [2009], it is not possible to infer the inclination angle by means of two-dimensional line-of-sight stellar kinematics, alone, unless kinematic features exist (e.g. kinematically decoupled cores) that put additional constraints on the intrinsic shape of galaxies. Even in the case of three integral axisymmetric orbit-based models, different inclinations above the lower limit that is given by the photometry are able to fit the LOSVD almost equally well. However, we can further constrain the inclination by simple observational arguments. Although the flattest Gaussian in our MGE limits the minimum possible inclination for the projection in an oblate axisymmetric case (Section 2.2.2), the deprojection of Gaussians close to the lower inclination limit of 59° generates intrinsically flat galaxies with unphysical axis ratios of $q = b/a \leq 0.2$. On the other hand, an edge-on configuration (even though possible) appears to be unlikely, too. MRK 1216 is much rounder than expected for a flat, oblate system that is observed at 90° , with an axis ratio that quickly converges to unity beyond $1 R_e$. We therefore choose an inclination of 70° that is in between these two extreme cases. To assess the reliability and robustness of our results with respect to changes in the inclination, we also explore models with a close to edge-on configuration of 85° and find that our parameter constraints are affected by less than 5 per cent. The upper limit of the stellar mass-to-light ratio increases by ~ 0.1 when increasing the inclination, which in turn leads to insignificant changes in the derived values for the black hole and dark halo values. In general, the results are very robust with respect to variations in the inclination. Changes in the parameter estimation, and in particular in the stellar mass-to-light ratio, are only significant if a large range of inclinations is probed or respectively the minimal observed axis ratio q is larger than 0.7, which translates to lower inclination limits of $i \leq 45^\circ$ [see also Cappellari et al., 2006].

We bi-symmetrise the observed kinematics beforehand. Although being fairly symmetric, the symmetrisation reduces noise and systematic effects which helps for the recovery of the higher order Gauss-Hermite moments in the models. The PA for the bi-symmetrisation is obtained by using the weighted first and second moments of the intensity distribution in the *PPAK* data ($PA_{kin} = 70.7^\circ$), and turns out to be in excellent agreement with the PA that is inferred from the high-resolution imaging ($PA_{phot} = 70.2^\circ$).

We construct $\sim 200\,000$ models to constrain the best-fitting parameters as well as all parameters within a relative likelihood of three standard deviations. Figure 2.5 (top left) shows the enclosed mass distribution of MRK 1216, derived from our entire set of models. The solid lines represent the stellar mass (red), black hole mass (blue), dark matter content (green) and total mass (black) for the best fit.

The dashed lines indicate 3σ confidence intervals for one degree of freedom. Based on these models, we obtain a total stellar mass of $\log(M_*/M_\odot) = 11.3^{+0.1}_{-0.2}$, a black hole mass of $\log(M_\bullet/M_\odot) = 9.4^{+0.6}_{-9.4}$, and a dark halo mass of $\log(M_{DM}/M_\odot) = 14.2^{+1.1}_{-2.2}$. Neither the black hole nor the DM halo parameters are very well constrained. The best fitting dark halo dominates at radii larger than $15''$ (i.e. ≥ 7 kpc), which is at the edge of the extent of our kinematic data. Interestingly, models without any dark matter are not able to recover the observations and can be ruled out.

Figure 2.5 (middle left) is a slice through the $M_\bullet - \Upsilon_H$ plane, i.e. we plot every combination of black hole mass and stellar mass-to-light ratio, marginalised over the dark halo parameters c_{DM} and f_{DM} .

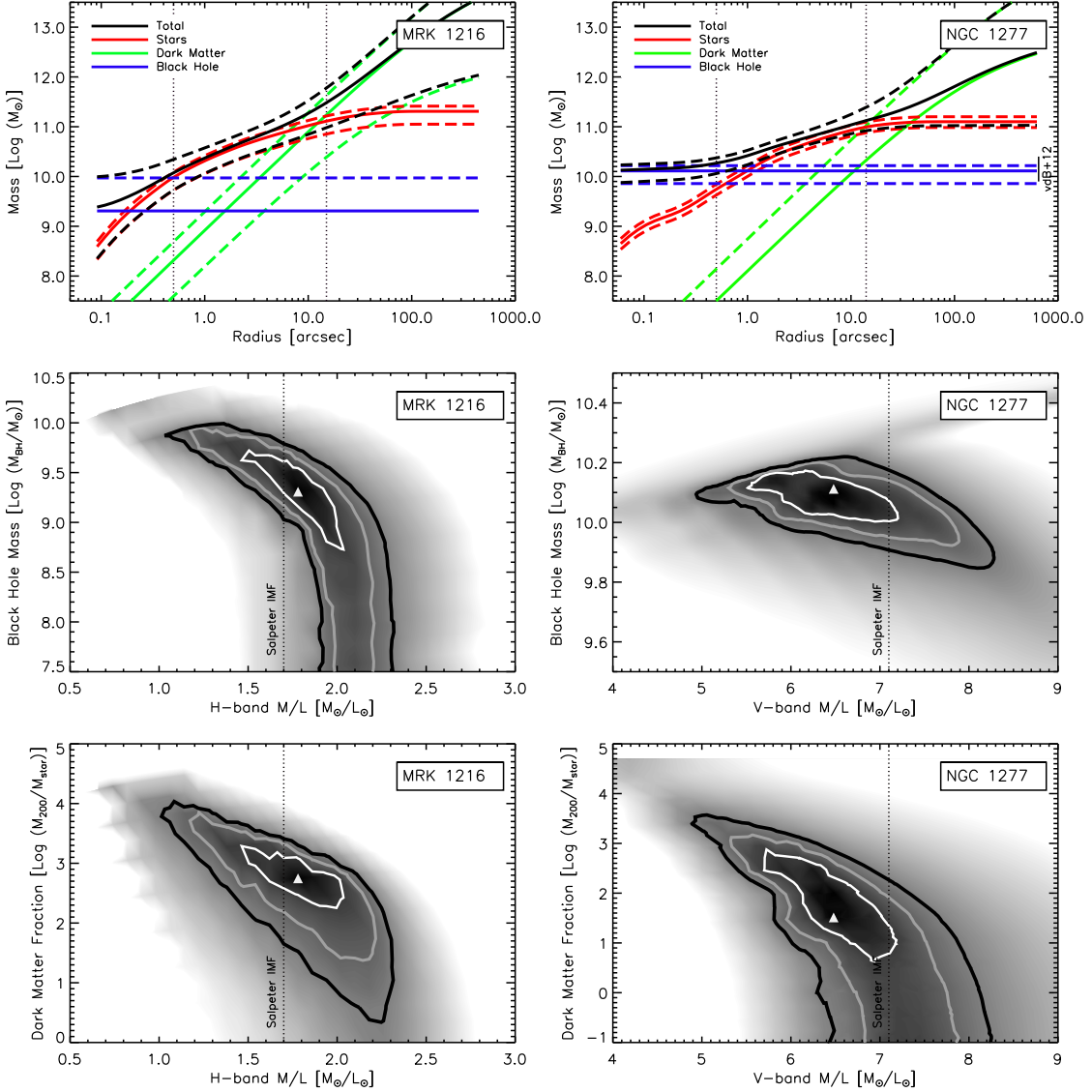


Figure 2.5: *Top*: Intrinsic enclosed mass profiles of MRK 1216 and NGC 1277. Solid lines represent best-fitting values, dashed lines are 3σ confidence intervals. The dotted vertical lines indicate the minimum and maximum extent of the kinematic data for each galaxy. For NGC 1277, we also depict an earlier estimate of the black hole mass from vdB12. *Middle*: Confidence contours of black hole mass vs. stellar mass-to-light ratio. *Bottom*: Confidence contours of dark matter fraction vs. stellar mass-to-light ratio. The lines denote the 68.3 (white), 95 (grey) and 99.7 (black) per cent quantiles of a χ^2 distribution with two degrees of freedom. As a reference, we overplot stellar mass-to-light ratio predictions of SSP models with a (single) power-law Salpeter IMF [Vazdekis et al., 1996, 2012] in the respective bands.

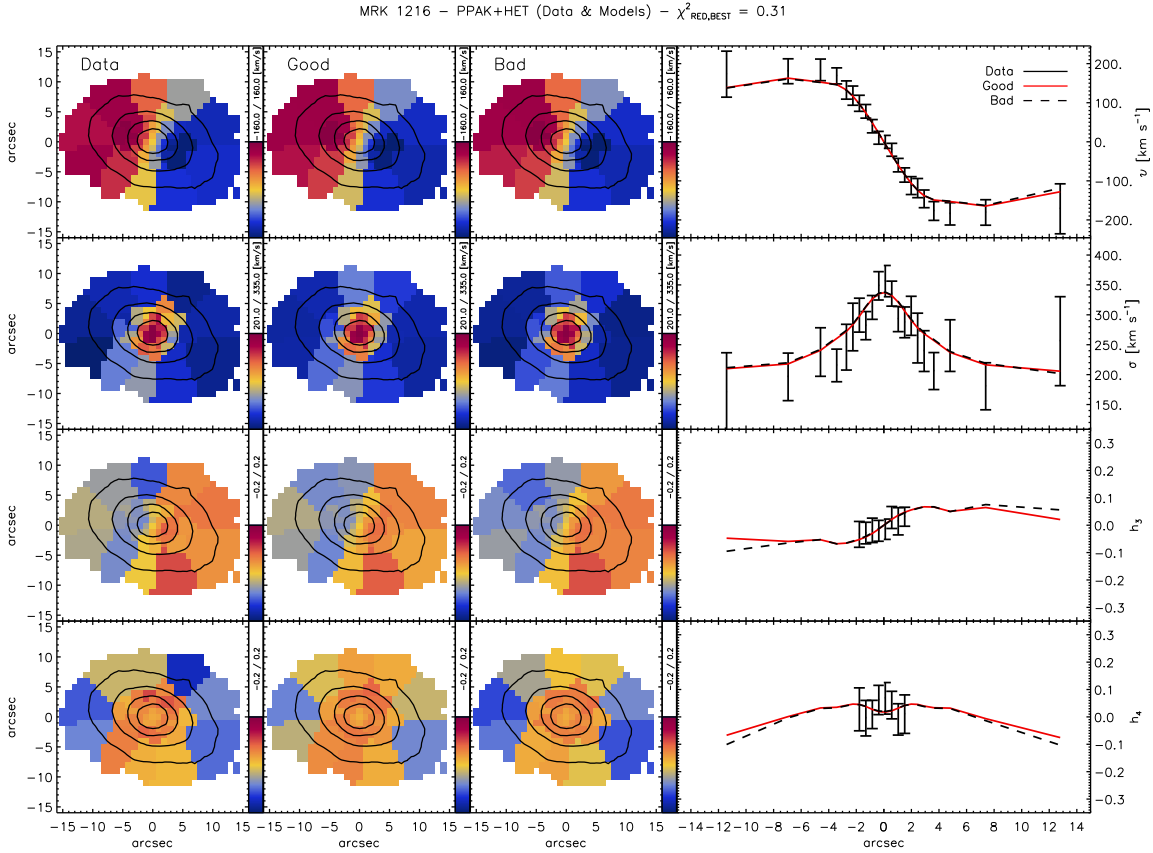


Figure 2.6: *First column:* PPAK IFU (bi-symmetrised) velocity, velocity dispersion, h_3 & h_4 maps of MRK1216, overplotted with contours of constant surface brightness. *Second column:* Best-fitting Schwarzschild model with a reduced χ^2 of 0.31. *Third column:* Bad model with $\log(M_{DM}/M_\odot) = -9$. *Fourth column:* One out of the three simultaneously fitted HET long-slit data with corresponding errors, best-fitting Schwarzschild model (red) and bad model (dashed). The IFU maps are oriented N.-E., i.e. north is up and east is left.

As is already visible in the enclosed mass profile plot, the best-fitting black hole mass is $\log(M_\bullet/M_\odot) = 9.4$. While we obtain an upper limit of $\log(M_\bullet/M_\odot) = 10.0$, the black hole is unconstrained at the lower boundary of the grid, at $\log(M_\bullet/M_\odot) = 7$. We therefore carry out additional tests at the lower end of the parameter space ($M_\bullet/M_\odot = 0$) which show that the presence of a black hole is not required, as models with no black hole are able to match the data as well. The stellar mass-to-light ratio in H -band spans a range of 1.0 - 2.3. The best-fitting model favours $\Upsilon_H = 1.8$. For comparison, stellar population synthesis (SPS) models with a single power-law Salpeter stellar initial mass function (IMF) [Vazdekis et al., 1996] predict a stellar mass-to-light ratio of 1.7 (assuming solar metallicity and an age of ~ 13 Gyr).

The bottom left panel in Figure 2.5 is analogous to the middle panel and displays the goodness-of-fit contours for the dark matter fraction f_{DM} and H -band stellar mass-to-light ratio Υ_H , marginalised over all remaining parameters. We observe closed contours that clearly call for a non-negligible amount of dark matter. The halo concentration in the models is unconstrained and can adopt any value within the range that is probed. The best fitting dark halo has a concentration of $c_{DM} = 10$, a mass of $\log(M_{DM}/M_\odot) = 14.2$ and a scale radius of $r_s = 110$ kpc.

The corresponding best-fitting Schwarzschild model kinematics of MRK1216 are shown in Figure 2.6. The plots display fits to the first four kinematic moments of the PPAK data, and one of the three

simultaneously fitted individual *HET* long-slits. Our models can accurately recover the kinematics of the *PPAK* and *HET* data, in particular the peak in the velocity dispersion profile and the flat and rapidly rotating velocity curve beyond $5''$. For illustration purposes we add a bad model to the plots. The bad model was chosen by following the ridge of minimum χ^2 beyond the 3σ confidence level and displays the predicted kinematics for the best-fitting model without a dark halo. The relative likelihoods of the two models are separated by $\Delta\chi^2 = \chi_b^2 - \chi_{b\ w/o\ dm}^2 = 15$ and the differences in the figures are barely distinguishable. Despite these similarities, we will show that dark matter is a necessary ingredient to successfully recover the observational constraints and well in line with our current understanding of the stellar build-up and properties of elliptical galaxies (see Section 2.5.3).

2.4.2.2 NGC 1277

For the dynamical analysis of NGC1277, our models explore the parameter ranges in $\log(M_\bullet/M_\odot) \in [7,11]$, $\Upsilon_V \in [2,10]$, $c_{DM} \in [5, 15]$, $\log(f_{DM}) = \log(M_{DM}/M_\star) \in [-9, 5]$ and $i \in [75]$. In contrast to vdB12, the freedom of the models is further restrained by fitting the *PPAK* and *HET* data at the same time. As in the case of MRK1216, we present the mass distribution, the black hole mass vs. stellar mass-to-light ratio and dark matter fraction vs. stellar mass-to-light ratio plots, which outline the limits for the individual parameters.

Figure 2.5 (top right) shows the enclosed mass profile with a total stellar mass of $\log(M_\star/M_\odot) = 11.1^{+0.1}_{-0.1}$, a black hole mass of $\log(M_\bullet/M_\odot) = 10.1^{+0.1}_{-0.2}$ and a dark halo mass of $(M_{DM}/M_\odot) = 12.6^{+1.9}_{-12.6}$, at a significance of 3σ . The kinematic data of NGC1277 show the same problems as the data of MRK1216, leading to poor constraints on the dark halo parameters. The vertical dotted line displays the extent of our kinematic information and illustrates the inability to constrain the dark matter halo, which becomes dominant only at larger radius for the best-fitting model. Here, the presence of dark matter is not necessary to fit the observed velocity moments.

We present contours of χ^2 as a function of M_\bullet and Υ_V in Figure 2.5 (middle right). Despite the low resolution data, the black hole mass is well constrained (see also Sec. 2.5.2.1 and 2.6). We obtain an upper limit of $\log(M_\bullet/M_\odot) = 10.2$ and a lower limit of $\log(M_\bullet/M_\odot) = 9.9$. The best-fitting V-band stellar mass-to-light ratio is $\Upsilon_V = 6.5^{+1.5}_{-1.5}$ and consistent with the mass-to-light ratio that is predicted from spectral synthesis fits [Vazdekis et al., 2010; Ricciardelli et al., 2012; Vazdekis et al., 2012] of NGC1277's deep, optical long-slit observations (T14), assuming a single power-law Salpeter IMF (see Section 2.6). Models with a black hole mass of $\log(M_\bullet/M_\odot) \sim 9$ - as suggested by the scaling relation between black hole mass and bulge luminosity $M_\bullet - L_{Bulge}$ [Gültekin et al., 2009; McConnell & Ma, 2013; Kormendy & Ho, 2013] - are clearly disfavoured and not able to recover the data (see also Section 2.5.2.1 and 2.5.2.2).

The confidence intervals for the dark halo are shown in the bottom right panel of Figure 2.5. In contrast to MRK1216, the 99.7 per cent contours cannot rule out models without dark matter. The best-fitting NFW profile has a concentration of $c_{DM} = 10$, a dark halo mass of $\log(M_{DM}/M_\odot) = 12.6$ and a scale radius of $r_s = 33$ kpc.

In Fig. 2.7, we show the bi-symmetrised *PPAK* kinematics, one of the three individual but simultaneously fitted *HET* long-slit kinematics, the best-fitting model and a bad model of NGC1277. Note that one of the three long-slit kinematics is identical with the data presented in vdB12. In this case, the *PPAK* velocities

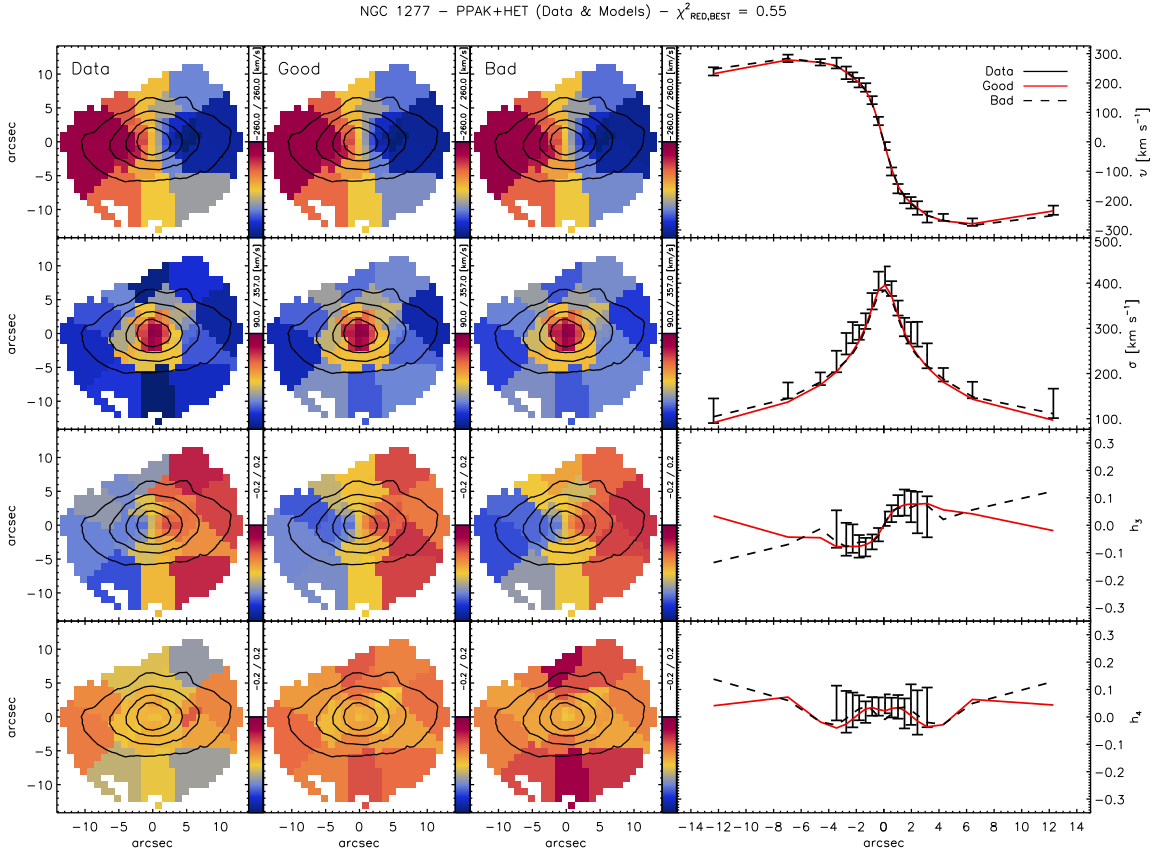


Figure 2.7: *First column:* PPAK IFU (bi-symmetrised) velocity, velocity dispersion, h_3 & h_4 maps of NGC 1277, oriented N-E with contours of constant surface brightness overlotted. *Second column:* Best-fitting Schwarzschild model with a reduced χ^2 of 0.55. *Third column:* Bad model with $\log(M_\bullet/M_\odot) = 9.5$ and $\Upsilon_V = 8.3$. *Fourth column:* One out of the three simultaneously fitted HET data with corresponding errors, best-fitting Schwarzschild model (red) and bad model (dashed).

and dispersions are fitted exceptionally well. Problems arise in fitting the HET velocity dispersion as the peak in the HET data differs by $\sim 60 \text{ km s}^{-1}$ from the peak in the PPAK cube (Section 2.3.4). The best fit predicts a slightly lower central dispersion in NGC 1277, which matches the PPAK data but is in contrast to the HET observations (see Section 2.6). We also emphasise that even though the h_4 values of the good model are slightly off along the minor axis, they are still within the measurement errors. For the illustration of a bad model we explicitly chose a model with a higher mass-to-light ratio and a black hole mass that is about a factor of 2 smaller than the lower limit. The $\Delta\chi^2$ of this fit is ~ 50 and well beyond the 3σ boundary. The difference between observed and modelled kinematics are most pronounced in the second and fourth column where the bad model clearly fails to fit σ and h_4 in the centre. The deviation in h_4 along the minor axis is also much stronger. In contrast to the good model, the bad model fails to reproduce the kinematics within the measurement errors, by underestimating the number of stars with line-of-sight velocities close to the average velocity.

Overall, our models are in good agreement with the results of vdB12, with tighter constraints especially on the lower end of stellar mass-to-light ratios and hence a slightly decreased upper limit of the black hole mass. This effect is mainly driven by lower estimates of the dark halo content that is constrained by the wide-field IFU data and higher stellar mass-to-light ratios which then propagate towards the centre.

2.5 Discussion

We summarise the findings and take a closer look into the results of our orbit-based dynamical models, their orbital structures and how they compare to the photometric analysis. In addition, we place the black hole masses back into the scaling relations, discuss the significance of our dark halo detections and finish with a concluding remark concerning the origin and evolutionary history of both galaxies

2.5.1 Orbital Structure

Apart from inferring the mass distribution, orbit-based dynamical models also allow a detailed probe of the orbital structure of galaxies. We can not only inspect the amount of mass that is assigned to each particular orbit, or orbit family in general, but also quantify the system's degree of anisotropy, which holds important clues about the processes that shaped its evolution [Bender et al., 1992]. The anisotropy profiles of early-type galaxies have been investigated extensively. While data and techniques differ, ranging from long-slit observations and spherical models [Kronawitter et al., 2000; Gerhard et al., 2001] to more general axisymmetric models [Gebhardt et al., 2003] that make use of the full 2D spectral information [Cappellari et al., 2007], there is a common agreement, namely that luminous, round and slowly rotating early-type galaxies are almost isotropic whereas oblate, fast-rotating galaxies span a large range of anisotropy profiles. The orbital structures in the dynamical models, though, have not been linked to the many and varied components that are observed via photometric decompositions of high resolution imaging, which also provide an independent record of a galaxy's evolutionary history. In the first part of this subsection we aim to provide this link by mapping the components in phase space to the multi-Sérsic components in Section 2.2.2 and 2.2.3. In the second part, we then present a direct comparison between the orbital distribution of the two compact objects in this work and a more general and representative sample of early-type galaxies.

In Figure 2.8 and 2.9, we show the orbital mass weights as a function of average radius (\bar{r}) and spin ($\bar{\lambda}_z = \bar{J}_z / (\bar{r} \times \bar{\sigma})$ - where \bar{J}_z is the average specific angular momentum of the orbits along the short z -axis and $\bar{\sigma}$ their average dispersion - and further examine the orbital structures by inspecting the ratio of radial to tangential velocity dispersion ($\sigma_r / \sigma_t = \sqrt{2\sigma_r^2 / (\sigma_\phi^2 + \sigma_\theta^2)}$) and the occupation fractions of the individual orbit families [de Zeeuw, 1985; Statler, 1987; de Zeeuw & Franx, 1991]. The averages are time averages per single orbit, which the Schwarzschild models keep track of.

Deciphering the mass distribution among the orbits as a function of angular momentum will provide the necessary link to the photometric components. Hitherto, only two other galaxies have been investigated in a similar manner. Walsh et al. [2012] presented the S0 galaxy NGC 3998 which showed a very clear non-rotating bulge and a non-maximal rotating disk. And Lyubenova et al. [2013] presented the E5 galaxy FCC 277 with a nuclear star cluster, which showed both a pro- and retrograde disk and a non-rotating component. A direct comparison to the photometric structures, though, was not within the scope of those investigations and has therefore been omitted so far.

In what follows, we present the orbital configuration only for the best-fitting models, but the general trend is preserved for most models that are within the statistical 3σ uncertainties.

2.5.1.1 MRK 1216

MRK 1216 rotates rapidly ($\sim 220 \text{ km s}^{-1}$) around the short axis. It is thus a fast-rotating, oblate early-type galaxy. The two-component photometric decomposition contains a small, flattened and massive bulge and an outer exponential envelope, with a bulge-to-total ratio of $B/T = 0.69$. However, the dynamical decomposition is not as straightforward as matching directly to these two Sérsic components; there is a large, extended, rotating structure ($\lambda_z = 0.0 - 0.5$) beyond $10''$; two, more centrally located, moderately rotating structures ($\lambda_z = 0.1 - 0.5$) between $1''$ and $5''$; an inner ($8''$) rapidly ($\lambda_z \sim 0.7$) and outer ($\geq 20''$) maximally rotating component ($\lambda_z \sim 1$), as well as some mass in two counter-rotating and one outer ($\geq 10''$) non-rotating structure (Fig. 2.8, left panel). The orbital structure is devoid of a massive, non-rotating component which harbours a major fraction of the stellar mass and hence we conclude that MRK 1216 does not contain a classical, non-rotating bulge. If anything, we identify the moderately rotating component at $\sim 1''$ as the bulge, with a dynamical B/T of 13 per cent, which however is in sharp contrast to the photometric B/T of the two-component decomposition.

Remarkably, the multiple component photometric fit of MRK 1216 with four Sérsics (Section 2.2.2) is in a much better agreement with the dynamical decomposition. The outer three photometric components can be mapped onto the 3 mildly rotating distinct components in the orbital configuration at $\sim 1''$, $4''$ and $15''$. All these photometric components have low ($n \sim 1$) Sérsic indices that are normally associated with an exponential disk, except for the outermost component that resembles an envelope with close to zero ellipticity. Adopting Sérsic component number two as the bulge gives a photometric B/T of 12 per cent (Sec. 2.2.2), which is in very good agreement with the dynamical B/T of 13 per cent. Moreover, the component around $15''$ carries a mass of 30 per cent and is almost as massive as the large, outer component in the photometry with a contribution of 35 per cent to the total mass. The most notable difference is between the third and most massive Sérsic in the photometry and the dynamical substructure at $4''$, which ought to contribute 45 per cent of the total stellar mass but only constitutes 20 per cent in the orbital configuration. We also note that the innermost photometric component is too small ($0.4''$) to be resolved by the dynamics while the rapidly rotating structure ($\lambda_z \sim 0.7$) at $8''$ has no photometric counterpart at all. Finally, the maximally rotating structure ($\lambda_z \sim 1$) at $20''$ is beyond the reach of our kinematic data and merely a result of an extrapolation, but is expected to correspond to a disk component whereas the photometry at those radii are dominated by the round outer halo.

MRK 1216's radial anisotropy profile is simple and almost isotropic with oscillations of only 30 per cent around $\sigma_r/\sigma_t = 1$ (Fig. 2.8, right panel). The largest deviation from isotropy appears within the central $1''$, which is attributable to the strong gravitational perturbation of the axisymmetric potential due to the presence of a black hole and hence the requirement of a non-negligible amount of stars in box orbits. Most of the mass resides in short-axis tube orbits whereas long-axis tube orbits, which are vital orbit types for triaxial and prolate systems [van de Ven et al., 2008; van den Bosch & van de Ven, 2009; van den Bosch & de Zeeuw, 2010], are totally absent.

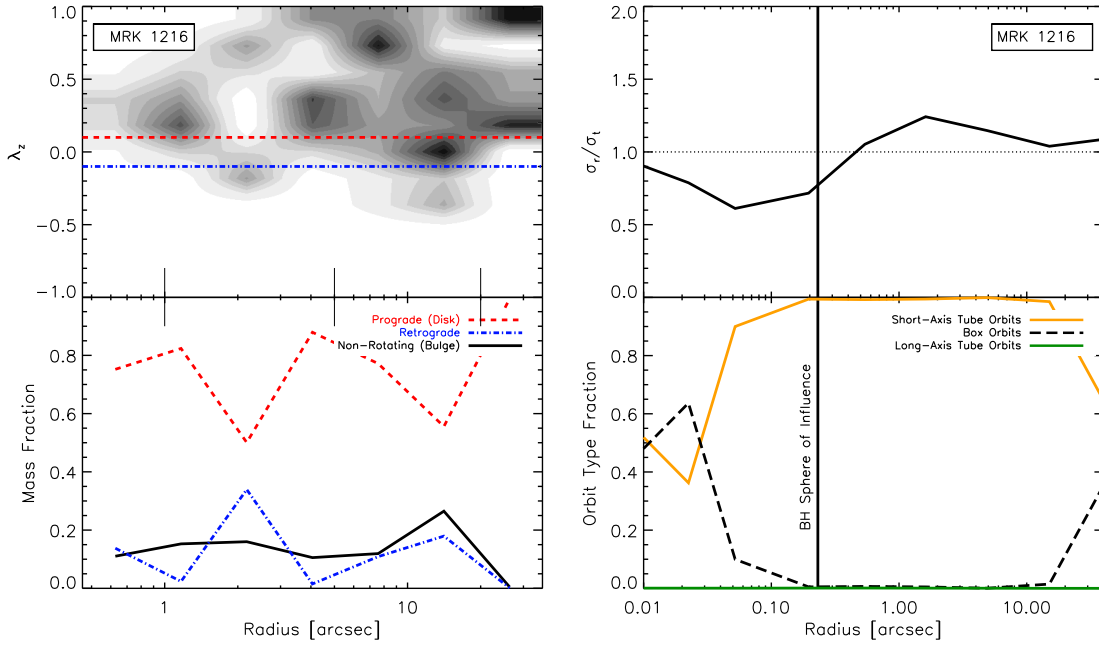


Figure 2.8: Orbital structure of MRK 1216 for the best-fitting model. *Top left*: Mass distribution along all orbits as a function of angular momentum along the short z -axis and radius. Mass located above (below) the red (blue) line is rotating strongly prograde (retrograde). *Bottom left*: Local mass fraction as a function of average radius, divided into a non-rotating bulge-like ($|\lambda_z| < 0.1$), prograde rotating disk-like ($\lambda_z > 0.1$) and retrograde rotating ($\lambda_z < -0.1$) component. This classification is based on the net angular momentum of the orbits along the z -axis. The long tick marks denote the effective radius of the photometric components in the multi-Sérsic fit. *Top right*: Profile of radial vs. tangential velocity dispersion. *Bottom right*: Mass fraction per orbit type as a function of radius. The vertical solid line denotes the predicted black hole sphere of influence. The orbital distribution below $0.4''$ is not resolved by the data and merely extrapolated by the models.

2.5.1.2 NGC 1277

NGC 1277 is also a flat, fast-rotating ($\sim 300 \text{ km s}^{-1}$) early-type galaxy and, as expected, our best-fitting dynamical model reveals a simple structure where most of its stars (≥ 80 per cent) reside in strongly rotating orbits between 1 and $20''$ (Fig. 2.9, left panel). We distinguish at least three individual components in phase space; a highly rotating one ($\lambda_z = 0.7 - 1$) between $5''$ and $10''$, containing 65 per cent of all stars; one moderately rotating and very extended component ($\lambda_z = 0.1 - 0.5$) between $0.5''$ and $3''$, which contains 23 per cent of the stellar mass, and a centrally located non-rotating one at $2''$, that harbours 3 per cent of all stars. The remaining 9 per cent are distributed among the tiny substructures at various positions. The lack of a massive, non-rotating ($\lambda_z = 0$) component in the dynamical decomposition suggests that this galaxy does not contain a pressure supported bulge. Moreover, due to the absence of a distinct, central, non-rotating component, this result does also not match with what we see and anticipate based on our results in the photometric two-component decomposition (Section 2.2.3), which has a bulge and an exponential disk with a $B/T = 0.75$. The massive bulge in the two-component fit is located around $\sim 3''$, where most of the mass in the orbital decomposition resides in rotating structures. While the massive bulge in the photometry could indeed be mildly rotating, similar to our identification of the dynamical bulge in the orbital structure of MRK 1216, the mass fractions at these radii are simply at odds and disfavour the simple two-component decomposition.

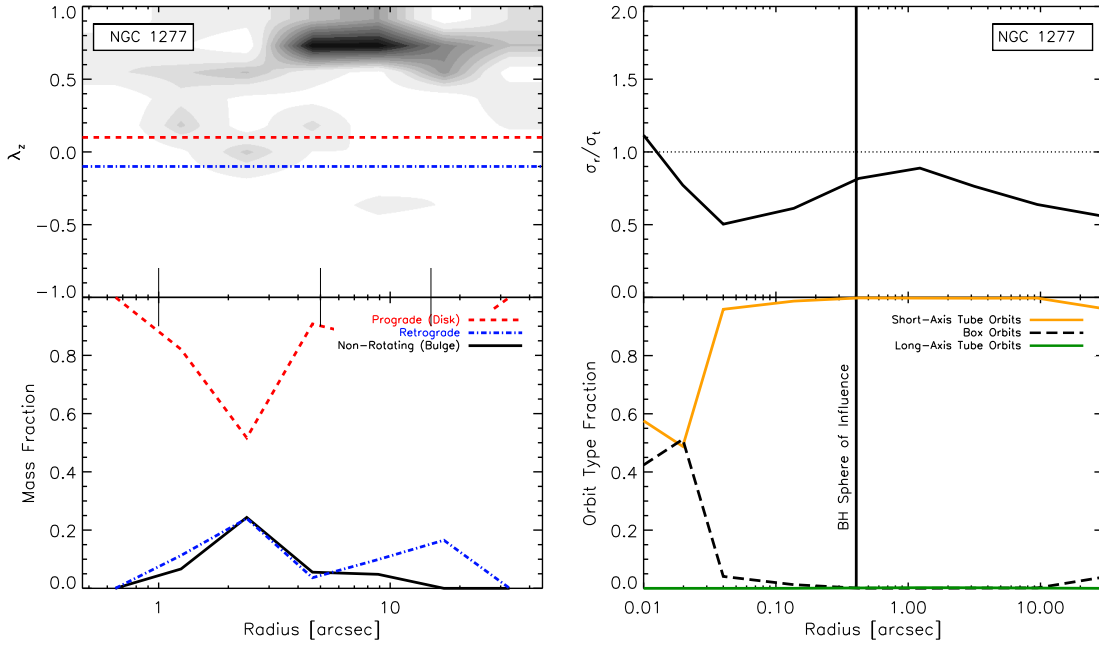


Figure 2.9: Orbital structure of NGC 1277 for the best-fitting model. *Top left*: Mass distribution along the orbits as a function of average angular momentum and radius. *Bottom left*: Local mass fraction as a function of radius for the individual components (see caption in Figure 2.8). *Top right*: Velocity anisotropy profile. *Bottom right*: Mass distribution along individual orbit types. Here again, radii below $0.4''$ are not resolved by our observations and have therefore to be treated with care.

The orbital structure is also not consistent with the 1D photometric analysis of NGC 1277 from Kormendy & Ho [2013], as they connected their inner flattened bulge with the outer round halo ($> 20''$) as a single component, which is more luminous than the disk in their analysis ($B/T = 0.55$). In the dynamical decomposition, however, these two components (i.e. bulge and outer halo) do not appear to be connected and most of the mass resides in the extended flat and rapidly spinning component ($\lambda_z \geq 0.7$).

In contrast, the overall dynamical structure has an intriguing resemblance to the multi-component Sérsic fit, which hints at an inner, exponential disk ($n \sim 1$) with a small contribution to the overall stellar mass (24 per cent); and most of the mass (53 per cent) settled in a flat, outer disk-like component that resembles the extended highly rotating structure in our orbital decomposition. Even though the low Sérsic index of the second innermost component in the photometric fit is usually associated with a disky component, we cannot rule out the existence of a mildly rotating, flattened spheroidal component. Given the match in the orbital and photometric decomposition, we therefore adopt this component as a lower limit to the bulge, with a $B/T = 0.24$ (see Sec. 2.2.3 and 2.5.2.2). The innermost photometric component ($\leq 0.5''$) is not resolved by our observations and, unfortunately, our stellar kinematics do not reach out to large enough radii to determine the dynamical structure of the outer halo that is expected at $15''$ and beyond. However, these substructures contain only a minor fraction (23 per cent) of the total stellar mass of this object.

Considering that the dynamical models of NGC 1277 are also axisymmetric, with deviations from axial symmetry close to the black hole, the resemblance between both galaxies in the mass weights of the

different orbit types is no surprise. Unlike MRK 1216, however, NGC 1277 is mildly radially anisotropic in the immediate vicinity of the black hole and becomes strongly tangentially anisotropic beyond (Fig. 2.9, right panel).

Dynamical orbit based decompositions are a good tool for unravelling components in phase space. In this work, we could trace back the spinning orbital components of MRK 1216 and NGC 1277 to the flattened, low Sérsic components in the photometry, which are commonly associated with rotating structures. Moreover, our models show that the two compact galaxies are rotationally supported while both the orbital and photometric structures indicate the lack of a central pressure supported, massive spheroidal component. A small, mildly rotating bulge could be present, given the match in mass and location of the second component in the photometric multi-Sérsic fits and the dynamical substructures. However, taking into account their flattening, low Sérsic index, small mass fraction and rotational support, these structures more likely correspond to rotating discs (maybe even thick disks), and can only be considered as a modest lower limit of a putative bulge (see e.g. Sec. 2.5.2.2).

It is also worth noting that although the models rely on the more general MGE, which is completely independent from the Sérsic fits and devoid of any physical interpretation, the orbital substructures bear no resemblance to it. The location and mass weights of the orbital structures do not match the individual Gaussians, which is most pronounced in Fig. 2.9 where the overall structure is clearly comprised of less than ten components.

Nevertheless, more decompositions are needed to get a better understanding. For instance, drawing boundaries between the substructures in phase space is not trivial, while the photometric models are often plagued by strong degeneracies between the individual components in the fit. In our case, the issue of connecting photometric and dynamical structures is most prominent in MRK 1216, where the mismatch in mass between the most massive photometric component in the multi-Sérsic fit and the mildly rotating orbital component at $4''$ is worrisome, while some minor components in the dynamical structure do not seem to have a photometric counterpart at all. Given that our Schwarzschild method is capable to recover the distribution function and hence the rich, internal dynamical structure of ETGs [van de Ven et al., 2008], this might hint at difficulties in a) recovering the stellar build-up by multi-component Sérsic fits to the photometry and/or in b) simply associating flat, (high-) low Sérsic components with (non-)rotating dynamical structures. Surely, modelling limitations, such as the assumption of axisymmetry (but see also Sec. 2.6) will also have a non-negligible effect on the recovery of the internal dynamics and their subsequent interpretation. More tests are therefore necessary, optimally of mock galaxy kinematics of purely rotational or pressure supported dynamical systems, to assess the robustness of our approach and the range of λ_z values that can be associated with these structures. This, in turn, will yield valuable information regarding the reliability and physical interpretation of photometric decompositions.

2.5.1.3 Classification And Comparison

In Emsellem et al. [2007, 2011], early-type galaxies were separated into two classes of systems based on their specific stellar angular momentum. Fast rotators reveal a high specific angular momentum,

comprise the majority of early-type galaxies, are close to axisymmetric in most cases and span a large range of anisotropy profiles [Cappellari et al., 2007], in contrast to slow rotators which appear to be nearly isotropic. MRK 1216 and NGC 1277 are both fast rotators, as is expected by their rapid rotation around the apparent short axis, with a specific angular momentum λ_R of 0.34 (0.41) and 0.25 (0.53) within one (three) effective radii.

To facilitate a comparison between the dynamical structure of the two compact galaxies in this work and a more general and representative sample of galaxies, such as presented within the SAURON framework, we follow the procedure and notation in Cappellari et al. [2007] and show the relation between the global anisotropy parameter $\delta = 1 - \Pi_{zz}/\Pi_{xx}$ [Binney & Tremaine, 1987] and the anisotropy parameter $\beta_z = 1 - \Pi_{zz}/\Pi_{RR}$, which describes the shape of the velocity dispersion tensor in the meridional plane. The values in this work have been measured within $3 R_e$, i.e. ~ 6 kpc and 3.5 kpc for MRK 1216 and NGC 1277 respectively. The measurements are based on a larger relative scale, in contrast to the SAURON sample which usually covers the kinematics only out to $\sim 1 R_e$, but corresponds much better to the SAURON measurements of typically larger ETGs in an absolute sense.

We confirm the picture of diverse anisotropy profiles of fast-rotating systems in Fig. 2.10. Here, MRK 1216 is located in a region that is populated by the bulk of fast-rotating galaxies in the SAURON sample. It's only slightly tangential anisotropic in the $\phi - r$ plane, which leads to the conclusion that most of its anisotropy can be traced back to a flattening of the velocity dispersion tensor in the meridional plane. While MRK 1216 follows the trend presented in Cappellari et al. [2007], that fast-rotating early-type galaxies are mainly flattened oblate systems, NGC 1277 is an outlier in every aspect and appears to belong (kinematically) to a totally different class of objects. It is flattened in z-direction, but also shows a substantial amount of tangential anisotropy in the plane orthogonal to the symmetry axis, which is necessary to account for the high and extended amplitude in rotational velocity. In the SAURON sample only one galaxy, NGC 4550 ($\beta_z = 0.43$ and $\delta = 0.56$), is highly dominated by tangential dispersion. In contrast to NGC 1277, though, NGC 4550 consists of two massive counter-rotating disks.

The difference between the two compact galaxies in our sample is not only a difference of orbital structure but also of sheer size (see Table 2.1), with MRK 1216 being almost twice as large as NGC 1277. Taking into account the similarity between MRK 1216 and the SAURON galaxies, this may indicate that MRK 1216 has already entered a path of becoming a regular, fast-rotating elliptical whereas NGC 1277 is still in its infancy.

2.5.2 Black Hole

2.5.2.1 Masses

A credible determination of M_\bullet requires a very thorough analysis. In the most optimal case, this is done by dynamical modelling of high-spatial resolution data that can resolve the black hole sphere of influence ($R_{SOI} = GM_\bullet/\sigma^2$), i.e. the region where the gravitational pull of the black hole dominates. However, even state-of-the-art adaptive optics can resolve R_{SOI} only for a limited number of galaxies, unless the black hole is either very nearby or very massive. The sphere of influence of NGC 1277 is about $1.6''$ - as measured from the best-fitting black hole mass of $\log(M_\bullet/M_\odot) \simeq 10.1$ and the effective

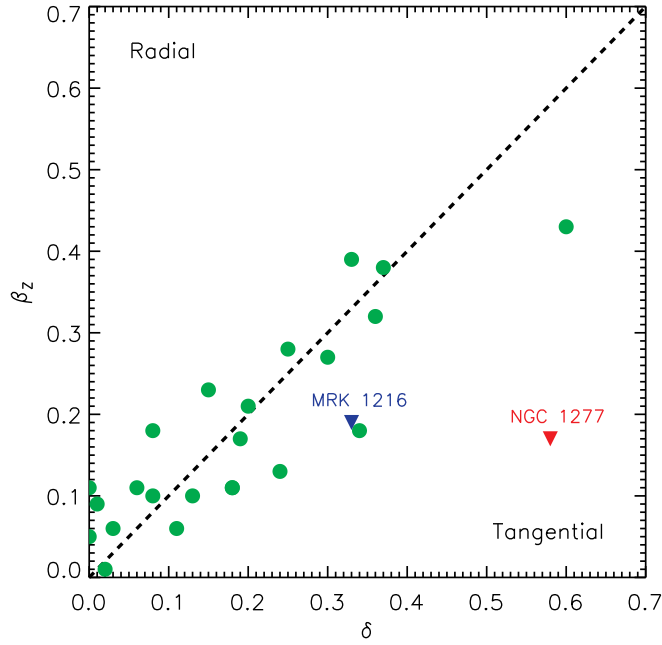


Figure 2.10: Anisotropy in the meridional plane (β_z) vs. global anisotropy (δ) of MRK 1216 (blue) and NGC 1277 (red), measured by our orbit-based dynamical models of the wide-field *PPAK* IFU and long-slit *HET* data within $3 R_e$. MRK 1216 follows the bulk of axisymmetric, fast-rotating ETGs in the SAURON sample (green), with a flattened velocity dispersion tensor in z-direction. NGC 1277 exhibits a distinct kinematic structure. Besides a flattening in the meridional plane, NGC 1277 is highly tangentially anisotropic in the plane orthogonal to the symmetry axis.

velocity dispersion in the *PPAK* data (Table 2.1) - and hence at the edge of being resolved by the *HET* kinematics. But this measurement of the sphere of influence is based on the assumption that the stellar density is well approximated by an isothermal sphere, and changes drastically if we adopt a more conservative estimate based on the region where the enclosed stellar mass equals the black hole mass, which yields $R_{SOI} = 0.9''$ (Fig. 2.5). Moreover, even if the sphere of influence is resolved, our measurements still rely on the seeing limited dispersion peak and h_4 values within the central $1''$ and caution should be exercised regarding the black hole mass reliability in NGC 1277 (but see also Section 2.6 for a more in-depth discussion of the black hole mass).

Nevertheless, the gravitational, and consequently the dynamical, influence of the black hole is clearly imprinted in the observed velocity moments. The rapid rise and distinct peak in the velocity dispersion profile as well as the positive values in h_4 indicate a strong mass excess within the central arcseconds. The high h_4 values imply an LOSVD with heavy tails and a considerable amount of rapidly rotating stars in the very centre, and these features can - as far as the models are concerned - be solved best with a central black hole mass of $\log(M_\bullet/M_\odot) \simeq 10.1$. Models with an ordinary SMBH of $\log(M_\bullet/M_\odot) \sim 9$, as suggested by $M_\bullet - L_{Bulge}$, are not able to recover the photometric and kinematic properties, as they fail to either fit the dispersion profile and/or the fourth Gauss-Hermite moment. In particular, the robustness of the h_4 measurement eliminates the possibility of a more moderate black hole measurement in favour of a higher mass-to-light ratio, as illustrated in Fig. 2.7.

The same, however, cannot be said for MRK 1216. Although the best-fitting model favours an over-massive SMBH, the total absence of a black hole cannot be ruled out. Models with and without a black

hole provide an almost equally good fit to the kinematics and thus are not able to discern between the various black hole mass scenarios, which is why (for the time being) our measurements can only be regarded as an upper limit. Upcoming high spatial resolution spectroscopic observations with *NIFS* (PI: Walsh) that resolve the sphere of influence will be able to tell the difference and show whether or not MRK 1216 follows the trend of NGC 1277.

2.5.2.2 Scaling Relations

We place both black hole masses back onto the $M_{\bullet} - L_{Bulge}$ relation (Fig. 2.11). To this end, we utilise the compilation of Sani et al. [2011] with bulge-disk decompositions of 57 galaxies, based on *Spitzer*/IRAC 3.6 μm mid-infrared imaging. The use of mid-infrared data has not only the advantage of less dust extinction susceptibility but is also a better tracer of the underlying stellar mass. To this sample, we add 10 black hole masses with 2MASS *K*-band luminosities and bulge-to-total ratios if available; five from disk galaxies, as presented in Kuo et al. [2011] and Greene et al. [2010b]; two in brightest cluster galaxies (BCG), published in McConnell et al. [2011]; one from a low-luminosity elliptical [Kormendy et al., 1997]; one from a high-dispersion lenticular galaxy [Rusli et al., 2011] and one from a recent merger galaxy [Kormendy et al., 2009], investigated in Gültekin et al. [2011]. The solid line in Figure 2.11 represents the black hole mass-bulge luminosity relation ($M_{\bullet} - L_{Bulge}$) derived in Sani et al. [2011], based on their bulge-disk decompositions of literature black hole host galaxies and a linear regression fit to the data. The blue and red error bars mark our findings for MRK 1216's and NGC 1277's black hole mass with a statistical uncertainty of 3σ . Their *K*-band bulge luminosities are based on the photometric decompositions in Section 2.2.2 and 2.2.3 of the *HST* *H*- and *V*-band images (using the second innermost component of the multi-Sérsic fit as a lower limit to the bulge luminosity while the bulge in the two-component Sérsic fit serves as an upper limit) and their total 2MASS *K*-band luminosities. The figure illustrates the exceptional position of NGC 1277. The best-fitting black hole mass remains a significant outlier from this relation and the 3σ lower bound, $\log(M_{\bullet}/M_{\odot}) = 9.9$, still overshoots the upper 99.7 per cent confidence envelope of the relation by at least one order of magnitude. Similarly, and given the difficulties in identifying a bulge in both the dynamical and photometric decompositions (Sec. 2.2.3 and 2.5.1.2), NGC 1277 is an outlier in the black hole mass-total luminosity relation in *K*-band [Läscher et al., 2014b], where the upper 3σ bound of this relation barely touches the lower 3σ limit of the black hole mass.

Interestingly, the black hole measurement in NGC 1277 is consistent with estimates of the scatter in the $M_{\bullet} - L_{Bulge}$ and $M_{\bullet} - \sigma$ relation in the optical [Gültekin et al., 2009; McConnell & Ma, 2013; Kormendy & Ho, 2013]. The best-fitting black hole mass is an outlier by a factor of ~ 8 (4) with respect to the mean predicted black hole mass in the $M_{\bullet} - L_{Bulge}$ ($M_{\bullet} - \sigma$) relation, but still within a 3σ (2σ) confidence if the intrinsic/cosmic scatter of 0.44 (0.38) dex is taken into account.

The consistency between the black hole mass of NGC 1277 and the $M_{\bullet} - L_{Bulge}$ relation in the optical is a result of a larger intrinsic scatter when compared to the relation in the mid-infrared, and expected if the black hole mass-bulge luminosity relation is just a tracer of a more fundamental link between black hole mass and bulge mass [Marconi & Hunt, 2003; Häring & Rix, 2004]. As NGC 1277 becomes an outlier in the tighter relation in the mid-infrared this could be interpreted i) as a hint for a different formation channel that lacks the physical interplay and causal link between the black hole and the spheroidal component

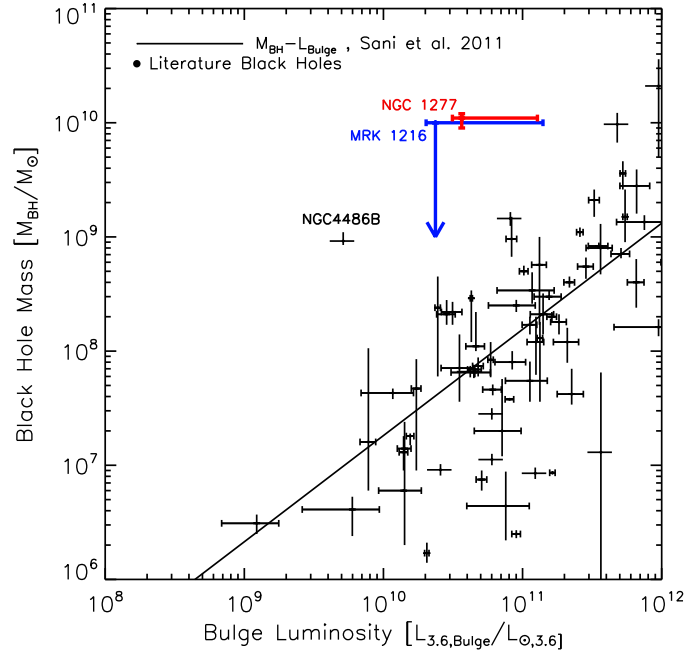


Figure 2.11: $M_{\bullet} - L_{3.6,Bulge}$ plot from Sani et al. [2011], with *Spitzer*/IRAC 3.6 μm bulge-disk decompositions and dynamical black hole mass measurements (including 1σ errors) for 57 galaxies. The red and blue error bars represent 3σ statistical uncertainties of NGC 1277's and MRK 1216's black hole mass. The lower limit for the black hole mass in MRK 1216 is consistent with no black hole. For the *K*-band bulge luminosities we adopt their total 2MASS *K*-band luminosities and the bulge-to-total ratios from our photometric multi-component decompositions of the *HST* *V*- and *H*-band images.

of its host [Silk & Rees, 1998] or ii) as an indication that the black hole mass-bulge luminosity relation is tightly coupled to the structural evolution and emergence of massive galaxies since $z = 2$, a path which NGC 1271 and a larger sample compact, elliptical, high central velocity dispersion galaxies in the nearby universe have avoided (see Chap. 4). In fact, by means of high spatial resolution observations with *NIFS*, Walsh et al. [2015] find a black hole mass of $\log(M_{\bullet}/M_{\odot}) = 9.5^{+0.1}_{-0.1}$ in NGC 1271, another compact, elliptical, high central velocity dispersion galaxy. The black hole mass in NGC 1271 is consistent with predictions of the black hole scaling relations based on its stellar velocity dispersion, but highly inconsistent with predictions based on its bulge luminosity, being one order of magnitude larger than expected. This is in agreement with the theory put forward in this chapter, namely that these objects are rotationally supported and devoid of a pressure supported bulge component, which might have formed through a few major and numerous minor merging events, as is currently claimed for the evolution of massive elliptical since $z = 2$.

An alternative but speculative example for an over-massive black hole formation channel is presented by Shields & Bonning [2013]. Based on gravitational radiation recoil during the final stages of two massive black hole mergers and the accompanied velocity kicks [Merritt et al., 2004], they argue that a massive black hole in a nearby galaxy could have been ejected and recaptured by NGC 1277. The probability of mergers which could produce kicks that exceed the escape velocity of the host is non-negligible [Lousto et al., 2010], but the ejected black hole would be accompanied by a hypercompact stellar system (HCSS) with a stellar mass of $M_{HCSS} \leq 10^{-2} \times M_{\bullet}$ [Merritt et al., 2009]. Consequently, we ought to observe

a considerable number of these free floating, compact stellar systems already in the Virgo cluster. The lack of any such observational evidence questions the likeliness of this scenario.

A different idea has been put forward by E13, to reconcile the black hole in NGC 1277 with predictions of the scaling relations. Here, individual dynamical models from N -body realisations have been chosen to match the *HET* and *HST* data in the very centre and over a wide radial range. A hand-picked model without dark matter and a black hole mass of $\log(M_{\bullet}/M_{\odot}) = 9.7$ shows an acceptable fit to the kinematics. However, no parameter search was done to find a best-fit model and confidence intervals. In particular, the models fail to fit all kinematic moments simultaneously and especially the fourth Gauss-Hermite moment, which seems to be the key discriminator between the various black hole mass scenarios.

The presence of a bar was also discussed briefly as an alternative explanation of the very distinctive kinematic moments. For instance, a model with no black hole but an edge-on bar was able to overcome the problem of fitting h_4 while a model with an end-on bar was a good fit to the remaining data. The truth could lie somewhere in between these two opposing bar configurations, with a more moderate black hole mass in addition. However, it is worth noting that we were not able to find any evidence for the presence of a bar in any of the data sets. Although limited by the spatial resolution of our kinematic observations, we see a clear trend for an anti-correlation between h_3 and v . The presence of a bar should break this trend over its projected length, as has been shown by N-body simulations of bar-unstable disks by Bureau & Athanassoula [2005] and observations of edge-on spiral galaxies [Chung & Bureau, 2004]. We also thoroughly inspected the high-resolution *HST* data and performed photometric decompositions with Galfit that included a bar. The decompositions, however, resulted in visually and statistically worse fits. Even though we do not rule out the possibility of a small (i.e. $\leq 1''$) end-on-bar, which would not be resolved by the currently available data, we raise concerns that a) this would be a special and unlikely case and b) that the same argument could be easily applied to a number of other dynamical black hole measurements. Finally, high-resolution spectroscopic observations with NIFS (PI: Richstone) have already been carried out for NGC 1277, which will shed light on this argument.

2.5.3 Dark Matter Halo

2.5.3.1 Dark Halo Detection

Based on our orbit-based models of the wide-field IFU data and the *HET* long-slit kinematics, we have no clear evidence for the presence of a dark halo in NGC 1277. In MRK 1216, on the other hand, the data can only be recovered with the addition of dark matter. We note, though, that the detection is only of a weak statistical nature. The best-fitting model without a dark halo deviates by $\Delta\chi^2 = 15$ from the overall best-fitting model, which is slightly beyond the 3σ confidence limit, as has been shown in Fig. 2.5. Given the four kinematic moments of the *PPAK* data and the three *HET* slits that are fitted simultaneously, the mean deviation per kinematic moment and bin is ~ 0.04 between both models and the predicted velocity moments are barely distinguishable in the IFU maps as well as in the major axis profiles of the long slits (Fig. 2.6). The difference in the relative likelihoods of both models is mostly attributable to the IFU kinematics, which account for 2/3 of the $\Delta\chi^2$. This is in contrast to e.g. the statistically stronger black hole detection in NGC 1277, where the difference between our best-fitting

model and a model with a black hole mass of $\log(M_{\bullet}/M_{\odot}) = 9.7$ is driven by a few central bins with a $\Delta\chi^2$ of 25 and clearly visible in the mismatch of the central velocity moments (Fig. 2.7).

In the case of MRK 1216, one would expect the outer bins to be the driver of the χ^2 difference, where the lack of the dark halo should lead to the most prominent deviation between a model with and without a dark halo. We show that this is not the case. In Fig. 2.12 we present the $\Delta\chi^2$ of the *PPAK* data between the best-fitting model without a halo and the overall best-fitting model as a function of radius. The plot reveals the central region ($\leq 5''$) as the cause of the $\Delta\chi^2$ difference. In addition to the statistical claim, this is a clear indication for additional dark mass that can be explained as follows: The absence of a dark halo naturally leads to an increase in the stellar mass-to-light ratio which mitigates the effects of missing mass in the outer parts. This is illustrated in Fig. 2.12, where the simple mass-follows-light model presents an equally good fit to the outer kinematics as the overall best-fitting model with a halo. The rise in *constant* mass-to-light ratio however leads to a mismatch between data and model (or best-fitting model and best-fitting model w/o a halo) in the central regions.

A natural way to resolve this issue and to make the mass-follows-light models fit the outer and inner data points would be a radially increasing mass-to-light ratio that adopts the best-fitting value for the central regions and steadily increases towards the outer parts to account for the outer bins. Indications for such a trend should be imprinted in the colour profiles of galaxies [Bell & de Jong, 2001; Bruzual & Charlot, 2003], attributable to variations in age and/or metallicity of the galaxy's stellar population as is expected if galaxies grow inside-out [Pérez et al., 2013; Patel et al., 2013]. We have therefore inspected the colour profiles of NGC 1277 and MRK 1216 based on *SDSS* $g - i$ and *HST* F814W-F160W imaging, but the lack of a significant trend with increasing distance from the centre in both does not promote the use of a stellar mass-to-light-ratio gradient in our models. This is also in accordance with the spectroscopic results of T14 for NGC 1277, which suggests a uniformly old stellar population with almost constant metallicity and α/Fe values. Even though spatial gradients in the colours (e.g. Franx et al. 1989; Tamura & Ohta 2003) and stellar population properties (e.g. Greene et al. 2013) of individual ETGs have been observed, which would justify the assumption of a radially varying Υ_{\star} , the analysis of a large sample of late- and early-type galaxies suggests that gradients for Υ_{\star} are in general negative [Tortora et al., 2011], which in turn would further increase the dark mass and hence the discrepancy between our models with and without a dark halo [see e.g. McConnell et al., 2013].

In principle, variations in the IMF could conceal a colour gradient in both compact objects while effectively increasing the stellar mass-to-light ratio. A recent study of radial trends in the IMF of individual, massive, high-dispersion galaxies however argues the converse and indicates that the observed trend of a bottom-heavy IMF is only a local property - confined to the central region of a galaxy - followed by a decrement of the IMF slope with increasing distance from the centre, and hence a radially decreasing stellar mass-to-light ratio [Martín-Navarro et al., 2015a].

Even if MRK 1216 and NGC 1277 did not assemble in the same way as the most massive ellipticals did and just evolved passively (see Section 2.5.4), there is currently no comprehensive theory of star formation that could explain the tendency of a more bottom heavy IMF in the less dense outskirts of galaxies.

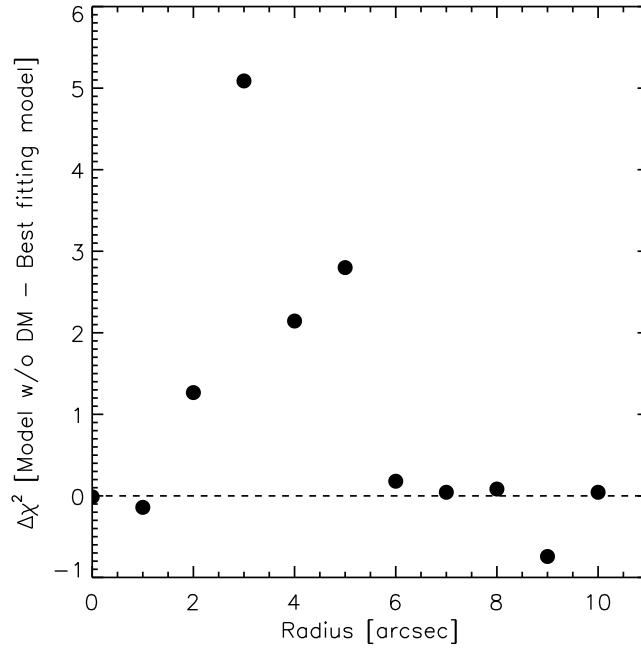


Figure 2.12: Total χ^2 difference of MRK 1216's *PPAK* data, between the best-fitting model without a dark halo and the overall best-fitting model, as a function of distance from the centre.

2.5.3.2 Dark Halos In Elliptical Galaxies

The results for the dark matter halos in our analyses are puzzling, in particular in the light of other orbit-based dynamical models with a similar extent in the stellar kinematic information of the full LOSVD (e.g. Rix et al. 1997; Thomas et al. 2007). While those investigations provided unambiguous evidence for the presence of dark matter in elliptical galaxies, we can only partially confirm this trend. For instance, Weijmans et al. [2009] examined the two early-type galaxies NGC 3379 and NGC 821. Based on SAURON data out to four effective radii, they obtained a dark matter contribution of at least 8 and 18 per cent to the total mass budget within one R_e . They also predicted a dark matter fraction of 30-50 per cent within four R_e and concluded that dark matter is necessary to explain the observed kinematics.

In particular NGC 3379, with a small effective radius of ~ 2 kpc, is easily comparable to our compact objects, where we provide a similar relative and absolute coverage of the LOSVD. But we can only present a dark halo detection in MRK 1216. Moreover, the relative contribution of dark matter to the total mass profile within one effective radius is 2 - 52 per cent and represents a considerable spread when compared to the values that have also been observed in e.g. the SAURON sample (~ 30 per cent) [Cappellari et al., 2006], or that is predicted by spherical representations of early-type galaxies under the Λ CDM framework [Napolitano et al., 2005]. For NGC 1277, the reverse is true as the models are able to recover the observations without the need of any dark matter and predict a maximal dark matter fraction of only 13 per cent within one effective radius.

2.5.3.3 NFW Profiles

The aforementioned numbers are based on the assumption that the dark halo profile in both galaxies is well described by a spherically symmetric NFW profile. As a further check of this hypothesis, we compare our results with a semi-analytic approach of Moster et al. [2010] that links the stellar mass of a galaxy to the mass of its dark matter halo. By comparing the galaxy mass function with the halo mass function they obtained a well-defined stellar-to-halo mass (SHM) relation, which enables the determination of a halo mass for a given stellar mass and vice versa.

In Figure 2.13 we overplot all results of our orbit-based dynamical models that are enclosed by the 99.7 per cent confidence limit and thus immediately test the consistency of our models with the standard cold dark matter paradigm (Λ CDM), which is the underlying cosmological model that defines the halo mass function. There is a small range of overlap between the predictions of our models and the SHM relation that would imply consistency with Λ CDM, but we also see a wide coverage of allowed halo masses due to the inability of our models to constrain the parameter space in c_{DM} and f_{DM} effectively. A different quantification of the SHM relation in terms of late- and early-type galaxies [Dutton et al., 2010] does not change anything in this respect, as the halo masses of both MRK 1216 and NGC 1277 still overshoot the upper and lower bound of these relations by about one order of magnitude.

The difficulty in detecting a dark halo in both galaxies, in particular in NGC 1277, and in constraining the dark halo parameters cannot simply be attributed to the use of larger 3σ confidence intervals in our study. More probably, the obstacle can be traced back to their compactness and high stellar masses within the small spatial extent that is probed by the available kinematic data. Given our best-fitting results, stellar masses are of the order of $\log(M_*/M_\odot) = 11.1$ within 7 and 5 kpc for MRK 1216 and NGC 1277 respectively. The contribution of a NFW halo to the total mass profile within the same range can be estimated to be of the order of $\log(M_*/M_\odot) = 10.5$ and 10.2 for MRK 1216 and NGC 1277, assuming that the mass-concentration relation [e.g. Bullock et al., 2001; Duffy et al., 2008; Macciò et al., 2008] and stellar-to-halo mass relation [e.g. Moster et al., 2010; Guo et al., 2010; Behroozi et al., 2010] holds. Accordingly, the dark halo would constitute ~ 25 per cent of the total mass budget in MRK 1216 and only ~ 13 per cent in NGC 1277, which would explain the statistically weak detection in the former and our struggle to verify the presence of dark matter in the latter.

2.5.4 The Origin Of Compact, Elliptical, High Central Velocity Dispersion Galaxies

MRK 1216 and NGC 1277 are unusual and rare galaxies in the nearby universe. Their detection was a result of the selection criteria of the HETMGs [van den Bosch et al., 2015] which, based on the sphere of influence argument, naturally looked for dense, high-dispersion objects that could possibly host very massive SMBHs. Still, the number of objects that are similar to both, even in the HETMGs, are limited and questions regarding their origin and evolution arise. Typically, the stellar populations are the first resort for exploring the (stellar) evolutionary history of a galaxy, but this would only be feasible for the long-slit spectroscopic data due to the short wavelength coverage of our IFU observations. We

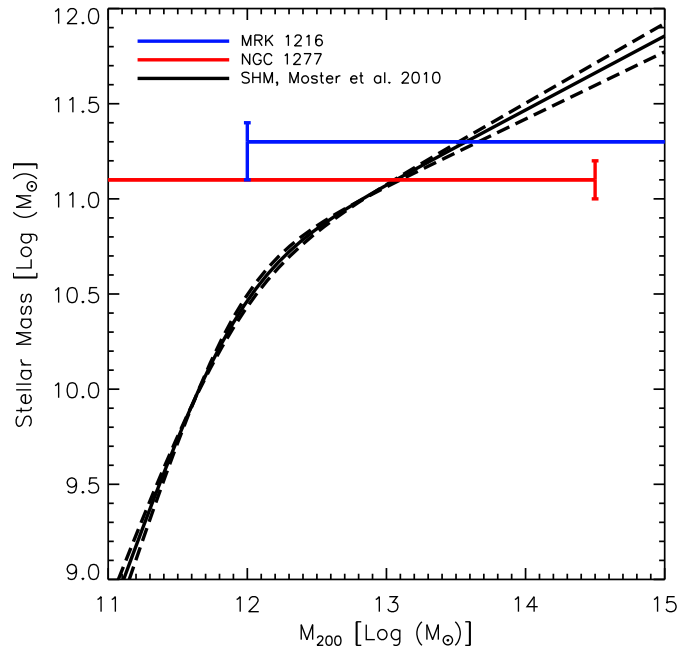


Figure 2.13: Stellar-to-halo mass (SHM) relation from Moster et al. [2010] (black line). Overplotted are stellar-to-halo mass predictions of MRK 1216 (blue) and NGC 1277 (red), derived from our entire set of Schwarzschild models. The plot displays upper and/or lower limits in the relevant range of $M_{200} = 10^{11} - 10^{15} M_{\odot}$. In the case of NGC 1277, the lower limit is consistent with no dark matter.

therefore focus on the already available data and find hints for a rather unremarkable and quiet past in their photometric and structural properties.

MRK 1216 is an isolated galaxy in the field, which has only two other galaxies within a search radius of 1 Mpc at its distance. It has no tidal signatures or asymmetries and any recent galaxy-galaxy interaction can therefore be ruled out. Given its compact shape and rotationally supported dynamical structure, an active merging history seems to be unlikely, too. Violent relaxation due to collisionless 1:1 or 1:2 mergers, for instance, commonly yields boxy, slow rotating ellipticals [e.g. Burkert & Naab, 2003; Naab & Burkert, 2003; Naab et al., 2006], which is at odds with the rapid rotation and dynamical characteristics of MRK 1216 and NGC 1277. We emphasise, though, that this formation scenario also fails in reproducing the detailed dynamical properties of massive ETGs in general [Burkert et al., 2008; Naab et al., 2014]. Similarly, violent relaxation due to dry (i.e. gas-poor) unequal mass mergers have been shown to be able to recover the photometric and kinematic properties of disk, fast-rotating ellipticals [Naab & Burkert, 2003; Naab et al., 2014]. However, unequal mass mergers tend to increase the galaxy size drastically [Naab et al., 2009; Oser et al., 2010; Hilz et al., 2013; Bédorf & Portegies Zwart, 2013], and are thus hard to reconcile with the sizes observed in both compact objects. On the other hand, dissipative equal mass mergers can reproduce fast-rotating ETGs [Naab et al., 2014], while also recovering the tilt in the FP [e.g. Robertson et al., 2006; Cox et al., 2006]. However, both MRK 1216 and NGC 1277 are outliers in the FP (see Fig. 4.6) and the non-negligible gas fractions involved in the merging process are expected to boost star formation activity, which is in contrast to the uniformly old age and star formation history of NGC 1277 (T14 and ?) unless the merging event has taken place at $z \geq 2$. As a result, the aforementioned simulated merger scenarios - which actually have been tailored to test and recover the formation and

evolution mechanisms of today's population of ETGs - fail to understand the two compact galaxies in this work.

In any case, this brings up the idea whether these two objects are representatives of a galaxy population that has (at some point) taken a significantly different path than the present-day massive galaxy population, which has grown in mass and size since $z = 2$ [van Dokkum et al., 2010] presumably through successive (minor and major) merging events. In fact, stellar age estimates of the present-day massive galaxy population [McDermid et al., 2015] are consistent with the inferred stellar ages of NGC 1277, and the range of allowed stellar mass-to-light ratios in our dynamical models cannot rule out the trend of a more bottom-heavy IMF with increasing stellar velocity dispersion, which is also commonly observed for the most massive ellipticals. Accordingly, both galaxies would present unaltered and passively evolved analogues of the quiescent galaxy population at much earlier times, which are thought to constitute the cores of today's massive ellipticals.

Indeed, the two galaxies are quantitatively similar to the quiescent galaxies at $z = 2$. Those are also found to be small [Daddi et al., 2005; Trujillo et al., 2006; Zirm et al., 2007; van Dokkum et al., 2008; van der Wel et al., 2008, 2014], possess extremely high dispersions [van Dokkum et al., 2009] and generally have a disk-like structure [van der Wel et al., 2011]. T14 were able to go beyond a simple structural, photometric and kinematic comparison by carrying out a stellar population analysis of NGC 1277. Based on long-slit spectra out to $\sim 3 R_e$ they found that NGC 1277 consists of a uniformly old stellar population (≥ 12 Gyr), formed during a very short-lived era at $z \geq 3$ with an intense star formation rate. This again is in good agreement with spectroscopic investigations of Kriek et al. [2006, 2009] and Toft et al. [2012] for individual quiescent galaxies at $z \sim 2$. Those have also very old stellar populations, with the bulk of their mass already assembled at $z \geq 3$, and are absent of any significant star formation. Recently, evidence has even mounted for a further evolutionary link with the sub-millimeter galaxies (SMGs) at $z \geq 3$ [Toft et al., 2014]. The SMGs not only provide the necessary ages and compact sizes but also the intense star formation rates - which could have been triggered by gas-rich (major) mergers at high redshifts [Naab et al., 2007; Wuyts et al., 2010] - to explain the old stellar populations of the quiescent galaxies at $z = 2$ (but see also Williams et al. 2014; Dekel & Burkert 2014 and Barro et al. [2014] for an alternative formation channel)

The resemblance between NGC 1277 and MRK 1216 and the quiescent galaxies at higher redshifts is remarkable. Nevertheless, we need to go beyond single anecdotal examples if we want to underpin the claim that the compact galaxies, found in the HETMGS, are passively evolved descendants of the quiescent population at $z \leq 2$. It is encouraging though that we have found 18 compact, high-dispersion, early-type galaxies in total, which will enable us to investigate in detail their photometric, structural, kinematic and stellar evolutionary properties.

2.6 Uncertainties

Our orbit-based dynamical analysis and its implications are afflicted by a number of moderate concerns, which we would like to highlight here.

- During the construction of our dynamical models we have assumed axisymmetric stellar systems. The models are robust with respect to changes in the inclination (Section 2.4.2.1) but the orbital structures can change rapidly when the assumption of axial symmetry is relaxed. Even mild triaxiality would alter the observed phase space structures in Fig. 2.8 and 2.9 noticeably, leading also to variations in the derived values of e.g. the black hole mass [van den Bosch & de Zeeuw, 2010]. In this respect, even the slightest twist in the PA can be interpreted as a deviation from axisymmetry. An MGE with a fixed PA for all Gaussians (Sec. 2.2.2) is a necessary but insufficient condition for the assumption of axial symmetry, as triaxial deprojections cannot be ruled out. However, the body of evidence that has been presented throughout this chapter, namely the fast and regular rotation around the short axis, the anti-correlation between v and h_3 , the negligible mis-alignment between the kinematic and photometric PA and results from shape inversions of a large sample of fast-rotating early-type galaxies [Weijmans et al., 2014], show that axial symmetry is a justified assumption of the intrinsic shape of both compact objects.
- Tightly linked to the black hole mass is the stellar mass-to-light ratio which in turn is degenerate with the dark matter halo [Gebhardt & Thomas, 2009]. The determination of Υ_* is therefore crucial in constraining the black hole, if the black hole sphere of influence is not resolved [Rusli et al., 2013]. In our set of dynamical models, the stellar mass-to-light ratio is assumed to be constant throughout the observed range of kinematics. This is also supported by the lack of colour gradients in both galaxies and an only mild change in the stellar population properties of NGC 1277 within a radial extent of ~ 3 effective radii (T14).

Despite emerging evidence for strong systematic variations in the IMF of early-type galaxies [e.g. Auger et al., 2010b; Dutton et al., 2011; Cappellari et al., 2012; Spiniello et al., 2012], predictions of SSP models with a single power-law Salpeter IMF [Vazdekis et al., 1996, 2012] are consistent with our orbit-based dynamical models of both NGC 1277 and MRK 1216. This has formerly been excluded at the 3σ level for NGC 1277 in vdB12. Whereas those conclusions based on spectral synthesis fits of NGC 1277's single SDSS aperture [Cid Fernandes et al., 2005] with Bruzual&Charlot models [Bruzual & Charlot, 2003], our values for the stellar mass-to-light ratios are derived from fits to the spatially resolved long-slit spectra (T14) based on MIUSCAT [Vazdekis et al., 2012; Ricciardelli et al., 2012] SPS models. Both approaches have been shown to provide similar answers, and the difference between the Υ_* values quoted in vdB12 and the values in this work is attributable to the choice of a lower mass cut-off of $0.01 M_\odot$ in the former and $0.1 M_\odot$ in the latter. We consider the values reported here as a conservative estimate. Hence the strong tendency towards a more bottom-heavy IMF in high dispersion galaxies [Treu et al., 2010; van Dokkum & Conroy, 2012; Conroy & van Dokkum, 2012; Ferreras et al., 2013; La Barbera et al., 2013; Spiniello et al., 2014] cannot be ruled out by our orbit-based dynamical analysis of MRK 1216 and NGC 1277, and would indeed favour the presence of a more moderate black hole mass. However, according to our Schwarzschild models, the upper range of possible mass-to-light ratios implies that the IMF in these two objects can only be more massive by ~ 15 and 25 per cent at most in NGC 1277 and MRK 1216, respectively, with respect to a Salpeter IMF. While this is largely consistent with the observed scatter in the relation between IMF slope and velocity dispersion in the aforementioned studies, exotic variations of the IMF - as predicted e.g. by the best-fitting relation in Treu et al. [2010] and Spiniello et al. [2014], which implies a shift in Υ_* by ~ 40 per cent for a stellar velocity

dispersion of 300 km s^{-1} - can be excluded.

- A major concern in the modelling of NGC 1277 remains the nuclear dust ring. Although contaminated regions have been generously masked while constructing the luminous mass model, this is by no means an appropriate physical account of dust extinction. Since our orbit-based dynamical models measure the enclosed mass within a given radius, an underprediction of the stellar mass in the nucleus will obviously bias the measurement towards higher black hole masses, although it would take a considerable amount of mass to be screened by dust ($\geq 50\%$ of the stellar mass within $1''$) to bring the black hole in line with the scaling relations.
- The biggest concern in the recovery of the individual mass contributions and in particular for the black hole mass in NGC 1277, though, remains the accuracy of the kinematic measurements. E13 has shown that the detection of an over-massive SMBH entirely hinges on the dispersion peak and the positive h_4 values in the centre. This is easily verified by our models, where most of the χ^2 difference between the best-fitting model and a model with a more moderate black hole mass of $\log(M_\bullet/M_\odot) = 9.5$ (Fig. 2.7) is attributable to the fits to σ and h_4 that contribute 3/4 of the $\Delta\chi^2$. In particular, the seeing limited measurements within $1''$ in the *HET* long-slits are the driver of this difference and question the reliability of the black hole mass estimate. Moreover, dust obscuration could also affect the measurement of the LOSVD, even though modest dust mass assumptions show that this is only significant for the large scale kinematics [Baes & Dejonghe, 2001].

The *PPAK* observations, although limited by their spatial resolution, provide an independent way to assess the accuracy of the *HET* measurements and the models in vdB12. As has been shown in Section 2.3.4, the central dispersion in the *PPAK* cube is considerably lower than the peak observed in the *HET* data. As a result, models that fit the combined data set predict a velocity dispersion that matches the *PPAK* data but slightly fails to do so for the peak in the *HET* data (Section 2.4.2.2). In addition, the central h_4 moments in the *PPAK* data, while still positive, are slightly below the *HET* measurements (Fig. 2.14), which is of concern considering that those values have been key in discriminating between the various black hole mass scenarios (Sec. 2.5.2.1). In principle, we could try to reconcile both data sets and let them meet in the middle. However, quantifying the offset between the long-slit and IFU kinematics is a non-trivial task, which is why we follow a different route and check the inter-consistency between both by fitting the *PPAK* data individually.

We display the results of these test models in Figure 2.15, and show $\Delta\chi^2 = \chi^2 - \chi_{min}^2$ as a function of black hole mass and dark halo mass (marginalising over all remaining parameters). The model predictions for NGC 1277 based on the *PPAK* data are shown on top with the predictions based on both data sets - already illustrated in Fig. 2.5 - plotted below. While the inferred values for the dark halo are identical, the *PPAK* only models of NGC 1277 yield a black hole mass of $\log(M_\bullet/M_\odot) = 10.0_{-0.4}^{+0.2}$. This is largely in agreement with the values derived in Section 2.4.2.2 and vdB12, although with a decreased lower limit for the black hole mass by a factor of two, and now consistent with the black mass in E13, which was previously ruled out. Here again, the main contribution to the $\Delta\chi^2$ between our best-fitting model and models that are ruled out by

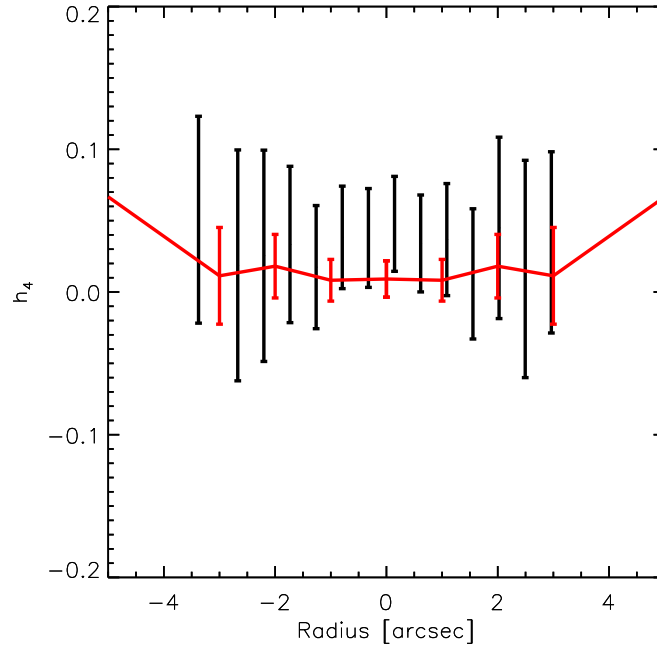


Figure 2.14: Comparison between one of the three *HET* long-slit (black) and *PPAK* IFU measurements (red) of the fourth Gauss-Hermite moment in NGC 1277. The *HET* measurements have been obtained along the apparent major axis. The *PPAK* measurements correspond to the values of the Voronoi-binned data, for which the bin centroids are located within a $1''$ wide strip along the major axis.

the statistical 3σ uncertainties comes from the velocity dispersion and the fourth Gauss-Hermite moment. In contrast to our fiducial models, however, which fitted both data sets simultaneously, the main driver in the fits to σ and h_4 cannot be traced back to the seeing limited innermost data points but is more uniformly distributed, as highlighted in the second and fourth row of Fig. 2.7.

We thus ascribe the decreased lower limit to the larger spatial resolution of the *PPAK* kinematics which is not able to resolve the sphere of influence of the massive black hole. For our conclusions we choose to give no preference to either one of the measurements and stick to the fiducial models in Section 2.4.2.2. Due to the lingering issues between both data sets, though, the very careful reader can adopt a lower limit of $\log(M_\bullet/M_\odot) = 9.6$ (but see also the next two points).

In the case of MRK 1216, the difference between the *PPAK* and *HET* kinematics is marginal (Sec. 2.3.3). Although the best-fitting model in Fig. 2.6 seems to be slightly off the measured *HET* dispersion, it is still well within the measurement errors. Hence, fits to the *PPAK* data alone do not show any difference in the derived values for black hole mass, stellar mass-to-light ratio and dark halo mass. We therefore do not present a comparison similar to Fig. 2.15 but rather refer the reader to the detailed analysis and modelling results in Section 2.4.2.1 and 2.5.3.1.

- In Morganti et al. [2013], Monte Carlo simulations of mock galaxy kinematics are utilised to estimate appropriate confidence intervals. Based on their made-to-measure particle code *nmagic*, they advocate the use of larger $\Delta\chi^2$ values to be able to recover their model galaxy parameters. While these findings are certainly interesting, there are significant differences in the modelling

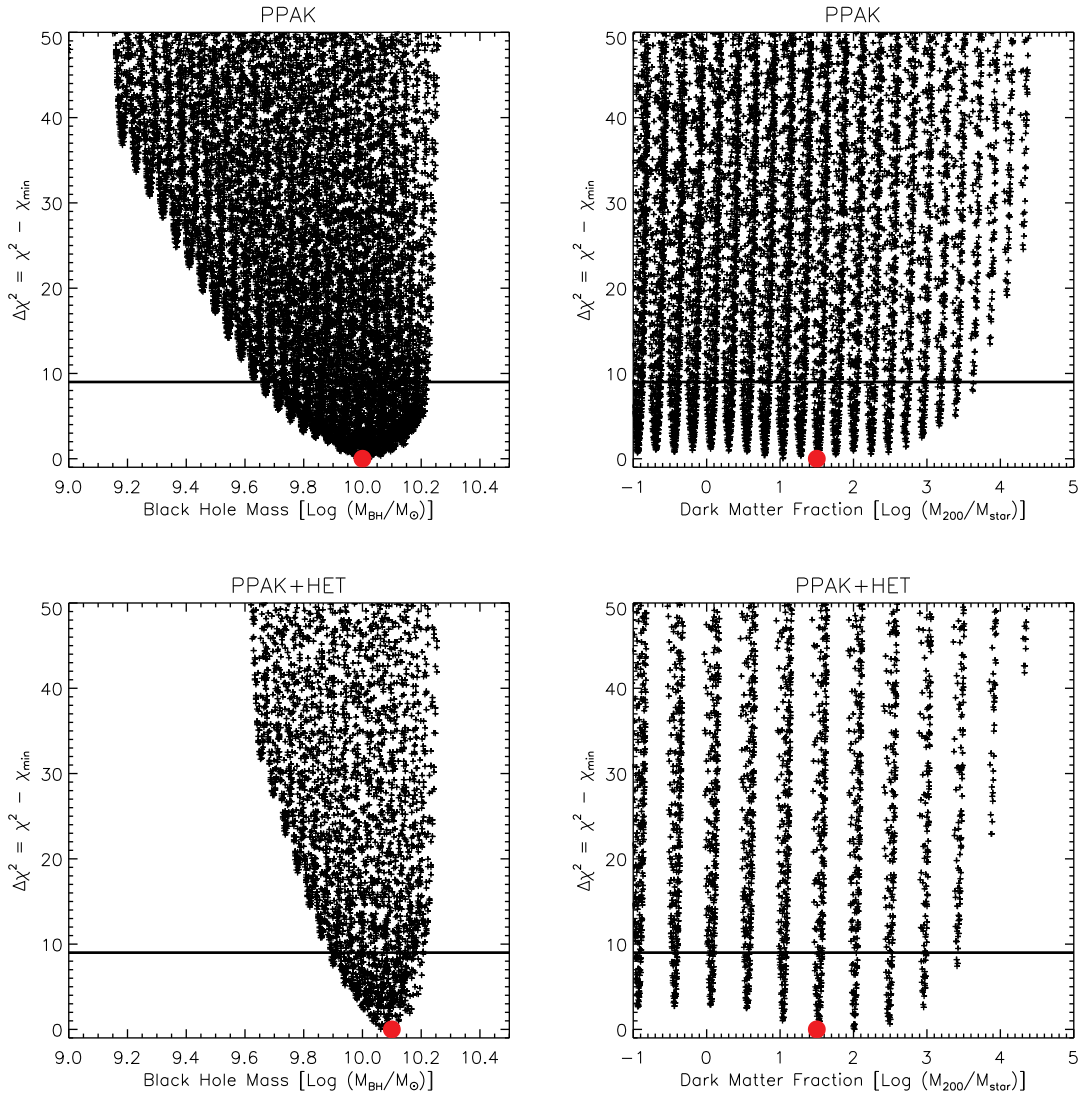


Figure 2.15: Comparison of the inferred values for black hole mass and dark matter halo based on NGC 1277's orbit-based models of the *PPAK* data only (top) and the combined *PPAK+HET* data set (bottom). The red dot marks the best-fitting value. The horizontal line denotes a $\Delta\chi^2$ difference of 9, which corresponds to statistical 3σ uncertainties for one degree of freedom.

approach as well as in the kinematic data set. The investigations of Morganti et al. [2013] are based on a single case study and more extensive tests are necessary to verify the reliability of their adopted confidence levels. The uncertainties in our parameter estimation are based on the commonly used $\Delta\chi^2$ values. After marginalising over the orbital weights as well as over e.g. Υ_* , c and f , we obtain formal 3σ errors of the black hole mass with a $\Delta\chi^2$ of 9. Alternatively, we can make use of the expected standard deviation of χ^2 for our parameter estimation, as promoted by e.g. van den Bosch & van de Ven [2009] in the case of IFU kinematics. The standard deviation in χ^2 is $\sqrt{2 \times (N - M)}$, where N is the number of kinematic constraints (i.e. the four kinematic moments v , σ , h_3 and h_4 in each bin) and M the number of free parameters in our models, namely the dark halo parameters c and f as well as the black hole mass M_\bullet and stellar mass-to-light ratio Υ_* . As a result, we obtain a lower limit for the black hole mass in NGC 1277 of $\log(M_\bullet/M_\odot) = 9.6$, which again is well in line with the estimate of the black hole mass based on

models of the *PPAK* only data and the black hole mass that was put forward by E13. Applying the same argument to MRK 1216, however, would imply consistency with models which do not contain a dark halo.

- Finally, we point out that all uncertainties presented here are solely statistical errors. A large uncertainty factor in any measurement of the black hole mass remains the estimate of systematic errors. These are hard to quantify and can arise not only through the use of modelling assumptions such as a constant mass-to-light ratio, axial symmetry and the adoption of a spherical NFW halo, but also through technical limitations as for instance a stellar template mismatch and the influence of the wavelength range that is used to infer the LOSVD. It is beyond the scope of this chapter to derive an assessment of each of these factors but we acknowledge that their total contribution most likely overshoots our statistical errors. Still, to provide a conservative estimate of the black hole mass - by taking into account the effects of systematic uncertainties - we simply follow the practice of Kormendy & Ho [2013] and adopt a 1σ error of $\Delta \log M_{\bullet} = 0.117$ (the mean of all literature 1σ black hole mass uncertainties). For NGC 1277, this yields a black hole mass of $\log(M_{\bullet}/M_{\odot}) = 10.1_{-0.4}^{+0.4}$ within a 3σ confidence interval, or $\log(M_{\bullet}/M_{\odot}) = 10.0_{-0.4}^{+0.4}$ if the fits to the *PPAK* data only are taken into account.

2.7 Summary

We have performed a detailed analysis of a suite of kinematic and photometric information of the two compact, nearby, high central velocity dispersion galaxies MRK 1216 and NGC 1277. Our analysis combined three different but complementary data sets; high spatial resolution imaging with the *HST*, low-resolution, long-slit spectroscopic observations with the *HET* and medium-resolution spectroscopic observations with the *PPAK* IFU.

We first analysed the reduced and combined *HST* images with multiple Sérsic components to infer the structure and morphology of each galaxy. Both galaxies show a very compact, early-type structure without any noticeable substructures. By means of a multi-component decomposition, we obtained estimates for a bulge luminosity. A decent fit was obtained with at least four components in both cases. We further parameterised the observed light distribution with a set of multiple Gaussians, which in turn was used to build axisymmetric dynamical models.

Kinematic information was extracted by fitting the binned spectra with a set of stellar libraries. The observations revealed a distinct central peak in the velocity dispersion - hinting at a very high mass concentration in the nucleus of both galaxies - and a fast and regular rotation around the short axis that is consistent with axial symmetry.

Our dynamical models rely on a triaxial implementation of Schwarzschild's orbit superposition method. Probing a wide range of parameters, we infer upper and lower limits for the individual gravitational contributions of black hole mass, stellar mass and dark matter halo. For NGC 1277 we obtained good constraints on the black hole mass of $\log(M_{\bullet}/M_{\odot}) = 10.1_{-0.2}^{+0.10}$ for the best fitting model, consistent with former measurements of vdB12. Even for high stellar mass-to-light ratios, the lower limit on the

black hole is considerably higher than predictions of the $M_{\bullet} - L_{Bulge}$ relation in the mid-infrared. In the case of MRK 1216, we only obtain an upper limit of $\log(M_{\bullet}/M_{\odot}) = 10.0$. High-resolution spectroscopic observations are thus needed to resolve the sphere of influence and to place firm constraints on its black hole mass.

Despite kinematic information out to ≥ 5 kpc, we were not able to constrain the dark halo parameters significantly. The models predict a dark matter contribution of up to 52 per cent in MRK 1216 and 13 per cent in NGC 1277 within one effective radius. Models without a dark halo are formally excluded at the 3σ level in MRK 1216, only. The difference between the best-fitting model without a halo and the overall best-fitting model is mainly driven by data points within $5''$. We show that this difference is due to an increase in the constant mass-to-light ratio in the dark-halo-free models to account for the outer kinematics, which then propagates towards the centre and leads to the observed mismatch. A radially increasing mass-to-light ratio could indeed recover the data without the need of a dark halo. But, if anything, recent investigations of massive early-type galaxies suggest a radially decreasing stellar mass-to-light ratio.

The stellar mass-to-light ratios span a range of 5.0 - 8.0 in V-band in NGC 1277 and 1.0 - 2.3 in H-band in MRK 1216. The best-fitting models are in good agreement with predictions of SSP models with a single power-law Salpeter IMF. Higher mass-to-light ratios - as have been observed in high dispersion galaxies - cannot be excluded. Nevertheless we place upper limits on possible deviations from the derived values.

The orbital structure is rotationally supported in both galaxies, which is consistent with the multi-component Sérsic decompositions of the deep *HST* images. This is highly indicative that MRK 1216 and NGC 1277 do not possess any pressure supported classical bulges that have formed through violent relaxation in late (i.e. $z \leq 2$), equal mass mergers. Successive minor and dissipative major merging events are unlikely too, as these tend to increase the galaxy size drastically and should yield more recent star formation activities, which are in contrast to their uniformly old stellar age estimates. Taking into account their compact, featureless and regular structures as well as their high dispersions and rapid rotation, these compact objects might well be unaltered descendants of the quiescent galaxy population at $z = 2$.

The massive dark halo of the compact, early-type galaxy NGC 1281

Abstract

We investigate the compact, early-type galaxy NGC 1281. Based on high spatial resolution imaging and wide-field integral field unit observations, we construct out orbit-based dynamical models and hereby constrain its dark and luminous matter content. Under the assumption of mass-follows-light, our models predict a stellar M/L of $\Upsilon_* = 2.8 \pm 0.1$ in H -band. This mass-to-light ratio is not only higher than expected from stellar population synthesis models with a Salpeter IMF, but the models clearly fail to recover the line-of-sight velocity distribution and hence call for a significant amount of dark matter in this galaxy. Models with a dark halo recover the kinematics well and indicate that NGC 1281 is a dark matter dominated galaxy with a contribution of up to 90 per cent to the total enclosed mass within 5 effective radii (≈ 7 kpc), irrespective of the exact halo parameterisation. When parameterising the dark matter halo with a spherical NFW profile, we find a dark halo mass of $11.4 \leq \log(M_{DM}/M_\odot) \leq 11.8$ within 7 kpc and a stellar M/L of 0.6 - 1.1 in H -band. However, this stellar mass-to-light ratio is much lower than predicted by an old stellar population based on a canonical Kroupa ($\Upsilon_* = 1.3$) or Salpeter ($\Upsilon_* = 1.7$) IMF. Moreover, the halo mass within the kinematic extent is one order of magnitude larger than expected from simulations within the Λ CDM framework and an extrapolation of the dark halo profile yields cluster-sized dark halo masses of $10^{15} M_\odot$. Adopting a stellar mass-to-light ratio of 1.7, as indicated by our stellar population synthesis fits, yields a more reasonable dark halo to stellar mass ratio of $\log(M_{200}/M_*) = 2.5$ within 7 kpc, but these models fit the kinematics worse and deviate from the best-fitting NFW model by more than 5σ . A non-NFW dark halo profile might solve the discrepancy between the unphysical consequences of the best-fitting dynamical models and models based on more reasonable assumptions for the dark halo and stellar mass-to-light ratio, which are disfavoured according to our parameter estimation.

3.1 Introduction

In the cold dark matter paradigm (Λ CDM), galaxies form via cooling of gas in the potential wells of extended, virialised dark matter haloes. While this picture has been very successful in describing the local, large scale structures of the universe [Springel et al., 2006; Spergel et al., 2007], conflicts arise between the predictions and observations on galaxy scales as the resolution of cosmological N -body simulations steadily increase. The poster child of these lingering discrepancies is the "core-cusp" problem where the central dark matter density distribution of dwarf and low surface brightness galaxies indicate a cored-like behaviour [Moore, 1994; McGaugh & de Blok, 1998], in contrast to the simulations which show a clear cusp [Navarro et al., 1996]. However, the Galaxy, too, stubbornly refuses to provide evidence of a significant amount of massive dark subhalos, commonly known as the "Missing Satellites Problem" [Kauffmann et al., 1993; Klypin et al., 1999; Moore et al., 1999a; Boylan-Kolchin et al., 2011].

Efforts to reconcile both, models and observations, have focused on complex baryonic feedback processes on the theoretical side. Issues on the observational side however are manifold. Although proof for the presence of dark matter in galaxies dates back to the 80s, based on extended neutral gas discs that map the dark halo at many effective radii in late-type galaxies [Rubin et al., 1980; van Albada et al., 1985], the detection of halos in early-type galaxies (ETGs) is not as straightforward due to the lack of similar features. Different tracers have therefore been employed - e.g. planetary nebulae [Douglas et al., 2007; Coccato et al., 2009], globular clusters [Côté et al., 2003] and hot X-ray gas [Humphrey et al., 2006] - but the dynamical modelling of each of these brings along its own set of assumptions and leads to partially conflicting answers [e.g. Romanowsky et al., 2003; Pierce et al., 2006]. The bulk of work has therefore focused on the analysis of stellar kinematics with two-integral axisymmetric Jeans models or state-of-the-art orbit-based dynamical models which are more conclusive and indicate that dark matter is a key ingredient in galaxies [Rix et al., 1997; Cappellari et al., 2006; Thomas et al., 2007; Cappellari et al., 2013a]. The spatial coverage of the stellar kinematics, however, is usually limited to regions where the stellar mass is assumed to dominate the total mass budget, and the attempt to break the degeneracy between the stellar and dark mass in these regions is therefore complicated. As a consequence, the halo parametrisation remains a matter of debate and the amount of dark matter strongly varies between no dark matter in some individual cases and a more typical dark matter contribution of up to ~ 50 per cent to the total enclosed mass within one effective radius.

In this chapter, we present orbit-based dynamical models of the compact, early-type galaxy NGC 1281. The data acquisition and analysis of NGC 1281 has been carried out as part of a larger program that aims at the detailed study of compact, elliptical, high central stellar velocity dispersion galaxies [see Chapter 2; van den Bosch et al. 2015; Walsh et al. 2015]. The program's target sample was a result of the Hobby-Eberly Massive Galaxy Survey (HETMGS), which based on the sphere of influence argument looked for dense, high central velocity dispersion galaxies that are candidates for hosting (over-)massive supermassive black holes (SMBH). We yet lack high spatial resolution spectroscopic observations which will enable us to resolve the dynamics close to the SMBH, but complementary data sets of high spatial resolution imaging and integral-field unit (IFU) observations are now available to study its internal structure and large scale mass distribution. In particular the wide-field IFU data presented here extends to ~ 5 effective radii (R_e) (≈ 7 kpc) which should be sufficient for a dynamical constraint on the dark matter halo.

This chapter is organised as follows: Section 3.2 presents the data, consisting of deep *HST* imaging and wide-field *PPAK* IFU stellar kinematics. In Section 3.3, we construct out orbit-based dynamical models of NGC 1281 to constrain its stellar and dark content. We discuss the reliability and significance of our findings in Section 3.4 and summarise our results in Section 3.5.

Throughout this chapter we adopt 5th year results of the Wilkinson Microwave Anisotropy Probe (*WMAP*) [Hinshaw et al., 2009], with a Hubble constant of $H_0 = 70.5 \text{ km s}^{-1} \text{ Mpc}^{-1}$, a matter density of $\Omega_M = 0.27$ and a cosmological constant of $\Omega_\lambda = 0.73$.

3.2 Data

3.2.1 HST Imaging

For brevity, we refer the reader to Sec. 2.2, which covers in detail the data acquisition and reduction pipelines. Here, we confine ourselves to only a brief description of the main steps.

Photometric data of NGC 1281 have been obtained by the *HST* WFC3 in *H*-band (F160W), as part of program GO: 13050 (PI: van den Bosch), resulting in a total of three dithered full- and four sub-array exposures with a total integration time of ~ 1400 s. The purpose of the 1.7s short sub-array exposures is to mitigate the effect of saturation in the nucleus of the long 450s full-arrays. The seven flat-field calibrated exposures are reduced and combined via *Astrodrizzle* [Gonzaga et al., 2012] to obtain a super-sampled image with a resolution of $0.06''/\text{pixel}$, while correcting for geometric and photometric distortions.

For the photometric analysis, we make use of the point-spread function (PSF) of the Cosmic Assembly Near-Infrared Deep Extragalactic Survey (CANDELS) [van der Wel et al., 2012]. The PSF is created with *TinyTim* [Krist, 1995] in the F160W filter and drizzled to replicate the final PSF at the desired plate scale of $0.06''$.

NGC 1281 is a compact, elliptical galaxy in the Perseus cluster with an E5 morphological classification according to the NASA/IPAC Extragalactic Database (NED). Redshift measurements of this object place it at a Hubble-flow distance of $60 \pm 1 \text{ Mpc}$, at which $1''$ corresponds to an absolute scale of 0.29 kpc . A circular aperture that contains half of the light has a size of $R_{1/2} = 4.5''$. The galaxy has a total apparent magnitude of $M_{H,Vega} = 10.57$ ¹. We further investigate its photometric properties by carrying out a single- and two Sérsic decomposition of the high-resolution *H*-band imaging while generously masking any contamination by fore- and background objects. A single Sérsic fit has an apparent magnitude of $M_{H,Vega} = 10.37$ with an effective (semi major axis) radius of $6.8''$, a projected axis ratio ($q = b/a$) of 0.63 and a single Sersic index of $n = 3.9$. Residuals of this fit are strong and show an overestimation of the outer and inner SB profile. Moreover, the residuals also reveal the presence of a central dust disk with an apparent minor to major axis ratio of 0.35 and a semi-major axis length of 0.3 kpc . Assuming that this intrinsically flat disk traces the position angle (PA) of its host, we can infer the inclination of this galaxy to be 70° . A fit with two Sérsic components improves the fit considerably. Here, a rather

¹All magnitudes presented throughout this chapter are corrected for Galactic extinction based on SDSS re-calibrated values [Schlafly & Finkbeiner, 2011] of infrared dust maps [Schlegel et al., 1998]

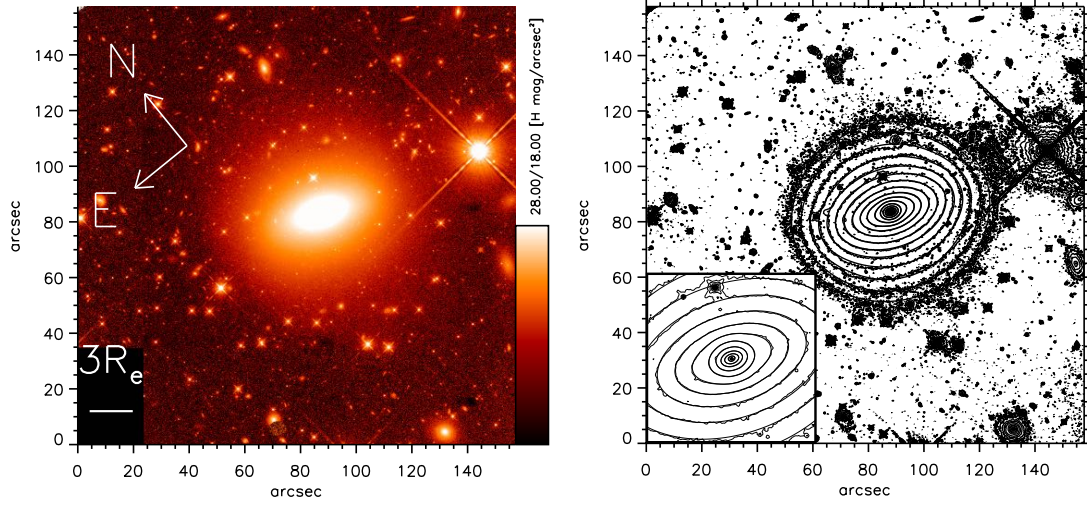


Figure 3.1: *Left*: *HST* *H*-band image of NGC 1281, which covers a field of $150 \square''$, with a final scale of $0.06''/\text{pixel}$. *Right*: Contour map of the same image. The MGE contours are over-plotted in black. The bottom left plot shows the accurate reproduction of the surface brightness profile within the central 30 arcsec^2 .

Table 3.1: Multi-Gaussian-Expansion of NGC 1281's *HST* (F160W) *H*-band image. The columns display the number of each Gaussian, beginning with the innermost one (1), the central surface density (2), the dispersion (3) and the corresponding Sérsic index (4) as well as the apparent flattening (5).

# of components	$I [L_{\odot} pc^{-2}]$	$\sigma [\text{arcsec}]$	n	q
1	149727.11	0.15	0.5	0.58
2	5002.1391	0.40	0.5	0.99
3	19213.442	0.78	0.5	0.60
4	6795.0136	1.49	0.5	0.65
5	2058.1459	1.83	0.5	0.99
6	1515.6123	5.04	0.5	0.52
7	464.61811	9.64	0.5	0.59
8	59.584718	15.71	0.5	0.90

flat ($q = 0.7$), inner ($R_e = 1.7''$), bulge-like component ($n = 2.2$) with a magnitude of $M_{H,Vega} = 11.61$ is embedded in a flat ($q = 0.6$), outer ($R_e = 10''$), disk-like ($n = 1.3$) component with a magnitude of $M_{H,Vega} = 10.97$. The fit has a bulge-to-total ratio (B/T) of 0.55.

To obtain a stellar mass model, we parameterise its surface brightness profile by a set of multiple Gaussians [MGE; Monnet et al., 1992; Emsellem et al., 1994]. In our case, the MGE consists of 8 Gaussians with a common centre and a fixed position angle (PA) of 69° , measured counter-clockwise from the y-axis to the galaxy major axis, with the image aligned N.-E. (i.e. north is up and east is left). In Fig. 3.1, we illustrate the deep *HST* *H*-band image (left) and the MGE parameterisation (right). The MGE accurately reproduces the SB profile of this object throughout the whole radial extent. There is no position angle twist in the photometric profile and the PA varies by less than 3° between the inner- and outermost isophotes.

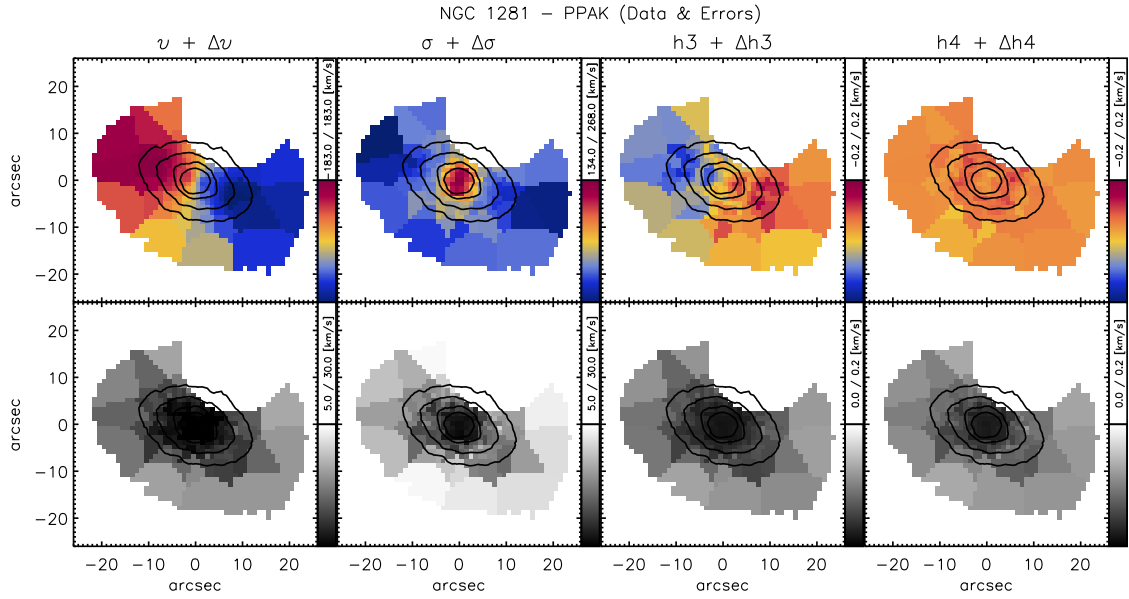


Figure 3.2: *Top*: PPAK IFU stellar kinematic maps of NGC 1281, of the mean velocity v , velocity dispersion σ , and Gauss-Hermite moments h_3 and h_4 . The maps show fast rotation around the short axis of 183 km s^{-1} and a central velocity dispersion of 268 km s^{-1} . Overplotted are contours of constant surface brightness from the same data cube. The empty region above the centre is generously masked due to the presence of a bright foreground star. *Bottom*: Corresponding uncertainty maps. Maps are oriented N.-E., i.e. north is up and east is left.

3.2.2 PPAK Kinematics

Kinematic data of NGC 1281 have been obtained at the 3.5m telescope at Calar Alto, with the *Potsdam Multi Aperture Spectrograph* (Roth et al. 2005) in the *PPAK* mode (Verheijen et al. 2004, Kelz et al. 2006), making use of the low-resolution V500 grating. This setup has a resolving power of $R = 850$ at 5400 \AA and a spectral resolution of 6.3 \AA FWHM across the nominal $3745 - 7500 \text{ \AA}$ spectral range, corresponding to an instrumental velocity dispersion of 150 km s^{-1} . The *PPAK* IFU consists of 382 $2.7''$ diameter fibres, which are bundled to a hexagonal shape and cover a field of view (FOV) of $1.3' \times 1.3'$. 331 of the total 382 fibres are science fibres that provide a 100 per cent covering factor with a 3 dither-pointing strategy while 36 fibres, located $72''$ away from the centre, are used to sample the sky.

The observing strategy was defined by the overall goal to acquire wide-field stellar kinematics out to several effective radii. This was accomplished on January 5 and 6, 2013 with a total exposure time of 6 hours on-source, achieved by 3 complete runs with 3 dither-pointings of 2400s each, divided into 2 frames à 1200s.

The data reduction follows the dedicated reduction pipeline of the Calar Alto Legacy Integral Field Spectroscopic Area (CALIFA) Survey [Sánchez et al., 2012; Husemann et al., 2013] and includes bias and straylight subtraction, cosmic ray rejection [Husemann et al., 2012], optimal fibre extraction, fibre flat-fielding, flexure correction and wavelength and flux calibration using spectrophotometric standard stars. The sky spectrum is the mean of only the 30 faintest sky fibres - to exclude any contamination by stars or low SB brightness objects - and subtracted from its associated science exposure. The 3

dither-pointings are then resampled to the final data cube with a $1''$ sampling using a distance-weighted interpolation algorithm [Sánchez et al., 2012].

We extract the line-of-sight velocity distribution (LOSVD) by fitting the spatially binned spectra [Cappellari & Copin, 2003] with a non-negative, linear combination of stellar templates [Cappellari & Emsellem, 2004] from the Indo-U.S. stellar library [Valdes et al., 2004] in the vignetting and sensitivity limited useful spectral range of 4200-7000 Å. The spectra were binned to reach a minimum S/N of 40 in each Voronoi zone, resulting in a total of 167 bins that cover the stellar kinematics of NGC 1281 out to $\sim 25''$ (i.e. 5 effective radii or roughly 7 kpc). Fig. 3.2 displays the two-dimensional mean line-of-sight velocity v , the velocity dispersion σ and the higher order Gauss-Hermite moments h_3 and h_4 per bin on the plane of the sky. The kinematic maps reveal extended, fast and regular rotation around the short axis, with a maximum velocity of $\sim 183 \text{ km s}^{-1}$. The peak in velocity dispersion is $\sim 268 \text{ km s}^{-1}$ and drops to 135 km s^{-1} for the outermost bins. Moreover, we measure a strong anti-correlation between v and h_3 , as is expected for axisymmetric systems [Bureau & Athanassoula, 2005; Chung & Bureau, 2004], and throughout positive h_4 values within the whole radial extent. Errors on the kinematic moments are small, with mean values of 9 km s^{-1} and 15 km s^{-1} for v and σ and 0.05 and 0.06 for h_3 and h_4 respectively. The radial increase in the measurement errors is due to NGC 1281's compactness. The surface brightness and hence the S/N of the individual spaxels drops rapidly and the outermost bins cannot accumulate enough spaxels to reach the target S/N.

To replicate the PSF of the *PPAK* observations, we fit a PSF convolved, reconstructed image to the MGE of the *HST* high-resolution data. The PSF is expanded by multiple, round Gaussians and in our case the image is well reproduced by two components with a dispersion of $1.53''$ and $5.39''$ and corresponding weights of 84% and 16% respectively.

3.3 Dynamical Analysis

3.3.1 Schwarzschild Models

The dynamical analysis relies on a triaxial implementation of Schwarzschild's orbit superposition method [van den Bosch et al., 2008]. Based on a non-negative, linear super-position of orbits in a given gravitational potential, we fit the observational constraints and hereby infer the contributions of the underlying gravitational constituents, consisting of black hole, stars and dark matter to the total mass budget. The reliability of this approach has been tested extensively and proven to be a powerful method to infer the internal mass distribution and dynamical structure of galaxies [van de Ven et al., 2008].

For our mass model, we consider three gravitational sources; the stellar mass M_* , which is the deprojected intrinsic luminosity density times a constant stellar-mass-to light ratio Υ_* , the black hole mass M_\bullet of a central SMBH and the dark halo, parameterised by a spherically symmetric NFW profile [Navarro et al., 1996] with concentration c_{DM} and total viral mass $M_{DM}=M_{200}$. The models cover a large range in parameters space of $\Upsilon_* \in [0.4, 3.0]$, $\log(M_\bullet/M_\odot) \in [8.0, 10.4]$, $c_{DM} \in [6, 16]$ and $\log(M_{DM}/M_*) \in [-2, 6]$.

Within these mass models we calculate a representative orbit library, consisting of 7533 orbits sampled along 31 logarithmically spaced equipotential shells out to $150''$. Every shell is used as a starting point for 9 orbits in each of the radial and angular direction. During orbit integration the projected and intrinsic quantities are stored and PSF convolved for comparison with the data. Finally, the models recover the binned LOSVD in a least-square sense by linearly adding up the contributions of the orbital building blocks.

Here, we restrict ourselves to an oblate axisymmetric stellar system. Given the fast and regular rotation around its apparent short-axis, the negligible variation in the photometric PA and the results of shape inversions of a large sample of fast-rotating ETGs [Weijmans et al., 2014], axial symmetry is a well justified assumption of the intrinsic shape of NGC 1281. Hence, the inclination is the only free viewing parameter that is needed to deproject the MGE-parameterised surface brightness and to infer the stellar mass density and hence the stellar gravitational potential of the galaxy (assuming an absolute magnitude for the sun in H -band of 3.39).

The flattest Gaussian in our fit has an axis ratio of $q = 0.52$ (Table 3.1), which implies possible inclinations of $60^\circ - 90^\circ$ (with 90° being edge-on). In our case, though, the inclination is reasonably well constrained by the central dust disc to be 70° . Nevertheless, to assess the reliability of our results with respect to changes in the inclination, we have also probed a more edge-on view of 80° and found no significant deviations (< 5 per cent) for the parameter constraints that are reported below.

3.3.2 Modelling Results

The results of our orbit-based dynamical models are presented in Fig. 3.3. The top panel shows the total enclosed intrinsic mass (black), the stellar mass (red), the dark matter content (green) and the black hole mass (blue) as a function of radius. The solid lines denote the values for the best-fitting model, with the dashed lines indicating the statistical 3σ uncertainties for one degree of freedom. We obtain a stellar mass of $\log(M_*/M_\odot) = 10.6^{+0.1}_{-0.1}$, a dark halo mass of $\log(M_{DM}/M_*) = 4.5^{+1.0}_{-1.5}$ and a black hole mass of $\log(M_\bullet/M_\odot) = 10.0^{+0.1}_{-0.1}$. At small radii ($\leq 3''$) the black hole is the dominant contributor to the total mass budget but quickly released from its role by the dark halo, which already takes over at $\sim 4.5''$ (i.e. $1 R_e$ or roughly 1.3 kpc). The total enclosed mass within the kinematic extent is $\log(M_{TOT}/M_\odot) = 11.6^{+0.2}_{-0.2}$.

We show the black hole mass and dark matter content as a function of stellar mass-to-light ratio in the middle and bottom panel. Here, the white, grey and black lines denote 68, 95 and 99 per cent quantiles of a χ^2 distribution with two degrees of freedom. Both the black hole mass and the dark halo mass are tightly constrained which is a result of the narrow predictions for the stellar mass-to-light ratio in H -band of $\Upsilon_* = 0.6 - 1.1$. Note that although the contours of the dark halo mass are well defined, the exact halo shape is not. Within the statistical uncertainties, the models can adopt any concentration within the range that is probed. Moreover, the scale radius is $200'' \leq r_s \leq 3500''$ (i.e. $60 \text{ kpc} \leq r_s \leq 1000 \text{ kpc}$) and hence promotes a constant density slope of the dark halo within the kinematic extent.

Clearly models without a dark halo cannot recover the details of the LOSVD. We illustrate this in Fig. 3.4, where we present (from left to right) the data, the overall best-fitting model ($c_{DM} = 10$, $\log(M_{DM}/M_*) = 4.5$, $\log(M_\bullet/M_\odot) = 10.0$ and $\Upsilon_* = 0.76$) and the best-fitting model without a halo ($\Upsilon_* = 2.8$, $c_{DM} =$

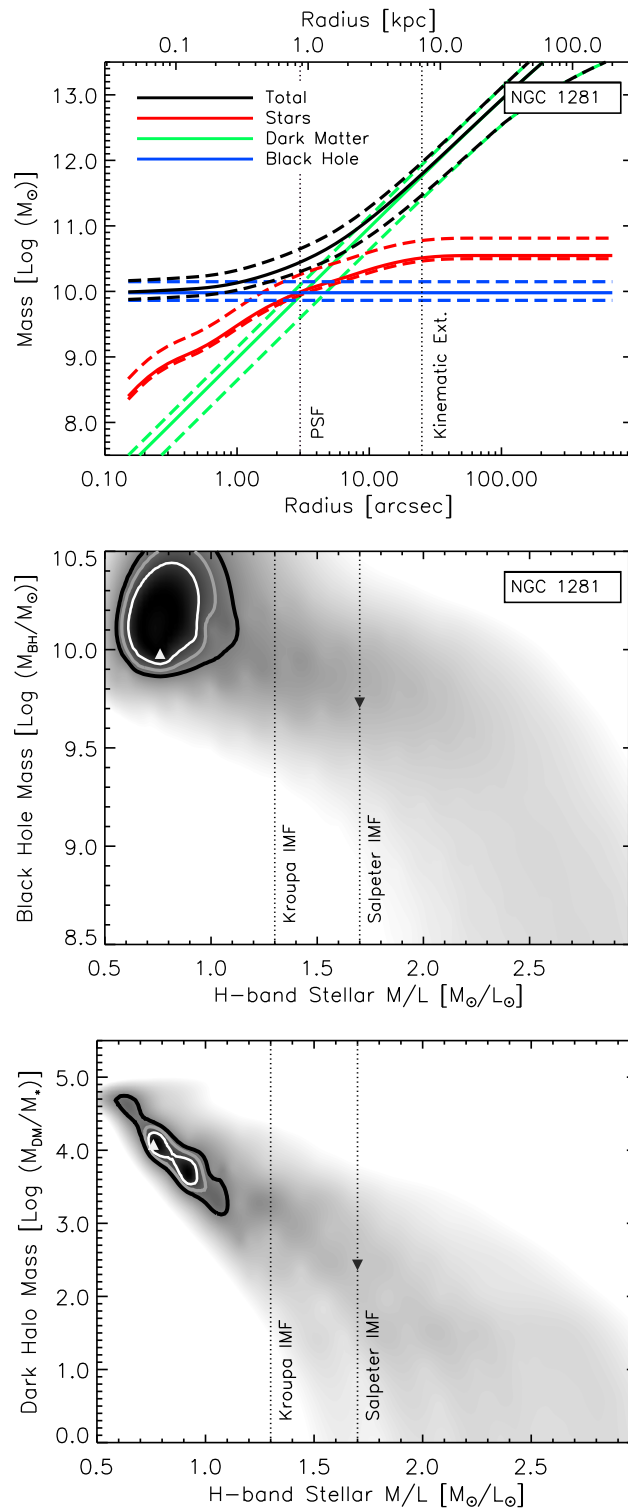


Figure 3.3: *Top*: Intrinsic enclosed mass distribution of NGC 1281 as a function of radius. Solid lines represent best-fitting values and dashed lines 3σ confidence intervals. The dotted vertical lines indicate the resolution limit and the extent of the kinematic observations. *Middle*: Confidence contours of black hole mass vs. stellar mass-to-light ratio. *Bottom*: Confidence contours of halo mass vs. stellar mass-to-light ratio. The white, grey and black lines represent 1-, 2- and 3σ confidence intervals for two degrees of freedom. The white triangle denotes the best-fitting dynamical model. The black triangle denotes the best-fitting model with a stellar M/L of 1.7, consistent with the stellar M/L inferred from the stellar population analysis. As a reference we overplot predictions of stellar mass-to-light ratios in *H*-band from SPS models with a Salpeter or Kroupa IMF assuming an age of 14 Gyr and solar metallicity.

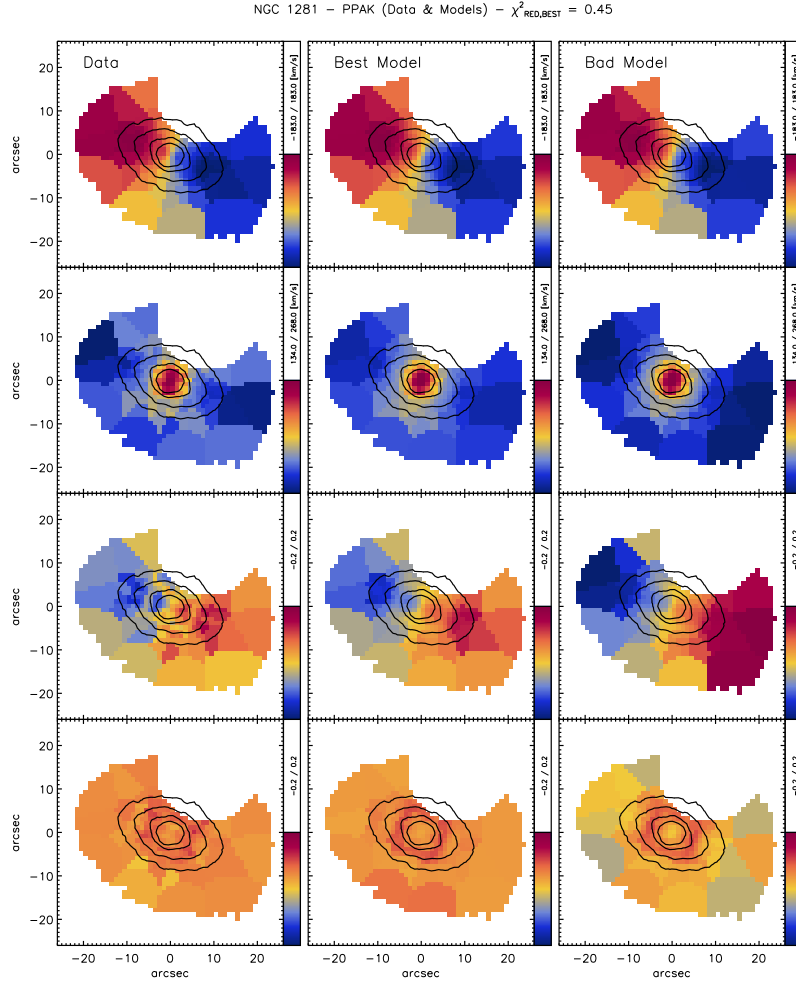


Figure 3.4: *First column*: PPAK IFU data consisting of the mean line-of-sight velocity v , velocity dispersion σ , h_3 and h_4 . All maps are oriented N.-E., i.e. north is up and east is left. *Second column*: Overall best-fitting Schwarzschild model predictions with a reduced χ^2 of 0.45. *Third column*: Best-fitting model without a halo, i.e. mass-follows-light (MFL). Models without a dark component cannot recover the LOSVD, and the best-fitting model w/o a halo deviates from the best-fitting dynamical model (which includes a massive dark halo) by $\Delta\chi^2 = 80$.

15, $\log(M_{DM}/M_*) = -2.0$ and $\log(M_\bullet/M_\odot) = 8.3$). The difference between the overall best-fitting model and the bad model is $\Delta\chi^2 \geq 80$, with most of the χ^2 difference attributable to the fit to v , σ and h_3 . Thus, the bad model is excluded at more than 5σ .

The best-fitting dynamical model prefers an extremely massive SMBH, a massive dark halo and a very low stellar mass-to-light ratio. Fig. 3.4 points at the outer velocity moments as the driver of these detections, and indeed model predictions beyond $1-2 R_e$ show strong deviations from the observations if more typical values for the stellar mass-to-light ratio, dark halo and black hole are adopted.

The strong constraints by the remote kinematic measurements are further exemplified in Fig. 3.5 where we provide a direct comparison between our fiducial models and test models which only fit the data within $1 R_e$. Both panels present the χ^2 contour levels of halo mass $\log(M_{DM}/M_*)$ vs. H -band stellar mass-to-light ratio Υ_* , with the test models on top and the fiducial models on the bottom. The plot provides unambiguous evidence for the power of the wide-field IFU kinematics, which are able

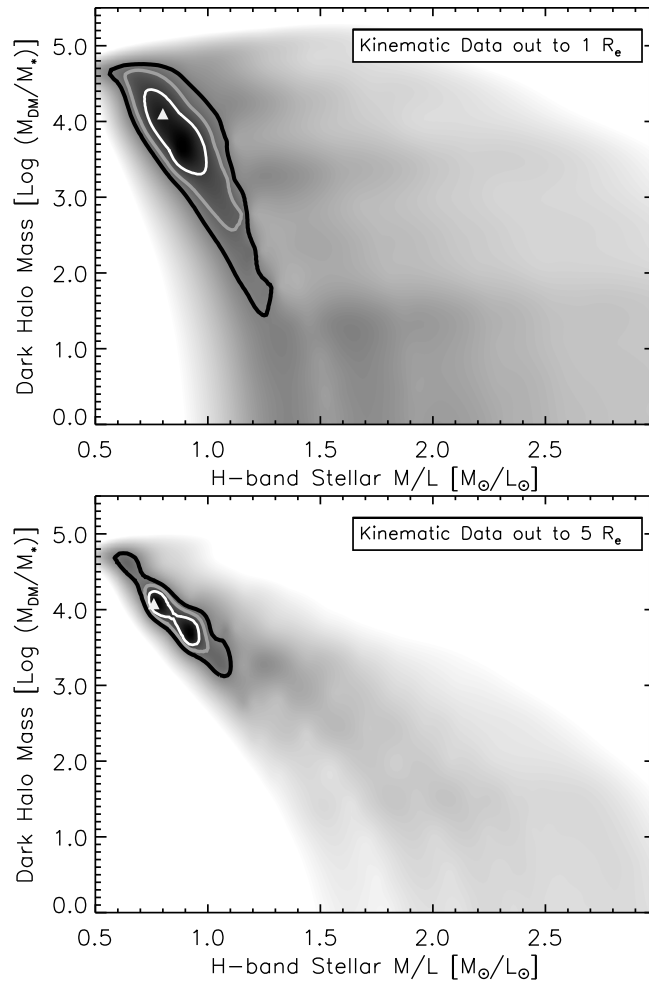


Figure 3.5: Comparison of the inferred values for the dark halo and stellar mass-to-light ratio of NGC 1281's orbit-based models. *Top*: Test models that are confined to fit the kinematic data within one effective radius. *Bottom*: Fiducial models that fit the available kinematic data out to $5 R_e$. The white, grey and black line denotes 1-, 2- and 3σ confidence intervals for two degrees of freedom. Test and fiducial models show similar best-fitting parameters, but the large-scale kinematics provide tighter constraints for the stellar mass-to-light ratio and the dark halo mass.

to effectively break the degeneracy between the dark halo and the stellar mass-to-light ratio. The massive dark halo is tightly constrained and the remarkably small, constant stellar mass-to-light ratio then propagates inwards and yields an unreasonably massive SMBH to explain the total dynamical mass in the centre. We also emphasise that the influence of the massive dark halo is already noticeable within the central $5''$, where the sharp rise in the enclosed mass profile can only be explained by an additional dark component. In this region, the test models yield dark halo masses which are in agreement with the dark halo masses of the fiducial models though with larger uncertainties.

3.4 Discussion

3.4.1 Alternative Halo Parameterisations

The dark halo mass in NGC 1281 is based on the assumption that the dark matter density profile is well approximated by a spherically symmetric NFW profile. To assess the robustness of the results with respect to changes in the halo parameterisation, we have constructed models with a spherical logarithmic halo which possesses a flat central density core and gives rise to an asymptotic constant circular velocity at very large radii. In Fig. 3.6 we plot the enclosed total mass as a function of radius for models with a NFW halo, a cored-logarithmic halo (CL) and, in addition, for models where mass-follows-light (MFL). The upper and lower line for each halo parameterisation corresponds to the upper and lower bound 3σ statistical uncertainty in the respective set of models.

Within the uncertainties the CL halo has a core radius of $60'' \leq r_c \leq 110''$ (i.e. $17 \text{ kpc} \leq r_c \leq 32 \text{ kpc}$) and a circular velocity of $1700 \text{ km s}^{-1} \leq v_c \leq 3200 \text{ km s}^{-1}$. Here again, the models prefer a constant slope for the dark matter density distribution and yield a stellar mass-to-light ratio of $0.8 \leq \Upsilon_* \leq 1$ in H -band.

The total enclosed mass of the NFW and CL models are in excellent agreement, being about $11.4 \leq \log(M_{TOT}/M_\odot) \leq 11.8$ within $25''$ ($\simeq 5 R_e$ or 7 kpc), and the slight deviations are most likely an effect of the coarse sampling strategy in the latter. The simple mass-follows-light models fail to keep pace and predict a total enclosed mass of $10.9 \leq \log(M_{TOT}/M_\odot) \leq 11.1$ within the same spatial extent. Moreover, the best-fitting MFL model has a mass-to-light ratio of 2.8 and deviates by $\Delta\chi^2 = 80$ from the best-fitting NFW and CL models, as illustrated in Fig. 3.4.

3.4.2 Implications And Caveats

According to our orbit-based dynamical models of the wide-field IFU data, NGC 1281 cannot be recovered without the presence of a dark halo (Fig. 3.4 and 3.5). Models with a dark halo provide a good fit to the LOSVD and yield a total enclosed mass of $11.4 \leq \log(M_{TOT}/M_\odot) \leq 11.8$ within the kinematic extent, irrespective of the adopted dark halo parameterisation (Fig. 3.6). Given its total luminosity and a stellar M/L of ≤ 1 (as indicated by our best-fitting dynamical models), this results in a dark matter contribution of 90 per cent to the total enclosed mass within $5 R_e$ ($\approx 7 \text{ kpc}$). Adopting an optimistic stellar M/L of ~ 2 in H -band would still imply a substantial halo-to-stellar mass ratio of 0.8. Based on these arguments, we can conclude that NGC 1281 is embedded in a massive dark halo, even if we would choose to remain ignorant regarding the details of its dark halo profile, black hole mass and stellar M/L.

3.4.2.1 The Dark Halo Profile

We obtain tight predictions for the total dark halo mass of $\log(M_{DM}/M_*) = 4.5^{+1.0}_{-1.5}$. The dark halo is hence not only one order of magnitude larger than the stellar mass within a comparatively small spatial extent of $5 R_e$ ($\approx 7 \text{ kpc}$), but also more than one order of magnitude larger than what is expected if the mass-concentration relation [Macciò et al., 2008] and stellar-to-halo mass relation [Dutton et al., 2010]

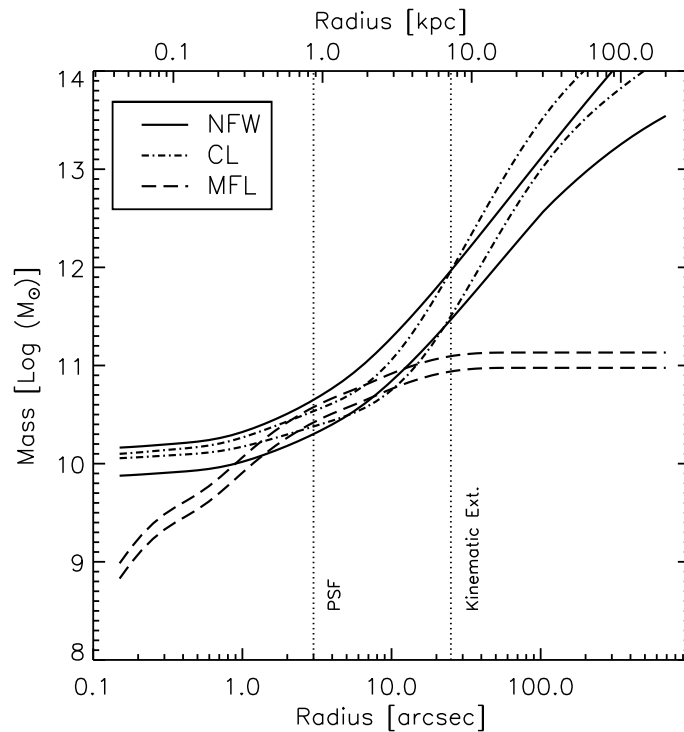


Figure 3.6: Enclosed total intrinsic mass as a function of radius for models with a NFW halo (solid), a cored-logarithmic halo (dash dot) and mass-follows-light models (long dash). The dotted vertical lines denote the lower resolution limit and the maximum of the *PPAK* kinematics. The upper and lower line for each halo assumption corresponds to the upper and lower bound of the statistical 3σ uncertainties. The cored-logarithmic and NFW halo parameterisations are in excellent agreement whereas the mass-follows-light models clearly underestimate the total enclosed mass at the maximum kinematic extent.

holds. In the context of Λ CDM cosmology, though, this is very unlikely and in clear contrast to what has been observed so far based on results of weak gravitational lensing [Mandelbaum et al., 2006], satellite kinematics [More et al., 2011] and halo abundance matching [Moster et al., 2010]. Consequently, a spherical NFW profile *cannot* be a fair assumption of the dark halo profile of this galaxy. The results for the NFW halo in our dynamical models can only be considered as an attempt to recover the high total enclosed dynamical mass (M_{TOT}) - which is not possible for simple MFL models - without an interpretation of the physical consequences for the values of choice. This is also illustrated by the preference of a constant dark matter density slope - in both the NFW and CL case - since the models try to maximise the dark matter contribution within the observational extent. Moreover, the necessity of a rapidly rising dark halo contribution leads to a tension between the stellar mass and dark mass in the central parts, and this tension can only be dissipated by significantly decreasing the stellar mass-to-light ratio to unrealistically low values (Sec. 3.4.2.3), which in turn calls for an unreasonably massive SMBH (Sec. 3.4.2.4).

In principle, the constant density slope could still be explained by an NFW profile if, e.g. the halo was stripped by the Perseus cluster environment. As the outer halo gets stripped, the collisionless dark matter particles could relax and the halo would puff up in the shallower gravitational potential well, similar to what has been predicted for the collisionless stellar components of dwarf NFW halos during the tidal disruption in MW-like potentials [Peñarrubia et al., 2006]. The relaxation and puff up of the dark matter halo could then shift the turnover radius further away, making it hard to constrain with

our limited FOV. But even if the halo is truncated, this does not solve the discrepancy between the halo mass of NGC 1281 and the halo masses that are predicted within the Λ CDM framework. The dark halo of NGC 1281 within $25''$ is still over-massive, and the relaxation due to stripping would imply that the unstripped halo was even more concentrated and massive before within the same spatial extent.

3.4.2.2 The Constant Stellar M/L

The most restrictive condition in our dynamical models is the assumption of a constant Υ_* . The stellar mass-to-light ratio in NGC 1281 is $0.6 \leq \Upsilon_* \leq 1.1$ and significantly lower than expected from an old stellar population (≥ 10 Gyr) of a canonical Kroupa IMF ($\Upsilon_* = 1.3$) or Salpeter IMF ($\Upsilon_* = 1.7$) (see Sec. 3.4.2.3). A radial variation of the stellar mass-to-light ratio, however, could mitigate the effect of missing mass in the remote regions and lower the predictions for additional dark mass while increasing Υ_* .

To this end we constructed dynamical models with a Υ_* gradient, covering single slopes of $\kappa \in [-0.5, 0.5]$. The functional form of the stellar mass-to-light ratio is then given by $\log(\Upsilon_\alpha) = \log(\Upsilon_{\alpha,0}) + \kappa \times \log(r/r_0)$, with r being the radius in arcseconds and $\Upsilon_{\alpha,0}$ the pivot stellar M/L at $r_0 = 0.1''$. The models include a SMBH and a NFW halo and the sampling in parameter space has not changed with respect to our fiducial models in Sec. 3.3.2. We found that models with slopes of $\kappa \in [-0.1, 0.3]$ can recover the observations very well. The best-fitting model with a slope is a statistically better fit than the best-fitting fiducial model ($\Delta\chi^2 = 20$), but this is expected given the increased freedom in the spatial variation of the stellar mass-to-light ratio. In general, the slopes are positive and driven by the need of a substantial amount of dark mass. The radial increase of the stellar mass-to-light ratio, however, cannot account for a significant fraction of the total dynamical mass due to the rapid decline of the stellar surface density of NGC 1281. Hence the predictions for the dark halo mass decrease only by 0.5 -1.0 dex, with the best-fitting model now located at $\log(M_{DM}/M_*) = 4$, $\log(M_\bullet/M_\odot) = 10.0$, $\Upsilon_{\alpha,0} = 0.8$ and $\kappa = 0.1$.

Moreover, a positive slope of 0.1 - 0.3 induces a change in the stellar mass-to-light ratio from 0.8 in the centre to 1.4 - 4.2 in the outermost regions. The existence of such gradients should be imprinted in the colour profiles of galaxies [Bell & de Jong, 2001], attributable to strong variations in their stellar population properties, but is not evident in the $g - i$ colour profile of NGC 1281 based on archival *SDSS* imaging (Fig. 3.7). The profile shows only a very gentle drop within 2 effective radii of about 0.1 mag, indicative of a negative gradient with an expected variation in the stellar M/L of 0.2 [Zibetti et al., 2009], which shows that the use of a constant Υ_* was a reasonable choice.

3.4.2.3 The Stellar IMF

NGC 1281 is a compact, elliptical, high central velocity dispersion galaxy and bears resemblance to the compact objects at redshift $z = 2$, which are thought to be the progenitors of the inner parts of today's massive elliptical galaxies. It is also very similar to NGC 1277, another high-dispersion galaxy which hosts an over-massive SMBH for its modest dimensions [van den Bosch et al., 2012]. The IMF of these objects could be significantly different from the IMF observed in the local volume, and indeed the universality of the IMF has been questioned recently, based on results from gravitational lensing [e.g. Treu et al., 2010],

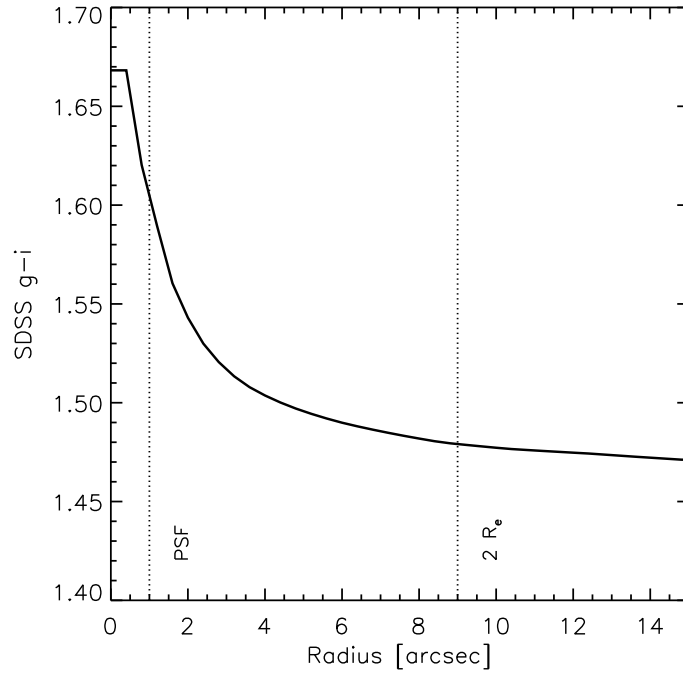


Figure 3.7: *SDSS g - i* colour profile of NGC1281. The first line is the mean PSF FWHM of the two particular *SDSS* bands and the second line denotes two effective radii as measured from the circular aperture of the high-resolution *HST* imaging. Within this range, the colour decreases only by ~ 0.1 mag and suggests no significant stellar M/L gradient.

stellar dynamics [e.g. Cappellari et al., 2012] and SPS fits to gravity sensitive features in the integrated spectra of ETGs [e.g. van Dokkum & Conroy, 2010]. These results suggest a bottom heavy IMF with increasing velocity dispersion which should in general lead to stellar mass-to-light ratios larger than those predicted by a Salpeter IMF, assuming that the shape of the IMF in these objects is similar to what is observed in the Galaxy. However, we have shown that models with high Υ_* can be excluded as they are not able to recover the features of the LOSVD and miss to replicate the high dynamical mass of NGC 1281, *if* the dark halo is parameterised by NFW or CL.

To obtain an independent measurement of the stellar M/L and to assess the reliability of the stellar M/L in our dynamical set of models with a NFW profile, we have carried out a line-strength analysis of NGC 1281 based on our *PPAK* observations. The analysis suggests a very old (~ 14 Gyr) stellar population throughout the galaxy (Fig. 3.8). The metallicity decreases from solar in the centre to -0.17 dex at $3 R_e$, and the IMF slope, parameterised following Vazdekis et al. [1996] and La Barbera et al. [2013], varies from $\Gamma_b = 2.3$ in the central regions to $\Gamma_b = 1.3$ in the outskirts. Given these best-fitting stellar population parameters - and under the assumption of a bimodal IMF - the expected radial variation in the *H*-band stellar M/L is $\Delta\Upsilon_* = 0.4$, where the extra variation of 0.2 with respect to the variation indicated by the colour profile (Fig. 3.7) is related to the fact that we allowed the IMF to vary. Although different IMF parameterisations could lead to different M/L values (while fitting equally well the strength of gravity-sensitive features), a M/L as low as inferred from the dynamical analysis ($\Upsilon_* = 0.7$) is only possible under the assumption of a very young (~ 5 Gyr) stellar population. However, the presence of such a young stellar component is ruled out by the line-strength analysis and the *SDSS g - i* colour profile.

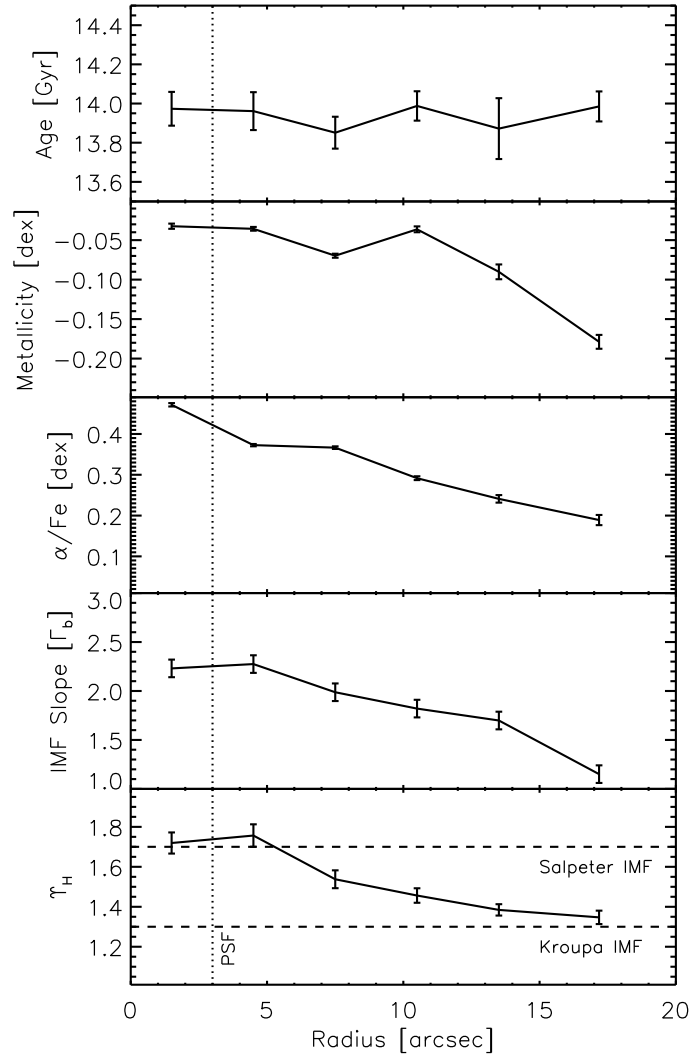


Figure 3.8: Stellar population properties of NGC 1281. The top three panels represent the age, metallicity and α -abundance as a function of radius. The fourth panel depicts the IMF slope. Under the assumption of a bimodal IMF, these stellar population properties can be turned into a stellar mass-to-light ratio (bottom panel). Constrained by the uniformly old stellar population, the resulting stellar mass-to-light ratio ranges between 1.7 (centre) and 1.3 (outskirts) and cannot be reconciled with the dynamical stellar M/L of 0.7 - 1.1 in the NFW models.

Adopting a stellar mass-to-light ratio of 1.7, as indicated by the stellar populations, is capable to decrease the halo-to-stellar mass ratio to $\log(M_{DM}/M_*) = 2.5$ (Fig. 3.3). Yet, fixing Υ_* provides a worse fit to the kinematics than our best-fitting dynamical model. The best-fitting model with $\Upsilon_* = 1.7$ deviates by $\Delta\chi^2 \geq 30$ from our overall best-fitting model, and it remains elusive why one should prefer a model which is excluded by a significance of more than 5σ .

Finally, we emphasise that - by tracing gravity-sensitive features in the spectra - the IMF slope strongly varies between the inner- and outermost regions. This shows that the systematic variation of the IMF might be a local, rather than a global property, which is tightly linked to the high stellar velocity dispersion regions [Martín-Navarro et al., 2015a].

3.4.2.4 The Black Hole

The models predict the presence of a black hole of $\log(M_{\bullet}/M_{\odot}) = 10_{-0.1}^{+0.1}$, but we strongly emphasise that this measurement is solely driven by the tight constraints for the dark halo and hence the stellar mass-to-light ratio. This cascade issue starts with the necessity to recover the high total enclosed mass with a steeply rising NFW halo, which already dominates the total mass budget beyond $1 R_e$. The massive dark halo drives down the stellar M/L by about a factor of 2-3, when compared to our stellar population analysis, to relieve the tension for the dynamical mass within the effective radius. This, in turn, yields a tension between the low stellar dynamical mass and the total dynamical mass in the centre, which gives rise to the unrealistically massive SMBH. Here again, the SMBH is more massive than expected and overshoots the upper bound of the M- σ relation [Gültekin et al., 2009; McConnell & Ma, 2013; Kormendy & Ho, 2013] by one order of magnitude.

Positive outliers from the currently adopted black hole scaling relations have been detected before. However, those with the strongest deviations from the predictions are usually also the most massive black holes located in the most massive galaxies, such as the brightest cluster galaxies (BCGs) NGC 3842 and NGC 4889 [McConnell et al., 2011]. According to our models, the black hole in NGC 1281 would comprise 20 per cent of the total baryonic mass. This is not only in contrast to the black hole scaling relations but would also pose a major difficulty for galaxy evolution, as it is not clear how such a massive black hole could have grown in a small galaxy that seems to be devoid of a very active merging history.

3.5 Summary

We have performed a dynamical analysis of the compact, elliptical galaxy NGC 1281. Based on high spatial resolution imaging and wide-field IFU stellar kinematics, we constructed orbit-based dynamical models to constrain the contribution of stars, black hole and dark matter to its total mass budget. In particular the large-scale kinematics out to $5 R_e$ ($\simeq 7$ kpc) provide strong constraints for the dark and luminous mass in this object.

According to our models, NGC 1281 is a dark matter dominated galaxy with a dark matter fraction of up to 90 per cent to the total enclosed mass within the kinematic extent, irrespective of the exact halo parameterisation. Even if our stellar M/L is underestimated due to the adoption of a NFW profile, which might not be a good proxy for the dark halo profile in this galaxy, a super-Salpeter IMF with a stellar M/L of ~ 2 would still imply a dark matter fraction of 80 per cent within the bounds of the kinematic data. Simple mass-follows-light models imply a stellar mass-to-light ratio of 2.8, but these models are not able to recover the high total enclosed dynamical mass and clearly fail to recover the features of the LOSVD.

Assuming that the dark halo profile can be parameterised by a spherical NFW halo, this yields a total dark halo mass of $\log(M_{DM}/M_{\odot}) = 15.0_{-1.5}^{+1.0}$. However, this halo mass is typically ascribed to the halo of galaxy clusters and in contrast to findings based on Λ CDM cosmology. The massive dark NFW halo, in turn, tightly constrains the stellar mass-to-light ratio in this object. The stellar mass-to-light ratio is $0.6 \leq \Upsilon_{\star} \leq 1.1$ and hence considerably lower than expected from our spectral analysis of its stellar populations. This result, however, arises from a tension between the dark and luminous matter. The

models need to recover the high total enclosed dynamical mass with a steeply rising NFW profile, which in turn leads to an over-estimation of dynamical mass in the inner parts that is solved by diminishing the stellar M/L.

A radial variation in the stellar mass-to-light ratio has been considered and models with a positive slope provide a good fit to the kinematics, but they cannot account for a significant fraction of total enclosed mass due to the rapid decline of the stellar surface brightness. Moreover, the positive slopes predict a variation in the stellar M/L, which should translate into a strong variation in colours. The lack of such a colour gradient, however, endorses the employment of a constant Υ_* .

The models predict a SMBH mass of $\log(M_\bullet/M_\odot) = 10_{-0.1}^{+0.1}$, but the black hole sphere of influence is not resolved by our observations. The detection is merely a result of the unrealistically low stellar mass-to-light ratio, which propagates inwards and predicts the presence of a massive SMBH to recover the central dynamical mass.

The structural and dynamical properties of compact, elliptical, high central velocity dispersion galaxies

Abstract

We present deep *Hubble Space Telescope* imaging and wide-field integral field unit stellar kinematics of seven compact, elliptical, high central velocity dispersion galaxies in the local universe, and construct orbit-based dynamical models to constrain their luminous and dark matter contribution to the total mass profile as well as their total mass density slopes. We first show that our galaxies are strong outliers in the Fundamental Plane of local early-type galaxies (ETGs), and significant outliers in the present-day mass-size relation. They are, however, consistent with the mass-size relation of compact, massive and passive galaxies at redshift $z = 2$, so-called "red nuggets" which are thought to be the progenitors of today's most massive elliptical galaxies. The compact sizes of our nearby galaxies imply high central stellar mass surface densities, which are in agreement with the stellar mass surface densities of the massive galaxy population at higher redshift. The dominance of the stellar mass component translates into high total mass density slopes, exceeding $\gamma = 2.1$. In merger simulations these high density slopes can be triggered by in-situ star formation during gas-rich major mergers of disk galaxies. The largest galaxies in our sample have already grown via disproportional mass accumulation in the remote regions, consistent with theories of the evolution of massive galaxies since $z = 2$ within which they form through numerous minor merging events. This all supports that we can use our sample of nearby galaxies as local analogues of the high redshift nuggets. In this way, we can show that the dark matter fraction within the effective radius is lower at higher redshift as the smaller effective radius encompasses less of the dark volume.

4.1 Introduction

The structural and dynamical properties of early-type galaxies (ETGs) are key to our understanding of their formation and evolution. The homogenous properties of the most massive ellipticals, including their evolved stellar populations and high metallicities [e.g. Bower et al., 1992; Gallazzi et al., 2006; Jimenez et al., 2007; Graves et al., 2009a,b; Kuntschner et al., 2010], boxy isophotes and high Sérsic indices [e.g. Kormendy & Bender, 1996; Kormendy et al., 2009], isotropic velocity distributions and non-rotating, pressure supported velocity profiles [e.g. Binney, 1978; Davies et al., 1983; van der Marel, 1991; Emsellem et al., 2007; Cappellari et al., 2007; Emsellem et al., 2011], are considered as cornerstones, which a successful theory of galaxy formation and evolution has to be able to reproduce. Understanding the formation and evolution of ETGs in general - i.e. of the entire population of disk, fast-rotators and boxy, slow-rotators - becomes even more important when considering that more than half of the stellar mass in the universe is confined to this class of objects and the spheroidal components of disk galaxies [Fukugita et al., 1998; Hogg et al., 2002; Bell et al., 2003; Baldry et al., 2004], which closely resemble elliptical galaxies of similar luminosity.

Monolithic collapse [Eggen et al., 1962] has long been considered the principal formation mechanism for galaxies in general and the population of ETGs in particular. However, the advent of deeper imaging and the possibility to obtain K -band number counts [Kauffmann & Charlot, 1998] as well as galaxy luminosity functions [Faber et al., 2007] at high redshift ($z \sim 1$) has effectively ruled out this simple formation scenario. An alternative to the monolithic collapse theory for the formation and evolution of ETGs is provided by the merging paradigm [Toomre & Toomre, 1972; Toomre, 1977] which, within a cosmological framework [White & Rees, 1978], predicts a hierarchical build-up of galaxies through successive minor and major merging events. Considerable efforts have therefore been made in developing high-resolution N -body simulations of dissipational and dissipationless (un-)equal mass mergers of (disk-)galaxies [Barnes, 1988, 1989; Barnes & Hernquist, 1996; Hernquist, 1992, 1993; Naab & Burkert, 2003; Jesseit et al., 2005; Robertson et al., 2006; Cox et al., 2006]. While these simulations have been remarkably successful in reproducing the global photometric and kinematic properties of disk, fast-rotating and boxy, slow-rotating ellipticals, discrepancies remain in recovering the detailed dynamics of the most massive, slow-rotating ellipticals [Burkert et al., 2008] as well as their chemical abundance ratios [Naab & Ostriker, 2009].

The issue of reproducing massive ETGs in the local universe is even more severe if their structural and morphological transformation through cosmic time is taken into account. By tracing back a population of galaxies at constant number density [van Dokkum et al., 2010], their detailed mass and size evolution can be recovered, indicating that the likely progenitors of today's red, massive galaxy population have been considerably smaller and denser at earlier times [e.g. Daddi et al., 2005; Trujillo et al., 2006; Zirm et al., 2007; van der Wel et al., 2008; van Dokkum et al., 2008; Szomoru et al., 2010, 2012; van der Wel et al., 2014]. Star formation was already quenched for a large fraction of this galaxy population (also commonly referred to as "red nuggets") and hence is unable to explain their drastic growth in size ($\sim 4\times$) and mass ($\sim 2\times$) since $z = 2$ [Kriek et al., 2006; Toft et al., 2007; Cimatti et al., 2008; Kriek et al., 2008, 2009; Williams et al., 2009; van Dokkum et al., 2010]. Moreover, these galaxies are disk [Toft et al., 2005; Trujillo et al., 2006; van der Wel et al., 2011; Chang et al., 2013], with small Sérsic indices, and have high velocity dispersions [van Dokkum et al., 2009; Bezanson et al., 2011; Toft et al., 2012; van de

Sande et al., 2013]. Here again, monolithic collapse fails to understand their evolution, as their present-day descendants would be too small and too low in number density [Kriek et al., 2008; Bezanson et al., 2009]. On the other hand, binary mergers of equal mass (disk-)galaxies result in a comparable growth in size and mass ($M \propto R_e$) [Hilz et al., 2012, 2013] and the required level of mergers would consequently lead to an overestimation of the local galaxy mass function at the upper end [McLure et al., 2013]. In addition, the dearth of passively evolved red nuggets in the local universe is at odds with the stochastic nature of major merging [Trujillo et al., 2009; Taylor et al., 2010], in which a non-negligible number is expected to survive unaltered [Hopkins et al., 2009b; Quilis & Trujillo, 2013].

Focus has therefore shifted to a two-phase growth, in which the assembly history of massive galaxies is dominated by an initial dissipative stage, where stars are formed in-situ, followed by an inside-out growth through few major and numerous minor merging events [Naab et al., 2009; Hopkins et al., 2009a; van Dokkum et al., 2010; Oser et al., 2010, 2012; Lackner et al., 2012; Hilz et al., 2012, 2013; Pérez et al., 2013; Patel et al., 2013; Bédorf & Portegies Zwart, 2013].

The theoretical efforts are motivated by snapshots in the evolution of ETGs, provided by objects in the local universe and observational progress in obtaining photometric and spectroscopic data of galaxies at higher redshift ($z \leq 2$). These, however, are notoriously difficult and expensive with current observational facilities and have only recently become available [e.g Vernet et al., 2011]. More importantly though, deriving accurate measurements of stellar masses for galaxies at $z = 2$, for instance, relies on fits to their spectral energy distribution (SED), which is basically untested at these redshifts. Similarly, stellar dynamical masses, the gold standard which does not suffer from the systematic uncertainties in stellar population synthesis (SPS) models [Conroy et al., 2009], are currently based on the measurement of the central velocity dispersions only [Kriek et al., 2009; van Dokkum et al., 2009; van de Sande et al., 2011; Toft et al., 2012; Bezanson et al., 2013; van de Sande et al., 2013] and viral mass estimators which are calibrated for the population of nearby ellipticals [Cappellari et al., 2006]. Hence, our understanding of the evolution of ETGs is prone to many systematic uncertainties in deriving accurate measurements as well as limited by the lack of spatially resolved kinematics and modelling assumptions.

Optimally, one would like to study the progenitors of today's massive galaxy population in the local universe, where high-resolution photometric and spectroscopic data will enable a detailed investigation of their structural and dynamical properties, such as their sizes and masses and their luminous and dark matter content. In this chapter, we present a small sample of nearby, compact, high central velocity dispersion galaxies (including MRK 1216, NGC 1277 and NGC 1281, which have been studied in detail in Chapter 2 and 3), which bear resemblance to the likely progenitors of today's massive galaxy population at redshift $z = 2$. Given high spatial resolution photometric observations with the *HST* and medium resolution spectroscopic observations with the *PPAK* IFU, we can measure their structural and kinematic properties which in turn yield information regarding their origin and (non-)violent growth. Moreover, the high quality of the suit of available photometric and kinematic data allows us to carry out orbit-based dynamical models, in order to derive accurate measurements of their luminous and dark matter content.

In Section 4.2 we briefly revisit the data acquisition and reduction pipelines and depict the data, consisting of deep *HST* imaging and wide-field IFU stellar kinematics. We exploit the wealth of photometric and spectroscopic information in Sec. 4.3, where we employ the fundamental plane (FP) and the specific

stellar angular momentum to characterise and classify the galaxies in our sample. We derive accurate stellar and dark masses by means of our orbit-based dynamical models in Sec. 4.4. We discuss our results in Sec. 4.5, drawing a comparison to galaxies at high redshift. Finally, we summarise our findings in Sec. 4.6.

Throughout this chapter we adopt 5th year results of the Wilkinson Microwave Anisotropy Probe (*WMAP*) [Hinshaw et al., 2009], with a Hubble constant of $H_0 = 70.5 \text{ km s}^{-1} \text{ Mpc}^{-1}$, a matter density of $\Omega_M = 0.27$ and a cosmological constant of $\Omega_\lambda = 0.73$.

4.2 Data

4.2.1 HST Imaging

We covered the photometric pipeline in detail in Sec. 2.2. For the sake of completeness, we encapsulate the most relevant information.

Single orbit imaging of six compact, high central velocity dispersion galaxies have been obtained with the *HST* WFC3 in *H*-band (F160W), as part of program GO: 13050 (PI: van den Bosch). The data consists of three dithered full- and four sub-array exposures with a total integration time of ~ 1400 seconds for each galaxy. The full-arrays are 450 seconds long exposures, covering a nominal field of view (FOV) of $136'' \times 123''$. The 1.7 seconds short $16'' \times 16''$ sub-array exposures of the high surface brightness nucleus serve the single purpose of mitigating possible saturation in the long full-arrays.

Observations in the near-infrared (NIR) F160W filter have been chosen to minimise the effect of dust extinction and line blanketing while being aware that the NIR is also a better tracer of the stellar mass. Contamination from more recent starbursting events is minimal at longer wavelengths and the stellar mass-to-light ratio (Υ_*) thus becomes a weaker function of the underlying stellar populations [Bell & de Jong, 2001; Cole et al., 2001].

The reduction and combination of the exposures is carried out via *Astrodrizzle* [Gonzaga et al., 2012]. Here, flat-field calibrated images are corrected for geometric distortions and drizzled onto a reference frame, where they are aligned according to the pointing information provided in the header of the respective files. The aligned images are then combined; the final output image is weighted by the exposure times of the individual input images. This final output image is then drizzled back onto the original, geometrically distorted but flat-field calibrated images to identify cosmic rays and bad pixels. The sky level in the individual exposures is determined by iterative sigma-clipping of uniformly distributed pixels. However, both the deep full- and sub-array exposures are dominated by galaxy light, either from the nucleus or the extended stellar halo of these objects. We therefore determine the sky level manually in less contaminated regions of the full-array exposures, while the background flux for the sub-array exposures is derived by measuring the flux difference between the sky subtracted full-arrays and the non-sky subtracted individual sub-arrays.

We present the final output of the photometric pipeline in Fig. 4.1, where we show four objects, namely NGC 1270, NGC 1271, NGC 2767 and UGC 2698. We refer the reader to Sec. 2.2.2 and 3.2.1, for the images

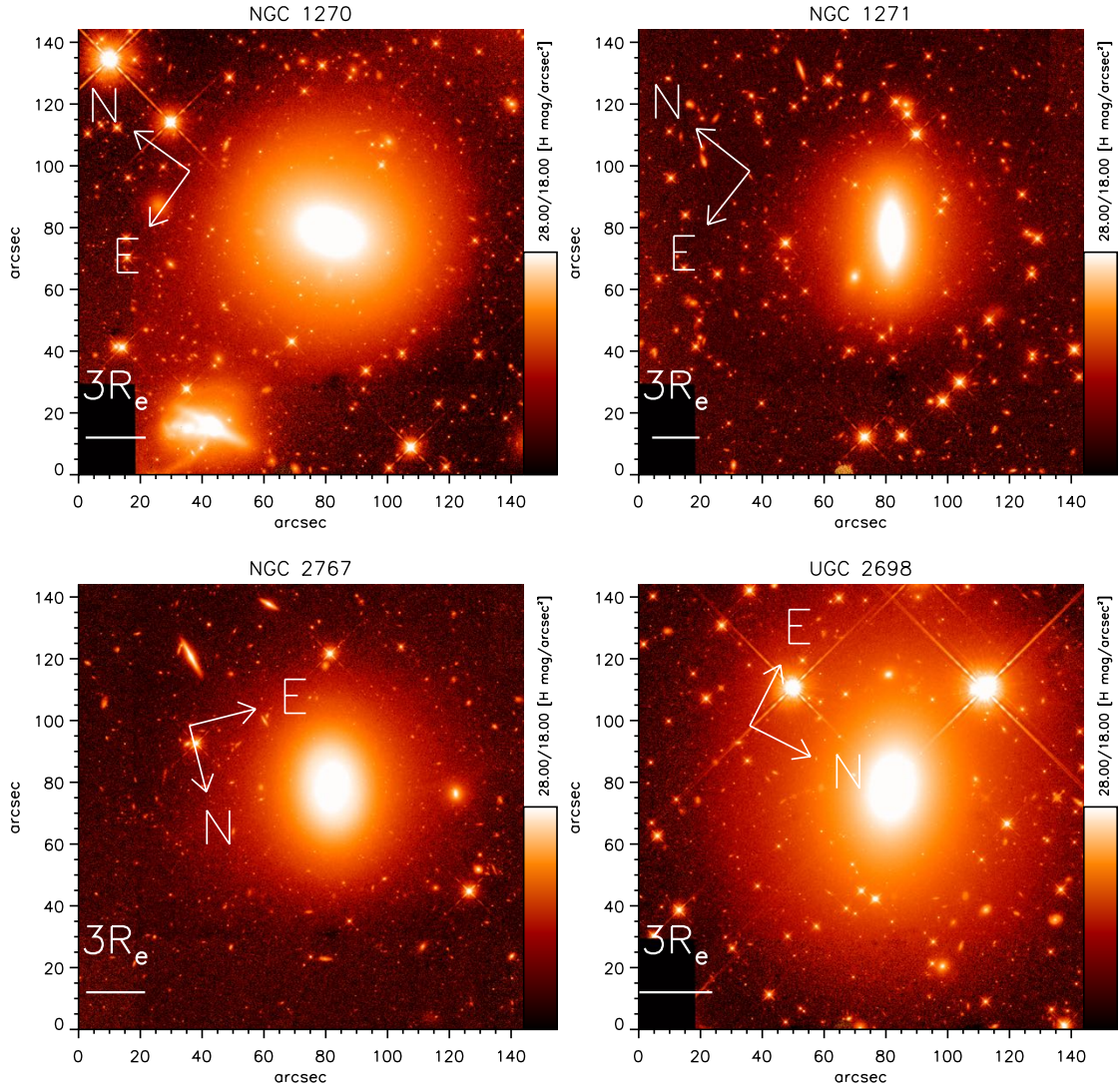


Figure 4.1: *HST* H-band image of NGC1270 (top left), NGC1271 (top right), NGC 2767 (bottom left) and UGC2698 (bottom right), with a FOV of $\sim 150 \square''$ (i.e. $\geq 50 \text{ kpc}^2$, given the distance of the closest object) and a final scale of $0.06''/\text{pixel}$.

and details of MRK 1216 and NGC 1281 respectively, and to van den Bosch et al. [2012] for an illustration of the *HST* V-band (F550M) image of NGC 1277, based on archival *HST* data (GO: 10546; PI: Fabian). The specifics of NGC 1277's photometric data are also summarised in Sec. 2.2.1 and 2.2.3.

In Sec. 4.4, we derive accurate stellar masses via our orbit-based dynamical models, which in turn need a stellar mass model within which a representative library of orbits can be calculated. The stellar mass model is obtained from a deprojection of the SB distribution for a given set of viewing angles. We parameterise the SB with a set of multiple, two-dimensional Gaussian functions [MGE; Monnet et al., 1992; Emsellem et al., 1994]. The Gaussians do not form a complete set and the deprojection is not unique, even for an axisymmetric stellar system [Rybicki, 1987], but the SB distributions of realistic multi-component galaxies are commonly well reproduced [Cappellari, 2002] and the MGE method is convenient, since the convolution with the point-spread function (PSF) as well as the deprojection can

Table 4.1: Photometric and kinematic properties of the sample of seven compact, elliptical, high central velocity dispersion galaxies, based on their *HST* WFC3 F160W imaging, except for NGC 1277 (see footnote). The columns depict the galaxy (1), the effective major axis radius from a single Sérsic fit (2), the flattening of the single Sérsic (3), the effective radius measured from a circular aperture that contains half of the light (4), the effective radius measured along the major axis of a best-fitting ellipse that contains half of the light, which we adopt as their true sizes throughout this chapter (5), the total apparent magnitude (extinction corrected) in *H*-band (except for NGC 1277) (6), the adopted distance (7), the *PPAK* velocity dispersion within the best-fitting ellipse that contains half of the light (8) the *PPAK* central velocity dispersion (9), the specific stellar angular momentum within one (10) and three effective radii (11).

Galaxy	$R_{e,ser}$ [kpc]	b/a	$R_{e,circ}$ [kpc]	$R_{e,ell}$ [kpc]	mag [H,Vega]	D [Mpc]	σ_e km s^{-1}	σ_c km s^{-1}	$\lambda_{r,1}$	$\lambda_{r,3}$
MRK 1216	2.8 ± 0.1	0.58	2.3 ± 0.1	3.0 ± 0.1	10.49	94 ± 2	288	338 ± 8	0.36	0.40
NGC 1270	2.1 ± 0.1	0.68	1.8 ± 0.1	2.2 ± 0.1	9.88	69 ± 1	321	400 ± 7	0.30	0.37
NGC 1271	2.1 ± 0.1	0.43	1.4 ± 0.1	2.0 ± 0.1	10.78	80 ± 2	244	303 ± 6	0.50	0.63
NGC 1277 ¹	1.3 ± 0.1	0.52	1.2 ± 0.1	1.3 ± 0.1	13.80	71 ± 1	293	355 ± 7	0.26	0.51
NGC 1281	2.0 ± 0.1	0.63	1.4 ± 0.1	1.7 ± 0.1	10.57	60 ± 1	220	268 ± 5	0.37	0.53
NGC 2767	2.8 ± 0.1	0.75	1.9 ± 0.1	2.3 ± 0.1	10.62	74 ± 1	200	240 ± 7	0.36	0.57
UGC 2698	4.1 ± 0.1	0.73	2.9 ± 0.1	3.4 ± 0.1	10.05	89 ± 2	294	365 ± 5	0.19	0.23

be handled analytically. The details of the MGE of the four galaxies displayed in Fig. 4.1 are given in Appendix A. All MGEs have been obtained with a constant position angle (PA) and a common centre for each galaxy. This is a necessary though insufficient condition for the deprojection in an oblate axisymmetric case, but reasonable given their small variation in the PA ($\Delta\text{PA} \leq 2^\circ$) and the acceptable reproduction of their SB profiles. Only NGC 2767 shows a variation of $\Delta\text{PA} \sim 16^\circ$ between the isophotes at 1 and 3 R_e (see Fig. 4.4), which might indicate that this galaxy is slightly triaxial.

The PSF has been adopted from the Cosmic Assembly Near-Infrared Deep Extragalactic Survey CANDELS [van der Wel et al., 2012], and has a size of $0.17''$ FWHM (see Sec. 2.2.1).

We further analyse the photometry by carrying out single Sérsic fits, but derive accurate sizes also in terms of the major axis radius of a best-fitting circular and elliptical isophote that contains half of the light. We adopt the elliptical effective radii as their true sizes throughout this chapter unless mentioned otherwise. As pointed out by Hopkins et al. [2010a] and illustrated in Cappellari et al. [2013a], this measurement of the effective radius is less prone to inclination effects. Given the high quality of our photometric observations, and in contrast to observations of the red, massive galaxy population at higher redshifts [e.g. van der Wel et al., 2014], we can follow the low SB wings down to more than 10 magnitudes below the central SB (see e.g. Fig. 2.1), and therefore do not need to rely on parameterised fits to derive accurate sizes. We present the photometric and kinematic properties of our sample in Table 4.1.

Note, that the effective radii, based on the measurement of a best-fitting ellipse that contains half of the light rather than a circular aperture, are systematically larger. Consequently, the effective velocity dispersions (see Sec. 4.2.2 and Tab. 4.1), as well as the stellar and dark matter fractions within the effective radius, change slightly with respect to the values reported in Chap. 2 and 3 for MRK 1216, NGC 1277 and NGC 1281. This, however, does not affect our conclusions in those sections regarding their classifications as fast rotators and e.g. their status as outliers in the black hole scaling relations.

4.2.2 PPAK Kinematics

The stellar kinematics of MRK1216, NGC1277 and NGC1281 have been presented in Sec 2.3 and 3.2.2. Here, we cover the data acquisition and reduction pipeline for the remaining galaxies, yielding the wide-field IFU kinematics which in turn are used for the kinematic analysis and as input for our orbit-based dynamical models. For a more detailed overview, though, we refer the reader to Sec. 2.3.1, where the kinematic pipeline is discussed in depth.

Spectroscopic data of the four remaining galaxies have been obtained at the 3.5m telescope at Calar Alto, with the *Potsdam Multi Aperture Spectrograph* [PMAS; Roth et al., 2005] and the *PPAK* fiber module [Verheijen et al., 2004; Kelz et al., 2006], making use of the low-resolution V500 grating. In brief, this setup has a resolving power of $R = 850$ at 5400 \AA and a spectral resolution of 6.3 \AA FWHM across the nominal spectral range of $3745 - 7500 \text{ \AA}$, which corresponds to an instrumental velocity dispersion of $\sigma = 150 \text{ km s}^{-1}$. The *PPAK* module consists of 382 fibres, each with a diameter of $2.7''$ projected on the sky. These are bundled to a hexagonal shape, covering a FOV of $\sim 1.3'$. A total of 36 fibres, bundled in pairs of 6 fibres each, are located $72''$ away from the centre with the purpose to sample the sky. The remaining fibres are science fibres and provide a 100 per cent covering factor when used with a 3-point dither pattern.

The wide-field IFU observations were taken over several nights between October 8 - 10, 2012, and January 4 - 6, 2013. For each galaxy, we obtained data with a total of 6 hours on-source integration, split into 3 complete runs with 3 dither-pointings of 2400 seconds each, divided into two frames à 1200 seconds.

The data reduction follows a dedicated pipeline which has been developed for the Calar Alto Legacy Integral Field Spectroscopy Area Survey (CALIFA) [Sánchez et al., 2012; Husemann et al., 2013] and includes bias subtraction, flat-fielding, cosmic ray cleaning, extraction of spectra, wavelength calibration, sky subtraction, and flux calibration using spectrophotometric standard stars. Spectra from the 3 pointings were then combined and resampled into a data cube with a $1''$ sampling, using a distance-weighted interpolation algorithm, followed by a correction for differential atmospheric refraction.

The 2D line-of-sight velocity distribution (LOSVD) has been extracted by fitting the spatially binned spectra [Cappellari & Copin, 2003] with a non-negative, linear combination of stellar templates [Cappellari & Emsellem, 2004], in the vignetting and sensitivity limited useful spectral range of $4200 - 7000 \text{ \AA}$. This spectral range covers important absorption features, including $H\beta$, Mgb and $Fe\ 5015$. The spectra were binned to reach a minimum S/N of 40 in each Voronoi zone, which is deemed sufficient to reliably extract the higher order Gauss-Hermite moments h_3 and h_4 [van der Marel & Franx, 1993; Bender et al., 1994], excluding spaxels with a $S/N < 4$. For the stellar templates, we make use of the Indo-U.S. stellar library [Valdes et al., 2004] with a nominal spectral resolution of 1.2 \AA FWHM. Sky and emission line features have been generously masked and Legendre polynomials of 15th order have been used for the fitting process.

¹The values reported here for NGC1277 correspond to the measurements based on archival *HST* F550M photometry. For the *H*-band size estimate, we make use of the 2MASS photometry. This yields a major axis radius of the half light isophote of 1.4 kpc.

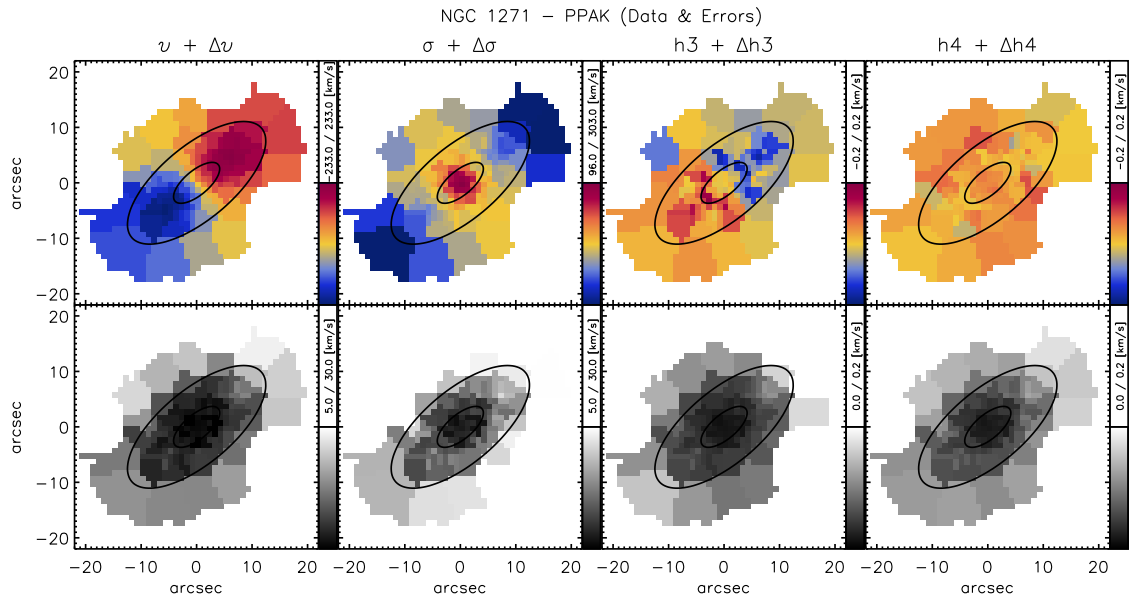
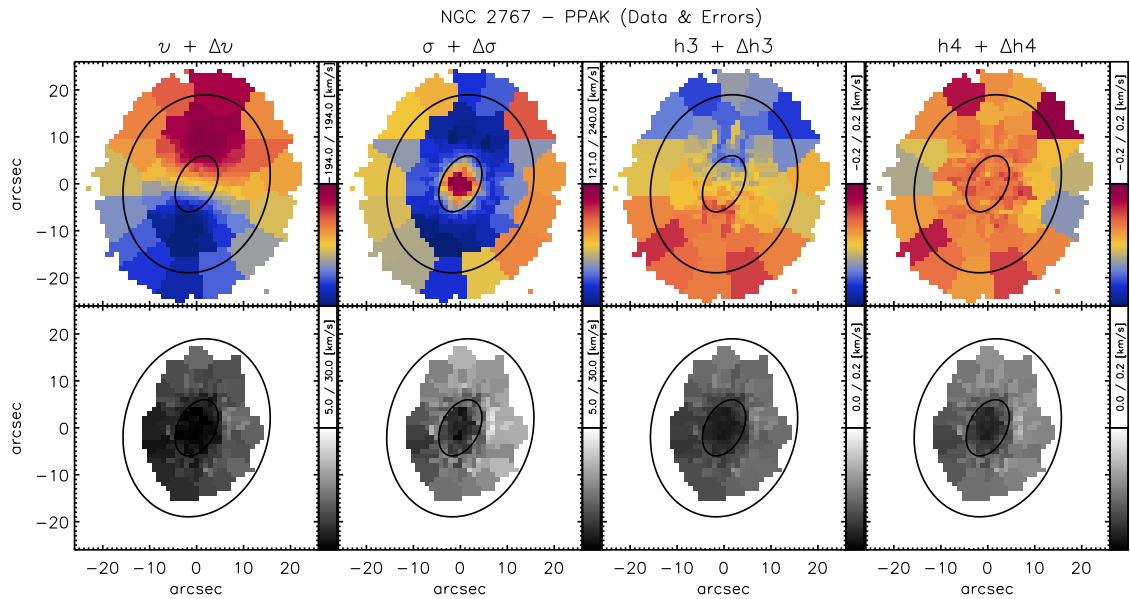


Figure 4.3: Same as Fig. 4.2, but for NGC1271.

Figure 4.4: Same as Fig. 4.2, but for NGC2767. The measurements of the LOSVD at $\sim 3R_e$ and beyond are unreliable, and larger errors (white shaded regions) have been assigned to exclude those measurements from the fitting process in the dynamical models.

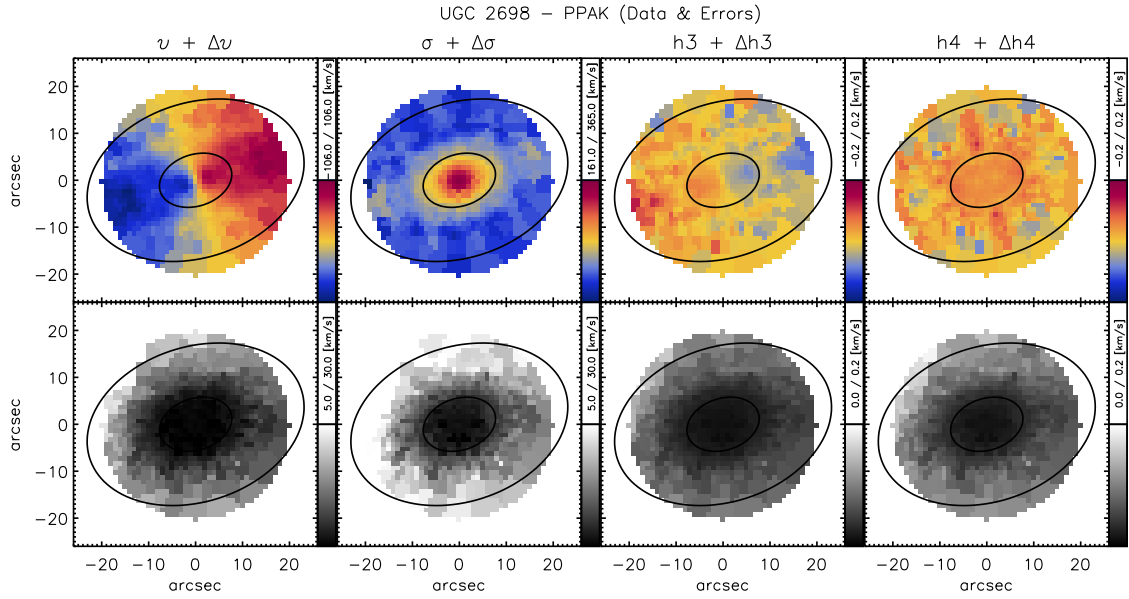


Figure 4.5: Same as Fig. 4.2, but for UGC 2698.

bins well beyond $3 R_e$, as those bins cannot accumulate enough spaxels to reach the target S/N. This is most pronounced in NGC 2767 where the velocity dispersion measurements beyond $3 R_e$ show a sudden, unphysical increase. A look at the spectral fits in these regions reveals that these measurements are unreliable, fitting noise rather than signal, which is why we chose to assign those bins particularly large errors and hence effectively excluded them from the fitting process in our orbit-based dynamical models in Sec. 4.4.

4.3 Classification

4.3.1 Fundamental Plane

Provided with the wealth of information in the deep photometric and spectroscopic data, we can already analyse important structural and kinematic properties of our sample. For this purpose, we derive their locations in the fundamental plane of ETGs, based on their central velocity dispersions in the *PPAK* data cube (σ_c), their effective radii ($R_{e,ell}$) in the *HST* imaging and their average surface brightnesses within this region (I_e). Fig. 4.6 illustrates the edge-on projection of the *H*-band FP, derived from an orthogonal error-weighted fit of more than 300 nearby elliptical galaxies, and the corresponding 1σ scatter in this relation [Zibetti et al., 2002]. Overplotted are the measurements of the seven compact galaxies in our sample. Given the lack of *HST* *H*-band photometry for NGC 1277, we made use of archival 2MASS imaging to derive the respective photometric parameters.

All galaxies are clear outliers in the FP, except NGC 1271, which is consistent with the 1σ lower bound of this relation. We emphasise, though, that the velocity dispersion σ_c in the *PPAK* data cube can only be considered as a conservative estimate of the central velocity dispersion in these objects. In fact, measurements of the central velocity dispersion of NGC 1271 based on adaptive optics (AO) assisted

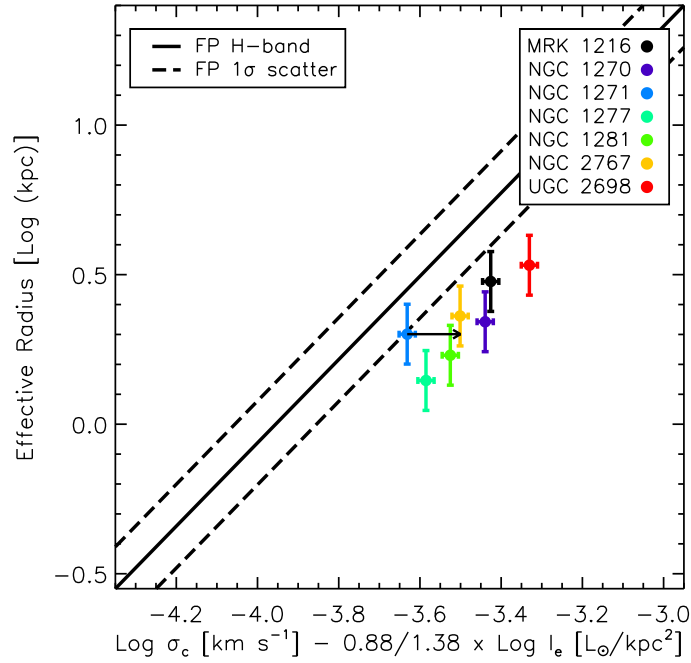


Figure 4.6: The edge-on projection of the H -band fundamental plane of elliptical galaxies in the local universe, with the associated 1σ scatter [Zibetti et al., 2002]. Over-plotted are the locations of the seven compact galaxies in our sample. For NGC 1277 we rely on 2MASS H -band photometry, in contrast to the HST H -band observations for the rest of the sample. All galaxies are clear outliers in the FP, except NGC 1271. The velocity dispersion in the $PPAK$ data cube, however, is underestimated and NGC 1271 becomes an outlier, too, when the central velocity dispersion of the AO assisted observations are taken into account (black arrow).

observations with Gemini North’s Near-Infrared Integral Field Spectrograph (*NIFS*) reveal a velocity dispersion of 396 km s^{-1} in the centre [Walsh et al., 2015]. Even if the central velocity dispersion in the *NIFS* data cube is super-resolved with respect to the literature long-slit observations employed in the Zibetti et al. [2002] sample, it partially compensates for the sudden rise in the velocity dispersion profile of these objects which is clearly not resolved in the *PPAK* data cube with its $2.7''$ fibre and a PSF of $\sim 3''$ FWHM. This indicates that indeed all compact ellipticals in our sample are inconsistent with the FP of ETGs in the local neighbourhood, and merely consistent with the associated 3σ scatter.

Assuming that our size measurement is a fair estimate of the intrinsic effective radius in these objects, the associated errors become comparatively small and are solely related to the adopted cosmology and corresponding uncertainty in distance, with a mean of $\Delta \log(R_e) = 0.1$. Likewise, the measurement errors of the central velocity dispersion are in the range of $5 - 10 \text{ km s}^{-1}$, yielding errors of the order of $\Delta(\log(\sigma_c) - (0.88/1.38) \times \log(I_e)) = 0.02$.

4.3.2 Specific Stellar Angular Momentum

Efforts to classify the population of ETGs have so far used the shape of their isophotes [Kormendy & Bender, 1996], the deficit/excess of light in their centre [Kormendy et al., 2009] or the amount of ordered versus random motion [Davies et al., 1983]. But while the latter attempt has been shown to be susceptible to projection effects [Burkert & Naab, 2005], the former tries to encompass the dynamical

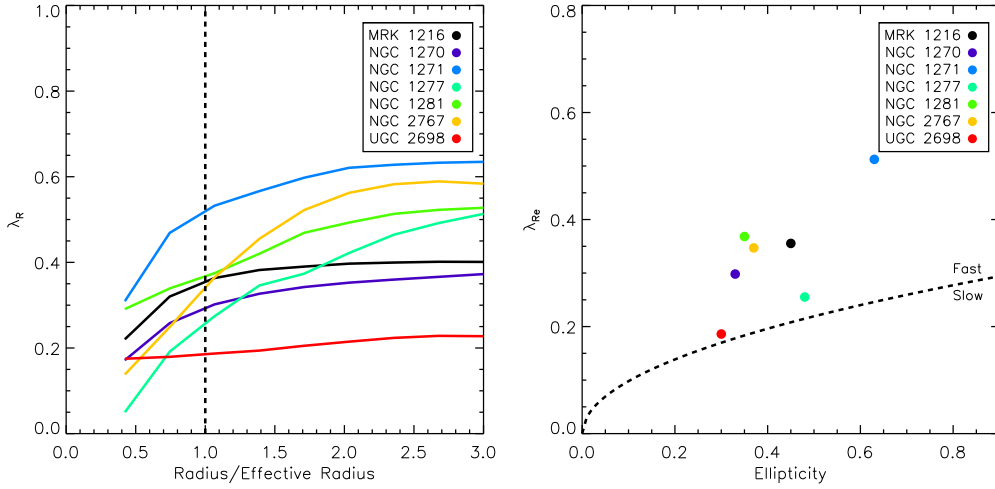


Figure 4.7: *Left*: Measurement of the specific stellar angular momentum of the compact, elliptical, high central velocity dispersion galaxies as a function of radius. The angular momentum profiles are already flattened for all galaxies, except NGC 1277, beyond 2 effective radii. The profile of UGC 2698, the largest galaxy in the sample, has been extrapolated to the last radial point, since the IFU observations cover the stellar kinematics only out to $\sim 2.5 R_e$. *Right*: The specific stellar angular momentum at $1R_e$, as a function of apparent ellipticity. All galaxies are fast rotators, as is expected from their fast and regular rotation.

state and evolutionary history of galaxies purely based on information encoded in their photometric profiles. The SAURON and ATLAS^{3D} surveys have conducted a large photometric and spectroscopic analysis of a volume-limited, representative sample of ellipticals in the nearby universe. They define a new parameter λ_r - the specific stellar angular momentum - which is effective in discriminating between the two classes of slow- and fast-rotating ETGs [Emsellem et al., 2007]. This classification scheme does not only provide a good estimate of the amount of large-scale rotation in galaxies, but more importantly is tightly related to the orbital configuration of galaxies [Cappellari et al., 2007] and hence is assumed to encompass information regarding their mass assembly history [e.g. Burkert et al., 2008; Naab et al., 2014].

We show the specific angular momentum profile in Fig. 4.7 (left panel) and the angular momentum at $1 R_e$ as a function apparent ellipticity (right panel), based solely on the *PPAK* kinematics extracted in Sec. 2.3.1, 3.2.2 and 4.2.2. All galaxies exhibit a flattened angular momentum profile already beyond $\sim 2 R_e$, except NGC 1277, which is the fastest rotating galaxy in our sample with a peak velocity of 276 km s^{-1} and a flat extended velocity curve out to several effective radii (Sec. 2.3.4).

The criterion for discriminating between fast- and slow rotators has been slightly revised, based on the larger ATLAS^{3D} sample. According to Emsellem et al. [2011], fast rotators have a specific angular momentum of $\lambda_r \geq 0.31 \times \sqrt{\epsilon}$ within one effective radius, where ϵ is the apparent ellipticity and 0.31 a factor to account for the trend of increasing λ_r with ϵ , with one and the same λ_r value being able to yield vastly different anisotropies. Nevertheless, even UGC 2698, the slowest rotating galaxy in our sample, remains a fast rotator. The apparent ellipticity is $\epsilon = 0.3$ within $1 R_e$ and remarkably close to the axis ratio of the single Sérsic fit (Table 4.1). The threshold thus increases to $\lambda_r = 0.17$, which, however, is still below the measurement of the specific angular momentum in UGC 2698 ($\lambda_r = 0.19$) at $1 R_e$.

4.4 Dynamical Analysis

4.4.1 Schwarzschild Models

We construct orbit-based dynamical models for the four remaining galaxies in our sample. For this purpose, we make use of the triaxial Schwarzschild code of van den Bosch et al. [2008]. The working principles and details of this method are discussed in Sec. 2.4. Here, we confine ourselves to a brief description of the main steps.

We start with a mass model within which a representative orbit library is being calculated. The orbit library comprises 7533 orbits, sampled along 31 logarithmically spaced equipotential shells between $0.003''$ and $150''$, where every shell is used as a starting point in each of the radial and angular directions. The orbits are numerically integrated and their projected and deprojected quantities are stored and PSF convolved for comparison with the data. We find a non-negative, linear superposition of the orbits that best matches the observational constraints, i.e. the binned LOSVD and the intrinsic and aperture masses provided by the MGE, in a χ^2 -sense. The contributions of the individual gravitational constituents are then varied, and the aforementioned steps are reiterated, in order to assess the confidence intervals of the parameters of interest.

Our mass model includes the stellar mass component M_* , which is the deprojected, intrinsic luminosity density times the constant stellar mass-to-light ratio Υ_* , the mass of a supermassive black hole M_\bullet and a dark matter component which is parameterised by a spherically symmetric NFW profile [Navarro et al., 1996, 1997] with concentration c_{DM} and total virial mass $M_{DM} = M_{200}$. The concentration is usually not well constrained by our orbit-based dynamical models (see e.g. Sec. 2.4.2.1, 2.4.2.2 and 3.3.2), which is why we fix the concentration to $c_{DM} = 10$. Our models thus probe the three parameter space in $\Upsilon_* \in [0.5, 3]$, $\log(M_\bullet/M_\odot) \in [7, 10.4]$ and $\log(M_{DM}/M_*) \in [-2, 5]$. For all galaxies, we assume an oblate axisymmetric shape. Given their fast and regular rotation around the short axis, the anti-correlation between v and h_3 , the lack of a position angle twist (except for NGC 2767, but see below) and results from shape inversions of a large sample of fast-rotating galaxies [Weijmans et al., 2014], axial symmetry is a well justified assumption of the intrinsic shape of these objects. Note, though, that NGC 2767 might still be slightly triaxial. Despite its rapid rotation around the short axis with $\sim 200 \text{ km s}^{-1}$, the misalignment of the PA between the inner and outermost isophotes is non-negligible (Sec. 4.2.1 and Fig. 4.4) and more extensive tests will have to be carried out to recover the intrinsic shape of this object.

Under the assumption of oblate axial symmetry, the inclination i is the only viewing parameter that is needed to pin down the intrinsic shape of the galaxy. Usually, the inclination is treated as another fitting parameter in the models, but difficult to constrain unless distinct kinematic features exist [Krajnovi et al., 2005; van den Bosch & van de Ven, 2009]. Models with different inclinations can therefore reproduce the LOSVD equally well, but the inclination will only have a significant role for the recovery of the stellar mass-to-light ratio (and hence also for the recovery of the black hole and dark halo mass) if highly face-on projections are allowed [Cappellari et al., 2006], which however is not the case for our sample. The minimum angle for the deprojection in an axisymmetric case is given by the flattest Gaussian in the respective MGE. For all galaxies, except NGC 1271, the possible range of inclinations is

at least $60^\circ \leq i \leq 90^\circ$, with 90° being edge-on. Slightly more face-on projections of 54° are allowed for UGC2698. On the other hand, the flattest Gaussian in NGC1271 has a flattening of $q = b/a = 0.23$, which implies that this galaxy has to be viewed more edge-on than 76° . We therefore adopt an inclination of 65° for NGC1270, NGC2767 and UGC2698, and an inclination of 85° in the case of NGC1271.

4.4.2 Modelling Results

We present our modelling results in Fig. 4.8 - 4.11, where we show contours of $\Delta\chi^2$ for the dark halo parameter $\log(M_{200}/M_\odot)$ and the H -band stellar mass-to-light ratio Υ_* in solar units. The red dot marks the location of the best-fitting model and the vertical line denotes $\Delta\chi^2 = 9$, i.e. the statistical 3σ model fitting uncertainty for the respective parameter. We do not show the parameter constraints for the black hole mass, since the *PPAK* kinematics are not able to resolve the black hole sphere of influence. We briefly highlight here the interesting aspects of the modelling results for each galaxy:

- NGC1270

We obtain a stellar mass-to-light ratio of $\Upsilon_* = 2.2_{-0.7}^{+0.1}$, i.e. a total stellar mass of $\log(M_*) = 11.5_{-0.2}^{+0.0}$, and a dark halo mass of $\log(M_{200}/M_\star) = 0_{-2}^{+2}$. The models yield a dark halo contribution of only 1_{-1}^{+10} per cent to the total mass budget within one effective radius. More importantly though, and despite kinematic data out to $\sim 5 R_e$, they cannot provide unambiguous evidence for the presence of a dark halo and rather prefer a best-fitting stellar M/L which is higher than expected from its uniformly old stellar population with an age > 10 Gyr, super solar metallicity and under the assumption of a single power-law Salpeter stellar initial mass function (IMF) [Ferré-Mateu et al., 2015]. The best-fitting model has a black hole mass of $\log(M_\bullet/M_\odot) = 9.2$, but the black hole is virtually unconstrained at the lower end of the parameter space and we therefore only refer to the upper limit of $\log(M_\bullet/M_\odot) = 10.3$.

- NGC1271

NGC1271 is a slightly smaller but more flattened and also more rapidly rotating galaxy (Tab. 4.1). Here again, our wide-field IFU data cover the kinematics out to at least $3 R_e$ (or 6 kpc respectively), but our orbit-based dynamical models cannot discriminate between models with and without a dark halo. The models yield parameter constraints of $\log(M_{200}/M_\star) = -1.5_{-0.5}^{+2.5}$ and $\log(M_\bullet/M_\odot) = 8.9_{-8.9}^{+0.8}$. Similarly, the best-fitting stellar M/L is high, $\Upsilon_* = 2.0_{-0.3}^{+0.1}$, and the lower bound is merely consistent with predictions of stellar population synthesis (SPS) fits with a single power-law Salpeter IMF and an old stellar population (> 10 Gyr) [Ferré-Mateu et al., 2015]. The dark halo contribution to the total mass budget within one effective radius is 0_{-0}^{+6} per cent.

- NGC2767

Interestingly, the models can break the degeneracy between the stellar M/L and the dark halo in NGC2767. Although the spatial extent of the LOSVD has been constrained to less than $3 R_e$ (i.e. less than 6 kpc), given the poor spectral fits for the recovery of the outer velocity moments (Sec. 4.2.2), we are able to rule out models devoid of dark matter. The dark halo parameter is tightly constrained to $\log(M_{200}/M_\star) = 1.0_{-0.5}^{+0.5}$ and the dark halo contribution to the total mass

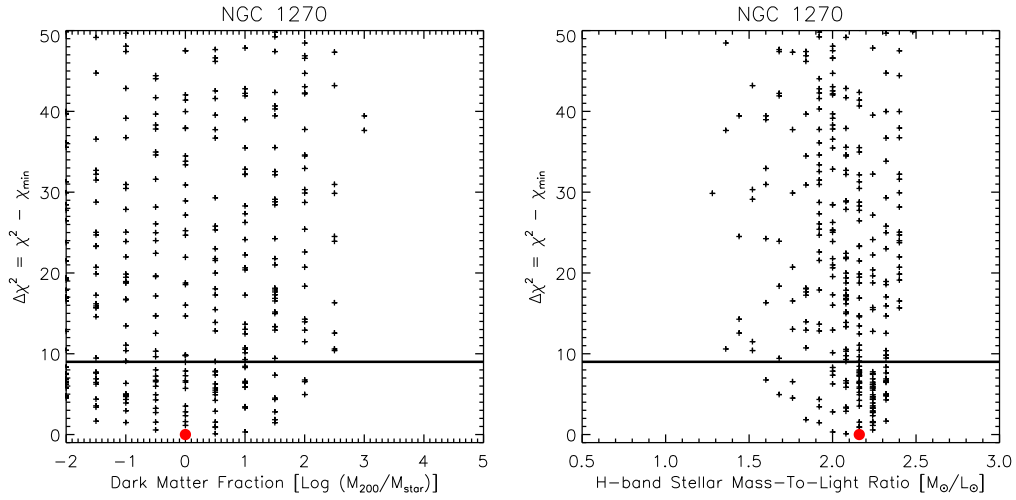


Figure 4.8: Orbit-based dynamical models of NGC1270. The figures show the fitting parameters $\log(M_{DM}/M_{\odot})$ and Υ_{*} as a function of $\Delta\chi^2$. The best-fitting parameters are marked by a red dot. The horizontal line denotes a $\Delta\chi^2$ of 9, which corresponds to a 3σ statistical uncertainty for one degree of freedom.

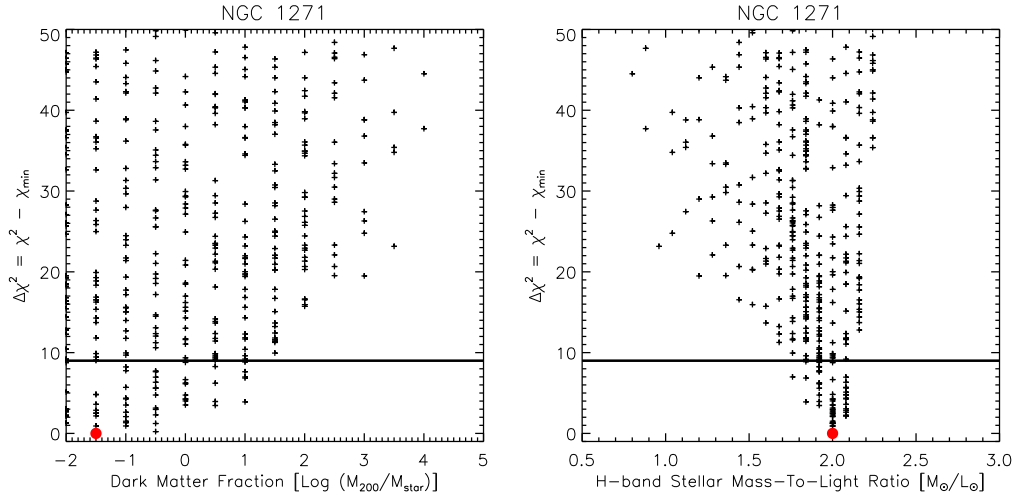


Figure 4.9: Same as Fig. 4.8, but for NGC1271.

budget is 6_{-4}^{+3} per cent within one effective radius. Yet, the stellar M/L with $\Upsilon_{*} = 2.1_{-0.3}^{+0.2}$ is still super-Salpeter and, as expected, the black hole mass is not constrained at all with $\log(M_{\bullet}/M_{\odot}) = 8.0_{-8.0}^{+1.5}$.

- UGC2698

UGC2698 is the most massive galaxy in our sample, with $\Upsilon_{*} = 1.5_{-0.2}^{+0.5}$ and hence a total stellar mass of $\log(M_{*}) = 11.5_{-0.1}^{+0.1}$. It's also the largest galaxy, being more than twice as large as NGC 1270 or NGC1271 and also considerably larger than NGC2767. Our kinematic data reaches out to $\sim 2.5 R_e$, but still covers a similar extent in an absolute scale as the other galaxies. However, despite this coverage of the stellar kinematics, we can neither constrain the black hole nor the dark halo.

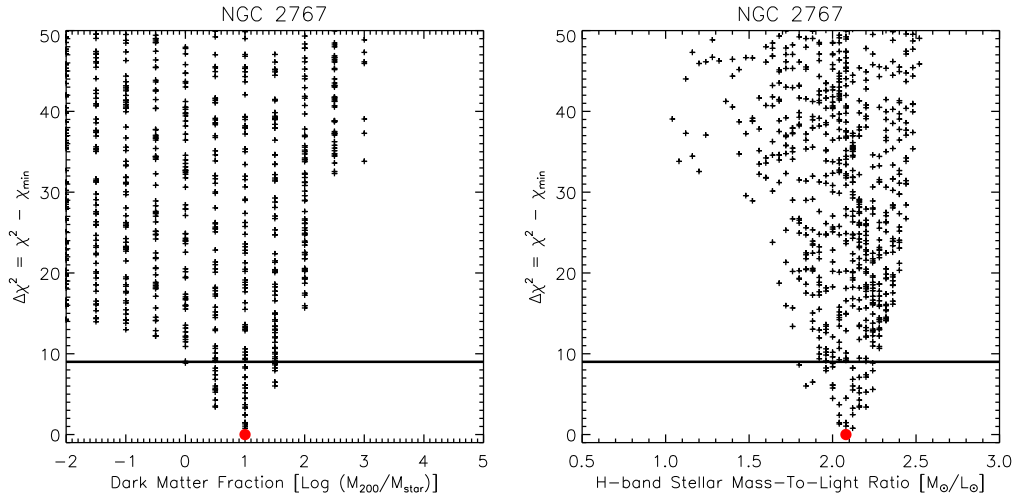


Figure 4.10: Same as Fig. 4.8, but for NGC 2767.

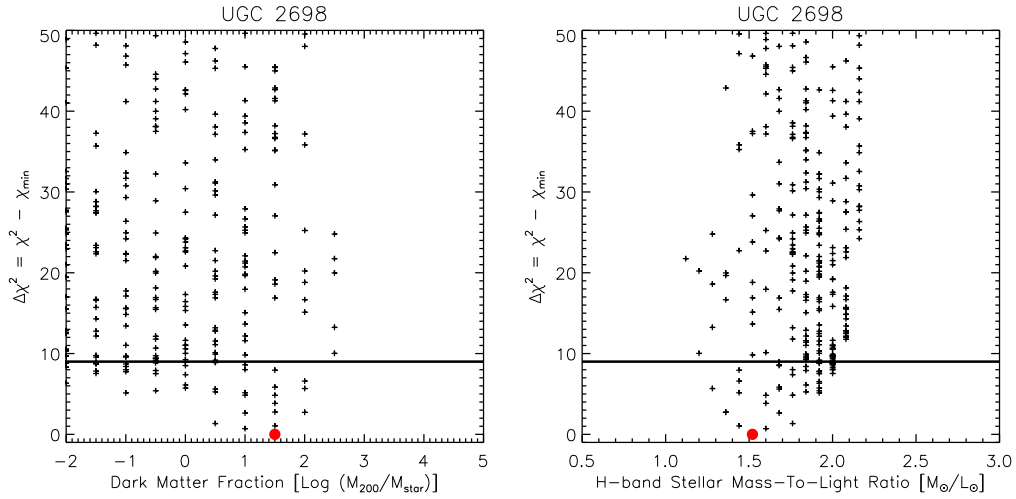


Figure 4.11: Same as Fig. 4.8, but for UGC 2698.

We obtain an upper limit of the black hole mass of $\log(M_{\bullet}/M_{\odot}) \leq 10.3$ and an upper limit of the dark halo of $\log(M_{200}/M_{\star}) \leq 2.0$, with a dark matter contribution of 12^{+13}_{-12} per cent to the total mass budget within one effective radius.

4.5 Discussion

4.5.1 The Mass-Size Relation

Massive ETGs have grown significantly in stellar mass and half-light size since redshift $z = 2$ [e.g. Trujillo et al., 2006; Franx et al., 2008; van Dokkum et al., 2008, 2010; van der Wel et al., 2008, 2014]. The progenitors of today's massive galaxy population are also found to be more flattened and disk-like [e.g. Toft et al., 2005; Trujillo et al., 2006; van der Wel et al., 2011; Chang et al., 2013], very compact [e.g.

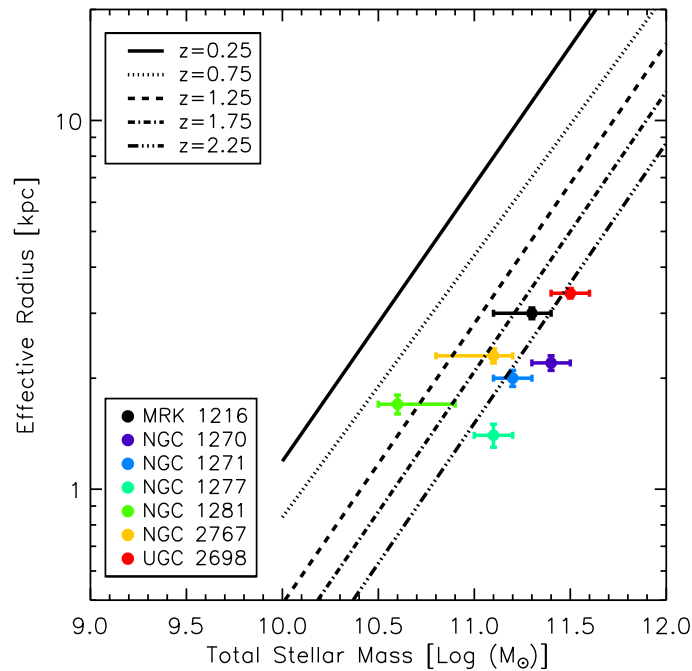


Figure 4.12: Mass-size relation of early-type galaxies at different redshifts, derived from the CANDELS/3D-HST survey [van der Wel et al., 2014]. The sizes of the compact galaxies have been derived from the deep *HST* *H*-band images, based on a best-fitting elliptical isophote that contains half of the light. The total stellar masses have been derived from our orbit-based dynamical models. All galaxies are outliers from the local mass-size relation.

Zirm et al., 2007; Buitrago et al., 2008; van Dokkum et al., 2008; Szomoru et al., 2010] with little to no ongoing star formation [e.g. Williams et al., 2009] and exceptional central velocity dispersion peaks [e.g. van Dokkum et al., 2009].

Descendants of the compact, red, massive galaxy population are rare in the local universe [Trujillo et al., 2009; Taylor et al., 2010; Saulder et al., 2015]. The agreement, however, between the photometric and kinematic properties of our compact, elliptical, high central velocity dispersion sample and the red nuggets is remarkable and suggests that these objects are actually passively evolved analogues. Corroborating evidence has been provided by the investigation of their dynamical structures in Sec. 2.5.1 and 2.5.4, indicating that these galaxies have not undergone a recent, active phase of a few major and numerous minor mergers, which is assumed to be the main driver of the mass and size evolution of massive ellipticals since $z = 2$ [e.g. Naab et al., 2009; Oser et al., 2010; Lackner et al., 2012; Oser et al., 2012; Hilz et al., 2012, 2013; Bédorf & Portegies Zwart, 2013]. Furthermore, the stellar populations of NGC 1277 [Trujillo et al., 2014] and NGC 1281 (Sec. 3.4.2.3) have been investigated in detail and stellar age estimates and star formation histories have also been derived for the remaining galaxies in our sample (except for UGC 2698) in Ferré-Mateu et al. [2015], showing that they are comprised of a uniformly old stellar population (> 10 Gyr) without a recent (i.e. < 10 Gyr) star formation event that might have been triggered by e.g. gas-rich "wet" mergers.

All galaxies in our sample are outliers in the FP of local ETGs (Fig. 4.6). By means of our orbit-based dynamical models, though, we have derived accurate total stellar masses and are now in a position to locate their position in the mass-size relation, both of which are viewed as basic parameters in theories

of galaxy formation and evolution. Fig. 4.12 exhibits our measurements of the seven compact galaxies in our sample, with the associated uncertainties in mass and size. Accurate measurements of stellar masses and sizes of a significant sample of galaxies through cosmic time have been obtained as part of the 3D-HST+CANDELS survey [van der Wel et al., 2014], where ETGs are distinguished as non actively forming stars through colour-colour selections. We overplot their mass-size relations in the redshift range $0 \leq z \leq 3$, obtained assuming a log-normal distribution with scatter $\sigma(\log R_e)$, intercept A and slope α , and the relation being parameterised by $R_e[\text{kpc}] = A (M_* / 5 \times 10^{10} M_\odot)^\alpha$. The figure convincingly demonstrates the affiliation of our compact objects with the sample at $z \geq 2$. All galaxies are significant outliers from the mass-size relation at $z = 0$ and a Kolmogorov-Smirnov test rules out the null hypothesis that the compact galaxies have been drawn from the same parent distribution of local ETGs, at better than 95 per cent confidence. NGC1281 is the only outlier from our sample, being consistent with the mass-size relation at $z \sim 1$. However, this is based on fits with a NFW profile which, as has been shown in Chap. 3, is not a fair assumption of the dark halo of NGC1281, yielding unreasonably low stellar mass-to-light ratios and consequently a low total stellar mass. Adopting a stellar M/L of 1.7, as suggested by the stellar population analysis, implies an increase of the stellar mass by a factor of ~ 2.5 and would move NGC1281 on top of the mass-size relation at $z = 2.25$.

It is worth noting that an overestimation of the stellar masses, due to an overestimation of the stellar M/L in the dynamical models, will affect our conclusions only marginally. Decreasing the stellar M/L by a factor of two, roughly consistent with expectations of their old stellar populations based on a Chabrier IMF, moves the galaxies towards the stellar mass-size relation at $1.25 \leq z \leq 1.75$, but the sample still remains a significant outlier from the present-day mass-size relation.

4.5.2 The Stellar Mass Surface Density

By virtue of the deep, high spatial resolution *HST* photometry, we can obtain accurate surface density profiles over a wide spatial range, out to regions where the SB is already more than 10 magnitudes below the central SB (see e.g. Fig. 2.1). Having constrained the stellar M/L dynamically (Sec. 2.4, 3.3 and 4.4), we can now turn the surface brightness profiles into surface mass density profiles, which are shown in Fig. 4.13.

The central stellar mass surface densities of the red, massive galaxy population at high redshift (light grey) are 2-3 times higher than for local ETGs (dark grey) [Bezanson et al., 2009; Szomoru et al., 2012, 2013]. This is a result of their remarkable compactness. The high stellar surface mass densities are assumed to be triggered by gas-rich major mergers at even higher redshift [Naab et al., 2007; Wuyts et al., 2010] of presumably even more compact, starbursting submillimeter galaxies (SMGs) [Toft et al., 2014] or by dynamical instabilities which feed galaxies with cold gas from the intergalactic medium (IMG) [Birnboim & Dekel, 2003; Kereš et al., 2005; Dekel et al., 2009; Dekel & Burkert, 2014].

The central stellar surface mass densities of our sample are in agreement with the values provided by the bulk of galaxies at high redshift. Considering that our compact galaxies are outliers in the local mass-size relationship (Fig. 4.12), this is expected. Self-evidently, the stellar mass surface density profiles are also steeper, with a sharp fall-off at large radii. Only two galaxies in our sample, MRK 1216 and UGC 2698, show a more extended profile, consistent with the density profiles of local ETGs in the remote regions.

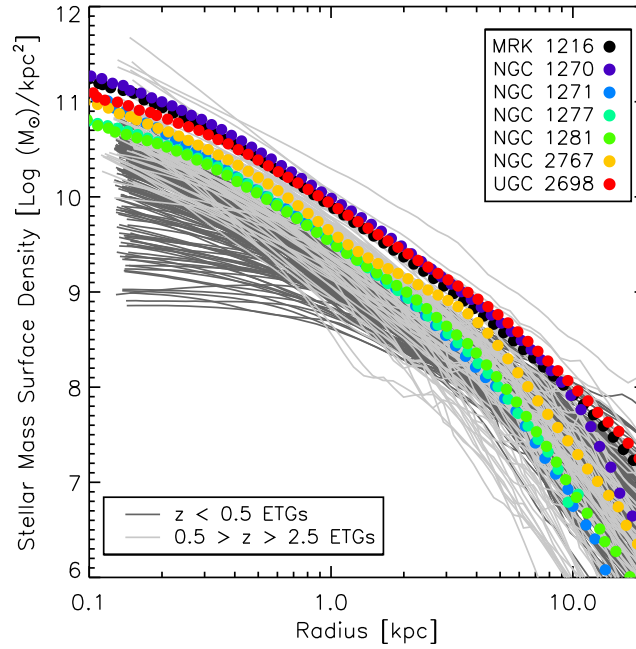


Figure 4.13: Stellar mass surface density profiles of massive ETGs at high (light grey) and low (dark grey) redshifts [Szomoru et al., 2013]. Overplotted are the stellar mass surface density profiles of the compact, elliptical galaxies, based on deep *HST* photometry and our orbit-based dynamical models of the wide-field IFU stellar kinematics. The stellar mass surface density profiles of our sample are consistent with those at high redshift.

These two objects, however, are at the same time two of the largest and most massive galaxies in our sample, with sizes and masses more than twice as large as for instance NGC 1277. This indicates that they have already grown considerably with respect to the rest of the sample and might have already entered the path of becoming a regular ETG, also promoted by our orbital analysis of MRK 1216 which closely follows the relationship between β_z and δ of a sample of nearby ETGs (see Sec.2.5.1.3). Moreover, the extended surface mass density profiles of MRK 1216 and UGC 2698 suggest that the growth in mass (and consequently in size) has been deposited in the outer parts. Indeed, integrating the density profile shows that the mass content in the outer regions has grown disproportionately, with ~ 40 per cent of the total stellar mass already being located beyond 5 kpc in MRK 1216 and UGC 2698, in contrast to e.g. NGC 1277 which only harbours 10 per cent of the total stellar mass at these radii.

The small sizes, density profiles and the disproportional growth in mass in the remote regions of the largest galaxies in our sample, endorse the theory in which our galaxies are expected to form the cores of massive, present-day ellipticals. As suggested by the density profiles, the evolution into massive spheroids is closely related to the accretion of low surface density material in the outer parts, while at the same time decreasing the central densities. Applying simple virial arguments, Bezanson et al. [2009] show that major merging cannot reduce the central surface mass densities, whereas minor merging may account for the decrease. Note though that subsequent minor merging events are expected to increase the scatter in ETG scaling relations [Nipoti et al., 2012], which is not observed. Additional processes such as adiabatic expansion due to significant mass loss during AGN feedback [Fan et al., 2008, 2010] could thus have a non-negligible role.

4.5.3 Stellar And Dynamical Masses

Deriving accurate masses is crucial to test the structural evolution of galaxies at high redshift. Yet, mass measurements of galaxies at $z \sim 2$ are sparse. Literature studies have so far focused on measurements of the central velocity dispersion [Kriek et al., 2009; van Dokkum et al., 2009; van de Sande et al., 2011; Toft et al., 2012; Bezanson et al., 2013; van de Sande et al., 2013] and employed virial mass estimators [Cappellari et al., 2006] to derive their dynamical masses, while relying on SPS modelling to assess their stellar mass content.

The high quality of our photometric and spectroscopic observations allow us to construct orbit-based dynamical models (Sec. 4.4), which are not affected by the systematic uncertainties and limitations of the aforementioned methods. We can therefore place tight constraints on the stellar and dynamical masses of our compact galaxy sample and - considering the striking similarities to the sample of red, massive and passive galaxies at $z = 2$ - gain insight into the structural properties of the red nuggets.

We present the ratio of stellar to dynamical mass within the effective radius in Fig. 4.14 (left). The mean ratio of low and high redshift galaxies are given by the horizontal lines [van de Sande et al., 2013]. The figure confirms and extends the notion that our compact galaxies are dominated by stellar mass within the effective radius. Only NGC1281 is an outlier. While this galaxy is dark matter dominated at large radii, the contribution of the stellar mass to the total mass budget is most likely underestimated within $1 R_e$ (Chap. 3). When excluding NGC1281 from the sample, we obtain a mean ratio of stellar to dynamical mass of 0.86 (highlighted by the black star) which is very close to the mean value of 0.9 inferred for massive, quiescent galaxies at $z \sim 2$.

The trend of an increasing stellar contribution with increasing redshift has been ascribed to the decrease in the effective radius and hence to the lower dark matter contribution within this small spatial extent, which is less steep than the stellar mass profile in these highly compact objects. Cosmological, hydrodynamical simulations confirm this picture in which the dark matter fraction decreases within the effective radius due to both the decrease in the effective radius and the increase in the baryonic density as a result of highly dissipational mergers which lead to compact stellar remnants [Hopkins et al., 2009b]. We emphasise, however, that the stellar and dynamical masses of the high redshift sample have been obtained under two assumptions, i) the adoption of Chabrier IMF [Chabrier, 2003], and ii) a virial mass estimate where non-homology is accounted by a Sérsic dependent virial factor [Cappellari et al., 2006]. To qualitatively assess the robustness of the latter approach, we compare the virial mass estimate of our galaxies within the effective radius to our dynamical mass estimate within the same spatial extent in Fig. 4.14 (right). The virial mass estimator systematically overpredicts the dynamical masses and hence the stellar mass fraction within the effective radius. On the other hand, variations of the IMF are not taken into account and the assumption of a Chabrier IMF might underpredict the stellar mass fraction. Our dynamical models present a major advance in this respect as they do not rely on the assumption of a stellar IMF, even though we assume that a NFW profile is a reasonable assumption of the dark halo profile in these galaxies. In fact, the range of stellar M/L in our models is systematically higher than expected of an old stellar population with a Chabrier or canonical Kroupa IMF ($\Upsilon_{\star} \sim 1.3$) [Kroupa, 2001], being able to even exclude them in individual cases. The range of stellar M/L is also partially exceeding expectations of a Salpeter IMF ($\Upsilon_{\star} \sim 1.7$) and, as a consequence, we cannot exclude the possibility of a more bottom-heavy IMF in these objects. Note, though, that the observed trend of

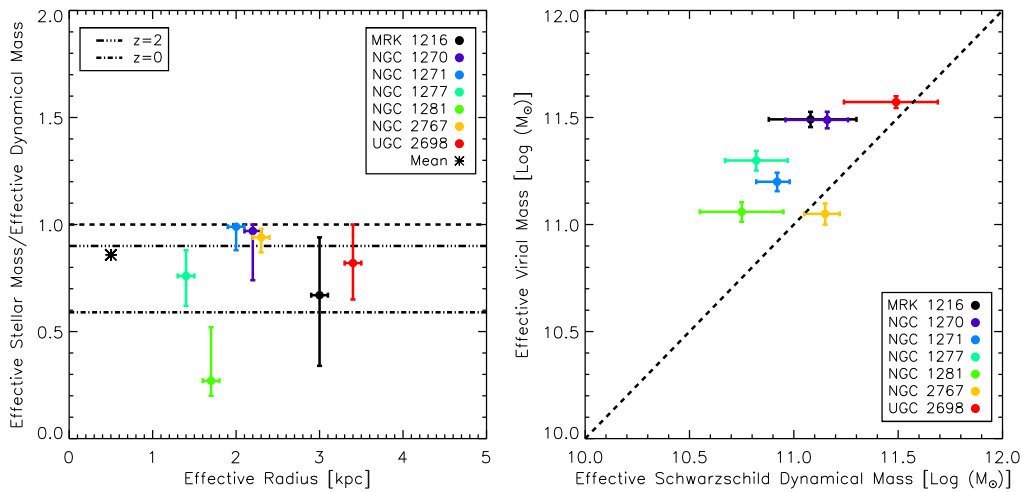


Figure 4.14: *Left*: Stellar mass vs. dynamical mass for the compact, elliptical, high central velocity dispersion galaxies, measured by our orbit-based dynamical models within the elliptical isophote that contains half of the light. The horizontal lines depict the ratio for local and high-redshift galaxies [van de Sande et al., 2013], and the star indicates the mean value of our sample. The stellar mass fraction to the total mass budget is much higher for the compact galaxies. *Right*: Comparison of the dynamical mass within the effective radius from the virial mass estimator and our orbit-based dynamical models. The locally calibrated virial mass estimator systematically overpredicts the dynamical mass.

a more bottom-heavy IMF is not necessarily an artefact of the stellar populations of our sample and thus of high redshift galaxies, but could simply be related to the claimed systematic variation of the IMF with increasing stellar velocity dispersion [Auger et al., 2010b; Treu et al., 2010; van Dokkum & Conroy, 2010, 2012; Conroy & van Dokkum, 2012; Cappellari et al., 2012; Spiniello et al., 2012; Dutton et al., 2012, 2013; Tortora et al., 2013].

We conclude that caution should be exercised when interpreting the evolution of the luminous and dark matter fractions within one effective radius; our findings indicate that the locally calibrated virial mass estimator is not a good proxy for the dynamical mass in these compact stellar systems, while the adoption of Chabrier IMF might underestimate their stellar masses. The stellar M/L of our orbit-based dynamical models are not exceeding a Salpeter-like IMF by much. Thus, the stellar populations of high and low redshift galaxies should not be fundamentally different, if our galaxies are indeed passively evolved analogues of high redshift red nuggets. Nevertheless, the decrease in size might not be the sole responsible for the decrease in the dark matter fraction and the increase in the stellar mass fraction. A contribution due to the systematic variation of the stellar IMF can affect the measurements, in particular for galaxies with high stellar velocity dispersions (as is the case for our sample and the red nuggets at redshift $z = 2$) where the variation of the IMF is expected to be the strongest.

4.5.4 The Total Mass Density Slope

Rather than dissecting the contribution of luminous and dark matter to the total mass budget, we can investigate the total mass profile, which is assumed to hold additional clues regarding the formation and evolution of galaxies. To this end, we illustrate the total mass density profiles as a function of radius and the total mass density slopes in Fig. 4.15. The slopes have been derived by a least squares,

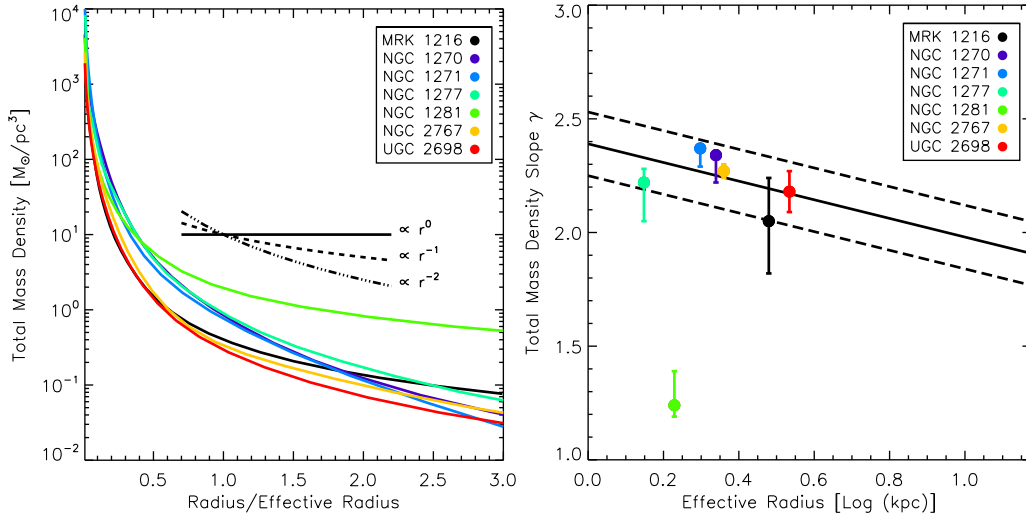


Figure 4.15: *Left*: The total mass density profiles of our compact, elliptical, high central velocity dispersion galaxies from our best-fitting dynamical models. The density profiles fall off steeper than the isothermal density profile, with $\rho \propto r^{-2}$. *Right*: The total mass density slopes as a function of radius. The density slopes are consistent with the relation between slope and effective radius of a large sample of SLOAN lens galaxies [Auger et al., 2010a], except again for NGC1281.

power-law fit to the total mass density profile of the best-fitting dynamical model, while the associated errors mark the maximum and minimum deviation from this slope of all models within the statistical 3σ uncertainty. The black lines on the left hand side depict density profiles with slopes of $\gamma = 0$, 1 and $\gamma = 2$, which corresponds to an isothermal density profile that is commonly observed for ETGs from both lensing and dynamics [e.g. Koopmans et al., 2006, 2009; Auger et al., 2010a; Barnabè et al., 2009, 2011]. Even though our galaxies follow the relation between slope and effective radius of a large sample of SLOAN Lens ETGs [Auger et al., 2010a], the total mass density slopes are higher than the isothermal profile and reflect the dominance of the baryonic density profiles within a few effective radii in these objects.

Interestingly, Remus et al. [2013] analysed a suite of total mass density slopes of galaxies formed via three different channels, i) binary mergers of (un-)equal mass spiral galaxies with varying gas fractions, ii) hydrodynamical, cosmological simulations within which spheroidal galaxies undergo several minor and major merging events and iii) hydrodynamical, cosmological simulations of central cluster galaxies. While their merging scenarios have been carried out in order to understand the formation mechanisms of local ellipticals, important information can be extracted concerning the formation of our compact sample and hence also the formation of the red, massive galaxy population at $z = 2$. Binary mergers with (and without) a significant fraction of gas fail in reproducing the total mass density slopes of typical Coma ellipticals [Thomas et al., 2007], but they are able to recover the high density slopes of our galaxies with $\gamma \geq 2.1$. The cosmological simulations are also capable to recover a large range of density slopes, depending on the dissipational nature of the merging events and the amount of stars that are formed in-situ, which increase the central baryonic density profile. However, given the subsequent accretion of smaller satellite galaxies, they also grow substantially in size and are generally larger than our galaxies and the red nuggets at high redshift (see Remus et al. 2013, Fig.8).

While the purely wet binary mergers are an unlikely formation scenario for present-day ellipticals [see also Burkert et al., 2008], they are qualitatively a plausible formation mechanism of compact, massive ellipticals at high redshift and thus for our sample. Actually, gas-rich disk mergers are more frequent at high redshift, and necessary to explain the old stellar populations and short formation timescales of the massive red galaxy population at $z = 2$. SMGs at $3 \leq z \leq 6$, for instance, are poster childs of gas-rich, compact and disky systems. Toft et al. [2014] show that their comoving number densities match the number densities of the red nuggets if their duty cycles are of the order of 42 Myr. The gas-rich major mergers would also be able to explain the positive deviation of the density slopes from $\gamma = 2.1$ of our compact galaxies. Given its dissipative nature, gas condenses in the centre of galaxies and gives rise to starburst events which increase the central stellar mass densities and hence the total mass density slope in these regions while keeping the galaxies compact.

4.6 Summary

In this chapter, we have carried out a detailed investigation of the photometric and kinematic properties of a sample of seven compact, elliptical, high central velocity dispersion galaxies in the nearby universe (≤ 100 Mpc). Based on deep *HST* imaging and wide-field IFU kinematics, we have shown that all seven objects are outliers in the FP of local ETGs. They are also disky fast rotators with sizes and central stellar velocity dispersions that resemble the population of massive and passive galaxies at $z = 2$.

We carried out orbit-based dynamical models to constrain their stellar mass-to-light ratios, black hole mass and dark matter content. The IFU kinematics cannot resolve the black hole sphere of influence and we can thus only present upper limits of the black hole mass. Despite kinematic data out to several effective radii, dark matter is only evident in three galaxies. The stellar mass-to-light ratios are in agreement with SPS models of a Salpeter IMF. However, we see a trend towards super-Salpeter values and can exclude stellar M/L based on an old stellar population of a single power-law Chabrier or Kroupa IMF in some individual cases.

By means of our orbit-based dynamical models, we could tightly constrain their stellar masses. We showed that our sample is highly inconsistent with the mass-size relation of ETGs in the present-day universe. They are, however, consistent with the mass-size relation of the red massive galaxy population at $z = 2$, a.k.a. red nuggets, which are assumed to be the progenitors of today's most massive ellipticals. Moreover, their central stellar mass surface densities are higher by a factor of 2-3 in comparison to the stellar mass surface densities of local, massive ETGs, and in agreement with the stellar mass surface densities of the red nuggets. The body of evidence presented throughout this chapter thus strongly indicates, that we have found passively evolved analogues of the red nuggets which provide an unprecedented view of the structural and dynamical properties of high redshift galaxies.

Adopting an NFW profile, we also constrained their dark halo contribution to the total mass budget. Within one effective radius, these compact, elliptical, high central velocity dispersion galaxies are highly dominated by the stellar component with a stellar-to-dynamical mass ratio of 0.82. Literature studies of stellar-to-dynamical mass ratios of $z = 2$ galaxies have been obtained via virial arguments and SPS models adopting a Chabrier IMF. Assuming that our galaxies are indeed passively evolved analogues of the massive galaxy population at $z = 2$, we show that the virial mass estimator systematically

overpredicts the dynamical masses while a Chabrier IMF might underpredict the total stellar mass. The high stellar-to-dynamical mass ratios are clearly driven by the low amount of dark matter due to the decrease in effective radius. Our dynamical results suggest that the stellar populations of high and low redshift galaxies are not fundamentally different. However, the systematic variation of the IMF with increasing stellar velocity dispersion has to be taken into account, given that our sample and the sample of massive and passive ETG at $z = 2$ exhibit exceptional stellar velocity dispersions.

The total mass density slopes of our sample exceed the density slope of an isothermal profile. This is driven by the high stellar mass concentration and the negligible contribution of dark matter within a few effective radii. Our total mass density slopes, while taking into account their compact sizes, are in agreement with the density slopes of gas-rich disk merger simulations. This provides corroborating evidence that the progenitors of our galaxies (and consequently the red nuggets) must have been disky, compact and gas rich systems, consistent with the population of submillimeter galaxies at even higher redshift ($z \geq 3$), which provide the necessary ages and star formation timescales.

Summary & Outlook

5.1 Summary

The overall objective of this thesis was to investigate in detail a sample of compact, elliptical galaxies with exceptional central velocity dispersions in the nearby universe. Motivation for this research came from the discovery of an over-massive supermassive black hole (SMBH) in one of our objects, and their striking resemblance to the compact, massive and quiescent galaxy population at $z = 2$. Moreover, our interest in these object has been fuelled by the challenge to provide unambiguous dynamical evidence for the presence of dark matter in the population of ETGs in general. To this end, we obtained deep high spatial resolution imaging with the *HST*, low spectral resolution long-slit spectroscopic observations with the *HET* and wide-field medium spectral resolution spectroscopic observations with the *PPAK* IFU, to analyse their photometric and kinematic properties. By means of state-of-the-art orbit-based dynamical models, we constrained the contribution of stars, a supermassive black hole and dark matter to the total mass budget and gained further insight into their stellar and dark structure and their formation and evolution histories.

Here, we briefly recapitulate our findings:

- **Chapter 2**

We started with the analysis of two compact galaxies, namely MRK 1216 and NGC 12177, to present our data and to outline our methods. We performed a Sérsic decomposition of the deep *HST* photometry to understand their stellar structure. Improved fits to their surface brightness profiles indicate that these objects are comprised of multiple low-Sérsic components, which are generally associated with highly rotating structures, consistent with the observed fast and regular rotation around the short axis. The line-of-sight velocity distributions (LOSVD) have been extracted, which show exceptional central velocity dispersion peaks that hint at high mass concentrations.

We carried out orbit-based dynamical models to obtain estimates of the stellar and dark masses in both objects. We confirm the presence of an over-massive black hole in NGC 1277 and present an upper limit of the black hole mass in MRK 1216. The stellar mass-to-light ratios are in agreement

with stellar population synthesis (SPS) models of a canonical Kroupa or Salpeter stellar initial mass function (IMF), but also consistent with a systematic variation of the IMF with increasing stellar velocity dispersion. Despite kinematics which cover the LOSVD out to ~ 3 effective radii in both objects, we can only present a dark halo detection in MRK 1216. The orbit-based dynamical models also allowed us to inspect their orbital structures, which hold additional information regarding their mass assembly history. Both galaxies show multiple, rotating substructures which could be linked to the multi-Sérsic decompositions, showing that simple single or two Sérsic fits are not a good proxy of the stellar structure even if they provide acceptable fits to the photometry.

Moreover, only MRK 1216 follows the tight relation of a large sample of nearby ETGs between the anisotropy in the meridional plane (β_z) and the global anisotropy parameter (δ), whereas NGC 1277 is a strong outlier. This might indicate that MRK 1216 has already entered a path of becoming a regular ETG. However, taking into account their uniformly old stellar populations, rapid rotation, the absence of tidal signatures and their relatively small sizes, a recent active merging history can be ruled out, nonetheless. Numerous minor mergers, the favoured evolution scenario for the mass and size growth of massive, quiescent galaxies since $z = 2$, would have increased their sizes dramatically. On the other hand, remnants of simulated dry major (disk-)mergers yield boxy, slow-rotating galaxies. Wet (disk-)mergers are successful in recovering many of their physical parameters, but they are expected to evolve galaxies towards the FP and the non-negligible gas fractions should result in more recent star formation activity, which however is at odds with the stellar populations and star formation histories of these two compact objects unless they have happened more than 10 Gyr ago. Thus all formation scenarios which aim to recover the population of today's ETGs cannot reproduce the physical properties of the two compact objects in this work.

Interestingly, their properties are in excellent agreement with the properties of the red nuggets at redshift $z = 2$. These are thought to be the progenitors of today's massive ellipticals and might have formed through wet mergers of highly disky, compact, starbursting galaxies at even higher redshift.

• Chapter 3

We expanded our knowledge of compact, elliptical, high central velocity dispersion galaxies by studying NGC 1281, a highly peculiar object in the Perseus cluster. Here again, the photometric and kinematic data show that this galaxy is very compact and rapidly rotating around the short axis, while the dispersion peak indicates a high concentration of mass in the centre. Our orbit-based dynamical models provided clear evidence for the presence of a massive dark halo, as simple mass-follows-light models failed to recover the observational constraints. The dark halo in NGC 1281 constitutes ~ 90 per cent of the total dynamical mass within 5 effective radii (~ 7 kpc), irrespective of the exact halo parameterisation. However, parameterising the dark halo with a spherical NFW profile yields unreasonably low stellar M/L and an over-massive SMBH. Moreover, extrapolating the dark profile results in a cluster-sized dark halo, which would have to be embedded in the Perseus cluster halo itself. The discrepancy stems from the necessity to recover the high, enclosed total dynamical mass within a very small spatial extent. This is accomplished by a massive dark halo. The massive dark halo, in turn, propagates into the central regions (i.e. $\leq 1 R_e$), where the tension between the stellar and dark mass is relieved by lowering the stellar

M/L. The stellar M/L, however, gives rise to an over-massive SMBH in the very centre, to recover the central dynamical mass. At the same time, the line-strength analysis of NGC 1281 suggests that this galaxy is comprised of an old stellar population, with a radial decrease in metallicity and α -abundance. The uniformly old stellar population cannot be reconciled with the low stellar M/L in the dynamical models, providing corroborating evidence for the fact that NFW is not a fair approximation of the dark halo profile in this object. As an aside, we traced the gravity-sensitive features in the spectra and showed that the systematic variation of the IMF is only a local property, which is confined to the high stellar velocity dispersion region.

- **Chapter 4**

We concluded with an investigation of the structural and dynamical properties of a total of seven compact, elliptical, high central velocity dispersion galaxies. By virtue of the high quality photometric and spectroscopic observations, we have derived accurate measurements of their sizes, total apparent magnitudes, surface brightness profiles, LOSVDs, central and effective velocity dispersions and specific stellar angular momenta as a function of radius. All galaxies in our sample are compact and fast-rotating, with an exceptional central velocity dispersion peak.

They are outliers in the Fundamental Plane of nearby ETGs. We constrained their stellar M/L, black hole mass and dark matter content with orbit-based dynamical models. We show that all compact galaxies in our sample are strong outliers from the mass-size relation in the present-day universe, but consistent with the mass-size relation of massive, quiescent galaxies at $z \simeq 2$. The stellar mass surface density profiles are also in line with the surface density profiles of galaxies at high redshift. In combination with literature studies of their stellar populations and star formation histories, this is indicative that we have found a sample of objects which are passively evolved analogues of the red nuggets, available for a study in unprecedented detail which is currently not possible for their counterparts at high redshift.

The surface mass density profiles of two of the largest galaxies in our sample illustrate that they have already grown via disproportional mass accumulation in the remote regions (i.e. ≥ 5 kpc), as is expected if they grow via minor mergers. As a matter of fact, our two largest galaxies have already quadrupled their mass content beyond 5 kpc and grown in size by a factor of ~ 3 , while their total masses have only increased by a factor of 2 with respect to the most compact and least massive objects in our sample. We also showed that all objects are dominated by stellar mass within the effective radius. The mean dark matter fraction within one effective radius in our sample, and consequently for the population of massive and quiescent galaxies at $z \simeq 2$, is much lower than observed for typical ETGs in the local universe. This is owed to the decrease of effective radius as a function of lookback time and hence the decrease of the volume which encompasses dark matter. In addition, we demonstrated that studies of galaxies at high redshift, based on virial arguments as well as on assumptions of the IMF, are prone to many systematic uncertainties.

The stellar mass-to-light ratios in our dynamical models are systematically higher than anticipated from an old stellar population with a Chabrier IMF. While they don't exceed expectations based on a single power-law Salpeter IMF by much, suggesting that the IMF of high and low redshift galaxies are not fundamentally different, they support recent claims in which the IMF varies systematically as a function of stellar velocity dispersion.

Finally, we investigated the total mass density slopes which are steeper than expected from an isothermal density profile. This is in agreement with the relation between slope and effective radius of a large sample of ETGs which act as gravitational lenses. Simulations show that compact outliers from the isothermal density profile are well reproduced by wet major mergers of compact (disk-)galaxies. This suggests that our sample, and analogue the population of massive, quiescent ETGs at $z = 2$, might have formed through merging of gas-rich galaxies at even higher redshifts, with the submillimeter galaxy population at $z \geq 2$ as likely progenitors.

5.2 Outlook

This thesis, in combination with efforts based on the extensive data set which has been acquired as part of this work, has accomplished a detailed examination of the passively evolved progenitors of today's most massive galaxies. As a result, we gained insight into their structural properties, constrained their stellar and dark content as well as their black hole masses. However, a significant number of topics haven't been addressed yet which will provide the basis for future work and enable us to obtain a more complete picture regarding i) the evolution of massive ETGs, ii) the link between their luminous and dark matter and iii) the role of their supermassive black hole.

The over-massive SMBHs in our compact galaxy sample have provided a first (purely dynamical) glimpse at the black hole demographics at higher redshifts. Our findings indicate that the growth of a black hole is not inevitably connected to the growth of a bulge component. At the same time, they question the method of decomposing galaxies photometrically into a simple bulge and disk component, as the photometric decompositions are at odds with the orbital structures in the dynamical models. An interesting aspect for future investigations would thus be the assessment of the robustness of the photometric and orbital analysis, which could be tested in recovering simulated galaxies from their mock kinematic and photometric data. This will also shed light on e.g. the validity of the black hole mass-bulge luminosity relation, where bulge luminosities have generally been obtained by means of a two-component decomposition [but see Läscher et al., 2014a,b].

A more fundamental concern regarding the black hole scaling relations arises from the poor sampling in the host galaxy parameter space. The current crop of black hole masses is concentrated at $\log(M_{\bullet}/M_{\odot}) = 8$ [Gültekin et al., 2009; McConnell & Ma, 2013; Kormendy & Ho, 2013]. Likewise, the sample occupies a tight locus in the size-luminosity relation [van den Bosch et al., 2015]. Increasing the diversity in the sample of dynamically constrained black hole masses is therefore crucial to discriminate between various black hole formation channels. For instance, massive elliptical galaxies are more abundant in dense environment than spiral galaxies [Dressler, 1980]. The black holes in early-type galaxies (ETGs) are therefore expected to grow significantly during mergers, whereas the growth of SMBHs in late-type galaxies (LTGs) is presumably dominated by the presence of non-axisymmetric features (e.g. bars) which can efficiently funnel cold material towards the centre [e.g. Shlosman et al., 1989; Hopkins & Quataert, 2010]. In fact, the dominance of different black hole growth mechanisms seems to be reflected in the different quantifications of the black hole scaling relations, with an intercept that differs by a factor of two if early- and late-type galaxies are fitted individually [McConnell & Ma, 2013] and a larger intrinsic scatter at the low mass end [Greene et al., 2010b]. Current efforts to increase the sample size, but

more importantly the sample diversity, are therefore under way. We have proposed to dynamically measure the black hole mass in 28 galaxies in the northern hemisphere, with *GEMINI/NIFS*. The sample covers a wide range of host galaxy properties and the black hole spheres of influence are expected to be resolved, based on their distance and central velocity dispersion measurements in the Hobby-Eberly Telescope Massive Galaxy Survey (HETMGs). Hereby, we aim to obtain a more complete census of local SMBHs and a better understanding of the role of the black hole in the evolution of galaxies.

We have shown for three out of seven galaxies in our sample that they are embedded in a dark halo. In one out of these three galaxies, the difference between the model kinematics with and without a dark halo can be clearly distinguished, whereas the difference in the two remaining galaxies is statistical in nature, even though with a confidence of more than 3σ . The difficulty in establishing the presence of dark matter in the remaining objects can be traced back to two effects, i) the compactness of their stellar mass distribution and ii) the comparatively small spatial extent of the kinematic data in an absolute sense. Given their compactness and high stellar mass densities, the mean dark halo contribution to the total mass budget within $1R_e$ is $\sim 10\%$ for our sample, and at the percentage level for the most compact objects (except NGC 1281). Our orbit-based dynamical models are thus not capable to distinguish between models with and without a dark halo, as the additional mass is easily compensated by a marginal increase in the stellar M/L. The dark matter fractions within the effective radius are well in line with expectations for the dark mass of a spherical NFW halo, assuming that the stellar-to-halo mass and mass-concentration relation holds. Accordingly, a spherical NFW halo would contribute ~ 50 per cent to the total mass budget at 8 kpc or $\sim 5 R_e$ for the most compact galaxies in our sample with stellar masses of the order of $\log(M_*/M_\odot) = 11.2^{+0.1}_{-0.1}$. Our kinematic data, however, is only at the edge of probing this region, where the dark halo is assumed to dominate the mass budget, and we thus fall short in providing unambiguous evidence for dark matter. Consequently, a larger spatial coverage in absolute terms is necessary, which could in principle be accomplished with even longer exposure times to push the remote spaxels above the S/N threshold.

In this respect, the recently commissioned *Multi Unit Spectroscopic Explorer* (*MUSE*) at the *VLT* presents an interesting alternative, even though it is located in the southern hemisphere and inappropriate for follow up observations of the galaxies presented in this paper, except for MRK 1216. The Narrow-Field Mode (NFM) of *MUSE* offers exquisite observations at a spatial resolution of $\leq 0.05''$ FWHM, that would be able to spatially resolve the kinematics close to the black hole in local, high stellar velocity dispersion galaxies. On the other hand, the Wide-Field Mode (WFM) provides a field of view (FOV) of $1' \times 1'$, at a spatial resolution of $\leq 0.4''$ FWHM, to obtain corresponding wide-field stellar kinematics that can probe the faint, dark matter dominated regions of compact galaxies (≥ 10 kpc).

The number of compact, elliptical galaxies with high central velocity dispersions is limited. We have examined seven objects in this work. Data, consisting of high spatial resolution photometric and medium resolution spectroscopic observations, are available for another eleven objects, as part of our dedicated strategy to inspect these highly interesting objects. Even though a non-negligible sample of compact, high stellar velocity dispersion galaxies have been detected in the meantime [Saulder et al., 2015], moving to higher redshifts to assess the structure and properties of galaxies through cosmic time is therefore inevitable. However, it has been demonstrated in this thesis that virial mass estimators and stellar population synthesis fits to the spectral energy distribution of high redshift galaxies are affected by systematic uncertainties. The highly sensitive *MUSE* is already capable to obtain spatially resolved

spectroscopic observations of galaxies to redshifts of, at least, $z \simeq 0.5$ [e.g. Bacon et al., 2015]. The resulting gas- and stellar kinematics in combination with deep photometric data will not only allow us to examine the mass and size evolution of massive ETGs in the last 5 Gyr, but also to inspect their dynamical state and orbital structure, which in turn hold important information regarding their growth and mass assembly history.

Multi-Gaussian Expansion

We present the Multi-Gaussian Expansion tables of the four compact, elliptical, high central velocity dispersion galaxies in Chapter 4, based on their high spatial resolution *HST* WFC3 imaging in the F160W filter. The expansions have been carried out under the well justified assumption of axisymmetry, i.e. with the same position angle for each Gaussian in the fit and a common centre.

The SB has been parameterised by multiple, two-dimensional Gaussians:

$$I_j(x', y') = I_{0,j} \exp\left(-\frac{1}{2\sigma_j'^2}\left(x'^2 + \frac{y'^2}{q_j'}\right)\right) \quad (\text{A.1})$$

where $I_{0,j}$ is the central surface brightness, σ_j' the dispersion along the projected major axis and q_j' the apparent flattening of each Gaussian component.

The total luminosity of each Gaussian is obtained as:

$$L = 2\pi I_{0,j} \sigma_j'^2 q_j' \quad (\text{A.2})$$

In an oblate axisymmetric case, i.e. intrinsic axis ratio of $b/a = 1$, the inclination i is the only free parameter to pin down the shape of the ellipsoid. The MGE, however, can only be deprojected for inclinations where:

$$\cos^2 i < q_{min}'^2 \quad (\text{A.3})$$

i.e. the minimum projected axis ratio in the MGE sets the lower inclination limit for the deprojection.

If an inclination has been chosen, the intrinsic luminosity density in cylindrical coordinates reads as:

$$\nu_j(R, z) = \frac{q_j' I_{0,j}}{\sqrt{(2\pi)\sigma_j q_j}} \exp\left(-\frac{1}{2\sigma_j'^2}\left(R^2 + \frac{z^2}{q_j'}\right)\right) \quad (\text{A.4})$$

where σ_j and q_j now denote the intrinsic dispersion and flattening.

Table A.1: Multi-Gaussian-Expansion of NGC1270's *HST* (F160W) *H*-band image, at a fixed PA of 15.79° (measured counter-clockwise with the image aligned N.-E., i.e. north is up and east is left). The columns display the number of each Gaussian, beginning with the innermost one (1), the surface density (2), the dispersion (3) and the corresponding Sérsic index (4) as well as the apparent flattening (5).

# of components	$I [L_\odot pc^{-2}]$	σ [arcsec]	n	q
1	132650.63	0.0064185	0.5	0.8222
2	110396.35	0.0168376	0.5	0.8222
3	85954.096	0.0414933	0.5	0.8222
4	9920.5893	0.0505985	0.5	0.4932
5	3298.0476	0.0632146	0.5	0.5504
6	59060.875	0.0965869	0.5	0.8222
7	23800.900	0.1856513	0.5	0.4932
8	37170.248	0.2123836	0.5	0.8222
9	4930.3207	0.2215776	0.5	0.5504
10	31960.227	0.4307827	0.5	0.4932
11	20537.720	0.4485513	0.5	0.8222
12	5809.7194	0.6049265	0.5	0.5504
13	21023.362	0.7641875	0.5	0.4932
14	9924.2282	0.9039556	0.5	0.8222
15	5891.1042	1.1583093	0.5	0.4932
16	5004.4278	1.3904290	0.5	0.5504
17	461.03988	1.6387519	0.5	0.4932
18	4200.7103	1.7415806	0.5	0.8222
19	2973.7113	2.7819705	0.5	0.5504
20	1559.1539	3.2420697	0.5	0.8222
21	1137.9496	4.9798336	0.5	0.5504
22	486.49005	5.8586783	0.5	0.8222
23	82.034219	6.7569947	0.5	0.8734
24	269.26023	8.1735058	0.5	0.5504
25	128.65376	10.255221	0.5	0.8222
26	36.916334	12.659926	0.5	0.5504
27	172.84216	13.991969	0.5	0.8734
28	28.695641	17.455523	0.5	0.8222
29	56.629717	18.794065	0.5	0.8734
30	2.0365826	19.598942	0.5	0.5504
31	5.2685361	28.983736	0.5	0.8222
32	0.8015330	47.058876	0.5	0.8222
33	0.0973425	76.200890	0.5	0.8222
34	0.0067910	133.39539	0.5	0.8222

Table A.2: Multi-Gaussian-Expansion of NGC 1271's *HST* (F160W) *H*-band image, at a fixed PA of -50.33° (measured counter-clockwise with the image aligned N.-E., i.e. north is up and east is left). The columns display the number of each Gaussian, beginning with the innermost one (1), the surface density (2), the dispersion (3) and the corresponding Sérsic index (4) as well as the apparent flattening (5).

# of components	$I [L_\odot pc^{-2}]$	σ [arcsec]	n	q
1	230496.20	0.0027964	0.5	0.7099
2	257728.75	0.0083482	0.5	0.7099
3	37821.357	0.0085383	0.5	0.3871
4	249528.15	0.0219926	0.5	0.7099
5	32818.108	0.0230908	0.5	0.3871
6	206350.03	0.0524812	0.5	0.7099
7	25704.838	0.0583863	0.5	0.3871
8	138708.32	0.1154338	0.5	0.7099
9	17971.886	0.1391011	0.5	0.3871
10	73308.817	0.2347042	0.5	0.7099
11	1106.4584	0.3053897	0.5	0.2306
12	11016.363	0.3122273	0.5	0.3871
13	127.37304	0.3466723	0.5	0.5630
14	30084.962	0.4438694	0.5	0.7099
15	5957.7905	0.6698236	0.5	0.3871
16	9398.8290	0.7880591	0.5	0.7099
17	2387.7957	1.1340874	0.5	0.2306
18	283.10339	1.2429302	0.5	0.5630
19	2198.4864	1.3257718	0.5	0.7099
20	2691.3108	1.3734856	0.5	0.3871
21	376.45613	2.1359594	0.5	0.7099
22	2833.7146	2.6606259	0.5	0.2306
23	1042.1296	2.6808934	0.5	0.3871
24	421.99088	3.0412323	0.5	0.5630
25	44.909802	3.3646646	0.5	0.7099
26	1662.8757	4.7949390	0.5	0.2306
27	339.62298	5.0444393	0.5	0.3871
28	2.5906886	5.5258174	0.5	0.7099
29	379.00630	5.8343182	0.5	0.5630
30	416.63526	7.4099059	0.5	0.2306
31	89.536758	9.1488333	0.5	0.3871
32	186.49363	9.4947538	0.5	0.5630
33	30.234870	10.695552	0.5	0.2306
34	43.743138	13.976030	0.5	0.5630
35	19.819043	15.893208	0.5	0.3871
36	3.1560776	19.791912	0.5	0.5630
37	3.6448137	26.733833	0.5	0.3871
38	0.5431667	43.834568	0.5	0.3871
39	0.0635840	71.363441	0.5	0.3871
40	0.0042027	124.74500	0.5	0.3871

Table A.3: Multi-Gaussian-Expansion of NGC 2767's *HST* (F160W) *H*-band image, at a fixed PA of 160.79° (measured counter-clockwise with the image aligned N.-E., i.e. north is up and east is left). The columns display the number of each Gaussian, beginning with the innermost one (1), the surface density (2), the dispersion (3) and the corresponding Sérsic index (4) as well as the apparent flattening (5).

# of components	$I [L_\odot pc^{-2}]$	σ [arcsec]	n	q
1	142261.74	0.0040270914	0.5	0.5078
2	111923.70	0.010818732	0.5	0.5078
3	10231.425	0.014512836	0.5	0.9697
4	80694.007	0.027046913	0.5	0.5078
5	16425.577	0.050174858	0.5	0.9697
6	53379.802	0.063659951	0.5	0.5078
7	20556.490	0.13654891	0.5	0.9697
8	31657.638	0.14301355	0.5	0.5078
9	16728.229	0.30962077	0.5	0.5078
10	19078.409	0.31209078	0.5	0.9697
11	96.765684	0.58891261	0.5	0.8976
12	12024.207	0.6186744	0.5	0.9697
13	7525.1008	0.64534992	0.5	0.5078
14	4941.8373	1.0928043	0.5	0.9697
15	2945.2114	1.2887121	0.5	0.5078
16	1251.8233	1.7701199	0.5	0.9697
17	212.08281	2.2011206	0.5	0.8976
18	993.79779	2.4714198	0.5	0.5078
19	182.11160	2.7081838	0.5	0.9697
20	10.333052	4.1408405	0.5	0.9697
21	287.07583	4.5836735	0.5	0.5078
22	255.18233	5.2089229	0.5	0.8976
23	4.1395413	7.2246799	0.5	0.6159
24	69.971297	8.2245197	0.5	0.5078
25	299.32149	8.9505949	0.5	0.6159
26	148.59086	9.4196787	0.5	0.8976
27	14.399325	14.302497	0.5	0.5078
28	37.200869	14.563405	0.5	0.8976
29	2.6924723	21.027004	0.5	0.8976
30	2.5054515	24.140549	0.5	0.5078
31	0.36469752	39.855518	0.5	0.5078
32	0.042577507	65.638718	0.5	0.5078
33	0.0029336188	116.82428	0.5	0.5078

Table A.4: Multi-Gaussian-Expansion of UGC 2698's *HST* (F160W) *H*-band image, at a fixed PA of 108.61° (measured counter-clockwise with the image aligned N.-E., i.e. north is up and east is left). The columns display the number of each Gaussian, beginning with the innermost one (1), the surface density (2), the dispersion (3) and the corresponding Sérsic index (4) as well as the apparent flattening (5).

# of components	$I [L_{\odot} pc^{-2}]$	σ [arcsec]	n	q
1	55810.516	0.0076895948	0.5	0.7116
2	67019.099	0.022569373	0.5	0.7116
3	24594.631	0.023466641	0.5	0.8130
4	69635.380	0.058516044	0.5	0.7116
5	17781.965	0.059566658	0.5	0.8130
6	606.51355	0.097973973	0.5	0.8210
7	62086.800	0.13766874	0.5	0.7116
8	11562.277	0.14219986	0.5	0.8130
9	680.90388	0.29516813	0.5	0.8210
10	44358.659	0.29694510	0.5	0.7116
11	6758.9329	0.32137993	0.5	0.8130
12	25361.368	0.58743846	0.5	0.7116
13	210.10926	0.62657946	0.5	0.5907
14	3485.2714	0.69107431	0.5	0.8130
15	666.55370	0.78152096	0.5	0.8210
16	11380.483	1.0811795	0.5	0.7116
17	1601.8227	1.4212409	0.5	0.8130
18	544.39725	1.8710355	0.5	0.8210
19	3872.9430	1.8729647	0.5	0.7116
20	453.40098	2.3259153	0.5	0.5907
21	632.28189	2.8216743	0.5	0.8130
22	984.72294	3.0745850	0.5	0.7116
23	363.26004	4.0747910	0.5	0.8210
24	183.27843	4.8415961	0.5	0.7116
25	215.41008	5.3892035	0.5	0.8130
26	538.69574	5.4710727	0.5	0.5907
27	23.416082	7.4750586	0.5	0.7116
28	194.46055	8.1753931	0.5	0.8210
29	312.35828	9.8433704	0.5	0.5907
30	63.155683	9.9492970	0.5	0.8130
31	1.3767565	12.042072	0.5	0.7116
32	78.331756	15.188533	0.5	0.5907
33	80.967136	15.317646	0.5	0.8210
34	15.513297	17.851410	0.5	0.8130
35	5.6794414	21.912840	0.5	0.5907
36	25.778210	26.985287	0.5	0.8210
37	3.2160768	31.019604	0.5	0.8130
38	6.1471613	45.168034	0.5	0.8210
39	0.56064874	52.422665	0.5	0.8130
40	1.0649699	72.552956	0.5	0.8210
41	0.081551607	86.635925	0.5	0.8130
42	0.12779005	114.01669	0.5	0.8210
43	0.0095982972	142.47255	0.5	0.8130
44	0.0073986472	186.72150	0.5	0.8210
45	0.0006708539	253.51215	0.5	0.8130

Bibliography

- Abazajian, K., Adelman-McCarthy, J. K., Agüeros, M. A., et al. 2003, *AJ*, 126, 2081
- Abel, T., Bryan, G. L., & Norman, M. L. 2000, *ApJ*, 540, 39
- . 2002, *Science*, 295, 93
- Alcock, C., Allsman, R. A., Axelrod, T. S., et al. 1996, *ApJ*, 461, 84
- Arnaboldi, M., Freeman, K. C., Mendez, R. H., et al. 1996, *ApJ*, 472, 145
- Auger, M. W., Treu, T., Bolton, A. S., et al. 2010a, *ApJ*, 724, 511
- Auger, M. W., Treu, T., Brewer, B. J., & Marshall, P. J. 2011, *MNRAS*, 411, L6
- Auger, M. W., Treu, T., Gavazzi, R., et al. 2010b, *ApJ*, 721, L163
- Bacon, R., Brinchmann, J., Richard, J., et al. 2015, *A&A*, 575, A75
- Baes, M., & Dejonghe, H. 2001, *ApJ*, 563, L19
- Baldry, I. K., Glazebrook, K., Brinkmann, J., et al. 2004, *ApJ*, 600, 681
- Barnabè, M., Czoske, O., Koopmans, L. V. E., Treu, T., & Bolton, A. S. 2011, *MNRAS*, 415, 2215
- Barnabè, M., Czoske, O., Koopmans, L. V. E., et al. 2009, *MNRAS*, 399, 21
- Barnes, J. E. 1988, *ApJ*, 331, 699
- . 1989, *Nature*, 338, 123
- Barnes, J. E., & Hernquist, L. 1996, *ApJ*, 471, 115
- Barro, G., Faber, S. M., Pérez-González, P. G., et al. 2014, *ApJ*, 791, 52
- Barth, A. J., Martini, P., Nelson, C. H., & Ho, L. C. 2003, *ApJ*, 594, L95
- Bédorf, J., & Portegies Zwart, S. 2013, *MNRAS*, 431, 767
- Behroozi, P. S., Conroy, C., & Wechsler, R. H. 2010, *ApJ*, 717, 379
- Bell, E. F., & de Jong, R. S. 2001, *ApJ*, 550, 212

- Bell, E. F., McIntosh, D. H., Katz, N., & Weinberg, M. D. 2003, *ApJS*, 149, 289
- Bender, R. 1988, *A&A*, 193, L7
- Bender, R., Burstein, D., & Faber, S. M. 1992, *ApJ*, 399, 462
- . 1993, *ApJ*, 411, 153
- Bender, R., Saglia, R. P., & Gerhard, O. E. 1994, *MNRAS*, 269, 785
- Bendo, G. J., & Barnes, J. E. 2000, *MNRAS*, 316, 315
- Bennert, V. N., Auger, M. W., Treu, T., Woo, J.-H., & Malkan, M. A. 2011, *ApJ*, 742, 107
- Bernardi, M., Sheth, R. K., Annis, J., et al. 2003, *AJ*, 125, 1866
- Bezanson, R., van Dokkum, P., van de Sande, J., Franx, M., & Kriek, M. 2013, *ApJ*, 764, L8
- Bezanson, R., van Dokkum, P. G., Tal, T., et al. 2009, *ApJ*, 697, 1290
- Bezanson, R., van Dokkum, P. G., Franx, M., et al. 2011, *ApJ*, 737, L31
- Binney, J. 1977, *ApJ*, 215, 483
- . 1978, *MNRAS*, 183, 501
- Binney, J., & Merrifield, M. 1998, *Galactic Astronomy*
- Binney, J., & Tremaine, S. 1987, *Galactic Dynamics*
- Birnboim, Y., & Dekel, A. 2003, *MNRAS*, 345, 349
- Blumenthal, G. R., Faber, S. M., Primack, J. R., & Rees, M. J. 1984, *Nature*, 311, 517
- Bogdán, Á., Forman, W. R., Zhuravleva, I., et al. 2012, *ApJ*, 753, 140
- Bournaud, F., Duc, P.-A., & Emsellem, E. 2008, *MNRAS*, 389, L8
- Bower, R. G., Benson, A. J., Malbon, R., et al. 2006, *MNRAS*, 370, 645
- Bower, R. G., Lucey, J. R., & Ellis, R. S. 1992, *MNRAS*, 254, 601
- Boylan-Kolchin, M., Bullock, J. S., & Kaplinghat, M. 2011, *MNRAS*, 415, L40
- Boyle, B. J., & Terlevich, R. J. 1998, *MNRAS*, 293, L49
- Bromm, V., Coppi, P. S., & Larson, R. B. 1999, *ApJ*, 527, L5
- Bromm, V., & Loeb, A. 2003, *ApJ*, 596, 34
- Bruzual, G., & Charlot, S. 2003, *MNRAS*, 344, 1000
- Buitrago, F., Trujillo, I., Conselice, C. J., et al. 2008, *ApJ*, 687, L61
- Bullock, J. S., Kolatt, T. S., Sigad, Y., et al. 2001, *MNRAS*, 321, 559
- Bullock, J. S., Kravtsov, A. V., & Weinberg, D. H. 2000, *ApJ*, 539, 517

- Bundy, K., Fukugita, M., Ellis, R. S., et al. 2009, *ApJ*, 697, 1369
- Bundy, K., Treu, T., & Ellis, R. S. 2007, *ApJ*, 665, L5
- Buote, D. A., Gastaldello, F., Humphrey, P. J., et al. 2007, *ApJ*, 664, 123
- Bureau, M., & Athanassoula, E. 2005, *ApJ*, 626, 159
- Burkert, A., & Naab, T. 2003, in *Lecture Notes in Physics*, Berlin Springer Verlag, Vol. 626, *Galaxies and Chaos*, ed. G. Contopoulos & N. Voglis, 327
- Burkert, A., & Naab, T. 2005, *MNRAS*, 363, 597
- Burkert, A., Naab, T., Johansson, P. H., & Jesseit, R. 2008, *ApJ*, 685, 897
- Burstein, D., Davies, R. L., Dressler, A., et al. 1987, *ApJS*, 64, 601
- Cappellari, M. 2002, *MNRAS*, 333, 400
- Cappellari, M., & Copin, Y. 2003, *MNRAS*, 342, 345
- Cappellari, M., & Emsellem, E. 2004, *PASP*, 116, 138
- Cappellari, M., Bacon, R., Bureau, M., et al. 2006, *MNRAS*, 366, 1126
- Cappellari, M., Emsellem, E., Bacon, R., et al. 2007, *MNRAS*, 379, 418
- Cappellari, M., McDermid, R. M., Alatalo, K., et al. 2012, *Nature*, 484, 485
- Cappellari, M., Scott, N., Alatalo, K., et al. 2013a, *MNRAS*, 432, 1709
- Cappellari, M., McDermid, R. M., Alatalo, K., et al. 2013b, *MNRAS*, 432, 1862
- Carlberg, R. G. 1986, *ApJ*, 310, 593
- Carollo, C. M., Bschorr, T. J., Renzini, A., et al. 2013, *ApJ*, 773, 112
- Cassata, P., Giavalisco, M., Guo, Y., et al. 2011, *ApJ*, 743, 96
- Cassata, P., Giavalisco, M., Williams, C. C., et al. 2013, *ApJ*, 775, 106
- CDMS II Collaboration, Ahmed, Z., Akerib, D. S., et al. 2010, *Science*, 327, 1619
- Chabrier, G. 2003, *ApJ*, 586, L133
- Chanamé, J., Kleyna, J., & van der Marel, R. 2008, *ApJ*, 682, 841
- Chandrasekhar, S. 1943, *ApJ*, 97, 255
- Chang, Y.-Y., van der Wel, A., Rix, H.-W., et al. 2013, *ApJ*, 762, 83
- Chung, A., & Bureau, M. 2004, *AJ*, 127, 3192
- Ciardullo, R., Jacoby, G. H., & Dejonghe, H. B. 1993, *ApJ*, 414, 454
- Cid Fernandes, R., Mateus, A., Sodré, L., Stasiska, G., & Gomes, J. M. 2005, *MNRAS*, 358, 363
- Cimatti, A., Nipoti, C., & Cassata, P. 2012, *MNRAS*, 422, L62

- Cimatti, A., Cassata, P., Pozzetti, L., et al. 2008, *A&A*, 482, 21
- Clauwens, B., Schaye, J., & Franx, M. 2014, *ArXiv e-prints*, arXiv:1406.0854
- Coccatto, L., Gerhard, O., Arnaboldi, M., et al. 2009, *MNRAS*, 394, 1249
- Cole, S., Norberg, P., Baugh, C. M., et al. 2001, *MNRAS*, 326, 255
- Colpi, M., Mayer, L., & Governato, F. 1999, *ApJ*, 525, 720
- Conroy, C., Gunn, J. E., & White, M. 2009, *ApJ*, 699, 486
- Conroy, C., & van Dokkum, P. G. 2012, *ApJ*, 760, 71
- Côté, P., McLaughlin, D. E., Cohen, J. G., & Blakeslee, J. P. 2003, *ApJ*, 591, 850
- Cowie, L. L., Songaila, A., Hu, E. M., & Cohen, J. G. 1996, *AJ*, 112, 839
- Cox, T. J., Dutta, S. N., Di Matteo, T., et al. 2006, *ApJ*, 650, 791
- Crain, R. A., Eke, V. R., Frenk, C. S., et al. 2007, *MNRAS*, 377, 41
- Cretton, N., de Zeeuw, P. T., van der Marel, R. P., & Rix, H.-W. 1999, *ApJS*, 124, 383
- Croton, D. J., Springel, V., White, S. D. M., et al. 2006, *MNRAS*, 365, 11
- Daddi, E., Renzini, A., Pirzkal, N., et al. 2005, *ApJ*, 626, 680
- Damjanov, I., Hwang, H. S., Geller, M. J., & Chilingarian, I. 2014, *ApJ*, 793, 39
- Davies, R. L., Efstathiou, G., Fall, S. M., Illingworth, G., & Schechter, P. L. 1983, *ApJ*, 266, 41
- de Vaucouleurs, G. 1948, *Annales d'Astrophysique*, 11, 247
- de Zeeuw, T. 1985, *MNRAS*, 216, 273
- de Zeeuw, T., & Franx, M. 1991, *ARA&A*, 29, 239
- Dekel, A., & Burkert, A. 2014, *MNRAS*, 438, 1870
- Dekel, A., & Silk, J. 1986, *ApJ*, 303, 39
- Dekel, A., Stoehr, F., Mamon, G. A., et al. 2005, *Nature*, 437, 707
- Dekel, A., Birnboim, Y., Engel, G., et al. 2009, *Nature*, 457, 451
- Di Matteo, T., Springel, V., & Hernquist, L. 2005, *Nature*, 433, 604
- Diehl, S., & Statler, T. S. 2007, *ApJ*, 668, 150
- Diemand, J., Kuhlen, M., Madau, P., et al. 2008, *Nature*, 454, 735
- Dijkstra, M., Haiman, Z., Mesinger, A., & Wyithe, J. S. B. 2008, *MNRAS*, 391, 1961
- Djorgovski, S., & Davis, M. 1987, *ApJ*, 313, 59
- Douglas, N. G., Napolitano, N. R., Romanowsky, A. J., et al. 2007, *ApJ*, 664, 257

- Dressler, A. 1980, *ApJ*, 236, 351
- . 1984, *ApJ*, 281, 512
- Dressler, A., Lynden-Bell, D., Burstein, D., et al. 1987, *ApJ*, 313, 42
- Duffy, A. R., Schaye, J., Kay, S. T., & Dalla Vecchia, C. 2008, *MNRAS*, 390, L64
- Dutton, A. A., Conroy, C., van den Bosch, F. C., Prada, F., & More, S. 2010, *MNRAS*, 407, 2
- Dutton, A. A., Macciò, A. V., Mendel, J. T., & Simard, L. 2013, *MNRAS*, 432, 2496
- Dutton, A. A., Mendel, J. T., & Simard, L. 2012, *MNRAS*, 422, L33
- Dutton, A. A., Conroy, C., van den Bosch, F. C., et al. 2011, *MNRAS*, 416, 322
- Efstathiou, G. 1995, in *Lecture Notes in Physics*, Berlin Springer Verlag, Vol. 463, *Galaxies in the Young Universe*, ed. H. Hippelein, K. Meisenheimer, & H.-J. Röser, 299
- Eggen, O. J., Lynden-Bell, D., & Sandage, A. R. 1962, *ApJ*, 136, 748
- Einasto, J., Kaasik, A., & Saar, E. 1974, *Nature*, 250, 309
- Emsellem, E. 2013, *MNRAS*, 433, 1862
- Emsellem, E., Monnet, G., & Bacon, R. 1994, *A&A*, 285, 723
- Emsellem, E., Cappellari, M., Krajnovi, D., et al. 2007, *MNRAS*, 379, 401
- . 2011, *MNRAS*, 414, 888
- Faber, S. M. 1973, *ApJ*, 179, 731
- Faber, S. M., & Jackson, R. E. 1976, *ApJ*, 204, 668
- Faber, S. M., Willmer, C. N. A., Wolf, C., et al. 2007, *ApJ*, 665, 265
- Fabian, A. C. 1999, *MNRAS*, 308, L39
- . 2012, *ARA&A*, 50, 455
- Falcón-Barroso, J., Sánchez-Blázquez, P., Vazdekis, A., et al. 2011, *A&A*, 532, A95
- Fan, L., Lapi, A., Bressan, A., et al. 2010, *ApJ*, 718, 1460
- Fan, L., Lapi, A., De Zotti, G., & Danese, L. 2008, *ApJ*, 689, L101
- Fan, X., Narayanan, V. K., Lupton, R. H., et al. 2001, *AJ*, 122, 2833
- Fan, X., Strauss, M. A., Schneider, D. P., et al. 2003, *AJ*, 125, 1649
- Ferrarese, L., & Merritt, D. 2000, *ApJ*, 539, L9
- Ferré-Mateu, A., Mezcua, M., Trujillo, I., & Balcells, M. 2015, submitted to *ApJ*
- Ferreras, I., La Barbera, F., de la Rosa, I. G., et al. 2013, *MNRAS*, 429, L15
- Forman, W., Jones, C., & Tucker, W. 1985, *ApJ*, 293, 102

- Franx, M., Illingworth, G., & Heckman, T. 1989, *AJ*, 98, 538
- Franx, M., van Dokkum, P. G., Schreiber, N. M. F., et al. 2008, *ApJ*, 688, 770
- Franx, M., Labbé, I., Rudnick, G., et al. 2003, *ApJ*, 587, L79
- Fukugita, M., Hogan, C. J., & Peebles, P. J. E. 1998, *ApJ*, 503, 518
- Gallazzi, A., Charlot, S., Brinchmann, J., & White, S. D. M. 2006, *MNRAS*, 370, 1106
- Gates, E. I., Gyuk, G., & Turner, M. S. 1996, *Phys. Rev. D*, 53, 4138
- Gebhardt, K., & Thomas, J. 2009, *ApJ*, 700, 1690
- Gebhardt, K., Bender, R., Bower, G., et al. 2000, *ApJ*, 539, L13
- Gebhardt, K., Richstone, D., Tremaine, S., et al. 2003, *ApJ*, 583, 92
- Gerhard, O., Kronawitter, A., Saglia, R. P., & Bender, R. 2001, *AJ*, 121, 1936
- Gerhard, O. E. 1993, *MNRAS*, 265, 213
- Gerhard, O. E., & Binney, J. J. 1996, *MNRAS*, 279, 993
- Gibson, B. K., & Mould, J. R. 1997, *ApJ*, 482, 98
- Gonzaga, S., Hack, W., Fruchter, A., & Mack, J. 2012, *The DrizzlePac Handbook*
- Graff, D. S., & Freese, K. 1996, *ApJ*, 467, L65
- Graves, G. J., Faber, S. M., & Schiavon, R. P. 2009a, *ApJ*, 693, 486
- . 2009b, *ApJ*, 698, 1590
- Greene, J. E., Ho, L. C., & Barth, A. J. 2008, *ApJ*, 688, 159
- Greene, J. E., Murphy, J. D., Comerford, J. M., Gebhardt, K., & Adams, J. J. 2012, *ApJ*, 750, 32
- Greene, J. E., Murphy, J. D., Graves, G. J., et al. 2013, *ApJ*, 776, 64
- Greene, J. E., Peng, C. Y., & Ludwig, R. R. 2010a, *ApJ*, 709, 937
- Greene, J. E., Peng, C. Y., Kim, M., et al. 2010b, *ApJ*, 721, 26
- Gültekin, K., Richstone, D. O., Gebhardt, K., et al. 2011, *ApJ*, 741, 38
- . 2009, *ApJ*, 698, 198
- Guo, Q., White, S., Li, C., & Boylan-Kolchin, M. 2010, *MNRAS*, 404, 1111
- Haehnelt, M. G., & Rees, M. J. 1993, *MNRAS*, 263, 168
- Häring, N., & Rix, H.-W. 2004, *ApJ*, 604, L89
- Hernquist, L. 1992, *ApJ*, 400, 460
- . 1993, *ApJ*, 409, 548

- Hill, G. J., Nicklas, H. E., MacQueen, P. J., et al. 1998, in Society of Photo-Optical Instrumentation Engineers (SPIE) Conference Series, Vol. 3355, Society of Photo-Optical Instrumentation Engineers (SPIE) Conference Series, ed. S. D'Odorico, 433
- Hilz, M., Naab, T., & Ostriker, J. P. 2013, MNRAS, 429, 2924
- Hilz, M., Naab, T., Ostriker, J. P., et al. 2012, MNRAS, 425, 3119
- Hinshaw, G., Weiland, J. L., Hill, R. S., et al. 2009, ApJS, 180, 225
- Hogg, D. W., Blanton, M., Strateva, I., et al. 2002, AJ, 124, 646
- Hopkins, A. M., & Beacom, J. F. 2006, ApJ, 651, 142
- Hopkins, P. F., Bundy, K., Hernquist, L., Wuyts, S., & Cox, T. J. 2010a, MNRAS, 401, 1099
- Hopkins, P. F., Bundy, K., Murray, N., et al. 2009a, MNRAS, 398, 898
- Hopkins, P. F., Hernquist, L., Cox, T. J., Keres, D., & Wuyts, S. 2009b, ApJ, 691, 1424
- Hopkins, P. F., & Quataert, E. 2010, MNRAS, 407, 1529
- Hopkins, P. F., Croton, D., Bundy, K., et al. 2010b, ApJ, 724, 915
- Hubble, E. 1926, Contributions from the Mount Wilson Observatory / Carnegie Institution of Washington, 324, 1
- Huchra, J., & Brodie, J. 1987, AJ, 93, 779
- Hui, X., Ford, H. C., Freeman, K. C., & Dopita, M. A. 1995, ApJ, 449, 592
- Humphrey, P. J., Buote, D. A., Gastaldello, F., et al. 2006, ApJ, 646, 899
- Husemann, B., Kamann, S., Sandin, C., et al. 2012, A&A, 545, A137
- Husemann, B., Wisotzki, L., Jahnke, K., & Sánchez, S. F. 2011, A&A, 535, A72
- Husemann, B., Jahnke, K., Sánchez, S. F., et al. 2013, A&A, 549, A87
- Hyde, J. B., & Bernardi, M. 2009, MNRAS, 396, 1171
- Jahnke, K., & Macciò, A. V. 2011, ApJ, 734, 92
- Jahnke, K., Bongiorno, A., Brusa, M., et al. 2009, ApJ, 706, L215
- Jeans, J. H. 1902, Royal Society of London Philosophical Transactions Series A, 199, 1
- Jesseit, R., Naab, T., & Burkert, A. 2005, MNRAS, 360, 1185
- Jimenez, R., Bernardi, M., Haiman, Z., Panter, B., & Heavens, A. F. 2007, ApJ, 669, 947
- Jones, D. H., Read, M. A., Saunders, W., et al. 2009, MNRAS, 399, 683
- Jorgensen, I., Franx, M., & Kjaergaard, P. 1996, MNRAS, 280, 167
- Kauffmann, G. 1996, MNRAS, 281, 487

- Kauffmann, G., & Charlot, S. 1998, *MNRAS*, 297, L23
- Kauffmann, G., White, S. D. M., & Guiderdoni, B. 1993, *MNRAS*, 264, 201
- Kelz, A., Verheijen, M. A. W., Roth, M. M., et al. 2006, *PASP*, 118, 129
- Kereš, D., Katz, N., Weinberg, D. H., & Davé, R. 2005, *MNRAS*, 363, 2
- Khochfar, S., & Silk, J. 2006, *ApJ*, 648, L21
- Kitayama, T., Yoshida, N., Susa, H., & Umemura, M. 2004, *ApJ*, 613, 631
- Klypin, A., Kravtsov, A. V., Bullock, J. S., & Primack, J. R. 2001, *ApJ*, 554, 903
- Klypin, A., Kravtsov, A. V., Valenzuela, O., & Prada, F. 1999, *ApJ*, 522, 82
- Kochanek, C. S. 1996, *ApJ*, 457, 228
- Komatsu, E., Dunkley, J., Nolta, M. R., et al. 2009, *ApJS*, 180, 330
- Koopmans, L. V. E., Treu, T., Bolton, A. S., Burles, S., & Moustakas, L. A. 2006, *ApJ*, 649, 599
- Koopmans, L. V. E., Bolton, A., Treu, T., et al. 2009, *ApJ*, 703, L51
- Koposov, S., Belokurov, V., Evans, N. W., et al. 2008, *ApJ*, 686, 279
- Kormendy, J. 1977, *ApJ*, 218, 333
- . 1988, *ApJ*, 325, 128
- Kormendy, J., & Bender, R. 1996, *ApJ*, 464, L119
- Kormendy, J., Bender, R., & Cornell, M. E. 2011, *Nature*, 469, 374
- Kormendy, J., Fisher, D. B., Cornell, M. E., & Bender, R. 2009, *ApJS*, 182, 216
- Kormendy, J., & Ho, L. C. 2013, *ARA&A*, 51, 511
- Kormendy, J., & Kennicutt, Jr., R. C. 2004, *ARA&A*, 42, 603
- Kormendy, J., & Richstone, D. 1995, *ARA&A*, 33, 581
- Kormendy, J., Bender, R., Magorrian, J., et al. 1997, *ApJ*, 482, L139
- Krajnovi, D., Cappellari, M., Emsellem, E., McDermid, R. M., & de Zeeuw, P. T. 2005, *MNRAS*, 357, 1113
- Kriek, M., van der Wel, A., van Dokkum, P. G., Franx, M., & Illingworth, G. D. 2008, *ApJ*, 682, 896
- Kriek, M., van Dokkum, P. G., Labbé, I., et al. 2009, *ApJ*, 700, 221
- Kriek, M., van Dokkum, P. G., Franx, M., et al. 2006, *ApJ*, 649, L71
- Krist, J. 1995, in *Astronomical Society of the Pacific Conference Series*, Vol. 77, *Astronomical Data Analysis Software and Systems IV*, ed. R. A. Shaw, H. E. Payne, & J. J. E. Hayes, 349
- Kronawitter, A., Saglia, R. P., Gerhard, O., & Bender, R. 2000, *A&AS*, 144, 53
- Kroupa, P. 2001, *MNRAS*, 322, 231

- Kroupa, P., Theis, C., & Boily, C. M. 2005, *A&A*, 431, 517
- Kuntschner, H., Emsellem, E., Bacon, R., et al. 2010, *MNRAS*, 408, 97
- Kuo, C. Y., Braatz, J. A., Condon, J. J., et al. 2011, *ApJ*, 727, 20
- La Barbera, F., Ferreras, I., de Carvalho, R. R., et al. 2012, *MNRAS*, 426, 2300
- La Barbera, F., Ferreras, I., Vazdekis, A., et al. 2013, *MNRAS*, 433, 3017
- Lackner, C. N., Cen, R., Ostriker, J. P., & Joung, M. R. 2012, *MNRAS*, 425, 641
- Larson, R. B. 1969, *MNRAS*, 145, 405
- . 1974, *MNRAS*, 169, 229
- Läscher, R., Ferrarese, L., & van de Ven, G. 2014a, *ApJ*, 780, 69
- Läscher, R., Ferrarese, L., van de Ven, G., & Shankar, F. 2014b, *ApJ*, 780, 70
- Läscher, R., van den Bosch, R. C. E., van de Ven, G., et al. 2013, *MNRAS*, 434, L31
- Lauer, T. R., Faber, S. M., Richstone, D., et al. 2007, *ApJ*, 662, 808
- Li, C., & White, S. D. M. 2009, *MNRAS*, 398, 2177
- Libeskind, N. I., Frenk, C. S., Cole, S., et al. 2005, *MNRAS*, 363, 146
- Loeb, A., & Rasio, F. A. 1994, *ApJ*, 432, 52
- Lotz, J. M., Jonsson, P., Cox, T. J., et al. 2011, *ApJ*, 742, 103
- Lousto, C. O., Nakano, H., Zlochower, Y., & Campanelli, M. 2010, *Phys. Rev. D*, 81, 084023
- Lynden-Bell, D. 1976, *MNRAS*, 174, 695
- Lyubenova, M., van den Bosch, R. C. E., Côté, P., et al. 2013, *MNRAS*, 431, 3364
- Macciò, A. V., Dutton, A. A., & van den Bosch, F. C. 2008, *MNRAS*, 391, 1940
- Madau, P., & Dickinson, M. 2014, *ARA&A*, 52, 415
- Madau, P., Diemand, J., & Kuhlen, M. 2008, *ApJ*, 679, 1260
- Madau, P., & Rees, M. J. 2001, *ApJ*, 551, L27
- Magorrian, J., Tremaine, S., Richstone, D., et al. 1998, *AJ*, 115, 2285
- Mamon, G. A., & Łokas, E. L. 2005a, *MNRAS*, 362, 95
- . 2005b, *MNRAS*, 363, 705
- Man, A. W. S., Toft, S., Zirm, A. W., Wuyts, S., & van der Wel, A. 2012, *ApJ*, 744, 85
- Mandelbaum, R., Seljak, U., Kauffmann, G., Hirata, C. M., & Brinkmann, J. 2006, *MNRAS*, 368, 715
- Marconi, A., & Hunt, L. K. 2003, *ApJ*, 589, L21

- Marcum, P. M., O'Connell, R. W., Fanelli, M. N., et al. 2001, *ApJS*, 132, 129
- Markarian, B. E. 1963, *Soobshcheniya Byurakanskoj Observatorii Akademiyi Nauk Armyanskoj SSR Erevan*, 34, 3
- Martín-Navarro, I., Barbera, F. L., Vazdekis, A., Falcón-Barroso, J., & Ferreras, I. 2015a, *MNRAS*, 447, 1033
- Martín-Navarro, I., La Barbera, F., Vazdekis, A., et al. 2015b, *ArXiv e-prints*: 1505.01485, arXiv:arXiv:1505.01485
- Mateo, M. L. 1998, *ARA&A*, 36, 435
- Matteucci, F., & Greggio, L. 1986, *A&A*, 154, 279
- McConnell, N. J., Chen, S.-F. S., Ma, C.-P., et al. 2013, *ApJ*, 768, L21
- McConnell, N. J., & Ma, C.-P. 2013, *ApJ*, 764, 184
- McConnell, N. J., Ma, C.-P., Gebhardt, K., et al. 2011, *Nature*, 480, 215
- McDermid, R. M., Alatalo, K., Blitz, L., et al. 2015, *MNRAS*, 448, 3484
- McGaugh, S. S., & de Blok, W. J. G. 1998, *ApJ*, 499, 41
- McLure, R. J., Pearce, H. J., Dunlop, J. S., et al. 2013, *MNRAS*, 428, 1088
- Méndez, R. H., Riffeser, A., Kudritzki, R.-P., et al. 2001, *ApJ*, 563, 135
- Merloni, A., Bongiorno, A., Bolzonella, M., et al. 2010, *ApJ*, 708, 137
- Merritt, D., Milosavljevi, M., Favata, M., Hughes, S. A., & Holz, D. E. 2004, *ApJ*, 607, L9
- Merritt, D., Schnittman, J. D., & Komossa, S. 2009, *ApJ*, 699, 1690
- Minkowski, R. 1962, in *IAU Symposium, Vol. 15, Problems of Extra-Galactic Research*, ed. G. C. McVittie, 112
- Miralda-Escudé, J., & Kollmeier, J. A. 2005, *ApJ*, 619, 30
- Monnet, G., Bacon, R., & Emsellem, E. 1992, *A&A*, 253, 366
- Moore, B. 1994, *Nature*, 370, 629
- Moore, B., Ghigna, S., Governato, F., et al. 1999a, *ApJ*, 524, L19
- Moore, B., Quinn, T., Governato, F., Stadel, J., & Lake, G. 1999b, *MNRAS*, 310, 1147
- More, S., van den Bosch, F. C., Cacciato, M., et al. 2011, *MNRAS*, 410, 210
- Morganti, L., Gerhard, O., Coccato, L., Martínez-Valpuesta, I., & Arnaboldi, M. 2013, *MNRAS*, 431, 3570
- Mortlock, D. J., Warren, S. J., Venemans, B. P., et al. 2011, *Nature*, 474, 616
- Moster, B. P., Somerville, R. S., Maulbetsch, C., et al. 2010, *ApJ*, 710, 903
- Mushotzky, R. F., Loewenstein, M., Awaki, H., et al. 1994, *ApJ*, 436, L79

- Naab, T., & Burkert, A. 2003, *ApJ*, 597, 893
- Naab, T., Burkert, A., & Hernquist, L. 1999, *ApJ*, 523, L133
- Naab, T., Jesseit, R., & Burkert, A. 2006, *MNRAS*, 372, 839
- Naab, T., Johansson, P. H., & Ostriker, J. P. 2009, *ApJ*, 699, L178
- Naab, T., Johansson, P. H., Ostriker, J. P., & Efstathiou, G. 2007, *ApJ*, 658, 710
- Naab, T., & Ostriker, J. P. 2009, *ApJ*, 690, 1452
- Naab, T., Oser, L., Emsellem, E., et al. 2014, *MNRAS*, 444, 3357
- Napolitano, N. R., Capaccioli, M., Romanowsky, A. J., et al. 2005, *MNRAS*, 357, 691
- Napolitano, N. R., Romanowsky, A. J., Capaccioli, M., et al. 2011, *MNRAS*, 411, 2035
- Navarro, J. F., Frenk, C. S., & White, S. D. M. 1996, *ApJ*, 462, 563
- . 1997, *ApJ*, 490, 493
- Navarro, J. F., Hayashi, E., Power, C., et al. 2004, *MNRAS*, 349, 1039
- Newman, A. B., Ellis, R. S., Bundy, K., & Treu, T. 2012, *ApJ*, 746, 162
- Nipoti, C., Treu, T., Leauthaud, A., et al. 2012, *MNRAS*, 422, 1714
- Nowak, N., Saglia, R. P., Thomas, J., et al. 2008, *MNRAS*, 391, 1629
- Omukai, K., & Nishi, R. 1998, *ApJ*, 508, 141
- Oogi, T., & Habe, A. 2013, *MNRAS*, 428, 641
- Oort, J. H. 1932, *Bull. Astron. Inst. Netherlands*, 6, 249
- Oser, L., Naab, T., Ostriker, J. P., & Johansson, P. H. 2012, *ApJ*, 744, 63
- Oser, L., Ostriker, J. P., Naab, T., Johansson, P. H., & Burkert, A. 2010, *ApJ*, 725, 2312
- Ostriker, J. P. 1980, *Comments on Astrophysics*, 8, 177
- Ostriker, J. P., Peebles, P. J. E., & Yahil, A. 1974, *ApJ*, 193, L1
- Padmanabhan, N., Seljak, U., Strauss, M. A., et al. 2004, *New Astronomy*, 9, 329
- Pahre, M. A., Djorgovski, S. G., & de Carvalho, R. R. 1998, *AJ*, 116, 1591
- Patel, S. G., van Dokkum, P. G., Franx, M., et al. 2013, *ApJ*, 766, 15
- Peñarrubia, J., McConnachie, A., & Babul, A. 2006, *ApJ*, 650, L33
- Peñarrubia, J., McConnachie, A. W., & Navarro, J. F. 2008, *ApJ*, 672, 904
- Peebles, P. J. E. 1980, *The large-scale structure of the universe*
- Peletier, R. F., Davies, R. L., Illingworth, G. D., Davis, L. E., & Cawson, M. 1990a, *AJ*, 100, 1091

- Peletier, R. F., Valentijn, E. A., & Jameson, R. F. 1990b, *A&A*, 233, 62
- Peng, C. Y. 2007, *ApJ*, 671, 1098
- Peng, C. Y., Ho, L. C., Impey, C. D., & Rix, H.-W. 2002, *AJ*, 124, 266
- Pérez, E., Cid Fernandes, R., González Delgado, R. M., et al. 2013, *ApJ*, 764, L1
- Perlmutter, S., Aldering, G., Goldhaber, G., et al. 1999, *ApJ*, 517, 565
- Petri, A., Ferrara, A., & Salvaterra, R. 2012, *MNRAS*, 422, 1690
- Petrosian, A., McLean, B., Allen, R. J., & MacKenty, J. W. 2007, *ApJS*, 170, 33
- Pierce, M., Beasley, M. A., Forbes, D. A., et al. 2006, *MNRAS*, 366, 1253
- Poggianti, B. M., Calvi, R., Bindoni, D., et al. 2013, *ApJ*, 762, 77
- Press, W. H., & Schechter, P. 1974, *ApJ*, 187, 425
- Quilis, V., & Trujillo, I. 2013, *ApJ*, 773, L8
- Rawle, T. D., Smith, R. J., Lucey, J. R., & Swinbank, A. M. 2008, *MNRAS*, 389, 1891
- Rees, M. J., & Ostriker, J. P. 1977, *MNRAS*, 179, 541
- Remus, R.-S., Burkert, A., Dolag, K., et al. 2013, *ApJ*, 766, 71
- Renzini, A., & Ciotti, L. 1993, *ApJ*, 416, L49
- Ricciardelli, E., Vazdekis, A., Cenarro, A. J., & Falcón-Barroso, J. 2012, *MNRAS*, 424, 172
- Richards, G. T., Strauss, M. A., Fan, X., et al. 2006, *AJ*, 131, 2766
- Richstone, D., Ajhar, E. A., Bender, R., et al. 1998, *Nature*, 395, A14
- Riess, A. G., Filippenko, A. V., Challis, P., et al. 1998, *AJ*, 116, 1009
- Rix, H.-W., de Zeeuw, P. T., Cretton, N., van der Marel, R. P., & Carollo, C. M. 1997, *ApJ*, 488, 702
- Robertson, B., Cox, T. J., Hernquist, L., et al. 2006, *ApJ*, 641, 21
- Romanowsky, A. J., Douglas, N. G., Arnaboldi, M., et al. 2003, *Science*, 301, 1696
- Roth, M. M., Kelz, A., Fechner, T., et al. 2005, *PASP*, 117, 620
- Rubin, V. C., Ford, W. K. J., & Thonnard, N. 1980, *ApJ*, 238, 471
- Rusli, S. P., Thomas, J., Erwin, P., et al. 2011, *MNRAS*, 410, 1223
- Rusli, S. P., Thomas, J., Saglia, R. P., et al. 2013, *AJ*, 146, 45
- Rybicki, G. B. 1987, in *IAU Symposium, Vol. 127, Structure and Dynamics of Elliptical Galaxies*, ed. P. T. de Zeeuw, 397
- Sambhus, N., Gerhard, O., & Méndez, R. H. 2006, *AJ*, 131, 837
- Sánchez, S. F., Kennicutt, R. C., Gil de Paz, A., et al. 2012, *A&A*, 538, A8

- Sánchez-Blázquez, P., Forbes, D. A., Strader, J., Brodie, J., & Proctor, R. 2007, *MNRAS*, 377, 759
- Sánchez-Blázquez, P., Peletier, R. F., Jiménez-Vicente, J., et al. 2006, *MNRAS*, 371, 703
- Sandage, A., & Visvanathan, N. 1978a, *ApJ*, 225, 742
- . 1978b, *ApJ*, 223, 707
- Sani, E., Marconi, A., Hunt, L. K., & Risaliti, G. 2011, *MNRAS*, 413, 1479
- Sargent, W. L. W., Young, P. J., Lynds, C. R., et al. 1978, *ApJ*, 221, 731
- Saulder, C., van den Bosch, R. C. E., & Mieske, S. 2015, *ArXiv e-prints*, arXiv:1503.05117
- Schlafly, E. F., & Finkbeiner, D. P. 2011, *ApJ*, 737, 103
- Schlegel, D. J., Finkbeiner, D. P., & Davis, M. 1998, *ApJ*, 500, 525
- Schmidt, R. W., & Allen, S. W. 2007, *MNRAS*, 379, 209
- Schuberth, Y., Richtler, T., Hilker, M., et al. 2010, *A&A*, 513, A52
- Schulze, A., & Gebhardt, K. 2011, *ApJ*, 729, 21
- Schwarzschild, M. 1979, *ApJ*, 232, 236
- Shakura, N. I., & Sunyaev, R. A. 1973, *A&A*, 24, 337
- Sheth, R. K., Bernardi, M., Schechter, P. L., et al. 2003, *ApJ*, 594, 225
- Shields, G. A., & Bonning, E. W. 2013, *ApJ*, 772, L5
- Shields, G. A., Menezes, K. L., Massart, C. A., & Vanden Bout, P. 2006, *ApJ*, 641, 683
- Shlosman, I., Frank, J., & Begelman, M. C. 1989, *Nature*, 338, 45
- Silk, J. 1977, *ApJ*, 211, 638
- Silk, J., & Rees, M. J. 1998, *A&A*, 331, L1
- Smith, R. J. 2014, *MNRAS*, 443, L69
- Somerville, R. S., Hopkins, P. F., Cox, T. J., Robertson, B. E., & Hernquist, L. 2008, *MNRAS*, 391, 481
- Spergel, D. N., Verde, L., Peiris, H. V., et al. 2003, *ApJS*, 148, 175
- Spergel, D. N., Bean, R., Doré, O., et al. 2007, *ApJS*, 170, 377
- Spiniello, C., Trager, S., Koopmans, L. V. E., & Conroy, C. 2014, *MNRAS*, 438, 1483
- Spiniello, C., Trager, S. C., Koopmans, L. V. E., & Chen, Y. P. 2012, *ApJ*, 753, L32
- Springel, V., Frenk, C. S., & White, S. D. M. 2006, *Nature*, 440, 1137
- Springel, V., Wang, J., Vogelsberger, M., et al. 2008, *MNRAS*, 391, 1685
- Statler, T. S. 1987, *ApJ*, 321, 113

- Stoughton, C., Lupton, R. H., Bernardi, M., et al. 2002, *AJ*, 123, 485
- Szomoru, D., Franx, M., & van Dokkum, P. G. 2012, *ApJ*, 749, 121
- Szomoru, D., Franx, M., van Dokkum, P. G., et al. 2013, *ApJ*, 763, 73
- . 2010, *ApJ*, 714, L244
- Tamura, N., & Ohta, K. 2003, *AJ*, 126, 596
- Tan, J. C., & McKee, C. F. 2004, *ApJ*, 603, 383
- Taylor, E. N., Franx, M., Glazebrook, K., et al. 2010, *ApJ*, 720, 723
- Terlevich, R., Davies, R. L., Faber, S. M., & Burstein, D. 1981, *MNRAS*, 196, 381
- Thomas, D., Maraston, C., Bender, R., & Mendes de Oliveira, C. 2005a, *ApJ*, 621, 673
- Thomas, J., Saglia, R. P., Bender, R., et al. 2005b, *MNRAS*, 360, 1355
- . 2007, *MNRAS*, 382, 657
- . 2004, *MNRAS*, 353, 391
- . 2011, *MNRAS*, 415, 545
- Toft, S., Gallazzi, A., Zirm, A., et al. 2012, *ApJ*, 754, 3
- Toft, S., van Dokkum, P., Franx, M., et al. 2005, *ApJ*, 624, L9
- . 2007, *ApJ*, 671, 285
- Toft, S., Smoli, V., Magnelli, B., et al. 2014, *ApJ*, 782, 68
- Tonry, J. L. 1984, *ApJ*, 283, L27
- Toomre, A. 1964, *ApJ*, 139, 1217
- Toomre, A. 1977, in *Evolution of Galaxies and Stellar Populations*, ed. B. M. Tinsley & R. B. G. Larson, D. Campbell, 401
- Toomre, A., & Toomre, J. 1972, *ApJ*, 178, 623
- Tortora, C., Napolitano, N. R., Cardone, V. F., et al. 2010, *MNRAS*, 407, 144
- Tortora, C., Napolitano, N. R., Romanowsky, A. J., et al. 2011, *MNRAS*, 418, 1557
- Tortora, C., Romanowsky, A. J., & Napolitano, N. R. 2013, *ApJ*, 765, 8
- Tremaine, S., Gebhardt, K., Bender, R., et al. 2002, *ApJ*, 574, 740
- Treu, T., Auger, M. W., Koopmans, L. V. E., et al. 2010, *ApJ*, 709, 1195
- Trujillo, I., Cenarro, A. J., de Lorenzo-Cáceres, A., et al. 2009, *ApJ*, 692, L118
- Trujillo, I., Ferré-Mateu, A., Balcells, M., Vazdekis, A., & Sánchez-Blázquez, P. 2014, *ApJ*, 780, L20
- Trujillo, I., Förster Schreiber, N. M., Rudnick, G., et al. 2006, *ApJ*, 650, 18

- Valdes, F., Gupta, R., Rose, J. A., Singh, H. P., & Bell, D. J. 2004, *ApJS*, 152, 251
- Vale, A., & Ostriker, J. P. 2004, *MNRAS*, 353, 189
- Valentinuzzi, T., Poggianti, B. M., Saglia, R. P., et al. 2010, *ApJ*, 721, L19
- Valluri, M., Merritt, D., & Emsellem, E. 2004, *ApJ*, 602, 66
- van Albada, T. S., Bahcall, J. N., Begeman, K., & Sancisi, R. 1985, *ApJ*, 295, 305
- van de Sande, J., Kriek, M., Franx, M., et al. 2011, *ApJ*, 736, L9
- . 2013, *ApJ*, 771, 85
- van de Ven, G., de Zeeuw, P. T., & van den Bosch, R. C. E. 2008, *MNRAS*, 385, 614
- van den Bosch, F. C. 1997, *MNRAS*, 287, 543
- van den Bosch, R. C. E., & de Zeeuw, P. T. 2010, *MNRAS*, 401, 1770
- van den Bosch, R. C. E., Gebhardt, K., Gültekin, K., et al. 2012, *Nature*, 491, 729
- van den Bosch, R. C. E., Gebhardt, K., Gültekin, K., Yıldırım, A., & Walsh, J. 2015, *ArXiv e-prints*, arXiv:1502.00632
- van den Bosch, R. C. E., & van de Ven, G. 2009, *MNRAS*, 398, 1117
- van den Bosch, R. C. E., van de Ven, G., Verolme, E. K., Cappellari, M., & de Zeeuw, P. T. 2008, *MNRAS*, 385, 647
- van der Marel, R. P. 1991, *MNRAS*, 253, 710
- van der Marel, R. P., & Franx, M. 1993, *ApJ*, 407, 525
- van der Wel, A., Holden, B. P., Zirm, A. W., et al. 2008, *ApJ*, 688, 48
- van der Wel, A., Rix, H.-W., Wuyts, S., et al. 2011, *ApJ*, 730, 38
- van der Wel, A., Bell, E. F., Häussler, B., et al. 2012, *ApJS*, 203, 24
- van der Wel, A., Franx, M., van Dokkum, P. G., et al. 2014, *ApJ*, 788, 28
- van Dokkum, P. G., & Conroy, C. 2010, *Nature*, 468, 940
- . 2012, *ApJ*, 760, 70
- van Dokkum, P. G., Kriek, M., & Franx, M. 2009, *Nature*, 460, 717
- van Dokkum, P. G., Förster Schreiber, N. M., Franx, M., et al. 2003, *ApJ*, 587, L83
- van Dokkum, P. G., Franx, M., Kriek, M., et al. 2008, *ApJ*, 677, L5
- van Dokkum, P. G., Whitaker, K. E., Brammer, G., et al. 2010, *ApJ*, 709, 1018
- Vazdekis, A., Casuso, E., Peletier, R. F., & Beckman, J. E. 1996, *ApJS*, 106, 307
- Vazdekis, A., Ricciardelli, E., Cenarro, A. J., et al. 2012, *MNRAS*, 424, 157

- Vazdekis, A., Sánchez-Blázquez, P., Falcón-Barroso, J., et al. 2010, *MNRAS*, 404, 1639
- Verheijen, M. A. W., Bershadsky, M. A., Andersen, D. R., et al. 2004, *Astronomische Nachrichten*, 325, 151
- Vernet, J., Dekker, H., D'Odorico, S., et al. 2011, *A&A*, 536, A105
- Verolme, E. K., Cappellari, M., Copin, Y., et al. 2002, *MNRAS*, 335, 517
- Vestergaard, M. 2009, ArXiv e-prints, arXiv:0904.2615 [astro-ph.CO]
- Vestergaard, M., & Osmer, P. S. 2009, *ApJ*, 699, 800
- Volonteri, M. 2010, *A&A Rev.*, 18, 279
- Volonteri, M., & Rees, M. J. 2005, *ApJ*, 633, 624
- Walsh, J. L., van den Bosch, R. C. E., Barth, A. J., & Sarzi, M. 2012, *ApJ*, 753, 79
- Walsh, J. L., van den Bosch, R. C. E., Gebhardt, K., et al. 2015, submitted to *ApJ*
- Walter, F., Carilli, C., Bertoldi, F., et al. 2004, *ApJ*, 615, L17
- Wandel, A., Peterson, B. M., & Malkan, M. A. 1999, *ApJ*, 526, 579
- Weijmans, A.-M., Cappellari, M., Bacon, R., et al. 2009, *MNRAS*, 398, 561
- Weijmans, A.-M., de Zeeuw, P. T., Emsellem, E., et al. 2014, *MNRAS*, 444, 3340
- Wess, J., & Zumino, B. 1974, *Nuclear Physics B*, 70, 39
- Whalen, D., Abel, T., & Norman, M. L. 2004, *ApJ*, 610, 14
- White, S. D. M., & Frenk, C. S. 1991, *ApJ*, 379, 52
- White, S. D. M., & Rees, M. J. 1978, *MNRAS*, 183, 341
- Wilkinson, M. I., & Evans, N. W. 1999, *MNRAS*, 310, 645
- Williams, C. C., Giavalisco, M., Cassata, P., et al. 2014, *ApJ*, 780, 1
- Williams, R. J., Quadri, R. F., Franx, M., van Dokkum, P., & Labbé, I. 2009, *ApJ*, 691, 1879
- Willman, B., Dalcanton, J. J., Martinez-Delgado, D., et al. 2005, *ApJ*, 626, L85
- Willott, C. J., Percival, W. J., McLure, R. J., et al. 2005, *ApJ*, 626, 657
- Woo, J.-H., Treu, T., Malkan, M. A., & Blandford, R. D. 2006, *ApJ*, 645, 900
- . 2008, *ApJ*, 681, 925
- Woodley, K. A., Gómez, M., Harris, W. E., Geisler, D., & Harris, G. L. H. 2010, *AJ*, 139, 1871
- Worthey, G., Faber, S. M., Gonzalez, J. J., & Burstein, D. 1994, *ApJS*, 94, 687
- Wu, X.-B., Wang, F., Fan, X., et al. 2015, ArXiv e-prints, arXiv:1502.07418
- Wuyts, S., Cox, T. J., Hayward, C. C., et al. 2010, *ApJ*, 722, 1666

- Wyithe, J. S. B., & Loeb, A. 2012, MNRAS, 425, 2892
- York, D. G., Adelman, J., Anderson, Jr., J. E., et al. 2000, AJ, 120, 1579
- Zibetti, S., Charlot, S., & Rix, H.-W. 2009, MNRAS, 400, 1181
- Zibetti, S., Gavazzi, G., Scodreggio, M., Franzetti, P., & Boselli, A. 2002, ApJ, 579, 261
- Zirm, A. W., van der Wel, A., Franx, M., et al. 2007, ApJ, 656, 66
- Zucker, D. B., Belokurov, V., Evans, N. W., et al. 2006, ApJ, 643, L103
- Zwicky, F. 1937, ApJ, 86, 217